CeNTE
Annual Report 2023

SPIS TREŚCI

IPPLM: Institute of Plasma Physics and Laser Microfusion

WPW7X: W7X Exploitation

Title: W7-X experimental data analysis and PHA diagnostic system upgrade

Authors: T. Fornal, M. Gruca, S. Jabłoński, M. Kubkowska, Ł. Syrocki

Introduction

The PHA diagnostics modernization plan aimed to increase the measurement capabilities of the spectrometer in terms of operation at high count rates, as well as to improve statistics. Before the next planned experimental campaign, where higher heating powers will be obtained, it is necessary to improve the diagnostic efficiency to work at high counting rates.

Moreover, analysis of the PHA data were conducted together with simulations based on the data collected during the latest experimental campaign OP2.1, as well as the previous campaign OP1.1. The focus was mainly on investigating W lines in the PHA spectra, impurity concentration, impurity decay time, and searching for possible indications of fast electron presence. Another task involved the examination of the initial experimental data from the C/O monitor and simulating the potential impact of the O^{6+} line on the overall measured O^{7+} signal by the C/O monitor system.

Results

Preparation and commissioning of diagnostics and software tools

As part of the modernization of PHA diagnostics on W7-X, a new SDD detector was purchased for the first channel of the spectrometer. The detector flange was designed and modernized to adapt it to the new detectors (heat removal system, vacuum connectors, preamplifier output). The possibility of replacing the remaining detectors was also analysed to modernize the entire spectrometer to work in the high counting rate regime. The process of designing a new "detector box" has begun, which will enable the installation of new detectors and the optimal connection of a digital amplitude analyser. Tests of the new detector were also carried out using an X-ray tube to optimize the operation of the digital amplitude analyser. Energy calibration of the new detector (Fe source and X-ray tube) was also performed. As part of the adaptation of the software to support PHA diagnostics, necessary changes were introduced in the power supply and calibration modules.

In the year 2023, analyses of the PHA data were also performed. The data were collected during the last experimental campaign OP2.1. In these studies, the data were modeled using numerical codes such as the upgraded RayX code (called SimXRay) and the Flexible Atomic Code to simulate plasma impurities, providing insights into impurity content, electron temperature and effective ion charge. Results demonstrate successful agreement between experimental and simulated spectra, allowing for a comprehensive understanding of plasma parameters and impurity behavior in W7-X (see *Figure 1*).

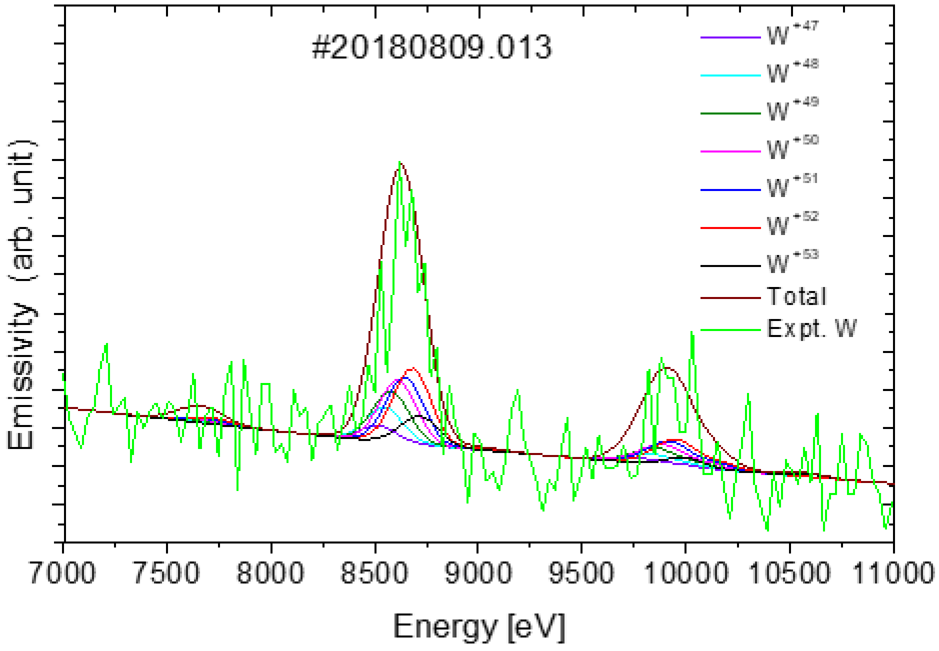

Figure 1. Example of simulated X-ray lines of W^{+51} ion, taking into account experimental temperature and density profiles obtained by the Thomson Scattering diagnostic and fractional abundance of tungsten, using FAC code.

Moreover, a set of analyses was conducted on titanium decay times that were injected into the plasma during the OP 2.1 experimental campaign at Wendelstein 7-X. The study focused on the relationship between t_{dec} and plasma parameters, revealing a nearly linear decrease in Ti decay time with increasing Electron Cyclotron Resonance Heating power (see *Figure 2. Decay time variation for different ECRH heating values [MW].Figure 2*). Other attempts were made also to conduct similar analyses for other elements like iron and tungsten, however, the more consistent and higher quality data needs to be collected in order to proceed further.

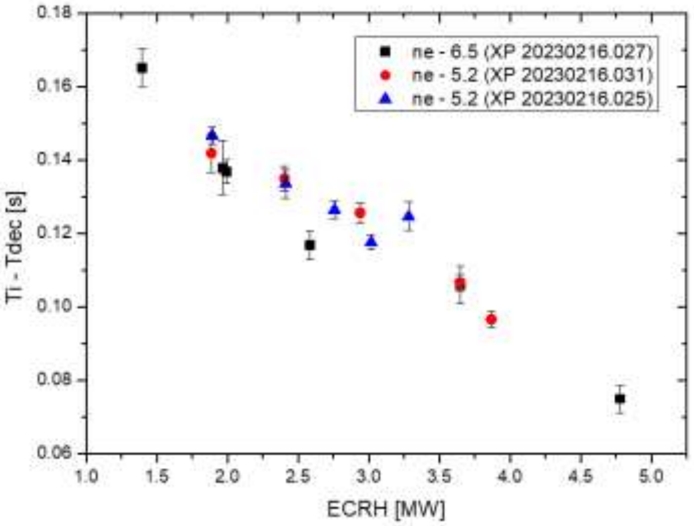

Figure 2. Decay time variation for different ECRH heating values [MW].

Finally, a study to evaluate carbon and oxygen content in specific discharges using PHA system (e.g., 20180807.012@5.05s) was conducted, aiming to compare measurements with impurity transport and radiation models. The analysis has shown relatively constant impurity levels with a slight increase in carbon. Additionally, an investigation into detecting fast electrons using PHA diagnostics across multiple experiments did not confirm their presence, suggesting possible limitations in PHA statistics or sensitivity to subtle changes (see Figure 3).

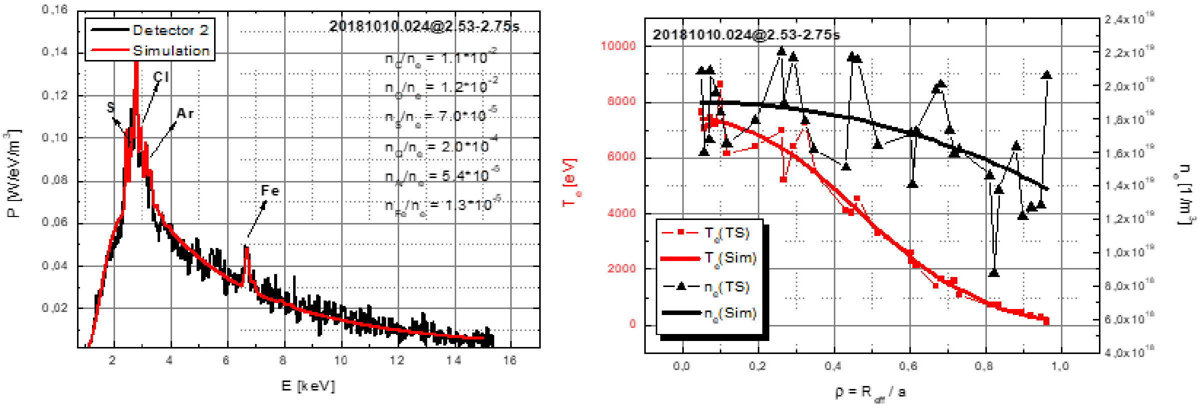

Figure 3. Exemplary graph indicating the absence of observable evidence for the existence of fast electrons.

The work related to C/O monitor included studies of assessing the impact of the O^{6+} line on O^{7+} emissivity measurements conducted by the system in the W7-X. Simulations were performed to understand the potential impact of the O^{6+} line on the measured signal originating from the Lyman-α line. The analysis revealed that the O^{6+} line has a negligible impact on the overall measured signal, supporting the reliability of the C/O monitor system for accurately measuring the O^{7+} signal level in experimental discharges (see *Figure 4* and *Figure 5*).

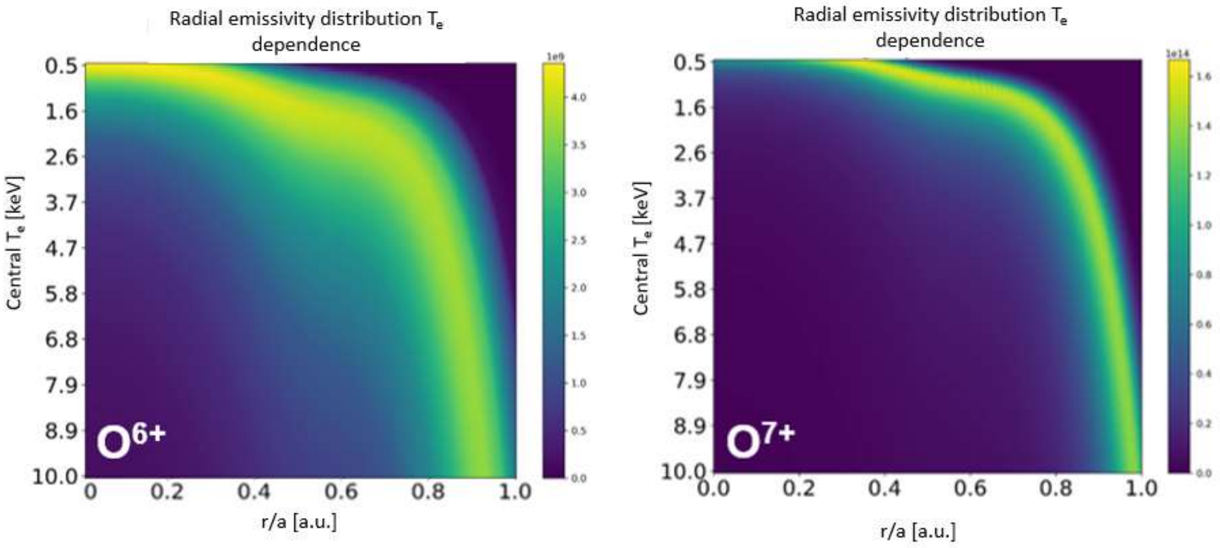

Figure 4. Emissivity distribution of the O6+ (1.6 nm) and O7+ (represented in different colors) lines, as a function of changes in the profiles of central plasma temperature depending on the maximum value of the normalized plasma radius function (r/a).

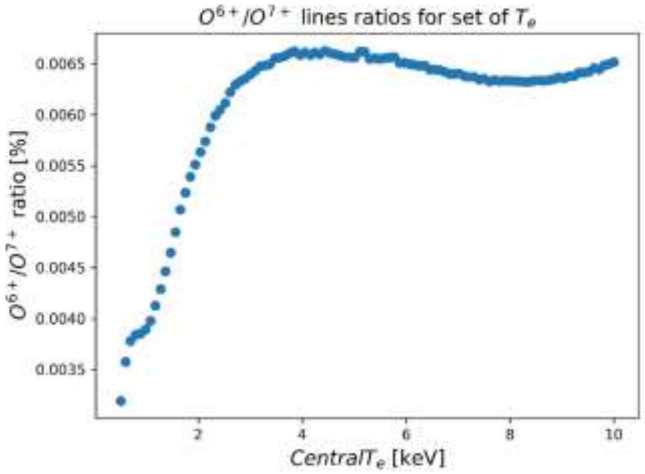

Figure 5. Ratio of radiation intensity for the O6+ (1.86 nm) line to the O7+ (1.9 nm) line as a function of electron temperature distributions. The x-axis represents the maximum values of electron temperatures [keV] at the plasma center, while the y-axis represents the percentage ratio of the total intensities of both lines.

Conclusions

The planned task for the modernization of PHA diagnostics in 2023 has been successfully accomplished. Additionally, all tasks related to data analysis were completed without. However, the experiments involving impurity pellet injections were not successful due to malfunctions in W7-X. As a result, they will need to be repeated during OP 2.2.

Collaboration

W7-X team

References

[1] T. Fornal – “Investigation of oxygen signal level measured by the C/O monitor system from the W7-X plasmas”, Poster, Plasma 2023, Warsaw, Poland
[2] I. Książek – “First results obtained by the C/O monitor system”, Poster, Plasma 2023, Warsaw, Poland
[3] Ł. Syrocki – “Theoretical Interpretation of Soft X-ray Spectra Collected by the Pulse Height Analysis System on Wendelstein 7-X Stellarator”, Oral presentation, Plasma 2023, Warsaw, Poland

Research Unit: Institute of Plasma Phyiscs and Laser Microfusion

WPTE: Tokamak exploitation

Title: Tokamak Eploitation

Author: A. Chomiczewska

Introduction

In the WPTE work package, work was carried out on four devices: JET, MAST-U, TCV, and WEST in 2023. Tokamak ASDEX Upgrade was in an extended shutdown period during which important hardware updates were installed. In 2023, WPTE focused on nine defined research topics (RT), but in parallel, a campaign of analysis and modeling of experiments performed on the JET tokamak in previous years was carried out to continue the work started. It should be emphasized that IPPLM scientists participated in the third and final experimental campaign using a deuterium-tritium fuel mixture (DTE3) in the JET fusion device. The result was a world record of 69 MJ of energy from the D-T fusion reaction using only 0.2 mg of fuel in a single discharge lasting 5 s.

Results

In various experiments on the JET tokamak, the influence of hydrogen isotopes (H, D, T) on the impurity behaviour was investigated. The dimensionless and dimensional isotope identity experiment between pure D and T L-mode plasmas has been performed for the first time in the JET W/Be wall In the first approach, the discharges with matched dimensionless quantities of normalised Larmor radius $\rho*$, normalised collisionality $\nu*$, normalised beta β_N, and safety factor q, were compared to minimize indirect effects and emphasize direct isotope effects. In the second approach, the engineering quantities such as toroidal magnetic field, plasma current, plasma electron density and NBI power were matched. Higher plasmas radiation, Ni and W impurity content in T plasmas in comparison to D plasmas was measured in both isotope scaling experiments. The results with the COREDIV code confirmed similar observations from the numerical simulations. It was found that the main core radiators in the examined plasmas were Ni and W impurities. The observed differences in the core impurity behaviour were related to different impurity transport in D and T plasmas. Besides, central impurity radiation was also influenced by differences in T_e in this plasma region between D and T plasmas. The density difference, necessary for creating the dimensionless match, dominated over the isotope mass effect on the Be source measured at the limiter. In the dimensionless pair comparison, Be influx was higher in D discharge. This is explained by lower ne in D plasma and therefore stronger Be sputtering. In the dimensional case, the Be source was higher in T plasma. In that approach, for similar n_e a clear isotope effect on the Be source was observed. Higher divertor plate temperatures, than those measured in both experiments, are needed for W sputtering by D or T. In the dimensionless isotope identity experiment, the experimental observations were in line with impurity simulations, which showed that W in the divertor region was mainly sputtered by Ni in T plasmas and by Be in D plasmas, not by hydrogen isotopes. However, in the dimensional isotope identity experiment, Be impact on W sputtering in T plasmas is stronger in comparison to the dimensionless case.

The investigation also focused on the evaluation of the plasma triangularity(δ) impact on the impurity radiation in H, D, T and DT plasmas. The variations of δ were in the range of 0.21-0.31. The results confirm the rise in Be flux with plasma isotope and lower δ leading to higher plasma density close to the plasma wall. The dominant role of W as a source of plasma radiation has also been confirmed. For mid-Z impurities and W, the variations in their densities due to δ change are negligible and the rise in their densities is observed with higher isotope mass, although this effect is often masked by the dominant role of ELM frequency on the impurity level. The impurity radiation losses based on bolometry are the highest for T plasmas and the lowest for H, whereas for DT pulses they are between D and T, which is consistent with the former analyses.

Two scenarios in deuterium-tritium were thoroughly tested in support of a possible ITER scenario: the Hybrid scenario (low plasma current, low density) and the ITER- Baseline scenario (high plasma current and high density). Differently from the Hybrid scenario, the pulses of the D-T Baseline could not be sustained for more than 1-2 seconds, due to disruption caused by excessive radiation, while the pulses of the Baseline scenario in D could be sustained for the full pulse duration. Among the many possible reasons for this behaviour in D-T baseline plasmas is that the high level and the large broadening of the electron density profile (both typical aspects of the D-T pulses) cause the above-mentioned D-T plasma disruptions. The data analysis as well as the numerical simulations with the code COREDIV have clearly shown that the uncontrolled increase of the electron density, not that of the tungsten influx (as was erroneously thought at the beginning), was the cause of the strong increase of the radiated power which led to discharge disruption of the D-T Baseline JET pulses. The W influx was even lower in D-T plasmas than in D plasmas and the W residence time is comparable in D and D-T plasmas. The comparison of fast time-dependent data with the time-averaged data used for the numerical model showed that the Neo-Classical, theory predicts a very strong W inward pinch at the pedestal which should lead to impurity accumulation in D-T plasmas, due to the very high density gradient between the sepatrix and the pedestal top. On the other hand, COREDIV results show a quite modest impurity inward pinch, balanced by the outward pinch caused by ICRF central heating and by impurity diffusion in the central plasma. Another interesting result of COREDIV simulations is the higher impurity retention capability of the divertor in D-T than in D plasmas, which contributes, together with the lower impurity fluxes, to a lesser impurity density in D-T.

The influence of N, Ar+N and Ne impurity seeding on plasma performance in JET tokamak was investigated. IPPLM staff analysed the behaviour of intrinsic impurities (e.g. W, Be, Ni, Fe, Cu), plasma radiation and the impurity transport. The conducted research has shown that increased N seeding leads to changes in temperatures and densities in the pedestal area and affects the transport of impurities. An outflow of admixtures towards the separatrix was observed. As the amount of gas injected increases, the amount of impurities in the central plasma decreases. In the case of different Ar and N ratios, it was observed that both the plasma radiated power and impurity concentrations are higher with higher Ar injection and the lowest N level.

Analysis of neutron camera data showed that the baseline discharges with Ne seeding are characterized by the occurrence of annular neutron emission profiles. Decreases in emissivity in the centre of the plasma and local asymmetries are observed. This allows us to hypothesize the influence of Ne on the decrease in the ion temperature in the JET tokamak plasma core.

Activities in connection with JET experiment RT22-05-HDL “Physics of divertor detachment and its control for ITER, DEMO and HELIAS operation” - subtask HDL (“H-mode Density Limit”), which started in 2022 under the scientific coordination of IPPLM staff, continued in 2023. The plasma density limit was tested using fuel injections in the form of pellets or gas puffs. The analysis showed that, near the separatrix, a region of very steep electron densities was observed. Despite observing clearly higher density in the near- and far-SOL with gas dosing than with pellets, the overall difference in separatrix density between pellet and gas-fueled cases just before the HDL appeared to be very small. This behaviour was also influenced by the densities and temperatures prevailing in the divertor region.

The experiments conducted on the TCV tokamak focused, among others, on the analysis of the development of the scenario with high plasma heating power in L-mode, as well as on research related to limiting the deposited power by N seeding. It turned out that with the increase of the N, the carbon concentration and the effective plasma charge Zeff decreased. The ion temperature increases slightly. In the case of rotation velocity, no correlations were found with the injected N. In the experiment conducted on the TCV tokamak, which was aimed at optimizing the high β plasma scenario, the influence of the presence of an internal electron transport barrier (eITB) in the plasma and, in the second approach, an edge transport barrier (ETB) was investigated. Based on the analysis of (Charge Exchange Recombination Spectroscopy (CXRS) diagnostics data, it was concluded that in the case of the ETB scenario, higher values of rotation velocity are also achieved for higher β_N values. In the scenario consisting of a combination of both eITB+ETB approaches almost flat rotation velocity profiles between normalized plasma radius ρ=0.5-1 are observed. The lowest carbon concentrations were observed for the ETB scenario, intermediate for eITB+ETB, and the highest for the ITB scenario.

Numerical simulations were also performed for the TCV tokamak using the SOLPS-ITER code. As a result of the analyses, the assumed parameters of the numerical model were verified. Based on several analyses there have been developed an analytical approach to obtain the plasma diffusivity coefficient profiles with the use of experimental plasma profiles and the diffusivity equation. The simulation results showed that as a result of N seeding into the edge plasma, an increase in the radiation of the near-wall plasma was achieved, as well as a reduction in the energy flux reaching the divertor plates and a decrease in the divertor plasma temperature.

In 2023, work was carried out to optimize the operation of SXR diagnostics on the WEST tokamak. The tasks concerned the data acquisition module, testing and preparation of model detectors for the complete tomography system.

IPPLM staff continued supporting the JET fast ion losses diagnostic, KA3, ensuring in particular that adequate diagnostic settings (CCD camera/PMT array settings) were in place at all times with varying isotope mixture/plasma composition to avoid loss of physics data due to saturation or low signal to noise. In 2023, these adjustments were critically important during the third round of DT experiments on JET (JET-DTE3), which took place in September 2023 (campaign C46) and for the subsequent Tritium removal campaign (C47). KA3's alpha detection capability had already been instrumental to the success of the previous (JET-DTE2) campaign, which took place in 2021, and in DTE3 completion and extension of DTE2 experiments were sought.

IPPLM staff with experience in piloting JET plasmas („Session Leader" competency) continued their close involvement to support the execution of the JET campaigns in 2023. This included both on-site and off-site support. Session Leaders are responsible for the advance programming (Reference Session Leaders) and actual execution of the JET pulses in the JET control room (Duty Session Leaders) as well as the coordination of all the control room personnel. In addition, it is their responsibility to ensure all the technical requirements of JET Operations are complied with and wherever non-standard ways of operating JET are needed special approval documentation has to be produced.

Conclusions

IPPLM researchers were involved in experimental and theoretical analysis of experiments conducted on different tokamaks. They worked as the Session Leaders and as VSO system operators in the JET control room during experimental sessions. IPPLM staff was responsible for data analysis from the VUV, Vis, SXR, and CXRS spectroscopy, bolometry systems, neutron camera and alpha losses diagnostics to study impurity behaviour, changes in radiation and neutron emission profiles in different experimental conditions. The numerical investigations of different discharges were also performed using COREDIV, SOLPS-ITER codes. Reports on performed data analysis and theoretical simulations were presented during numerous working group meeting, Task Force meetings. The results were also presented in the relevant conferences and publications in journal papers.

Related 2023 articles and conference presentations:

1. Ivanova-Stanik et al. Influence of the impurities in the hybrid discharges with high power in JET ILW, Nucl. Fusion 62 (2022) 066010 (9pp), https://doi.org/10.1088/1741-4326/ac2a89
2. G. Telesca et al., Core-SOL simulations of high-power JET-ILW pulses fuelled with gas and/or with pellets, Contrib. Plasma Phys. 2022; e202100186. https://doi.org/10.1002/ctpp.202100186
3. J. Mailloux et al., Overview of JET results for optimising ITER operation, Nucl. Fusion 62 (2022) 042026 (34pp), https://doi.org/10.1088/1741-4326/ac47b4

4. H Nyström et al. Effect of resistivity on the pedestal MHD stability in JET, Nucl. Fusion 62 (2022) 126045, https://doi.org/10.1088/1741-4326/ac9701
5. M. Nocente et al. Fusion product measurements by nuclear diagnostics in the Joint European Torus Deuterium-Tritium 2 campaign, Review of Scientific Instruments 93 (2022) 093520, https://doi.org/10.1063/5.0101767
6. G. Telesca aet.al. Core-SOL simulations of high-power JET-ILW pulses fuelled with gas and/or with pellets, Contrib. Plasma Phys. 2022; 62:e202100186, https://doi.org/10.1002/ctpp.202100186
7. B. Lomanowski et al. Experimental study on the role of the target electron temperature as a key parameter linking recycling to plasma performance in JET-ILW, Nucl. Fusion 62 (2022) 066030, https://doi.org/10.1088/1741-4326/ac5668
8. M. T. Curie at al. A survey of pedestal magnetic fluctuations using gyrokinetics and a global reduced model for microtearing stability, Physics of Plasmas 29 (2022) 042503, https://doi.org/10.1063/5.0084842
9. T. Tala eta al. Role of NBI fuelling in contributing to density peaking between the ICRH and NBI identity plasmas on JET, Nucl. Fusion 62 (2022) 066008, https://doi.org/10.1088/1741-4326/ac5667
10. J. Bucalossi et al. Operating a full tungsten actively cooled tokamak: overview of WEST first phase of operation. Nuclear Fusion (2022) 62, 042007, https://doi.org/10.1088/1741-4326/ac2525
11. D. Mazon, M. Chernyshova, A. Jardin, Y. Peysson, K. Król, P. Malard, T. Czarski, A. Wojeński, K. Malinowski, D. Colette, K.T. Poźniak, G. Kasprowicz, W. Zabołotny, R.D. Krawczyk, P. Kolasiński, M. Gąska, P. Linczuk, J. Bielecki, M. Scholz, D. Dworak and the WEST Team."First GEM measurements at WEST and perspectives for fast electrons and heavy impurities transport studies in tokamaks". Journal of Instrumentation (2022) 17, 01073. https://doi.org/10.1088/1748-0221/17/01/C01073
12. E. R. Solano et al. Recent progress in L–H transition studies at JET: tritium, helium, hydrogen and deuterium. Nuclear Fusion (2022) 62, 076026. https://doi.org/10.1088/1741-4326/ac4ed8
13. P. Vincenzi et al. Power balance analysis at the L-H transition in JET-ILW NBI-heated deuterium plasmas, Plasma Physics and Controlled Fusion (2022) 64, 124004, https://doi.org/10.1088/1361-6587/ac97c0
14. H. Reimerdes et al. Overview of the TCV tokamak experimental programme, *Nucl. Fusion* (2022) 62**,** 042018 https://doi.org/10.1088/1741-4326/ac369b
15. U. Stroth et al. Progress from ASDEX Upgrade experiments in preparing the physics basis of ITER operation and DEMO scenario development. Nuclear Fusion (2022) 62, 042006, https://doi.org/10.1088/1741-4326/ac207f

Research Unit: Institute of Plasma Phyiscs and Laser Microfusion

WPSA: JT-60SA Exploitation

Title: SA-EN.FE.11-T001-D002 Report on CAD works and MCNP simulations for Neutronics assessments; SA-SE.CM.M.03-T005-D003 Report on edge transport modelling for relevant initial research phase scenarios; Preparation of exploitation of JT-60SA

Authors: Barbara Bieńkowska, Sabahattin Akbas, Ewa Łaszyńska (SA-EN.FE.11-T001-D002) and Piotr Chmielewski (SA-SE.CM.M.03-T005-D003); M. Chernyshova, M Dobrut

Introduction

(1) SA-EN.FE.11-T001-D002 & SA-SE.CM.M.03-T005-D003

The task was divided on studies of neutronics assessment and modelling of research scenarios.

The first task aimed to prepare a neutronic model of the VUV diagnostic of the JT-60SA tokamak as a support for F4E. The model was done based on CAD design. The requirements for such a task are described in [1]. MCNP [2] is the reference code for nuclear analyses, thus the neutronic model was prepared for this code.

The final CAD model of the diagnostic was received from F4E in September 2023. The first step was simplifying the CAD design with the aim of Ansys SpaceClaim 3D modeling software. Simplifying the model involves removing rounds, welds, chamfers, smaller screws, washers, etc, and also the replacement of splines and tori with surfaces allowed by MCNP.

The model is complex and consists of 8 main components. The number of the bodies in the model is equal to 2705. A large amount of them are screws, bolts, heads, and washers which are the main cause of the complexity. Most of them can be removed from the model and the volumes of the removed parts can be included in the adjacent components. The remaining holes can be filled, and the volumes of the components have to be adjusted to the original ones corrected by the volumes of deleted parts. It is essential to preserve the volumes. The volumes of the components in the simplified CAD model mustn't differ from the original ones by more than 1-2%. If the shape of the solid is complicated it is advised to split it into several simpler bodies (boxes or cylinders).

The second step is converting the simplified CAD model to the MCNP input. This was done by SuperMC code [3, 4]. Every solid from the CAD is converted to one MCNP cell. The space between the solids is converted to void cells generated by SuperMC. Some geometry errors were found at that stage, then were fixed in the CAD and the model was reconverted. The resulting neutronic input consists of 407 solid cells and 281 void cells. Because the model is complex, it was decided first to convert each of the 8 main components separately and to perform 8 so-called lost particle checks to find any remaining geometry errors that cannot be seen in CAD. This test involves defining a spherical surface surrounding the entire model as an inward-directed, biased cosine source of neutrons and running MCNP. The 8 tests were performed for 10^9 histories and after recognizing and correcting all geometry errors there were no lost particles. Then the whole model was converted into MCNP neutronic input and the lost particles check was performed again for the whole model.

The third step is the materials and densities assignment according to the bill of materials. As a result of three steps the MCNP model of the diagnostic with the materials, densities, and description of every cell as a comment is created. The bill of materials for the VUV diagnostic for JT-60SA tokamak has not been provided yet by F4E. Thus the materials assignment will be done in 2024.

IPPLM team participated in six JT-60SA neutronics progress meetings organized by F4E from July to December 2023. Some methods for the simplification process were presented to the IPPLM team during the mentioned meetings. F4E organized also a 2-days in-person workshop in Barcelona devoted to getting acquainted with the tools and principles of CAD simplification and conversion to the MCNP neutronic model. During the workshop, The CAD model of the Thomson Scattering diagnostic for JT-60SA was provided for exercise. The set of tools prepared and proven by F4E was presented and explained. The knowledge gained during the workshop was used for this task. The results of the task were presented remotely at the beginning of 2024 to F4E.

The second task focused on research on edge plasma in the JT-60SA device in scenario number 2 [6]. Numerical simulations were conducted using the multi-fluid code SOLPS-ITER, which applies the Monte Carlo method to describe neutral particles. Deuterium plasma seeded with argon atoms was considered. In previous studies, the influence of radiation from sputtered carbon atoms on the divertor plates was not investigated. Only the impact of the sputtering process itself on energy reduction in the divertor region was examined. The research focused on determining the possibility of energy scattering in the edge plasma and estimating the power reaching the divertor plates under various assumptions, taking into account the presence of carbon ions in the device's plasma.

(2) Preparation of exploitation of JT-60SA

This project was aimed at developing a concept for a radiation spectrometer in the VUV range for monitoring radiation from the JT-60SA tokamak divertor located in Japan. The main task of the group of IPPLM scientists throughout the project was to prepare the concept of a pumping system to achieve an adequate vacuum in the spectrometer chamber and to ensure the selection of a detector for recording radiation quanta at the optical end of the spectrometer system. The work also included participation in the development of the overall concept of the spectrometer, selection/selection of existing detectors in the selected photon range, selection of the appropriate detector design and parameters

Results

(1)

In case of first task, the resulting simplified CAD model consists of 407 bodies. Figure 1 presents the comparison of the original and simplified CAD models of VUV diagnostic for JT-60SA tokamak.

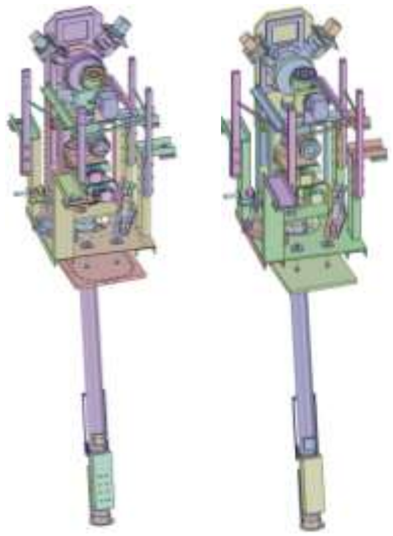

Figure 6 The original (left) and simplified (right) CAD model of the VUV diagnostic for JT-60SA.

The second part of task based on previous calculations and a series of simulations were conducted with varying fluxes of deuterium ions from the center and deuterium atoms introduced from the tokamak wall in the midplane region. These simulations allowed for the adjustment of deuterium and argon fluxes to achieve the prescribed value of the plasma flux entering the scrape-off layer (SOL) from the core of the plasma in scenario number 2, by appropriately adjusting the flux of introduced gases, while simultaneously achieving conditions close to plasma detachment from the divertor plates.

As part of the task, analyses were carried out to assess the impact of impurity ion radiation in deuterium plasma. The research revealed the significant role of carbon ion radiation in the tokamak's scrape-off layer (SOL). In comparison with calculations for plasma seeded only with argon, the results obtained indicated that the plasma radiates sufficiently to reduce the temperature on the plate to just a few electron volts for the assumed plasma electron density at the separatrix, as outlined in the scenario.

The numerical results confirm the importance of argon for energy dissipation in the edge plasma. However, considering carbon ions in the plasma led to a significant decrease in energy reaching the divertor plates and consequently a decrease in temperatures on both the inner and the outer plates. Furthermore, simulations conducted in the current year much better reflected the actual assumptions of JT-60SA operation scenarios by achieving plasma equilibrium for declared fluxes of deuterium ions and atoms from the core region and those introduced externally, $\Gamma_D = 2\times10^{21}\ s^{-1}$ and $\Gamma_{D2} = 4.0\times10^{21}\ s^{-1}$, respectively.

Simulations clearly demonstrate the significant impact of plasma seeding on the energy flux reaching the outer divertor plate surface. In the absence of plasma seeding, the maximum energy flux reaching the plate surface almost reaches 55 MWm^{-2}. However, even a small impurity flux value of $2.5\times10^{20}\ s^{-1}$ causes a decrease in power on the plate by about 60% to around 20 MWm^{-2}. The maximum decrease, equal to the maximum power to the plate of 2.4 MWm^{-2} in the vicinity of the separatrix (strike point), is achievable for a high argon doping flux of $9.5\times10^{20}\ s^{-1}$, corresponding to plasma in the so-called semi-detached regime. The analyses confirm that achieving the prescribed plasma parameters in scenario number 2 are feasible, but the use of argon atoms will be necessary to reduce the thermal load on the divertor.

(2)

The tasks planned to be carried out by the team from IPPLM in 2023 were only minor works related to the completion of the spectrometer preparation. The preparation of the spectrometer is in the handover and finalisation phase, as the device has been successfully installed on the tokamak and started collecting data. Therefore, the work last year was only concerned with the formal finalisation of the entire diagnostic system.

Due to the final phase of the project, the team from IPPLM provided assistance and knowledge support to the team of international scientists on both the vacuum system and the CCD detectors that were selected and purchased by IPPLM. Meetings on this issue were attended. Due to the end of the project, the work also involved the preparation of a final report on the entire project for the project manager from EUROfusion.

Conclusions

(1)

CAD works and MCNP simulations for Neutronics assessments:

1. The IPPLM team successfully started to cooperate with F4E as a support in neutronic assessment for JT-60SA tokamak.
2. The useful tools and methods were presented by F4E to IPPLM during 6 online progress meetings and a 2-day in-person workshop.
3. The CAD model of VUV diagnostic for JT-60SA provided by F4E was simplified and converted to MCNP according to the guidelines.

Edge transport modelling for relevant initial research phase scenarios

1. The research indicates that achieving the plasma parameters outlined in scenario number 2 is possible
2. Operation in scenario number 2 requires additional plasma seeding with argon impurity to reduce the power reaching the divertor plates.

(2)

The results obtained contribute to the general development of plasma physics and fusion devices, thus also bringing the achievement of controlled thermonuclear fusion closer to public use. Achieving such fusion is extremely important for the development of the economy, as obtaining a source of cheap energy is key to the development of society as a whole. In turn, working in international teams fosters further cooperation in the field of fusion energy science and technology.

Collaboration

Fusion for Energy, scientist from: CEA Cadarache (France), University of Tuscia (Italy) and ENEA, FTNSD C.R. Frascati (Italy) in frame of WPSA project. Consorzio RFX & ISTP, Padova, Italy

References

[1] 1. Pampin Garcia R. F4E Guideline – Nuclear AnalysesF4E IDM Quality document F4E IDM number 26NR86

[2] 2. Goorley T. Initial MCNP6 Release OverviewNuclear Technology, 180, pp 298-315 Paper https://doi.org/10.13182/NT11-135

[3] 3. Wu Y.Multi-functional Neutronics Calculation Methodology and Program for Nuclear Design and Radiation Safety EvaluationFusion Science and Technology 74(2018) 321-329 Paper https://doi.org/10.1080/15361055.2018.1475162

[4] 4. Wu Y.CAD-Based Monte Carlo Program for Integrated Simulation of Nuclear System SuperMC Annals of Nuclear Energy 82(2015) 161-168paperhttps://doi.org/10.1016/j.anucene.2014.08.058

[5] 5. Kulesza J. A. MCNP® Code Version 6.3.0 Theory & User ManualLos Alamos National Laboratory Tech. Rep Technical report https://doi.org/10.2172/1889957

[6] JT-60SA Research Unit http://www.jt60sa.org/pdfs/JT-60SA_Res_Plan.pdf Google Scholar, 2016

Research Unit: Institute of Plasma Phyiscs and Laser Microfusion

WPPRD: Prospective Research & Development

Title: Simulation Liquid metal target simulations

Authors: I. Ivanova-Stanik, P. Chmielewski, V. Pericoli-Ridolfini

Introduction

For EU DEMO with tungsten (W) divertor, it is postulated that the power load onto the plates must not exceed 5 MW/m^2, otherwise short-term damage of the surface of solid divertor targets and the material erosion in a tokamak reactor could become critical. Liquid Metal (LM) divertor is considered as an alternative to a standard tungsten one because it could greatly help in facing these problems and also even increase the maximum acceptable steady and transient heat loads. Most advanced technology is the capillary porous structure (CPS) or mesh in which liquid metal is wetted whilst slow replenishment by capillary forces ensures its cleaning and stability even with strong erosion. The power exhaust capabilities of such CPS-based liquid metals have been investigated experimentally in linear devices as well as in tokamaks, where they were exposed to high heat loads above 20 MW/m^2 , without great problems. Power handling experiments with a special liquid metal divertor module based on the capillary porous system technology were performed in the tokamak COMPASS with graphite (C) divertor targets.

The COMPASS Upgrade (COMAPASS-U) tokamak will be a tokamak with major radius R_0 = 0.894 m with high toroidal magnetic field(B_T = 5 T) and large plasma current (I_p = 2 MA). It will provide unique capabilities for addressing some of the key challenges in plasma exhaust physics, advanced confinement modes and advanced plasma configurations as well as for testing new plasma facing materials and liquid metal divertor concepts. COMPASS-U will be equipped with tungsten (W) divertor and a single LMD target (see Fig.1) installed on a divertor manipulator with cylindrical shape with vertical axis, thus surface orientation against the magnetic field deliberately increases $q_\perp/q_\parallel$ from sin(3°)=0.05 (usual in divertors) up to sin(45°)=0.7 (reaching thus attached plasma DEMO-relevant heat fluxes). The evaporated Li/Sn condensates at nearby PFCs kept at 350°C–500°C from which Li vaporises between shots to end up on the condenser (a plate cooled to room-temperature) in private flux region. The vessel cleaning from Sn (which does not vaporize below 500°C) is feasible by Argon glow discharge.

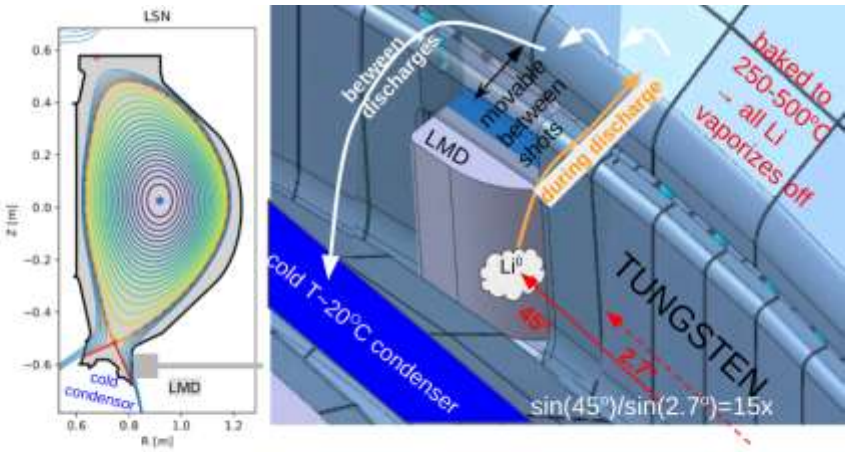

Figure 1. Cross-section of the COMPASS-U tokamak with the LMD target at the bottom. Right: The CPS LMD target in divertor.

The first aim of the work is to prepare an integrated analysis using the COREDIV code for COMPASS-U in order to assess, on the one hand, the influence of Li and Sn on the production of W, and on the other hand, what is the critical concentration of Li and Sn to be able to work in the high plasma confinement regime. The second aims at surveying the modelling results of the 2D multi-fluid edge code TECXY on the SOL behaviour when either lithium or tin is used as divertor target in the harsh plasma environment of COMPASS-U. The results with COREDIV code will be used as input parameters for HeatLMD code and will be comparison with SOLPS-ITER simulation.

The COREDIV, TEXCY and HeatLMD model

The physics model used in the COREDIV code is relatively complex. In the core, the 1D radial transport equations for bulk ions, for each ionization state of impurity ions and for the electron (T_e) and common ion temperature (T_i) are solved. The energy losses are determined by bremsstrahlung, synchrotron radiation, line radiation and ionization losses. Recycling and sputtering at the divertor plates are taken into account for both background and impurity ions. Data for sputtering are derived from. Evaporation is also considered in the COREDIV code. The tungsten (W) self-consistently calculated from sputtering at divertor targets due to all ions (main ion (D) and impurities (C, Li(Sn)). The prompt redeposition of tungsten is not used. The cross-field particle and energy diffusion coefficient are input parameters. The code was run in a steady-state mode, neglecting fast phenomena, such as ELMs.

The main tool is the 2D edge code TECXY, together with COREDIV.

The HeatLMD code is time dependent computer code which calculates liquid metal erosion, taking into account the processes: erosion (sputtering, thermal erosion, evaporation), prompt redeposition and vapor cooling of the incident plasma by radiative losses. Input parameters for HeatLMD code are the liquid metal divertor (LMD) geometry (magnetic incident angles, target thickness and backside cooling), density and temperature on the plasma in space and time for both inter-ELM and intra-ELM and the prompt redeposition coefficient. The LMD heat conduction equation in time is solved in 3D. The latent heat of vapor is also subtracted. For LMD target backside, it either assumes zero cooling, radiative cooling or constant backside temperature (thus its full absorption into e.g. a water cooling pipe). Output from HeatLMD is time evolution of the liquid metal target 3D temperature (especially time to reach equilibrium) and the Li (Sn) flux release into SOL including its prompt redeposition back to the surface.

Simulation results

Detailed integrated transport modelling with the METIS code yields density and temperature profiles during the flat-top with 4 MW of NBI heating and 1–2 MW of ECRH heating. The simulations with COREDIV code are prepared for the COMPASS Upgrade tokamak for the H-mode scenario # 3210 (see Fig.1) with the following main parameters: major and minor plasma radii R_0= 0.9 m, a = 0.27 m, elongation k = 1.7, plasma electron density $< n_e >_{vol} = 1.125\times10^{20}$ m^{-3}, plasma current I_p = 0.8 MA, toroidal magnetic field B_T = 2.5 T with 2 MW of auxiliary heating.

The $H98_{(y,2)}$ factor is adjusted in COREDIV in order to reproduce the temperature profiles. The density value at the separatrix (an input parameter for the simulation) is fixed to 30% of the average volume density. The ion and electron temperatures and densities obtained in METIS and COREDIV simulations for scenario # 3210 are shown on Fig. 2. The transport simulation in METIS code assumed that the effective charge state (Z_{EFF}) is 1.3. Main light impurities (C, B, O, N) are usually observed at trace levels in tokamaks with metal wall. In our simulations, we use small gas puffing by carbon (C), to approximate situation. As outlined above, strong localization of the liquid metal cassette, both in the toroidal and radial direction (see Fig. 1), we consider as equivalent to ”gas puffing” of Li(Γ_{Li}) or Sn (Γ_{Sn}) in the divertor chamber. The large difference in the atomic number (Z) between Li and Sn, Z_{Li} = 3 and Z_{Sn} = 50, is reflected in the radiation features.

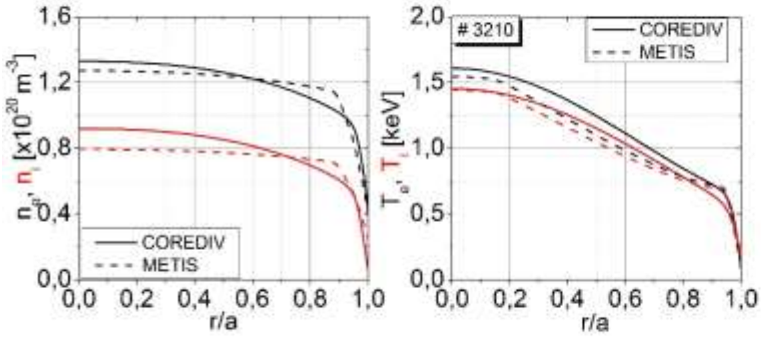

Figure 2. The electron and ion densities and temperature profiles from COREDIV and METIS code.

The simulation with COREDIV code is run with two different radial diffusion coefficient (D_{SOL}) in the scrape of layer (SOL): D_{SOL} = 0.3 and 0.5 m^2/s. The most significant quantities to be looked at are shown in Fig.3:

radiation fraction (f_{rad}), $_{Zeff}$, power to SOL ($P^{SOL)}$, to divertor plates (P^{PLATE}), power threshold (P_{LH}), total, Li and Sn radiation inside the SOL.

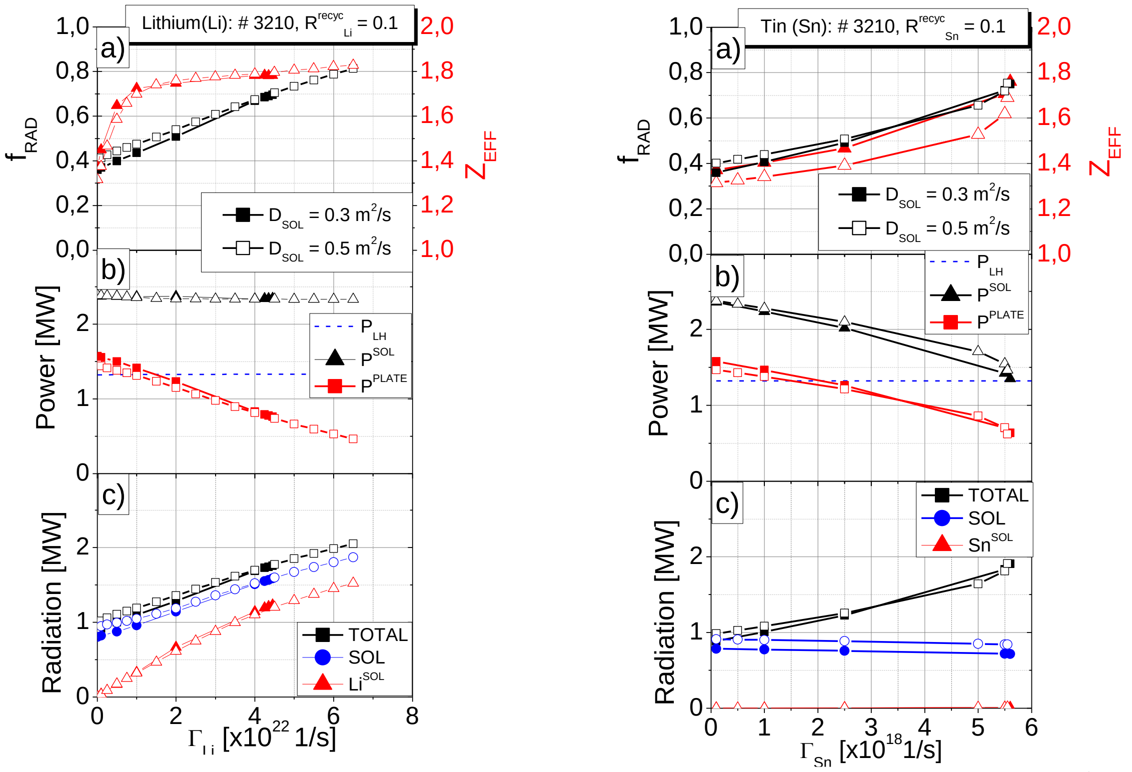

Figure 3.Plasma parameters versus Γ_{Li} (left) and Γ_{Sn} (right) for different radial diffusion in SOL 0.3 m²/s (full symbol) and 0.5 m²/s (open symbol): (a) radiation fraction(f_{RAD}) and Z_{EFF} , (b) power to plate (P^{PLATE}), to SOL (P^{SOL}) and L–H power threshold (P_{LH}) and (c) total radiation, radiation in SOL, Li (Li^{SOL}) and Sn (Sn^{SOL}) radiation in the SOL.

Upon increasing the puff level (Γ_{Li}, Γ_{Sn}), the total radiation increases for both Li and Sn to almost the same radiation fraction (~ 80%). For Li, this increase is mostly confined inside the SOL (see Fig. 3c). Consequently, the power to SOL changes negligibly, and P^{SOL} keeps about twice higher than the power threshold PLH, without any risk of losing the H-mode regime. Conversely, the Sn radiation is significant also in the core region (see Fig.3). Here the radiation can increase with the Sn injection rate to the point of dropping PSOL below the threshold for sustaining the H-mode. This occurs when $\Gamma_{Sn} > 5.5 \times 10^{18} s^{-1}$. This is also the reason why P^{PLATE} is progressively reduced, despite the Sn SOL radiation maintains almost constant (see Fig.3. right). The Z_{EFF} value grows for both cases from 1.3 to 1.8, but with different behaviour. In the case of Li, a strong increase is initially observed with the injection rate up to $\Gamma_{Li} > 1{\times}10^{22} s^{-1}$, after which Z_{EFF} keeps almost constant, conversely for Sn the increase is almost linear up to f_{RAD} =70%, after which it grows significantly faster (see Fig. 3a).

Since Li and Sn are gas puff, material of the divertor has no influence on the prompt redeposition. We calculated prompt redeposition separately, using a relatively simple description taking into account only single ionization process assuming that $T_e = T_i$. For Li, we use classical formula for prompt redeposition for the fraction of the redeposited ions to all sputtered atoms f_{prompt} is given by

- $f_{prompt} = 1/ (1 + \alpha(\lambda_{ion}/\rho_{D+}))$ for heavy ions (Sn, W),
- $f_{prompt} = 1/ (1 + (\lambda_{ion}/\rho)^2)$ for light ions (Li),

where λ_{ion} is the ionization length calculated from the ionization frequency and average thermal velocity and ρ^{D+} is the gyro-radius of D^+ ions in magnetic field. The prompt redeposition is sensitive to the energy distribution of the emitted atoms and for the case of Sn and W the Thompson's distribution has been used. The resulting f_{prompt} is incorporated into Li, Sn sputtering yield Y as follows: $Y = Y\,(1 - f_{prompt})$. Fig.4. presents the fraction of not promptly redeposited Li (left) and Sn (right) ions escaping from divertor plate as a function of temperature in 1.5 T (dot line) and 2.5 T (straight line) magnetic field for different electron densities. The vertical pink line indicates ion temperate at the strike point for # 3210 scenario from COREDIV simulation.

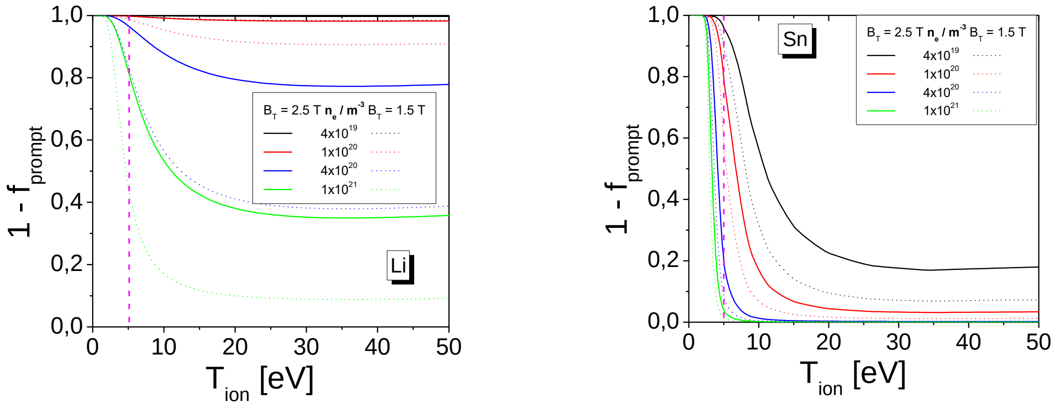

Figure 4. The fraction of not promptly redeposited Li (left) and Sn (right) ions escaping from divertor plate as a function of temperature in 1.5 T (dot line) and 2.5 T (straight line) magnetic field for different electron densities.

Analysis for scenario #24300 (B_T=4.25T, I_p =1.3MA, q_{95}=3.7, k=1.8, $_{PNBI}$=2.7 MW, P_{ECRH}=1MW) start to prepared with TECXY code. Based on the mesh from the SOLPS-ITER code generated mesh for TEXCY, which is presented in the Fig.5.

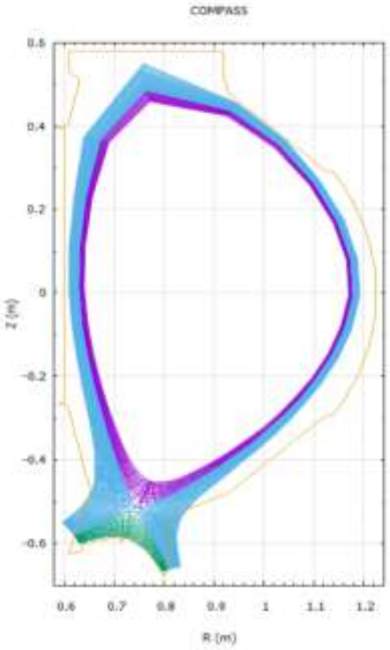

Figure 5. TECXY computing meshes for scenario # 24300 for COMPASS-U

Conclusions

The coupled COREDIV + HeatLMD codes performed self-consistent core-edge simulations of liquid tin and lithium divertor for the future COMPASS-U tokamak. Tungsten is negligibly produced only due to carbon and self-sputtering. COREDIV predicts core concentration of about 10-11% of Li (depending on the radial diffusion in SOL region) and of 0.025% for Sn. For the case with Sn, 80% of the core radiation is from Sn. Both Li and Sn have small influence on the W production.

Comparison with the results of the HeatLMD code showed that for scenario #3210 the expected Li concentration will be about 9%, and in the case of Sn 0.004% and there will be no problem with operation in H mode.

The results are presented in the International Conference on Research and Applications of Plasmas (PLASMA 2023) September 18-22, 2023 in Warsaw, Poland as poster: I.Ivanova-Stanik, J. Horacek, F. Jaulmes, V. Pericoli Ridolfini, J. Cecrdle," Integrated simulation with COREDIV code for COMPASS Upgrade tokamak",

Collaboration

Institute of Plasma Physics of the Czech Academy of Sciences, Prague, Czech Republic

Research Unit: Institute of Plasma Phyiscs and Laser Microfusion

WPPWIE - Plasma Wall Interaction and Exhaust

Title: Optimization of laser-based surface analysis diagnostics: Report on LIBS analysis by application of machine learning algorithm, Preparation of the LIBS device and first operational tests to make it suitable to be installed in the JET Remote Handling System (PWIE-SP X.4.T-T001-D009)

Authors: P. Gąsior, W. Gromelski, M. Ladygina, A. Kwaśnik

Introduction

In 2023, the work carried out within the framework of the WPPWiE program followed three main tracks. The first one focused on the development of machine learning models for fuel retention measurements using new generation fusion reactors. The second one dealt with the analysis of data obtained from an experiment in Finland using samples simulating fuel retention in beryllium layers. The third one was related to the preparation of the LIBS@JET experiment, which will take place in 2024 at the JET tokamak in Culham. Although experimental campaigns based on plasma discharges are no longer carried out at this tokamak, these should not be confused with the ongoing material research, which includes the LIBS@JET experiment.

The topics, objectives and methodologies of these tasks were very diverse, which contributed to the achievement of interesting results that are also important for the further development of research in the field of PWI.

In 2023, research on the development of machine learning models focused on conversion systems between reduced-dimensionality datasets obtained for simulation spectra and so-called quasi-experimental spectra prepared using a previously determined calibration function of the real measurement system. The data flow diagram is shown in Figure 1

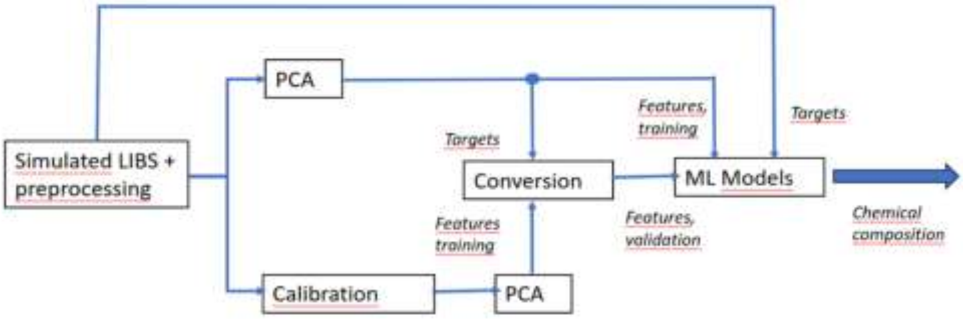

Figure 1. Idea of operation of the conversion system for ML supported LIBS trained on simulated spectra

Synthetic data was obtained using the previously developed SimulatedLIBS package and then subjected to preprocessing to achieve the appropriate signal dynamics. After that dimensionality reduction (PCA) was performed and in this form, data was used to train models for determining the chemical composition (ML models in the figure)1 according to the labels assigned at the synthesis stage.

Part of the data was calibrated with the transfer function of the real measurement system to generate quasi-experimental data. Then, they were subjected to dimensionality reduction and used as features to create conversion models, in which dimensionally-reduced simulation spectra were used as targets. After the model was trained, it was used to predict from quasi-experimental spectra that did not participate in the training process. The obtained predictions were used to validate the models for determining the chemical composition in order to confirm the effectiveness of the conversion.

Both the models for determining the chemical composition and the conversion of reduced data were implemented as DNNs (Deep Neural Networks). The parameters of these networks were optimized, such as the number of layers and neurons, the activation function, the regularization method, the cost function, and the method of its minimization. The research results are presented in the points concerning the relevant achievements.

Another research direction, i.e., the analysis of the results obtained in the experiment in Finland for samples simulating fuel retention in beryllium layers, consisted mainly of determining the depth profiles of the content of elements and isotopes in the laser-ablated layer. The aim of the research was to compare the LIBS results with material research (SIMS) and to assess the effectiveness of the LIBS method itself in estimating the chemical composition of layers containing accumulated fuel. The samples used in the experiment were specially prepared calibration samples and JET tokamak samples containing beryllium and deuterium.

The last task carried out within the WPPWiE program was the preparation of research plans and equipment for the LIBS4JET experiment, which will take place in 2024. As part of this task, the IFPiLM participated in organizational and design work, in particular concerning the system for transmitting the optical signal from the remotely controlled LIBS head to the spectrometer system used as the detection apparatus.

Results

Following successful verification of the models' ability for accurate qualitative and quantitative analysis of synthetic spectra in 2022, the primary scientific focus in 2023 shifted towards validating the conversion model. To achieve this objective, a set of spectra was generated using the SimulatedLIBS package. Subsequently, these spectra underwent preprocessing to ensure appropriate signal dynamics. Dimensionality reduction was then applied using Principal Component Analysis (PCA), resulting in a data representation with 9 principal components. This preprocessed data served as the training set for a neural network architecture consisting of three densely connected hidden layers, preceded by an input normalization layer. Regularization was implemented through dropout layers, randomly inactivating 30% of the neurons within each layer during training.

The development process utilized the Python programming language and leveraged functionalities from established libraries such as TensorFlow, Keras, Scikit-Learn, Pandas, NumPy, and Matplotlib.

The trained models were subjected to rigorous validation using data that was strictly excluded from both the dimensionality reduction and training processes. The validation results are presented in Figure 2

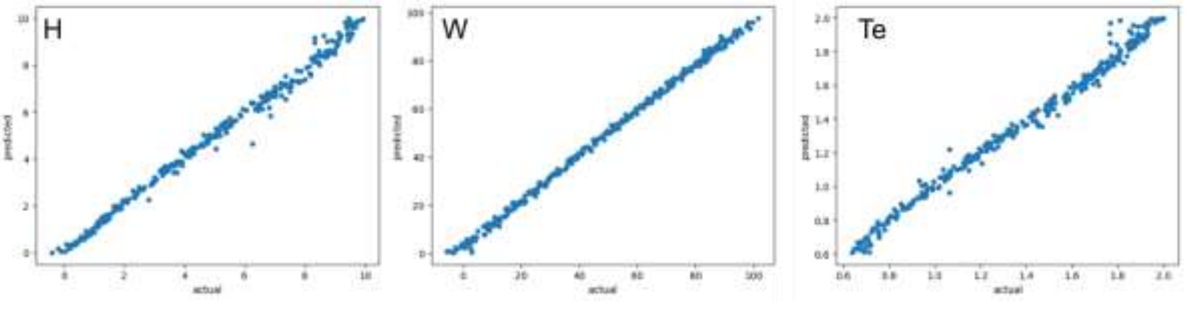

Figure 2 Prediction of hydrogen, tungsten content and electron temperature for synthetic data by the chemical composition model (actual – actual concentration, predicted – determined by the model)

The attempt to directly predict the desired parameters from the reduced quasi-experimental data resulted in erroneous outcomes, as observed in the top row of Figure 3. However, by employing a suitable Deep Neural Network (DNN) model for data conversion, the predictions were successfully rectified (bottom row of Figure 3).

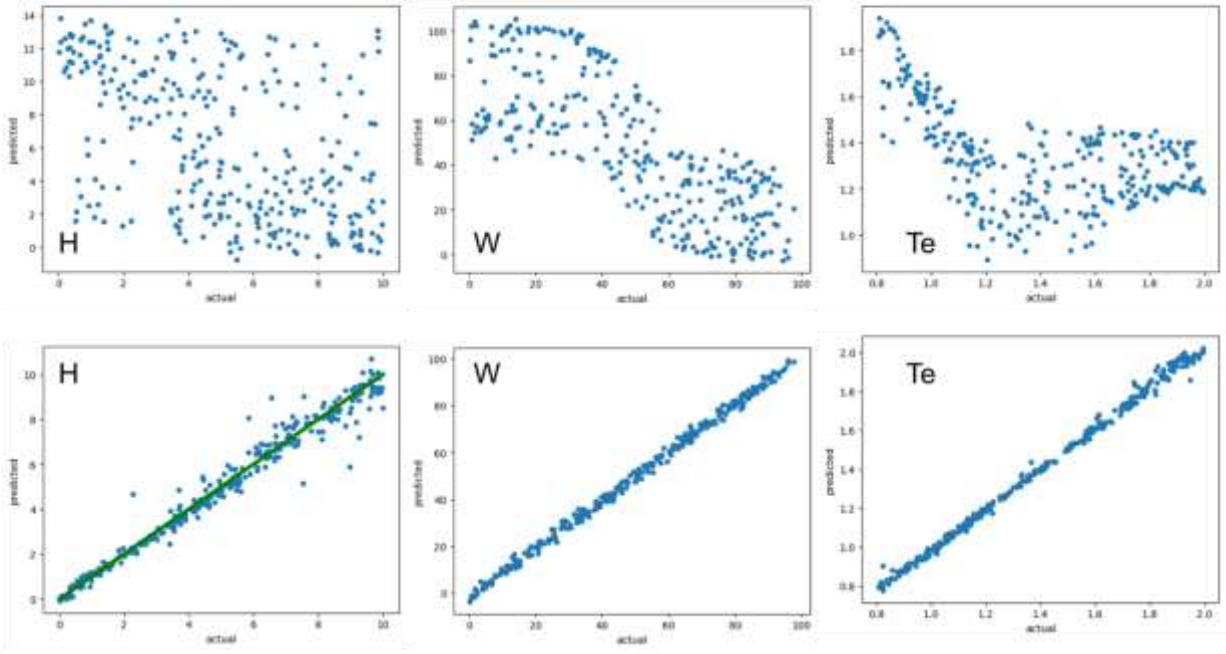

Figure 3 Chemical composition model prediction trained on synthetic data for quasi-experimental data before (top row) and after conversion (bottom row)

Studies on the chemical composition profiles of beryllium layers revealed a non-trivial and difficult to explain relationship between the ablation coefficient and the beryllium content in the layer. This relationship is shown in Figure 4. It is surprising because an increase in the content of residual gases leads to a decrease in ablation, which may seem counterintuitive. To explain this effect, detailed studies of the mechanical and thermal properties of beryllium layers should be carried out.

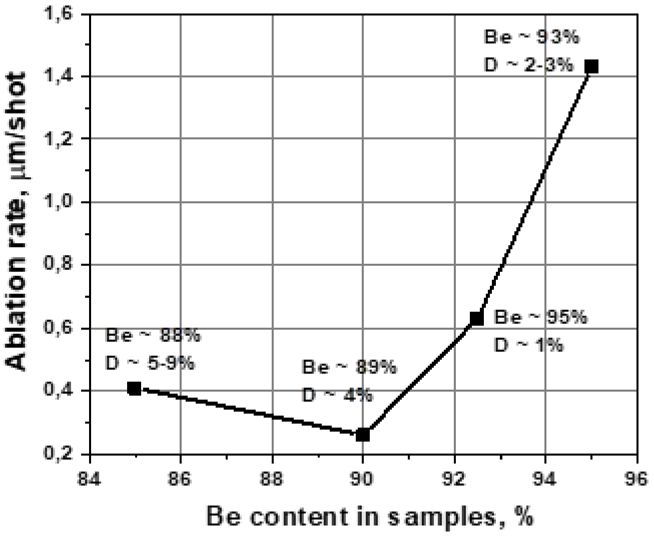

Figure 4 Dependence of the ablation co-efficient on the Be contents in the samples

Conclusions

The research in 2023 brought not only interesting scientific results but also significant progress in terms of adaptation of novel technologies into the development of thermonuclear fusion for clean energy production. Succesfull application of Machine Learning, especially Deep Neural Networks, which manifested its possibilities in numerous areas of science and technology may be an important stay on a way to next-step fusion devices.

Collaboration

ENEA, VTT, FZJ, CU, VTT, JET, DIFFER

Related 2023 articles and conference presentations:

1) P.G. Bhat, P. Gasior, e al, LIBS depth profiling of Be-containing samples with different gaseous impurity concentrations, Nucl. Mater. Energy. 37 (2023) 101549. https://doi.org/10.1016/J.NME.2023.101549.
2) PLASMA 2023:
   M. Ladygina, A. Marín Roldán, J. Karhunen, P. Paris, I. Jõgi, A. Hakola, J. Likonen, S. Almaviva, W. Gromelski, P. Gasior, J. Ristkok, P. Bhat, C. Porosnicu, C. Lungu, P. Veis , and JET contributors, Impurities monitoring in Be-based samples using LIBS diagnostics
   P. Gąsior, W. Gromelski, M. Kastek, A. Kwaśnik and M. Ladygina, Training ML based LIBS models on quasi-experimental data-set relevant for materials for next-step fusion reactors
3) EMSLIBS 2023
   P. Gąsior, W. Gromelski, M. Kastek, A. Kwaśnik and M. Ladygina, ANN-based features conversion of dimensionally reduced LIBS data for calibration on synthetic spectra
4) H.J. van der Meiden, S. Almaviva, A. Bultel, J. Butikova, V. Dwivedi, P. Gasior, W. Gromelski, A. Hakola, X. Jiang, I. Jõgi, J. Karhunen, M. Kubkowska, M. Laan, M. Ladygina, G. Maddaluno, A. Marín-Roldán, P. Paris, K. Piip, M. Pisarčík, G. Sergienko, M. Veis, P. Veis, S. Brezinsek and the EUROfusion WP PFC team, LIBS for fusion application: latest developments

Research Unit: Institute of Plasma Phyiscs and Laser Microfusion

WPDC: Diagnostics and Control

Title: Diagnostics and Control

Authors: M. Chernyshova, K. Malinowski, K. Mikszuta-Michalik, M. Jagielski, S. Jabłoński,
A. Izdebski, B. Bieńkowska, S. Akbas, Sabahattin, T. Fornal, R. Prokopowicz

Introduction

The overall objective of WPDC is to prepare the set of the diagnostics inevitable for DEMO operation and control. DEMO will rely on a number of diagnostic systems to control the plasma during operation. The combined Radiated Power (Prad) and Soft X-ray (SXR) Core Intensity diagnostic system is among them. This report relates to the further preparation of Prad/SXR measurements of the core plasma, which will be used for reliable plasma control (separatrix power loss monitoring) as required for DEMO. It can also be helpful for investigating heavy impurities profiles, MHD modes and locations, plasma positioning and shape. The purpose of measuring is to obtain information on the plasma radiation profile and, after tomographic inversion, the local emissivity to determine the radiation power. The overall aim is to maintain the separatrix power transition at the required level for DEMO to operate in H-mode.

Results

In 2023, the work was aimed at further development of a detection system based on gas electron multiplier (GEM) technology [1]. Last year the main efforts of the group were centred on the evaluation of the measurement accuracy, further study of the system requirements [2], [3], further development of the diagnostic concept and CAD model. In this context, the preparation of digital codes for the required radiation modelling was carried out. Introspectively, an evaluation of the accuracy of the foreseen measurement of the radiation power recorded by the system was done. This task was done for the preliminary concept of the gas chamber, allowing to obtain a first estimate and to develop a calculation procedure. Among other things, the tomographic reconstruction was analysed for different collimator diameters and their influence on the reconstruction accuracy. This year we continued to determine the effect of the magnetic field on the deviation of the position of the electrical signal from the original position without magnetic field. This year the calculations were performed for the thick GEM foils considered. In continuation of the thermal load calculations started last year, the thermal load was determined by means of ANSYS Fluent package at the detector location. The research was also aimed at determining materials capable of shielding neutron-sensitive diagnostic elements. Regarding the mechanical design of the diagnostic, work has also been related to determining the thickness and structure of the beryllium window between the tokamak vacuum vessel and the diagnostic chamber.

Regarding the activity relative to plasma radiation simulations, further work was done for detecting system composed of 26 horizontal and 26 vertical lines of sights (LOSs) which were proposed in 2022 based on the tomography accuracy analysis. The simulations of the radiation incident on the detector were made with the help of numerical programmes developed at IPPLM.

X-ray spectra were simulated for an electron temperature profile with a maximum value of Te=35 keV for the 26 x 26 collimator array in the side view and top view positions. The results included obtained quantum spectra for the collimators recording the maximum quanta (Side view: collimator 14, Top view: collimator 12). The main plasma component was H with considered impurities nHe/ne = 10^{-2}, nN/ne = 10^{-2}, nHe/ne = 10^{-2}, nAr/ne = 10^{-3}, nFe/ne = 10^{-3}, nKr/ne = 10^{-3}, nXe/ne = 10^{-4}, nW/ne = 10^{-5} (see [4], [2], [5]). Ion densities were calculated by solving the kinetic equations assuming collisional-radiative models [6] and using Te and ne profiles [7], [8].]

For the purpose of determining the optimum collimator diameter, a code for line of sight (LOS) and cone of sight (COS) imaging was needed for X-ray tomography using GEM detectors in a collimator system to work with the DEMO tokamak. Therefore, the computer code DEMO_LOS.exe was prepared. Among other things, the code uses operations using hyper-complex numbers (quaternions) to accurately represent geometrical correlations for the diagnosis in question.

The system under analysis consists of four rows of detectors, each containing 13 collimator-detector sets. Two sets look at the plasma from the side (SIDE view) and two from above (TOP view). All these requirements are reflected in the code, which, after loading a file containing data on the intersection coordinates of the LOSs of each detector row and information on the positions of the detector centres, is able to draw in 3D the LOSs and the bases of the viewing cones.

Additionally, for the purpose of testing the tomography algorithms, the following results were prepared: for pure H plasma, for H plasma with Xe(0.01504%) and for complex plasma containing H, He(1%), N(1%), Ne(1%), Ar(0.1%), Fe(0.1%), Kr(0.1%), Xe(0.01504%) and W(0.001%). Calculations were done for the ramp-up case for t = 2000 s. The maximum electron temperature was Te ~ 38 keV.

During the year 2023 further attempts have been made to prepare the acceptable, within diagnostics requirements, detector gas chamber configuration for DEMO Prad. The development of the concept required additional data for the selection of the detector working gas as well as the preparation of a new concept for the incident radiation filters. Magboltz was used through its interface in Garfield++ to generate gas tables for various gas mixtures.

These data allowed us to make a final choice of the main component of the gas mixture, as well as the electric field strength for the GEM foils and the gaps, the transfers, between them. Given the large distances for gas ions, the large conversion region, lighter gases should be chosen to try to reduce ion drift time and to speed up the detector or at least try to operate it as far away from the saturation limits as possible. This issue should be also be raised in the choice of the length of the conversion region, which is determined by the collimator diameter. The data obtained also allow us to determine the optimum values of the electric field (ab. 3 kV/cm) at maximum drift velocity and transversal diffusion, which can help to expand the avalanche and reduce the local electron concentration. The latter can counteract the development of breakdown in the gas at high concentration of charges in the avalanche. The avalanche expansion however should not reduce the energy resolution, since the added distances are very small, of order of submillimetre.

Simulations of the initial ionisation in a gas were also performed to help determine the gases on which the Prad sensor concept could be based. It was necessary to determine the distances over which the primary electrons propagate from the ionisation site during thermalisation in the gas. It was particularly important to consider these processes with respect to electrons that arise during fluorescence, since in this way part of the energy from the initial photon can be transported over quite large distances. Depending on this distance, the energy deposited in the gas will be considered as a dependent or independent process with respect to the main photon absorption process.

In 2023 work continued on the preparation of the gas sensor concept for Prad diagnostics. In this connection, calculations were made for all noble gases as well as their mixture with carbon dioxide. Before starting calculations in the direction of measurement accuracy by Prad diagnostics for the latter concept, simulations were also performed for different gases to determine the dependence of the distance, after which the quantum X will be adsorbed, on the energy under given gas conditions.

Statistical simulations were performed in Geant4 for the absorption of X-rays in a gaseous mixture with parameters corresponding to the first and second chambers of the two-chamber GEM detector for Prad diagnostics. Parameters such as range, percentage distribution of interaction effect, percentage of fluorescence phenomenon were taken into account. For example, for the krypton/xenon gas mixture considered in 2022 and for the low gas pressures then selected and additionally for 1 bar pressure in the current version of the concept, the results are as follows. As can be seen for 1 bar pressure in the lowest energy region, 1-2 keV, the range reaches 4-5 mm. Taking into account the obtained results, two mixtures based on neon for the first chamber for lower photon energies and on argon for the second chamber for higher photon energies were chosen for the new concept of gas chambers in the detector for diagnostics.

The concept of a detector for diagnostics also involved the development of materials for use outside as well as inside the gas chamber. The primary task in this respect was to propose and design attenuators/filters to be installed in front of the gas chamber to modify the incident radiation so that the detector operates, if not in optimal, at least not in incorrect conditions, and also to fulfil the measurement requirements of the plasma control.

In this regard, various materials, metals, were considered for attenuation and filtering of plasma radiation. The goal was to achieve a combination of filter materials that would limit the plasma emission to the level accepted by the GEM detector (for stable signal amplification and energy identification) and at the same time that the measured spectrum would include a sufficient fraction of low-energy radiation, e.g. 5-10% of the total measured emission in the gas chamber. The main materials considered were nickel, copper, aluminium, beryllium, titanium, chromium, iron. Consideration would have to be given to the activation intensity of the material, acceptability for DEMO operation, and absorption properties. The newly proposed filter was a mixture of Ni, Cr, Ti, Al, Be materials with varying degrees of the window coverage. The filter attenuation model takes into account the fluorescence emission from the filter materials. Therefore, their order is aligned (from higher to lower Z to the detector window) and the thicknesses are chosen so that all secondary emission from the previous material is absorbed by the next one. As it turned out later, DEMO is trying to limit the amount of nickel in the machine, so in the next version of the combined filter its presence will be excluded as much as possible.

For this version it was proposed to base on two chamber sensor with Ne based working gas (ab. 2 cm) in the first chamber and Ar based working gas (25 cm) in the second one, instead of previously considered Xe for the second chamber. The target photon range was selected to be 2-50 keV.

As a result of these developments it was possible to obtain satisfactory characteristics in which the measured spectrum optimally covered the low-energy part for the first detector chamber and also allowed to measure the high-energy part of the spectrum in the second detector chamber. The numerical application described in [4] and this report was used. The obtained results are presented in Figure 7.

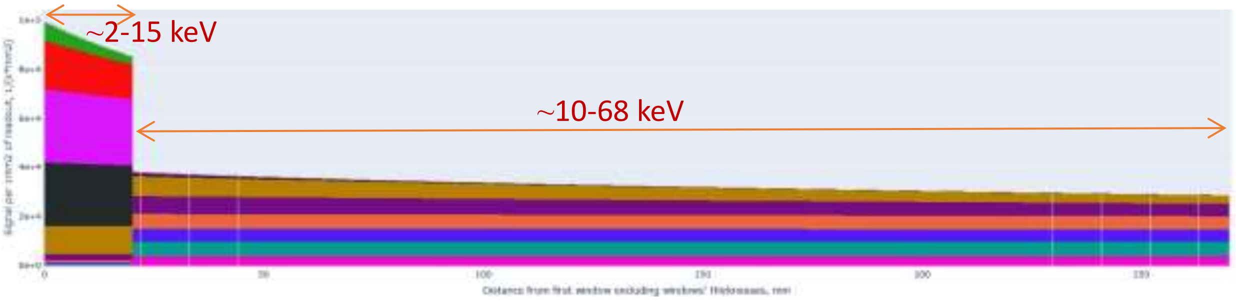

Figure 7. Photon counts per mm square of the readout plane for two chambers sensor: Ne based mixture of ab. 2 cm and Ar - of 25 cm.

Summary

The main activity conducted in 2023 can be summarized as follows:

- Work has been carried out on the further development of numerical tools for calculating and analysing plasma radiation for various scenarios;
- Work continued on the sensor concept, which required different characteristics for the different gases being considered for use as the working gas in the detector; a combination of filters (in a mixed version) was proposed, which made it possible to obtain the desired radiation spectrum and ensure acceptable operating conditions for the detector; the developed concept was assessed for its feasibility and new numerical tools were developed for further work on such problems;
- An initial analysis of the expected diagnostic measurement accuracy based on the proposed concept (for the non-optimal version of filters) was carried out when considering exclusively incident radiation;

- An analysis of the accuracy of tomographic reconstruction for various collimator diameters was carried out and its optimal size was proposed;
- The thermal load on the detector at its location was assessed;
- The following CAD model of the prototype detector has been developed;
- Work has begun on a closed gas system;
- Work continued on determining the influence of the magnetic field on the behaviour of generated charges in the gas volume;
- Mechanical analysis of the interface design at the boundary of the vacuum chamber and the sensor was carried out;
- An analysis of materials sufficient to provide neutron shielding of diagnostic elements was carried out.

Collaboration:

TUL, Lodz, Poland

References

[1] F. Sauli, "GEM: A new concept for electron amplification in gas detectors," Nuclear Instruments and Methods A **386**, p. 531, 1997.
[2] D. Mazon, "Final Report on Deliverables DC-2-T024-D001,-D002,-D003 T023-D001," [Online]. Available: https://idm.euro-fusion.org/?uid=2PJEED&version=v1.1&action=get_document.
[3] "DEMO Diagnostics and Control System Requirements Document (SRD)," https://idm.euro-fusion.org/?uid=2MNK4R&version=v3.0&action=get_document.
[4] M. Chernyshova et al., "Final report on conceptual studies for Prad, covering the technical specification," 2021. [Online]. Available: https://idm.euro-fusion.org/?uid=2MZ7GP.
[5] R. Dux, "Final Report on Plasma radiation and thermographic measurements contribution to spectroscopy," 2016. [Online]. Available: https://idm.euro-fusion.org/?uid=2MLQFF.
[6] S. Jabłoński et al., "Simulation of pulse height analysis soft X-ray spectra expected from W7-X," JINST 10 (2015) P10021.
[7] M. Siccinio et al., "DEMO physics challenges beyond ITER ," Fus. Eng. Design **156** (2020) 111603.
[8] M. Siccinio et al., "Development of the plasma scenario for EU-DEMO: status and plans," Fusion engineering and design (EU-DEMO special issue), accepted for publication, 2021.

Related 2023 articles and conference presentations:

1) S. Akbas, "Neutron Shielding Calculation for DEMO Radiated Power Measurement System", PLASMA2023 conference, Poster.
2) T. Czarski, "Reconstruction of plasma emissivity distribution in tokamak by approximation with base functions", PLASMA2023 conference, Poster.
3) M. Jagielski, Magnetic field influence on operation of planned GEM-based radiated power diagnostic for DEMO, PLASMA2023 conference, Poster.
4) M. Chernyshova, "Conceptual research on meeting tomographic reconstruction and measurement accuracy requirements: key factors in the development of a radiated power diagnostics for DEMO", PLASMA2023 conference, Poster.
5) M. Jagielski et al., "Hybrid Garfield++ simulations of GEM detectors for tokamak plasma radiation monitoring.", Fusion Engineering and Design, https://doi.org/10.1016/j.fusengdes.2023.113970.

Research Unit: Institute of Plasma Phyiscs and Laser Microfusion

WPAC: Advanced Computing

Title: Support of the imasification process of the EUROfusion codes to the IMAS database structure

Authors: P. Chmielewski, M. Gruca

Introduction

In 2023, there were continued studies initiated in the previous year, which involved the standardization of various codes used in institutions associated with the EUROfusion consortium into a unified database as part of preparations for the commissioning of the ITER reactor, which is under construction. Additionally, the development of the JOREK code proceeded, adapting the code to the characteristics of the TCV tokamak and improving the physical models contained within it.

Results

Regarding the development of the magnetohydrodynamic code JOREK, the objective was to implement and test non-equilibrium radiation terms in the code branch for the TCV tokamak in Switzerland. Specifically, diffusive and convective terms were tested to better reflect experimental conditions.

To faithfully represent experimental conditions on the TCV tokamak, it was necessary to implement diffusive and convective terms that reflected the real order of magnitude of thermal diffusion and convection. In the JOREK code branch for the TCV tokamak, an equation was implemented that takes into account both transverse and parallel thermal diffusion. The equation's consistency with the existing reduced MHD model was tested, convergence tests were conducted for cases with and without thermal diffusion. With the introduction of the equation, the convection coefficients are of the same order of magnitude. For model validation, the influence of the parallel convection coefficient on the density equation during discharges was presented in Figure 1, where Edge Localized Modes (ELMs) were observed.

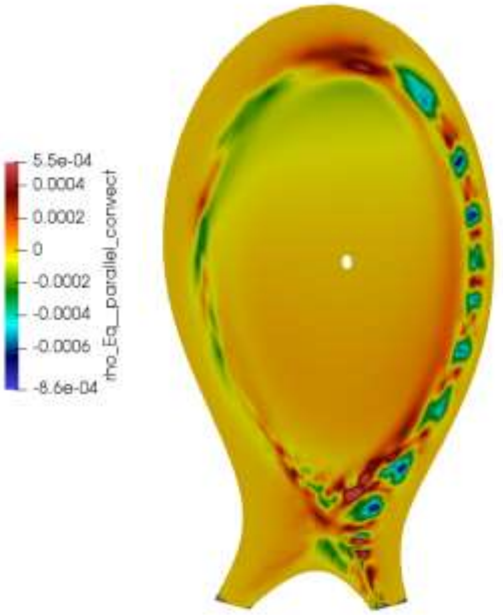

Fig. 1. Result of total density equation in function of termal convection coefficient (color bar). Visible plasma density perturbations related to MHD instabilities (ELMs).

As part of the work within the ACH package, the first version of the interface between the SOLEDGE3 code and the IMAS data environment was created. The program was tested for consistency with input data and made available to developers from the collaborating TSVV-3 team. The data structure unification process for the DYON code was also carried out. The development of an interface between the EIRENE code and the IMAS structure continued, and the creation of IMAS-compliant data structures for ERO2.0, GVEC, GRILLIX, and GBS codes was initiated.

This year, activities were focused on developing the interface between SOLPS and EIRENE. The actual SOLPS result was used as a starting point for generating the interface. The interface is planned to be completed in the next year. The IMAS interface for ERO2.0 was developed this year in accordance with the agreements with the EUROfusion TSVV project leaders. Both input and output interfaces are being developed using the available CPO interface as a starting point. Several meetings were conducted with members of the EIRENE and ERO teams to define IMAS data structure extensions required to unify the EIRENE and ERO2.0 codes. A method for storing specific code parameters and coefficients within the code structure was defined. Within the available

Generic Grid Description (GGD), simplified structures containing numerical grids for EIRENE, SOLPS-ITER, and ERO2.0 were created. The actions focused on defining the method of recording physical quantities in GGD-defined spaces and creating interfaces necessary for inputting numerical values at grid points for individual physical quantities. Work has also begun on scripts to read values of individual physical quantities stored in the unified IMAS structure and input them into the EIRENE and ERO2.0 code structures. As a result, once the discussed interface is completed, data sharing between codes will be possible regardless of the data structure and format in individual codes, using the IMAS data structure.

Additionally, major work on the interface for the DYON code has been completed. Both the input and output of the DYON code are connected to IMAS as per the original plan. Documentation regarding the interface was provided to DYON code developers and ACH members. Work on the user interface is ongoing and will continue next year along with the improvement and maintenance of documentation.

Work on the SOLEDGE3 code has resulted in the implementation of procedures for reading and writing the three-dimensional grid of the SOLEDGE3 code within the unified 'General Grid Description' standard of the IMAS structure. Functions for reading various types of grids for different divertor configurations were unified. Procedures for reading and writing magnetic field induction into the equilibrium IDS within IMAS were also created, both for two- and three-dimensional cases. Functions responsible for reading and writing plasma evolution (parameters such as electron and ion density and temperature, transverse velocity) within the edge profiles IDS were implemented. The interface has been made available to SOLEDGE3 code developers in the ACH-EUROfusion Gitlab repository. Further work is planned regarding the implementation of additional physical quantities resulting from the operation of the SOLEDGE3 code.

Conclusions

As a result, non-equilibrium radiation terms in the JOREK code were implemented to faithfully reflect the experimental conditions prevailing in the TCV tokamak, achieving a realistic representation of thermal diffusion and convection magnitudes in the modeled plasma. A method for storing specific code parameters was defined, and a way to record physical quantities in the GGD IMAS structure for the ERO2.0, SPLS-ITER, and EIRENE codes was developed. The conducted work will ultimately result in the unification and ability to share data obtained from different codes.

Work on reading and writing procedures for data in the IMAS structure for the DYON code has been completed. Procedures for reading and writing the three-dimensional grid of the SOLEDGE3 code within the unified 'General Grid Description' standard of the IMAS structure were executed and implemented.

The results of performed activities in international cooperation contribute to the knowledge and experience of IPPLM scientists. International collaboration strengthens the position of the Institute of Plasma Physics and Laser Microfusion on the international stage.

Collaboration

The Swiss Plasma Center, Ecole Polytechnique Fédérale de Lausanne; Poznań Supercomputing and Networking Center; IMAS, ITER Organisation.

References

[1] F. Imbeaux el al., Nucl. Fusion 55 (2015) 123006 (13pp)

Research Unit: Institute of Plasma Phyiscs and Laser Microfusion

WPSAE: Safety and Environment

Title: SAE-S.01.03-T003-D018: Activation of divertor components including dust (2023); SAE-S.01.03-T003-D021: Activation of penetrations and windows at equatorial, upper and lower ports (2023) and SAE-T.02.02-T001-D002 Report on requirements of the VV diagnostic dust monitoring systems

Author: E. Łaszyńska, P. Gąsior

Introduction

1) As part of the WPSAE (Safety and Environment) project, activation simulations are conducted, playing a crucial role in the design of the prototype DEMO thermonuclear power plant. They allow for predicting changes in chemical composition over time, estimating activation levels, decay heat, and radiation dose released from materials subjected to irradiation under specific experimental conditions. Results from such simulations are highly important for designing radiation shielding, developing maintenance schedules for specific devices, as well as planning material management for those remaining radioactive for extended periods.

The task assigned to IPPLM scientists in 2023 involved conducting activation simulations for individual divertor components, layers of divertor material dust subject to erosion due to interaction with plasma, and for individual diagnostic window materials in the locations of the middle and upper ports for the DEMO device.

2) Research within the framework of the WPSAE project was conducted in collaboration with ENEA and VT and focused on the development of dust diagnostics for the DEMO reactor. 2023 was the first year of this research, therefore it was of a fundamental nature and largely concerned the extrapolation of the design of such diagnostics from ITER to DEMO, which will operate under different conditions, particularly those related to higher ionizing radiation.

The main objective of the research was to identify potential measurement systems and tools that could be used to measure different types of dust (so-called hot dust deposited on the inner wall of the device, cold dust located in the divertor region) and the requirements they should meet in terms of the limits and nature of the identified dust. The mechanism of dust formation and its physical and chemical parameters were also analyzed.

Of importance for the extrapolation of the diagnostics foreseen for ITER was the recent design change involving the replacement of the beryllium wall with a tungsten wall, and consequently the change of dust from beryllium to tungsten. It was also necessary to take into account that the solutions foreseen and developed for ITER were developed and tested for carbon dust, while at the time materials such as graphite and CFC were popularly used as PFCs (Plasma facing components - elements in contact with the plasma).

Results

1) In the initial phase of the study, neutron transport simulations were conducted using the MCNP code to calculate neutron spectra for components of the divertor and the locations of diagnostic windows. These simulations were based on a geometric model derived from research within the WPDIV project. The divertor components and corresponding cells were identified using the MCNP model along with the CAD model for the divertor. Additionally, activation calculations were performed for thin layers of dust eroded from the Plasma Facing Components (PFC). The dust layers, their volumes, and masses were calculated based on the surface area of the PFC. Two Breeding Blanket models were considered: HCPB and WCLL. An example of neutron spectra calculated for the first divertor component for DEMO, considering two Breeding Blankets variants: HCPB (Helium Cooled Pebble Bed) and WCLL (Water Cooled Lithium Lead), are shown in Figure 1.

Activation simulations have been performed using FISPACT-II code. Results from the activation calculations provided insights into the radioactivity, decay heat, and radiation dose for each divertor component, dust layer, and diagnostic window material over various time intervals. An example result of activation simulations is presented in Figure 2.

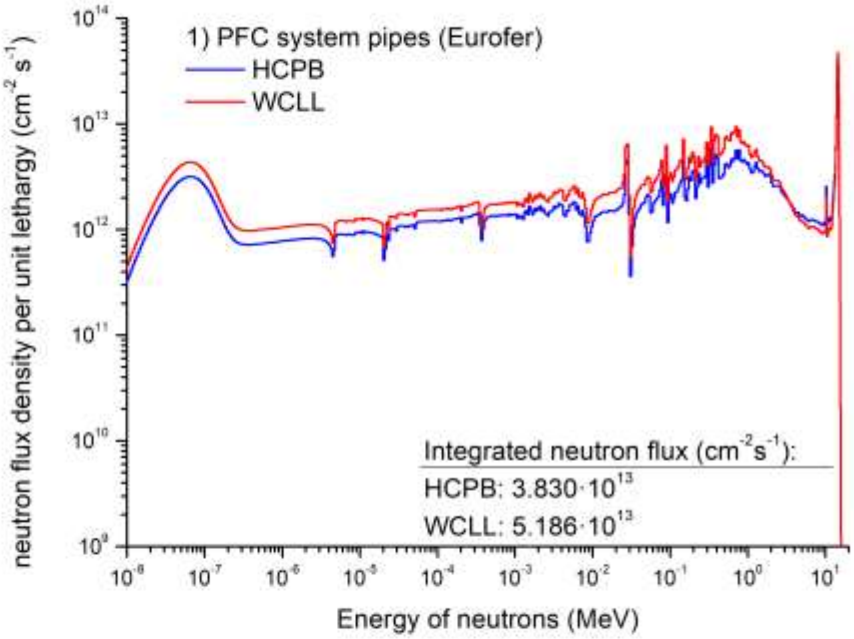

Figure 1. MCNP-calculated neutron spectrum for the first divertor component for DEMO, considering two Breeding Blankets variants: HCPB and WCLL.

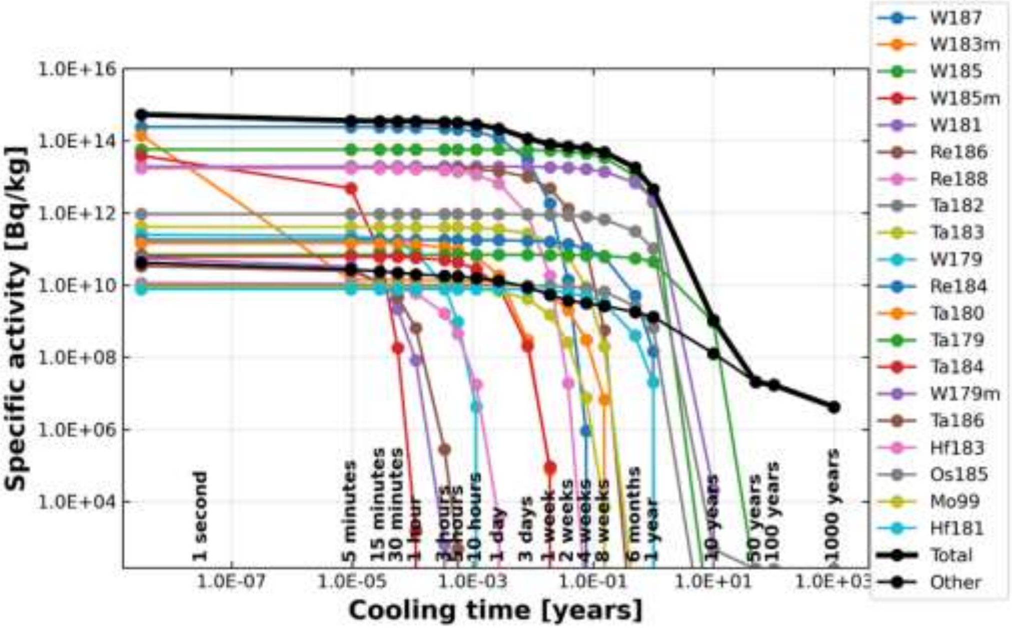

Figure 2. The calculated specific activity and its variation over time for individual nuclides forming in the Inboard IL PFC W monoblocks layer for DEMO.

The analysis demonstrated that results were generally higher for the DEMO model with WCLL BB due to the higher neutron flux.

2) The task is well concluded by the table present also in the submitted report in extended version.

Diagnostics	Opportunities	Risks
IVVS (In Vessel Viewing System)	○ Only diagnostic providing non local measure ○ Both visual and metrology information ○ Higher resolution achievable with FM scan / interferometric concept	- Surface coverage coupled with viewing angles might reduce resulting resolution - Higher resolution might be needed (e.g. 0.1 mm over DEMO surface results into >7 tons of dust * Dust Conversion Factor) - Degradation problems:
VIS/Infrared viewing systems	- The only diagnostics which can characterize dust on hot surface, - Indispensable for other purposes, thus it is granted that it will be available - Provides direct input to the overall figure of dust - Employs methods which are under rapid development these days.	- May require calibration /training and much computational power
Laser scattering methods	- Employs available Thomson scattering equipment, - Gives a good overview on grain distribution and concentration of mobilized dust - If properly calibrated, may provide information on overall amount of the cold dust	- Requires R&D activity which, however, may be at least partially done in laboratory conditions and further tested on tokamak (ITER)
QCM (Quartz Microbalance)	- Precise monitoring of the local accumulation of the mass - Easy to use (frequency measurements) and low cost - If correctly extrapolated based on a grid of sensor, may provide information on overall amount of the cold dust	- Only local measurements (requirement of application of a grid of sensors), - No information on dust parameters - Possible issues with irradiation - System maintainability over operational life
CDM (Capacitive Diaphragm Microbalance)	- Precise monitoring of the local accumulation of the mass - Easy to use (frequency measurements) and low cost - If correctly extrapolated based on a grid of sensor, may provide information on overall amount of the cold dust	- Only local measurements (requirement of application of a grid of sensors), - No information on dust parameters - System maintainability over operational life
Electrostatic sensors	- Precise monitoring of the local accumulation of the mass - Easy to use (electronic counter) and low cost, - Scarce information on the dust parameters (counts may be scaled on the particle	- Only local measurements (requirement of application of a grid of sensors), - Relatively low maturity, however, rather easy to develop

	diameter), especially if only tungsten dust is under measurements - If correctly extrapolated based on a grid of sensor, may provide information on overall amount of the cold dust	
Subdivertor endoscope	- In future may provide moderately comprehensive information (but still qualitative)	- Relatively complicated and time consuming - Better tailored for R&D applications, not a safety system
Dust Removable samples	- Can be flexibly used in a variety of material research characterization methods - Can provide detailed and accurate information on crucial factors as irradiation or retention	- Does not proved overall information on dust inventory - Does not constitute an online tool - Better tailored for R&D applications, not a safety system

Conclusions

1) Activation simulations were conducted for divertor components and dust layers for DEMO. These results are crucial for designing radiation shielding, developing maintenance schedules for the DEMO device, and planning the management of materials that will remain radioactive for long periods. A comparison of simulation results was performed for the DEMO model with two considered Breeding Blankets: HCPB and WCLL. The obtained results will influence the final choice of BB for DEMO. Calculations using FISPACT-II code were also carried out for various considered diagnostic window materials. The results obtained will allow for optimizing the material composition of diagnostic windows for the DEMO device.

Future research in 2024 will involve conducting activation calculations for a new electron accelerator model and considering materials for diagnostic window coatings in DEMO ports.

2) An important conclusion of the project was that the diversity of dust generated in such devices requires the use of multiple types of diagnostics to ensure protection against various eventualities that may arise due to the current lack of experience with such large systems. Important components of such diagnostics will include a special system for imaging the interior of the chamber, VIS and IR cameras, laser scattering diagnostics, endoscopes, sensors using microbalances, and dust collectors. Based on the analyses, ENEA, IFPiLM and VT prepared a joint report.

Collaboration

ENEA, VTT, UKAEA, CEA, IPP, JSI

Research Unit: Institute of Plasma Phyiscs and Laser Microfusion

WPENS: Early Neutron Source

Title: Early Neutron Source

Authors: B. Bieńkowska, K. Tymińska, R. Prokopowicz

Introduction

One of the important systems of the IFMIF-DONES (https://ifmif-dones.es/) device will be the neutron beam line. It will guide the neutrons from the Test Cell (TC) to the Complementary Experiments Room (CER). The system is at an early stage of design, which requires the development of general technical solutions to ensure that radiation protection requirements are met in the first place. Hence, before proceeding to the next phases of design work, it is extremely important to perform calculations verifying the correctness of the postulated solutions in terms of radiation protection. The neutron beam line consists of a neutron tube and a beam shutter. From the point of view of radiation protection, the most important element is the shutter. Its main task is to provide protection against radiation that will allow it to meet the relevant standards. The work carried out in 2023 was aimed at preparing tools in the MCNP code [1] to carry out calculations of radiation transport, in particular neutron and gamma rays, in the designed neutron beam shutter. These calculations will allow us to verify whether the proposed design solutions will provide sufficient protection against radiation. They will also be used to select the material from which the neutron tube will be made, by determining the influence of the aforementioned material on the quality of the neutron beam. The model developed in the MCNP code will also be used in the future to perform calculations of the level of radiation excited by neutrons in individual subassemblies and elements of the system under consideration. This task is a continuation of the task implemented in 2023.

The conceptual design of the neutron tube and the shutter is being developed at the National Centre for Nuclear Research under the task ENS-4.7.1.1-T018-03. The neutron shutter will consist of four shielding disks and a fifth disk with interchangeable filters for shaping the neutron spectrum. The rotating discs will be placed on the shaft and the whole system will be inserted into a special cavity in the wall. Depending on the position of the discs relative to each other and the neutron tube, the shutter will be in either the closed or open position.

Results

This year's shutter design includes changes from the 2023 design. A team of engineers from NCBJ delivered a new design of the shutter as a CAD model. On its basis, a geometrical model of the MCNP neutron shutter was developed. The SuperMC [2], [3] tool was used for this purpose. The MCNP model of the shutter was then integrated into the model of the entire DONES. The CAD models of the shutter in the closed and open positions are shown in Figure 1. The corresponding MCNP models of the shutter can be seen in Figure 2.

The obtained MCNP models are used for shielding, activation and analysis of materials from which a neutron tube can be built.

Based on the analysis of the cross-sections for the reaction with neutrons, the following materials were selected from which the neutron tube could be made: nickel, lead + steel outer tube, graphite + steel outer tube, zirconium (Zircalloy 4), copper, SS316 steel, aluminum PA4.

The neutron flux and neutron spectrum at the exit of the shutter were calculated using the open-position shutter model. These calculations were carried out for all variants of pipe materials. The results and their analysis will be presented in 2024.

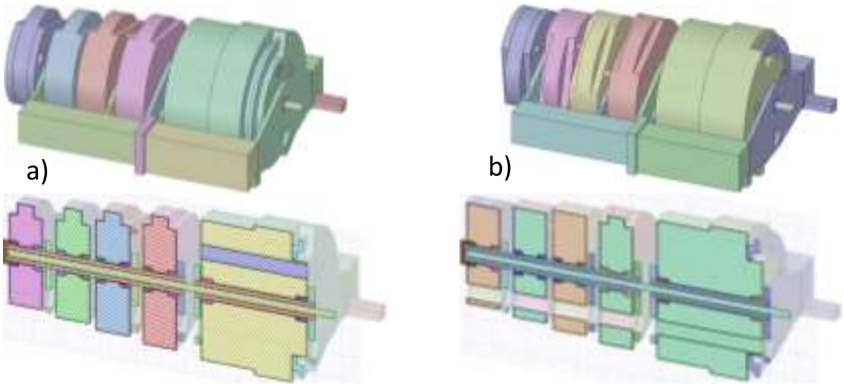

Figure 8 CAD models of a neutron shutter: (a) a closed position; (b) an open position.

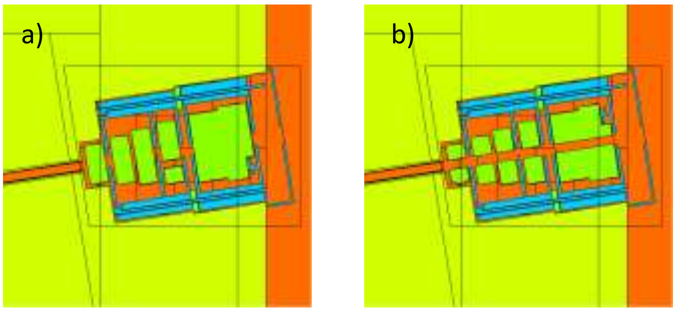

Figure 9 MCNP Shutter Models: (a) a closed position; (b) an open position

Conclusions

1. The MCNP model of the neutron beam shutter has been created and prepared for calculations
2. The set of materials for the neutron beam tube was considered.

Collaboration

NCBJ

References

[1] Goorley T. Initial MCNP6 Release Overview, Nuclear Technology, 180, pp 298-315
[2] Y. Wu, "Multi-functional Neutronics Calculation Methodology and Program for Nuclear Design and Radiation Safety Evaluation", Fusion Science and Technology 74 (2018), 321-329
[3] Y. Wu, "CAD-Based Monte Carlo Program for Integrated Simulation of Nuclear System SuperMC", Annals of Nuclear Energy 82 (2015), 161-168

Related 2023 articles and conference presentations:

1. Qiu Y. et al Overview of recent advancements in IFMIF-DONES neutronics activities, Fus. Eng. Des. Vol 201, April 2024, 114242

Research Unit: Institute of Plasma Phyiscs and Laser Microfusion

WPPrIO: Preparation for ITEROperation

Title: PrIO-5.3.ACT-T002-D003: Report on the IPPLM measurements of sample following DTE2 and contribution to pre-analysis of DTE3 and measurements in KN2

Authors: Ewa Łaszyńska

Introduction

Due to the lack of an existing facility for irradiating materials with a high-energy neutron source of 14 MeV, experiments conducted on the JET tokamak provide a unique opportunity to examine the activation behaviors of materials used as structural materials in thermonuclear reactor environments during actual DT fusion synthesis, albeit at lower neutron fluences than those expected in the ITER tokamak. These materials will be utilized for the production of key structural components of the tokamak, as well as heating and diagnostic systems. Under neutron irradiation, they may emit secondary radiation, which affects the operation and lifespan of key ITER tokamak components. Experimental data collected during measurements of samples of ITER tokamak structural materials irradiated in the tokamak environment will validate activation codes and nuclear data libraries used for fusion analysis.

Results

Selected ITER material samples and dosimetry foils were irradiated in the LTIS position on the JET tokamak during the DTE2 and TT campaigns [1]. After retrieval from the cassette, selected ITER material samples were sent to IFPiLM for high-resolution gamma spectrometry measurements. They were performed in 2022 at the Neutron and Gamma Radiation Diagnostics Laboratory. The radioactivity of products formed in irradiated ITER materials was determined with an uncertainty of 10%. The largest contribution to the total uncertainty of radioactivity is attributed to the uncertainty of gamma radiation detection efficiency.

To examine the behaviour of materials intended for use in constructing the ITER tokamak and the concentration of impurities present in them, dosimetry foil and ITER materials (CuCrZr, Alloy A286, and SS316L(N)) were irradiated during individual discharges of the DTE2 experimental campaign on the JET tokamak. The materials were irradiated at the KN2 6U irradiation end.

The main task assigned to scientists from IFPILM, scheduled for completion in 2023 as part of the WPPRIO project, involved conducting numerical simulations using the FISPACT-II code. These simulations aimed to determine the expected radioactivity of products formed in ITER tokamak materials and dosimetry samples irradiated during the DTE2 and TT campaigns on the JET tokamak. This includes both materials activated in the LTIS position and at the KN2 6U irradiation end during individual discharges of the DTE2 campaign.

Activation simulations began with the preparation of input files for the FISPACT-II code. Each file defined the composition of the respective sample based on material certificates provided by manufacturers. In the next step, an irradiation scenario was prepared based on the measurements of total neutron fluence for each discharge, measured by the KN1 fission chamber system on the JET tokamak. Neutron spectra for each sample irradiated in the cassette in the LTIS position, as well as for materials irradiated in the KN2 6U position, were calculated using the JET tokamak model and the MCNP code by a team of scientists from Slovenia. Nuclear reaction cross-sections data from the TENDL-2017 library were used in the activation calculations. The results of activation calculations using the FISPACT-II code for the CuCrZr sample irradiated in KN2 6U during discharge #99634 are presented in Table 1.

Table 1. Radioactivity of nuclear reaction products formed in the CuCrZr sample irradiated at the KN2 6U irradiation end during discharge #99634.

Nuclide	Radioactivity [Bq]	Uncertainty [Bq]
Cu 66	1.347E+07	2.24E+05
Cu 62	2.772E+06	2.03E+05
Co 62	1.101E+05	3.44E+04
Cu 64	3.875E+05	4.67E+03
Zr 90m	9.135E+05	8.97E+04
V 52	2.373E+04	2.65E+03
Co 60m	3.742E+05	2.15E+04
Co 62m	1.028E+04	4.14E+03
Ta182m	1.021E+07	2.68E+05
Nb 94m	5.786E+04	2.56E+03
Ni 65	3.981E+03	1.36E+03
V 53	3.385E+03	7.64E+02
Zr 89m	9.188E+02	9.03E+01
Co 61	1.837E+02	6.63E+01
Ta182	7.129E+00	6.83E-01
Mn 56	1.072E+01	5.24E-01
Cr 55	1.747E+03	1.61E+02
Zr 97	9.167E+00	3.65E-01
Co 60	9.778E-01	6.07E-02
Y 90m	6.141E+00	7.29E-01
Zr 89	5.203E+00	3.76E-01
Co 58m	3.942E+01	2.11E+00
Cr 51	1.462E+01	6.33E-01
Nb 92m	2.132E+00	3.35E-01
Ta180	9.191E+00	4.64E-01
Y 90	5.594E-01	8.34E-02

The results for all samples have been included in the technical report of the WPPrIO task for the year 2023. It is also worth mentioning that not all radionuclides resulting from calculations using the FISPACT-II code were visible in the gamma radiation spectrum recorded by the HPGe detector. This is due to the short half-life of many of the mentioned nuclides and not all nuclides emit gamma radiation, which can be measured using gamma spectrometry.

The next task assigned to scientists from IFPiLM was to estimate the expected radioactivity of nuclides that would arise in samples of ITER tokamak structural materials irradiated in the LTIS cassette during the DTE3 campaign on the JET tokamak, which took place in 2023.

The following assumptions were made for the calculations:

- Samples include Fe, CuCrZr, W, and Al-bronze.
- Total 14 MeV neutron budget: 7·10^20, 3.5·10^20.
- Duration of the experimental campaign: 20 days.

The results of activation calculations using the FISPACT-II code for the W sample (ITER#14) with a DT neutron budget of 7·10^20 are presented in Table 2.

Table 2. The results of calculations for the expected activity of nuclides that will be created in the W sample (ITER#14) irradiated in the LTIS cassette during the DTE3 campaign on the JET tokamak.

Nuclide	Radioactivity [Bq]	Uncertainty [Bq]
W 187	3,26E+05	3,83E+00
W 181	5,39E+03	5,32E+00
W 185m	2,75E+04	8,03E+00
Ta184	2,58E+02	3,28E+01
W 183m	4,30E+04	1,24E+01
W 185	3,77E+04	8,76E+00
Ta183	3,67E+02	3,15E+01
Ta186	2,05E+02	4,21E+01
Ta182	2,62E+01	1,56E+01
Hf181	2,56E+01	3,69E+01
Hf183	2,03E+02	1,48E+02
W 179	4,20E+02	1,19E+01
W 179m	9,06E+01	1,19E+01
Co 58	1,21E+00	8,67E+00
Hf179n	8,89E+00	7,17E+01
Ta179	2,96E+01	3,60E+01
Ni 57	4,43E-01	1,29E+01
Hf180m	1,38E+01	1,40E+02
Co 57	5,52E-01	1,07E+01
Co 58m	3,77E+00	1,04E+01
Co 60	1,23E-02	1,83E+01
W 183	0,00E+00	0,00E+00
Ta180	7,84E+00	5,18E+01
Fe 59	1,42E-02	2,75E+01

The next task was to conduct activation simulations using the FISPACT-II code for materials planned for irradiation in the KN2 6U position during individual discharges of the DTE3 campaign on the JET tokamak. These simulations were performed for the following materials: W, CuCrZr, Al, Nb, and Al-bronze.

Conclusions

Activation simulations were conducted using the FISPACT-II code for ITER tokamak structural materials irradiated in the LTIS position during the DTE2 and TT campaigns, as well as irradiated at the KN2 6U irradiation end during individual discharges of the DTE2 experimental campaign. The radioactivity of nuclides created in irradiated ITER tokamak materials was compared experimentally using gamma radiation spectrometry and determined through numerical simulations using the FISPACT-II code. It was discovered that in each irradiated sample of ITER tokamak materials, Zn65 was present, which originated from contamination of the samples during the material cutting process. Therefore, the samples designated for irradiation during the DTE3 campaign were subjected to polishing to remove contamination in the form of Zn. This will enable the investigation of real contaminants in materials originating from the production process and their impact on the overall radioactivity of the material.

In 2023, activation simulations were also performed to estimate the expected radioactivity of nuclides that would arise in ITER tokamak materials during their irradiation in the DTE3 campaign (for the LTIS and KN2 6U positions). This allowed for the optimization of geometry and measurement sequences.

Collaboration

UKAEA, ENEA, JSI, IFJ PAN, CEA

References

1. Packer, Lee; Batistoni, Paola; Bearcroft, Chris; Bradnam, Steven; Eardley, Edward; Fabbri, Marco; Fonnesu, Nicola; Ghani, Zamir; Gilbert, Mark; Gorzkiewicz, Krzysztof; Grove, Callum; Kierepko, Renata; Laszynska, Ewa; Lengar, Igor; Litaudon, Xavier; Loreti, Stefano; Turner, Anthony; Mietelski, Jerzy; Pillon, Mario; Savva, Marilia; Shand, Chantal; Stamatelatos, Ion; Vasilopoulou, Theodora; Villari, Rosaria; Wojcik-Gargula, Anna; Žohar, Andrej, „ITER materials irradiation within the D-T neutron environment at JET: post-irradiation analysis outcomes and recommendations", submitted to Nuclear Fusion

Related 2023 articles and conference presentations:

1. E. Laszynska, P. Batistoni, R. Kierepko, J. W. Mietelski, C. R. Nobs, L. W. Packer, R. Villari, A. Wojcik-Gargula and JET Contributors*, "Benchmark experiments with ITER materials irradiated in the JET tokamak – comparison of the neutron-induced activity results" – poster during PLASMA conference, Warsaw, Poland.

Research Unit: Institute of Plasma Phyiscs and Laser Microfusion

WPENR-IFE: Enabling Research

Title: Advancing shock ignition for direct-drive inertial fusion (CfP-FSD-AWP21-ENR-01-CEA-02)

Authors: Prof. D. Batani

Introduction

In 2023, the IFPiLM team participated in the EUROfusion project in the implementation of the tasks of the following packages: **WP3** and **WP5**.

Within **WP5** package: "*Magnetic-field-assisted implosion and ignition*" continued the analysis of research results obtained in previous experiments at PALS, regarding the generation of magnetized plasma jets using disk-coil (DC) disks, which enable both the generation of plasma from the disk from copper foil and the magnetic field, thanks to the coupling of the disk with a single-turn coil. The results of previous research presented in paper [1] confirmed the possibility of generating magnetic fields above 5 T when illuminating the targets with a DC 1-harmonic iodine PALS laser with an energy of about 0.5 kJ. This value of magnetic field induction seems to be sufficient, taking into account the scheme of implementing inertial fusion through magnetic implosion of laser disks [2-4]. In these experiments, by starting the compression process from a pre-seeded magnetic field of several Teslas, an induction level of several kT can be achieved in the compressed core as a result of its advection in the plasma flow [5, 6]. Such powerful magnetic fields are promising for magnetic inertial fusion because they reduce energy losses in the direction perpendicular to the magnetic field lines, which may be enough to limit a-particle fusion in a compressed core [7-9].

The results of previous measurements carried out at PALS using various diagnostic methods (3-frame complex interferometry combined with HE emission measurements) and 3D simulations have shown that the magnetic field generated in DC targets leads to the collimation of the HE stream, an increase in temperature and average electron energy, as well as to an increase in the HE current density [1]. Moreover, based on the measured angular distributions of electron energy spectra, 3D simulations were performed, which allowed to visualize the influence of the magnetic field on the HE flux and to obtain information about the spatiotemporal distributions.

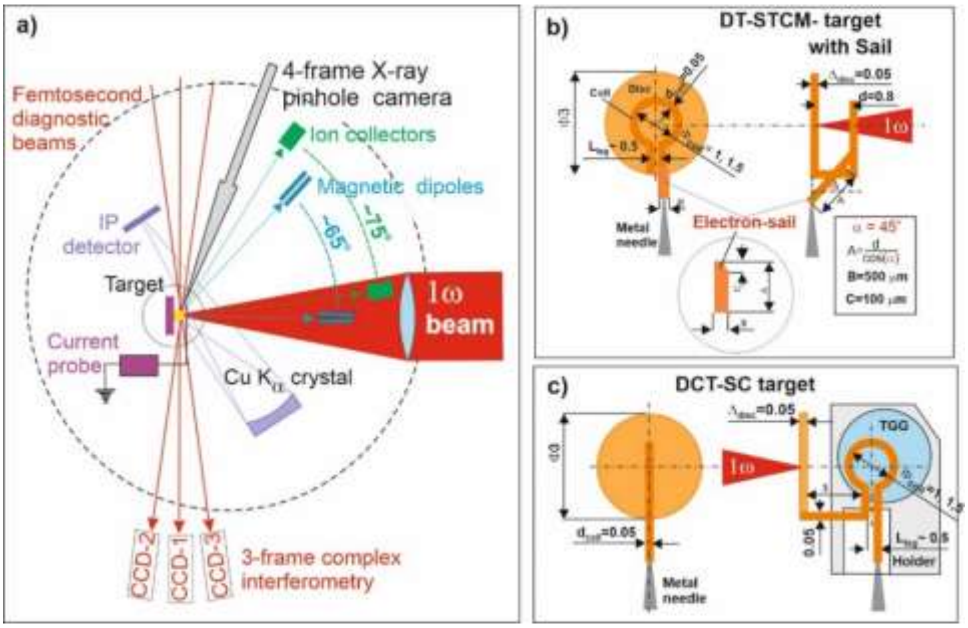

Fig. 1: *Experimental system: a) scheme of diagnostics location in the chamber, b) modified DC target construction (DT-STCM-S), c) DC target with a single-turn coil (DCT-SC) for measuring the magnetic field in the coil using the Faraday effect in TGG crystal.*

The results of these preliminary tests obtained by illuminating DC targets with the 1st harmonic radiation of the PALS iodine laser became the motivation to undertake further research with DC targets with a modified structure shown in Fig. 1b. An important element of the modification of the target construction is the so-called electron-sail, trapping electrons in the outer leg of the coil near the disk, which leads to an increase in the current flowing through the coil. The location of the diagnostics and the construction of the targets used in the experiment are shown in Fig. 1.

In order to obtain more detailed information about the influence of the magnetic field on the parameters of the created plasma streams, tests were carried out for DT-STCM targets made of Cu with different coil-to-disc distance (L = 0.8 and 1.6 mm) and with different coil diameters (Φcoil = 1 and 1.5mm).

To measure the magnetic field in the coil, DCT-SC targets were used with the construction shown in Fig. 1c, with the coil perpendicular to the disk, which enables measurements of the magnetic field using the Faraday effect in the TGG crystal placed in a special holder near the coil. The role of the handle constructed in this way is to shield the TGG against the degrading effects of X-ray radiation emitted from the ablation plasma.

Example results obtained from individual diagnostics are presented below.

A-Measurements using 3-frame complex interferometry [10-12]

The aim of the measurements was to visualize the process of creating magnetized plasma in DT-STCM targets with a modified construction (Fig. 1b) illuminated by the 1-harmonic PALS iodine laser of various intensities, and to obtain quantitative information on the influence of the magnetic field generated by the DT-STCM target coil on the space-team distributions of electron density and current density distributions responsible for the emission of hot electrons from the ablation plasma. Examples of complex interferograms illustrating the expansion of the plasma in the DT-STCM targets at different times and for different intensities obtained by changing the focus of the laser beam are shown in Fig. 2. The free expansion of the ablation plasma from the Cu disk is illustrated in Fig. 3.

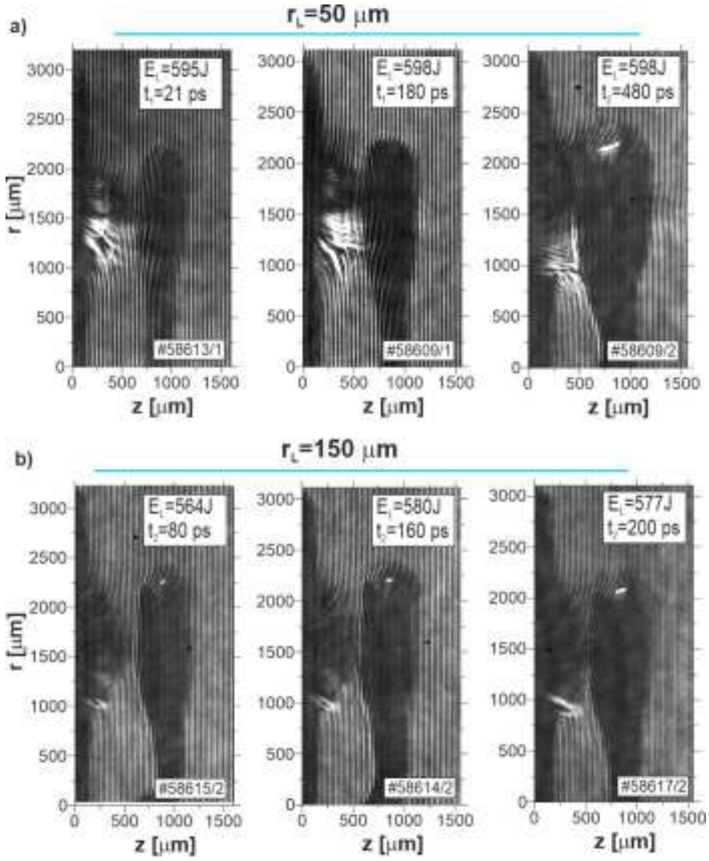

Fig. 2: Sequences of complex interferograms illustrating the plasma expansion in the DT-STCM targets at different times, in the case of illumination by the 1-harmonic PALS laser focused to different facal spot radii: a) rL=50 μm and b) rL=150 μm.

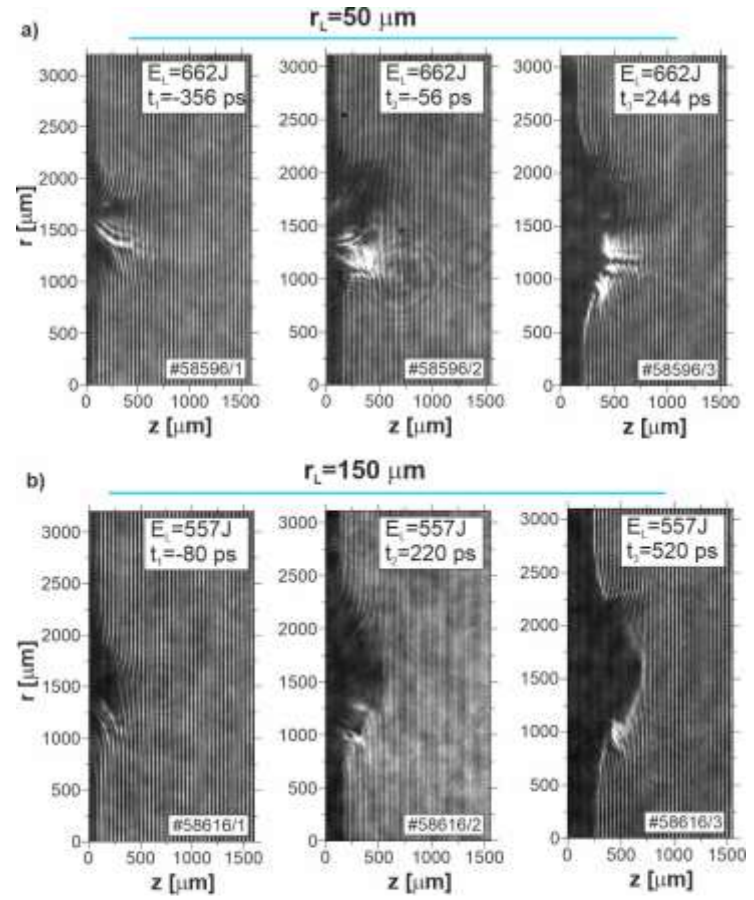

Fig. 3: Sequences of complex interferograms illustrating the expansion of plasma from the Cu disk at different times, in the case of illumination by the 1-harmonic PALS laser focused to different focal spot radii: a) r_L=50μm and b) r_L=150 μm.

In all interferograms, the modulation of interference fringes caused by the Faraday effect and the initial rotation of the polarizer in the measurement system is visible in the lower half. This asymmetry of the Faraday effect confirms the axial symmetry of spontaneous magnetic fields (SPM) in the ablation plasma. Qualitative differences between the interferograms regarding the modulation intensity of the interference fringes and their distribution clearly demonstrate the influence of the magnetic field on limiting the radial expansion of the plasma in the case of DT-STCM targets.

Quantitative information about the parameters of the plasma created in DT-STCM targets obtained on the basis of complex interferograms in Fig. 2 is shown in Fig. 4 and Fig. 5. Fig. 4 shows the electron density distributions and current density distributions at various moments of plasma expansion created in DT-STCM targets illuminated by the 1-harmonic PALS laser focused to a focal spot radius of r_L = 50 μm, and obtained on their basis: distributions of the total current (related to the movement of electrons towards and away from the target), linear density distributions and axial electron density profiles magnetized plasma flux, while Fig. 5 shows the same data obtained when illuminating the DT-STCM targets by a laser beam of lower intensity corresponding to an increase in the focal spot radius to r_L = 150 μm.

Electron density distributions and current density distributions at various moments of plasma expansion from a Cu disk illuminated by the 1-harmonic PALS laser focused to a focal spot radius of r_L = 50 μm, and the following obtained on their basis: total current distributions (direct and return), linear density distributions and axial profiles electron density of the magnetized plasma stream, are presented in Fig. 6.

As can be seen from Fig. 4 and Fig. 5, in both considered cases of illumination of DT-STCM targets, both the spatial distributions and the linear density distributions and axial electron density profiles obtained on their basis clearly demonstrate the limitation of the axial expansion of the plasma by the magnetic field generated by the coil DT-STCM shield visible as an increase in density at the plasma jet front. This effect is greater for a larger laser beam radius. In the case of free expansion from the Cu disk, Fig. 6, the plasma expands into a cone as expected, and the linear and axial density profiles decrease monotonically.

From comparison of current density distributions in the plasma created in DT-STCM targets at different laser beam focusing shows that increasing the laser beam radius leads to a significant change in the current density distribution. In the case of a smaller laser beam radius r_L = 50 μm (Fig. 4 c), most of the current flows in the central area with a cylinder radius r = 250 μm, while increasing the focal spot radius three times and forcing axial expansion (Fig. 5 c) causes the current to flow in area outside the center.

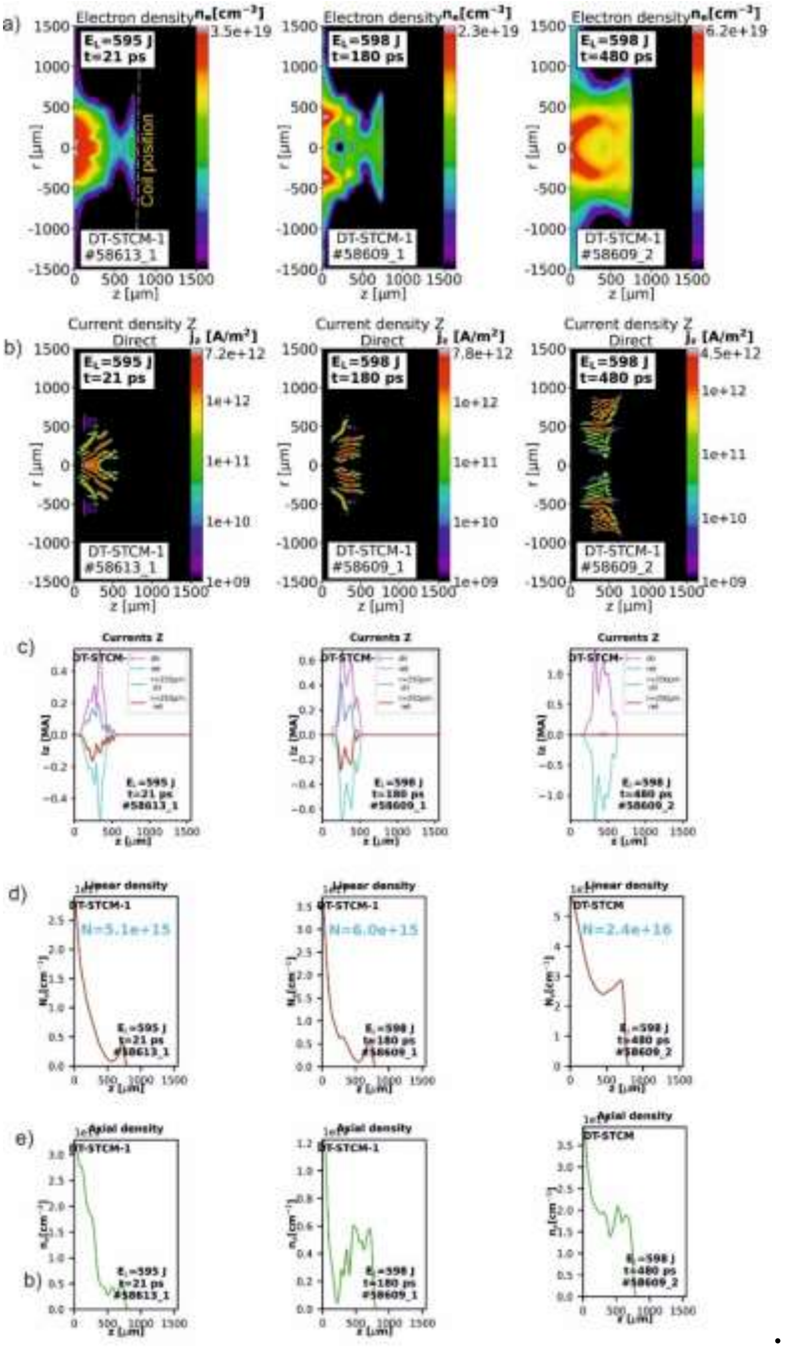

Fig. 4: Electron density distributions - (a) and current density distributions - (b) at various moments of plasma expansion in DT-STCM targets illuminated by the 1-harmonic PALS laser focused to a focal spot radius of r_L = 50 μm and obtained on their basis: c) distributions of total current (direct and return), d) distributions of linear density e) axial profiles of electron density of the magnetized plasma stream.

.

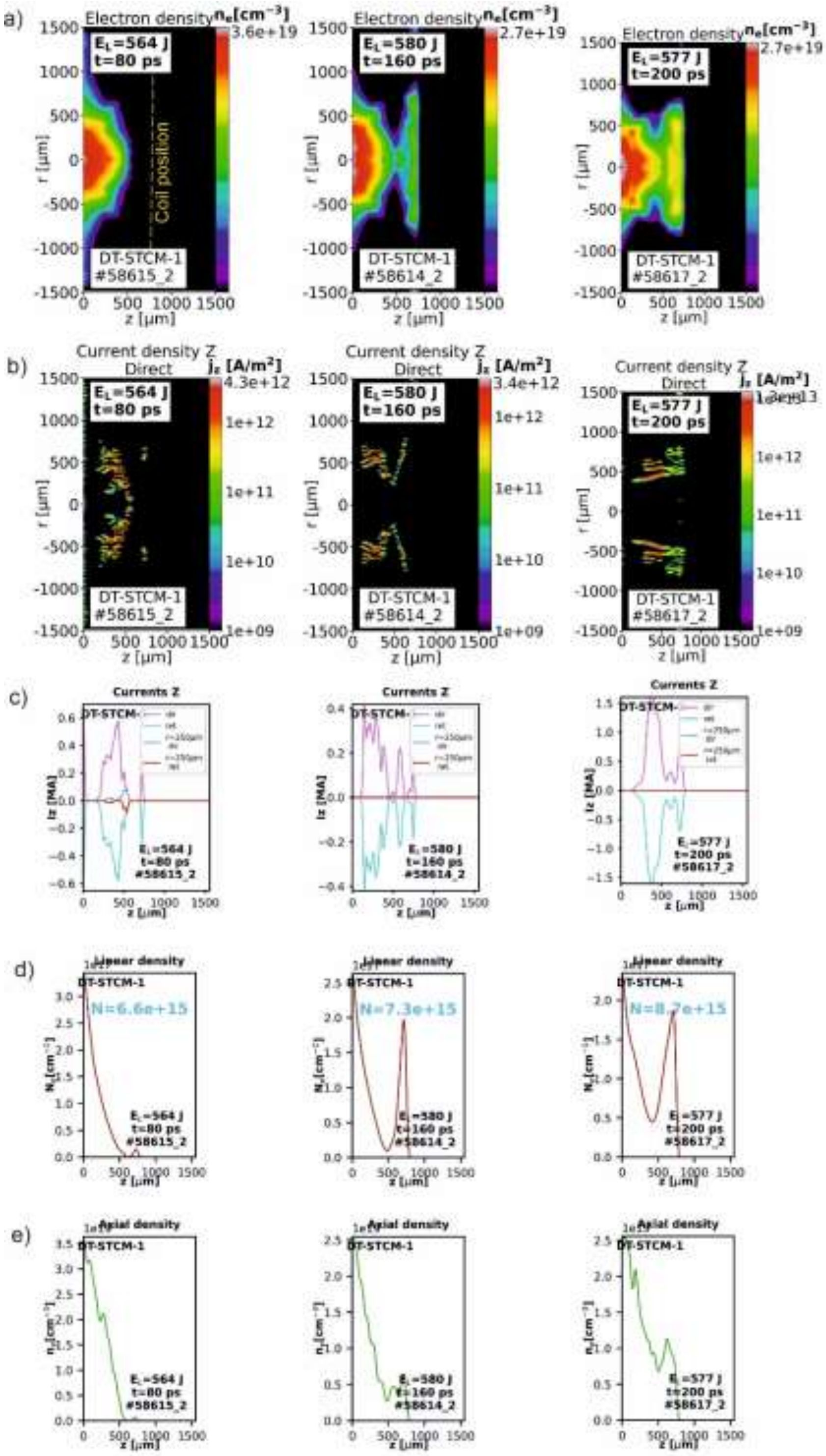

Fig. 5: Electron density distributions - (a) and current density distributions - (b) at various moments of plasma expansion in DT-STCM targets illuminated by the 1-harmonic PALS laser focused to a focal spot radius of r_L =1 50 μm and obtained on their basis: c) distributions of total current (direct and return), d) distributions of linear density e) axial profiles of electron density of the magnetized plasma stream.

.

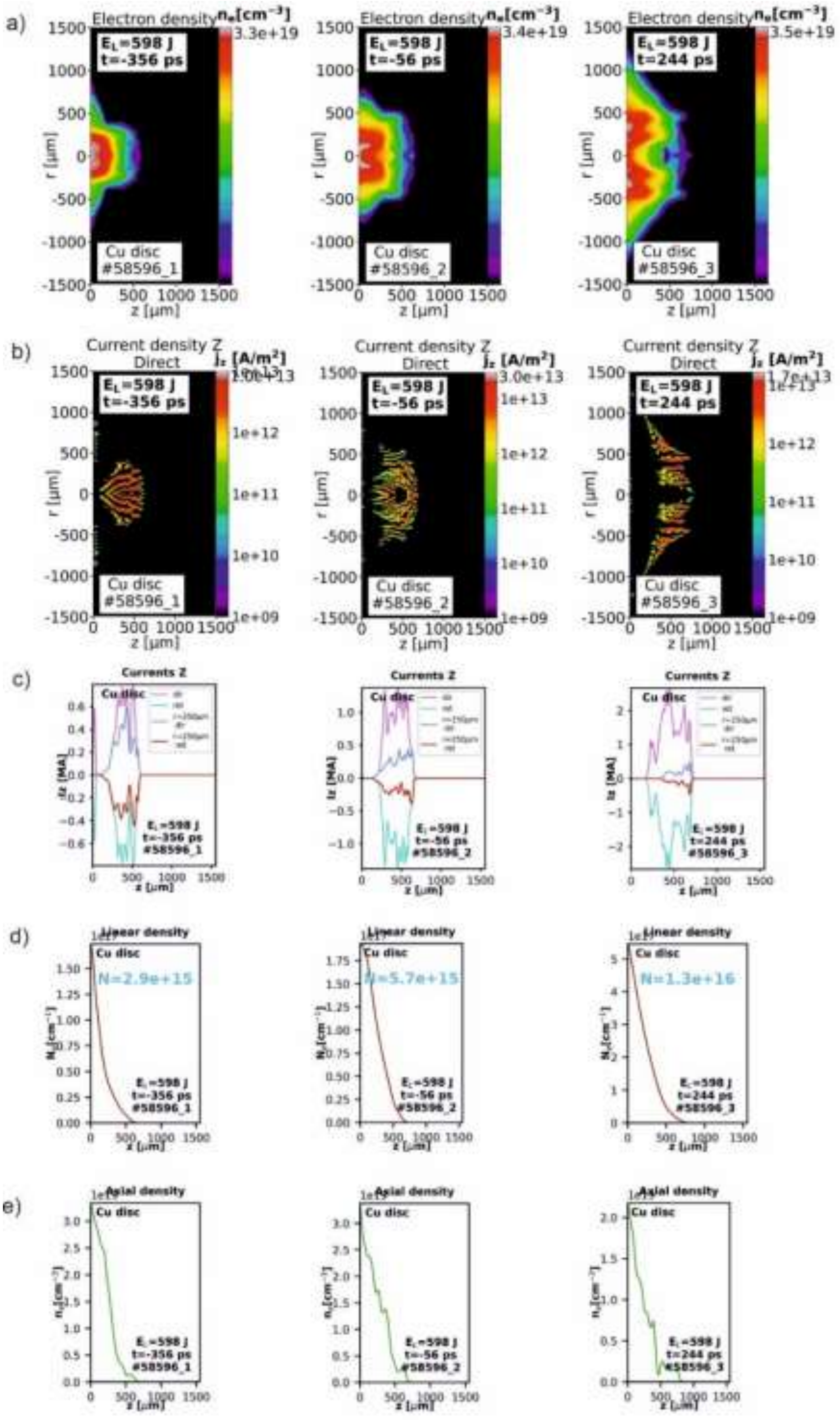

Fig. 6: Electron density distributions - (a) and current density distributions - (b) at various moments of plasma expansion from the Cu disk, illuminated by the 1-harmonic PALS laser focused to a focal spot radius of r_L = 50 µm, and obtained on their basis: c) total current distributions (direct and return), d) linear density distributions and e) axial profiles of the electron density of the magnetized plasma stream.

B-2D imaging of Kα line emission from Cu [13]

Kα line emission measurements from Cu were carried out to obtain information on hot emission (HE) parameters: (i) the total number of photons generated as a result of the interaction of HE with the disk, (ii) the energy and temperature of HE, as well as (iii) energy conversion laser radiation into HE energy deposited in the central focus and in the area outside the focus.

A summary of the results from 2D measurements of Kα line emission imaging from Cu for two construction of DT-STCM targets with a coil of different diameter and a Cu disc is presented in Table 1, while the dependencies of the HE energy deposited in the central focus and the conversion of laser radiation energy in HE energy as a function of intensity is shown in Fig. 7.

Tabela 1

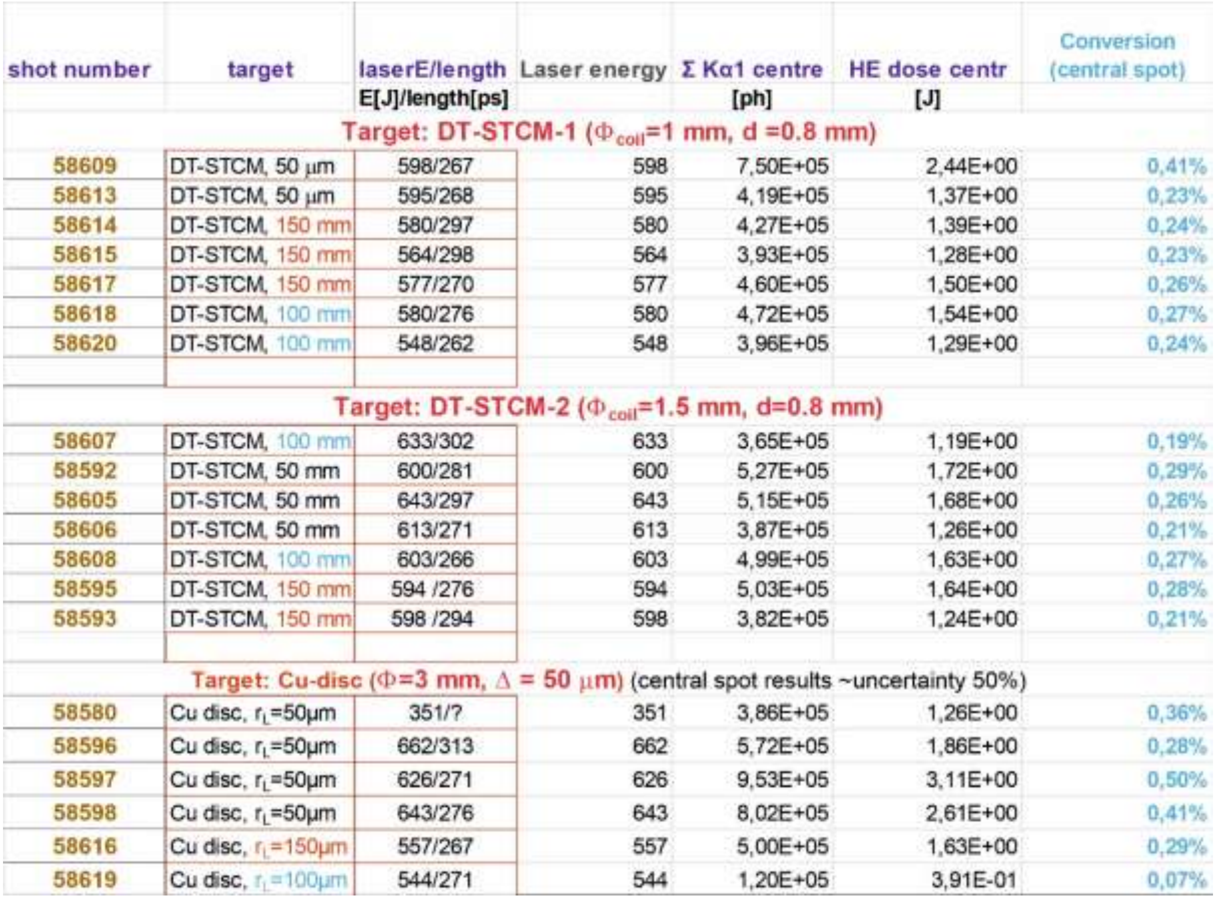

shot number	target	laserE/length E[J]/length[ps]	Laser energy	Σ Kα1 centre [ph]	HE dose centr [J]	Conversion (central spot)
Target: DT-STCM-1 (Φ_{coil}=1 mm, d =0.8 mm)						
58609	DT-STCM, 50 µm	598/267	598	7,50E+05	2,44E+00	0,41%
58613	DT-STCM, 50 µm	595/268	595	4,19E+05	1,37E+00	0,23%
58614	DT-STCM, 150 mm	580/297	580	4,27E+05	1,39E+00	0,24%
58615	DT-STCM, 150 mm	564/298	564	3,93E+05	1,28E+00	0,23%
58617	DT-STCM, 150 mm	577/270	577	4,60E+05	1,50E+00	0,26%
58618	DT-STCM, 100 mm	580/276	580	4,72E+05	1,54E+00	0,27%
58620	DT-STCM, 100 mm	548/262	548	3,96E+05	1,29E+00	0,24%
Target: DT-STCM-2 (Φ_{coil}=1.5 mm, d=0.8 mm)						
58607	DT-STCM, 100 mm	633/302	633	3,65E+05	1,19E+00	0,19%
58592	DT-STCM, 50 mm	600/281	600	5,27E+05	1,72E+00	0,29%
58605	DT-STCM, 50 mm	643/297	643	5,15E+05	1,68E+00	0,26%
58606	DT-STCM, 50 mm	613/271	613	3,87E+05	1,26E+00	0,21%
58608	DT-STCM, 100 mm	603/266	603	4,99E+05	1,63E+00	0,27%
58595	DT-STCM, 150 mm	594 /276	594	5,03E+05	1,64E+00	0,28%
58593	DT-STCM, 150 mm	598 /294	598	3,82E+05	1,24E+00	0,21%
Target: Cu-disc (Φ=3 mm, Δ = 50 µm) (central spot results ~uncertainty 50%)						
58580	Cu disc, r_L=50µm	351/?	351	3,86E+05	1,26E+00	0,36%
58596	Cu disc, r_L=50µm	662/313	662	5,72E+05	1,86E+00	0,28%
58597	Cu disc, r_L=50µm	626/271	626	9,53E+05	3,11E+00	0,50%
58598	Cu disc, r_L=50µm	643/276	643	8,02E+05	2,61E+00	0,41%
58616	Cu disc, r_L=150µm	557/267	557	5,00E+05	1,63E+00	0,29%
58619	Cu disc, r_L=100µm	544/271	544	1,20E+05	3,91E-01	0,07%

As can be seen from Fig. 7a in the case of the Cu disk (orange line), the energy and flux of hot electrons increases ~5 times with the increase in laser intensity in the range from 2.5x1015 to 3x1016 W/cm2, which is consistent with the results from paper [15].

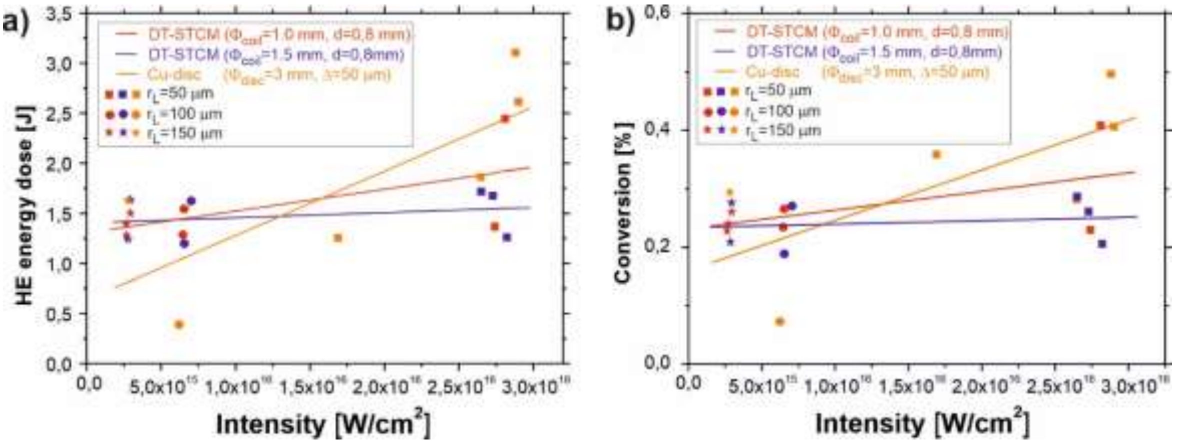

Fig. 7: Dependence of the HE dose deposited in the center of the target - (a) and the conversion of laser radiation into HE energy - (b) as a function of laser intensity, for DT-STCM targets with different coil radii and a Cu disc.

However, in the case of DT-STCM targets (red and blue lines), the increase in HE energy dose is much slower compared to Cu disks, due to the presence of an external magnetic field generated by the coil of the DT-STCM disk. As can be seen from Fig. 7a, only in the range of lower laser intensity is the energy of hot electrons deposited in the central part of the Cu disk in the presence of a magnetic field is higher than without it. Increasing the laser intensity does not lead to an obvious increase in the hot electron energy and the associated flux, but limits the dose of hot electron energy that is deposited in the central part of the Cu disk. This is consistent with the expectation that the magnetic field helps in overall containment because it reduces the radial transport of hot electrons inside the plasma and thus reduces the conversion of laser radiation to HE energy, as shown in Fig. 7b.

Taking into account the paper of [15], the relationships presented in Fig. 7 suggest that the HE flux and the efficiency of converting laser energy into HE energy increase non-linearly after exceeding the intensity threshold (~$8x10^{15}$ W/cm^2) of the laser pulse, which proves that the magnetic field generated by coil has a significant impact on the non-linear characteristics of the hot electrons produced inside the plasm. Since the mechanism of hot electron generation is attributed to parametric instabilities such as forced Raman scattering (SRS) and two-plasma decay (TPD), observations so far indicate that the magnetic field generated by the coil has a very significant impact on the occurrence of these instabilities. Moreover, at the mentioned intensity threshold, the self-focusing effect in the plasma must also be taken into account, which suggests that the self-focusing effect can also be controlled by the magnetic field generated by the coil.

C-Results of HE emission measurements using a multi-channel electron spectrometer

A particularly useful diagnostic that enabled the quantitative assessment of HE emission parameters emitted in the backward direction from the ablation plasma area were angular measurements of energy spectra using a multi-channel electron magnetic spectrometer. A 7-channel spectrometer was used for the measurements, enabling the measurement of electron energy in the range from 50 keV to 1.5 MeV [14] covering a total measurement angle of approximately 110 degrees, see Fig. 8. The purpose of the measurements was to obtain information about the influence of the magnetic field on the HE emission parameters generated from DT-STCM-S targets with a modified construction, Fig. 1b, illuminated by a 1-harmonic PALS laser of various intensities. The basis for obtaining information about the angular distributions of their energy and temperature were the angular energy spectra of HE emitted at different angles to the normal of target. To obtain information about the dependence of the above-mentioned parameters on the laser intensity, the targets were illuminated with a 1-harmonic laser beam with an energy of approximately 500 J focused to various focal spot radii: r_L = 50, 100 and 150 μm. The reference for formulating conclusions regarding the influence of the magnetic field on the parameters of HE emission from DT-STCM-S targets were measurements of HE emissions from "bare" Cu disks, carried out for the same lighting conditions as the DT-STCM targets.

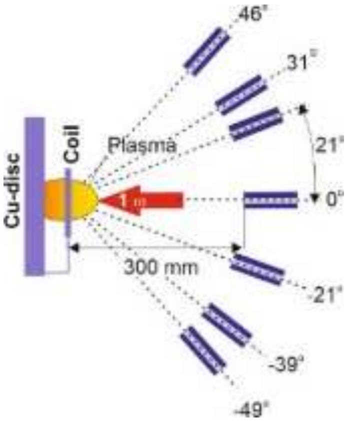

Fig. 8: Geometry of measuring HE angular energy spectra using a 7-channel magnetic electron spectrometer.

The angular distributions of: HE numbers per solid angle, HE energy and HE temperature obtained by illuminating DT-STCM targets with a coil with a diameter of Φ_{coil} = 1 mm using a 1-harmonic PALS laser focused to different focal spot radii are shown in Fig. 9, while above distributions for DT-STCM targets with a larger coil diameter ⍰coil = 1.5 mm and for a bare Cu disc are presented in Fig. 10 and Fig. 11, respectively.

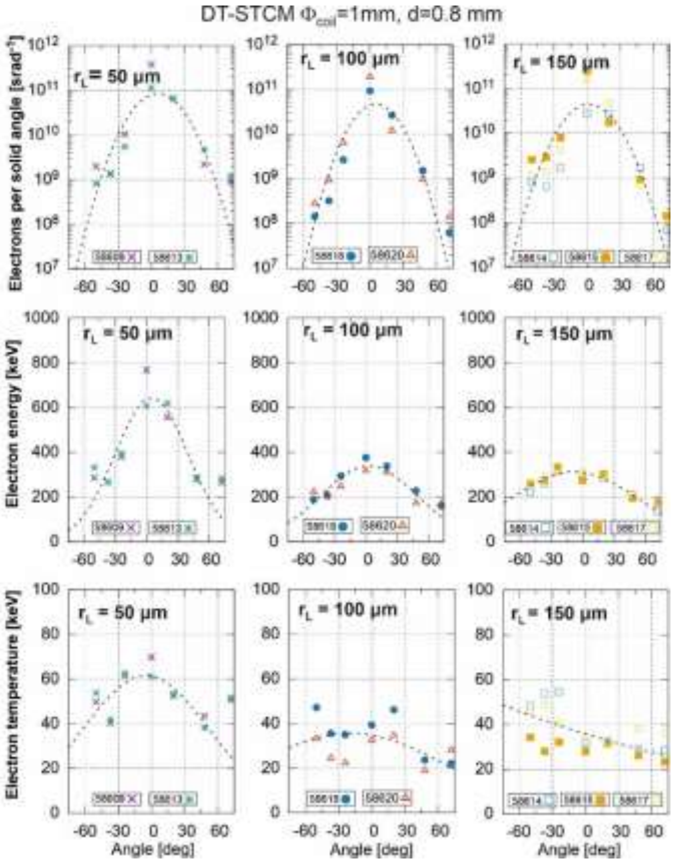

Fig. 9: Angular distributions of: a) HE number per solid angle, b) HE energy and c) HE temperatures corresponding to the illumination of DT-STCM targets with a coil with a diameter of Φ_{coil} = 1 mm using a 1-harmonic PALS laser focused to different focal spot radii.

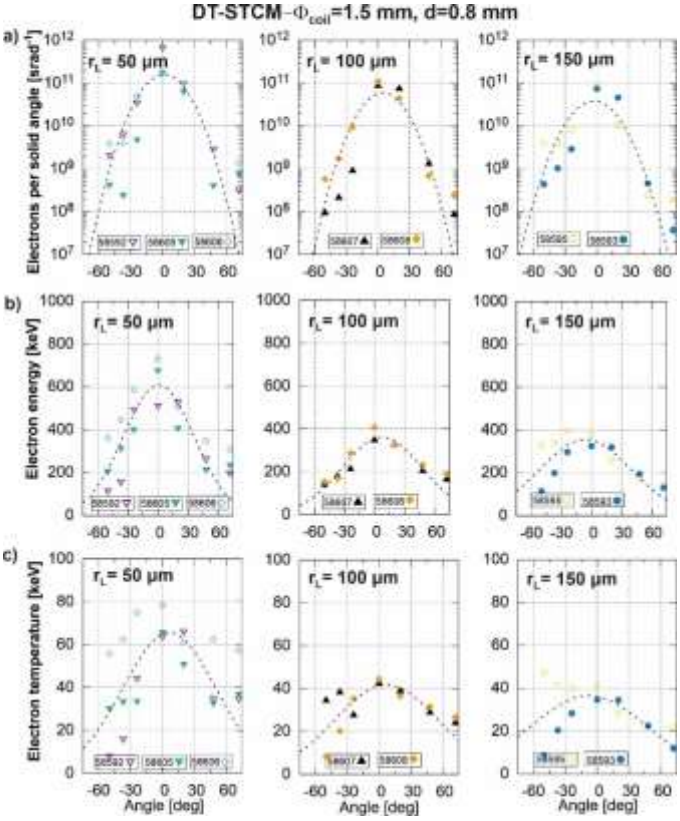

Fig. 10: Angular distributions of: a) HE number per solid angle, b) HE energy and c) HE temperatures corresponding to the illumination of DT-STCM targets with a coil with a diameter of Φ_{coil} = 1.5 mm using a 1-harmonic PALS laser focused to different focal spot radii.

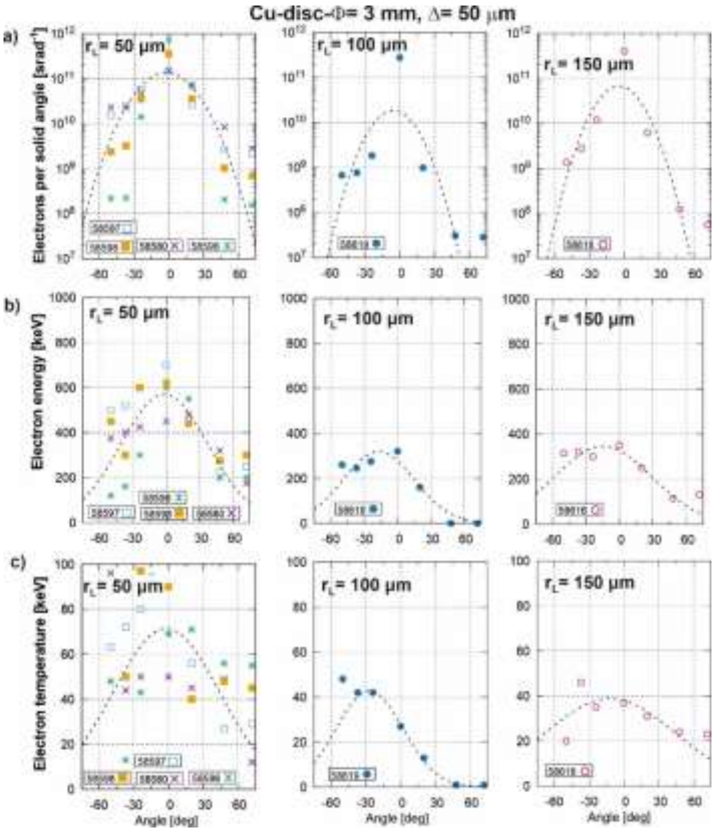

Fig. 11: Angular distributions of: a) HE number per solid angle, b) HE energy and c) HE temperatures corresponding to the illumination of bare Cu disks with a 1-harmonic PALS laser focused to different focal spot radii.

The comparison of HE emission parameters between the considered target structures depending on their lighting conditions is presented in the summary tables in Fig. 12, Fig. 13 and Fig. 14. Changes in the HE flux with increasing laser intensity for the considered constructions and targets are shown in Fig. 12. In the case of DT-STCM targets, these changes are very similar to those in the case of HE dose measured using K⍰ imaging diagnostics, Fig. 7. The results of both diagnostics are consistent and confirm that the magnetic field generated by the coil reduces the emission and transport of hot electrons inside plasma.

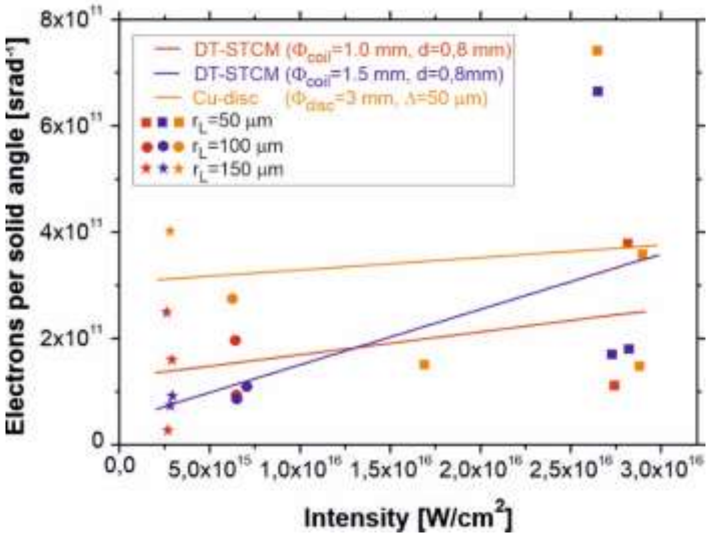

Fig. 12: Changes in the total HE flux for the considered target constructions as a function of laser intensity.

Fig. 13 shows the HE temperature changes for the considered target constructions depending on the laser intensity, determined on the basis of the slope of the HE energy spectra distributions obtained from measurements using an electron spectrometer. As can be seen from Fig. 13, the HE temperature increases linearly with the laser intensity and is consistent with the temperature scaling obtained by measuring the HE energy spectra emitted by tantalum plasma [15].

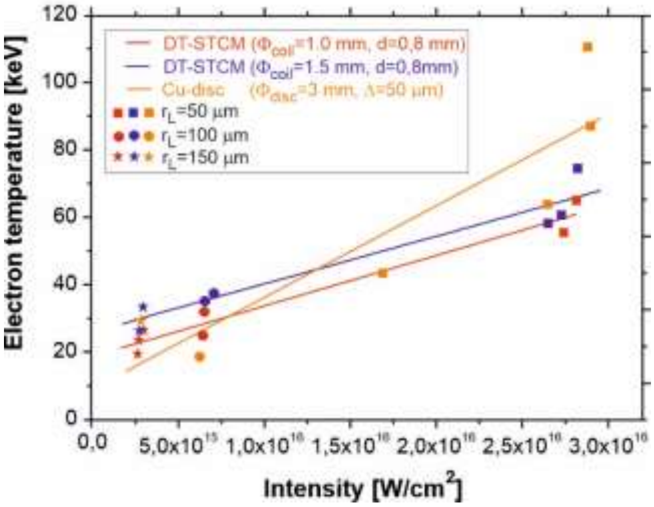

Fig. 13: HE temperature changes for the considered target constructions as a function of laser intensity.

Fig. 14 shows the maximum HE energy dependences for the considered target constructions. These relationships indicate that the HE energy increases with increasing laser intensity, both for DT-STCM disks and "bare" Cu disks. The results have a similar trend as for tantalum plasma in the published article [15].

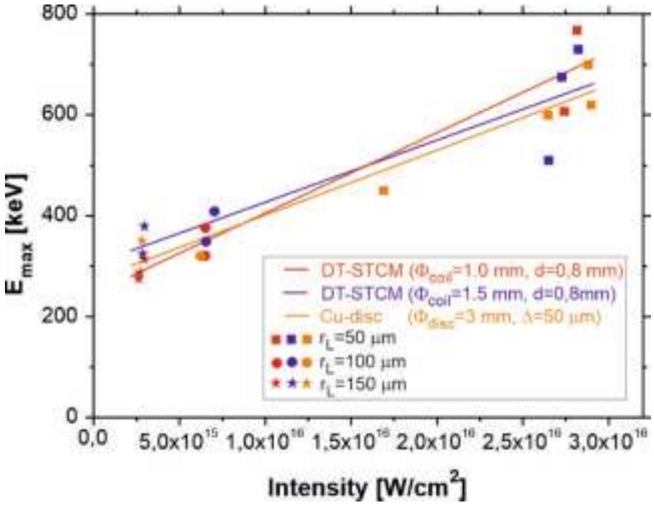

Fig. 14: Changes in the maximum HE energy for the considered target constructions as a function of laser intensity.

D- Numerical simulations and research

In order to better understand the influence of the external magnetic field on the properties of the stream of hot electrons (HE) generated in the laser-plasma interaction, the three-dimensional (3D3V) particle-in-cell computer code PIC EPOCH [16] was modified to enable numerical modeling of HE propagation in magnetic fields generated in disc-coil (DC) targets under the conditions of the PALS experiment. Unlike the previously developed simplified code dedicated to the above issues, the EPOCH code takes into account the interaction between electrons in the HE stream, the interaction between HE and other charged particles such as thermal electrons, protons and multi-charged ions emitted from the target, as well as the electric and magnetic fields generated by HE and other charged particles.

Example results illustrating the influence of electro-magnetic (EM) fields generated by HE and other moving particles - included in simulations performed using the EPOCH code, but not included in simulations using the previous code - are shown in Fig. 15.

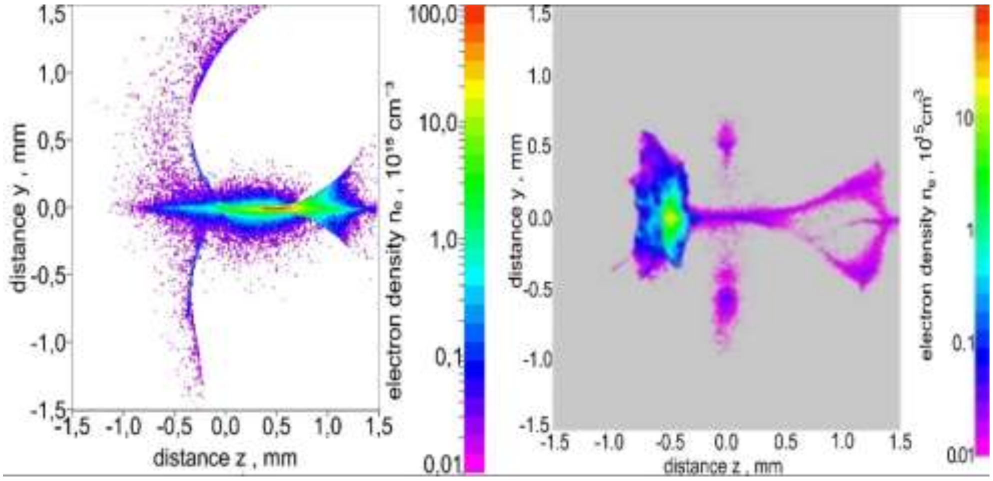

Fig. 15: 2D distribution of the density of HE propagating in the magnetic field created by the DC target coil located in the z = 0 plane perpendicular to the direction of z electron propagation. Simulation time t = 9 ps. On the left – HE density distribution without taking into account the interaction between charged particles and the EM fields generated by them. On the right – including EM fields.

As the figure shows, taking into account the interaction between moving particles (HE and others) and the EM fields generated by them has a significant impact on the characteristics of the HE stream. In particular, this results in a large (at least several times) reduction in the flux density and a significant increase in the angular divergence of the flux in the region of the disappearance of the magnetic field generated by the coil (z > 0.8 mm). Significant differences between the simulation results performed using the EPOCH code and the earlier, simplified code are also observed in the case of other HE stream characteristics.

The EPOCH code was used to numerically simulate the propagation of the HE flux generated from DC targets in the magnetic field generated in these targets under the conditions of the PALS experiment described above. The influence of the magnetic field generated by the DC target coil on the properties of the HE stream was investigated, in particular by comparing the characteristics of the HE stream generated from this target with the characteristics of the HE stream generated from a target without a coil, i.e. not generating a magnetic field. The basic input data for the 3D numerical simulation with the modified EPOCH code were electron energy spectra recorded with a multi-channel spectrometer in the case of disk targets without a coil (i.e. without a magnetic field), as well as data on the shape, dimensions and position of the coil in relation to the disk, and data about the magnetic field generated by the coil (current flowing through the coil) obtained from polarimetric measurements using the Faraday effect in a TGG crystal placed near the coil. In addition to HE, the simulation also took into account thermal electrons, Cu ions and protons accumulated at the disk surface. The initial positions and velocities of the particles (represented by a population of many millions of macroparticles) were determined using the Monte Carlo method based on knowledge of the electron energy spectra, the position of the HE source relative to the coil, and the diameter of the source area calculated from Ka measurements. Sample simulation results are shown below.

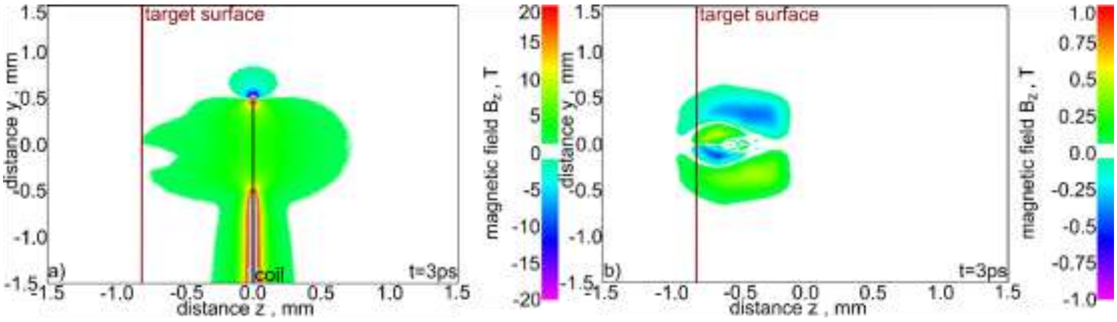

Fig. 16: Two-dimensional spatial distribution of the magnetic field along the axis of the laser beam for the selected simulation time t = 3ps. a – case with a coil generating a magnetic field, b – case without a coil.

Fig. 16 shows the 2D spatial distributions of the magnetic field along the laser beam axis for the case of a target with a coil (DC) and without a coil. Interestingly, in the latter case there is also a magnetic field of significant intensity and non-uniform spatial structure, the source of which is the movement of charged particles included in the simulation. In the DC system, we are dealing with a superposition of this field and the field generated by the coil, which ultimately leads to a complex structure of the magnetic field and, consequently, a highly heterogeneous and complex interaction between the field and the HE flux. A comparison of the two-dimensional hot electron density distributions for the HE flux propagating in the magnetic field of the coil generated in the DC target with the HE distributions for the case when there is no external magnetic field (target without a coil) is shown in Fig. 17. It can be seen that in the first case in the region where the field exists magnetic coil, there is a strong collimation of the HE flux in the advanced phase of the flux propagation (t = 9 ps), resulting in a significant increase in the HE concentration and current at the propagation axis (laser axis). However, after leaving the region of magnetic field, there is a rapid de-collimation of the HE flux and an increase in the angular divergence of the flux. As a result, the detection system located at a large distance from the DC target receives a low-density HE stream spread over a large solid angle, which is observed in the experiment. The main reason for the large angular divergence of the HE jet after the jet leaves the magnetic field region is the Coulombic repulsion between the jet electrons, which is not compensated by the coil magnetic field. In the region where the field occurs, it is strong enough (~ 5T) to enable effective compensation of the Coulomb forces and collimation of the flow. In the system without an external magnetic field (target without coil) - Fig. 17 d,e,f - we observe a large angular divergence of the HE stream, both in the advanced and initial phases of the stream propagation, because there is no factor that would compensate for the Coulombic repulsion of the stream electrons and the hydrodynamic expansion radial flow resulting from the relatively high HE temperature (> 10 keV) (hydrodynamic expansion is less important in the examined case, as it requires much longer times). It is worth adding that in the simplified code used earlier (not taking into account the interactions between particles), the de-collimation of the HE stream in the DC system observed above and consistent with the experiment could not be observed, because A comparison of the two-dimensional hot electron density distributions for the HE flux propagating in the magnetic field of the coil generated in the DC target with the HE distributions for the case when there is no external magnetic field (target without a coil) is shown in Fig. 17. It can be seen that in the first case in the region where the field exists magnetic coil, there is a strong collimation of the HE flux in the advanced phase of the flux propagation (t = 9 ps), resulting in a significant increase in the HE concentration and current at the propagation axis (laser axis). However, after leaving the region of magnetic field, there is a rapid de-collimation of the HE flux and an increase in the angular divergence of the flux. the repulsion between electrons was neglected.

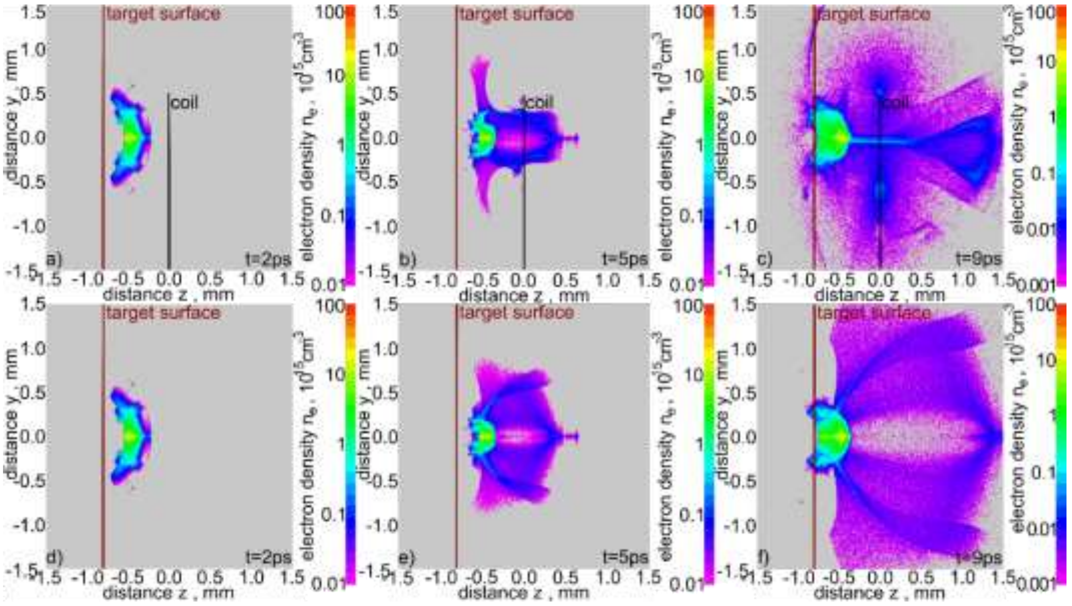

Fig. 17: 2D distributions of hot electron density in the y-z plane parallel to the laser beam axis in various phases of electron stream propagation. a, b, c – case of a target with a coil; d, e, f – target case without coil.

Magnetic fields affect not only the spatial characteristics of the HE flux, but also their energy spectrum. This is illustrated in Fig. 18. As can be seen, the magnetic field causes an increase in the number of electrons on the flow axis and a significant increase in the maximum energy of electrons

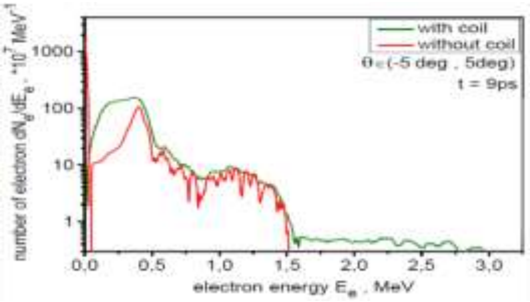

Fig. 18: Energy spectrum of hot electrons on the HE stream axis in the presence of a magnetic field generated in a DC system (green) and in the absence of a field (red).

Numerical studies using the modified EPOCH code, the sample results of which are presented above, allowed for a better understanding of the behavior of the stream of hot electrons produced by laser-plasma interaction in quasi-static magnetic fields generated in DC systems, and in particular helped to understand and properly interpret the results described above PALS experiment.

Within project also continued theoretical and numerical research on alternative variants of laser fusion such as fast ignition (FI) and shock ignition (SI). These variants enable achieving high fusion energy gain (≥ 100) required for a fusion reactor with lower requirements for the laser driver (e.g. lower total driver energy) and compressed DT fuel (e.g. lower compression ratio) than in the traditional variant ICF with spontaneous central ignition. Interest in alternative ICF variants enabling the achievement of "reactor" values of the fusion energy gain factor has increased especially in the last two years and was a consequence of achieving thermonuclear ignition for the first time in history at the National Ignition Facility in the USA. In [17] it was suggested that a beam of heavy ions generated by a laser may be a more effective "ignition" of thermonuclear fuel than the beams of protons or light ions previously proposed for this purpose. Potentially, ion beams can be used to ignite fuel, both in the FI and SI variants. In the latter case, the cylindrical configuration of the fusion target seems to be more advantageous, which also has the advantage of enabling the use of an external magnetic field that lowers the fuel ignition threshold. Recent numerical research by IFPiLM researchers related to alternative ICF variants was focused on the search for the type of (heavy) ion whose atomic mass is optimal from the point of view of achieving the ion beam parameters required for fuel ignition, as well as the search for optimal parameters of the laser driver producing the ion beam. The numerical studies used the advanced multidimensional (2D3V) particle-in-cell PICDOM code developed at IFPiLM, whose unique feature, rarely found in other PIC codes, is the ability to accurately dynamically (on line) model the ionization process of atoms for virtually any element. In particular, this allows for modeling the process of creating and accelerating heavy ions with a high-power laser. An example result of numerical simulations demonstrating the time histories of the intensities of Al, Ti, Cu, Ag and Au ion beams generated by a high-energy PS laser is shown in Fig. 19.

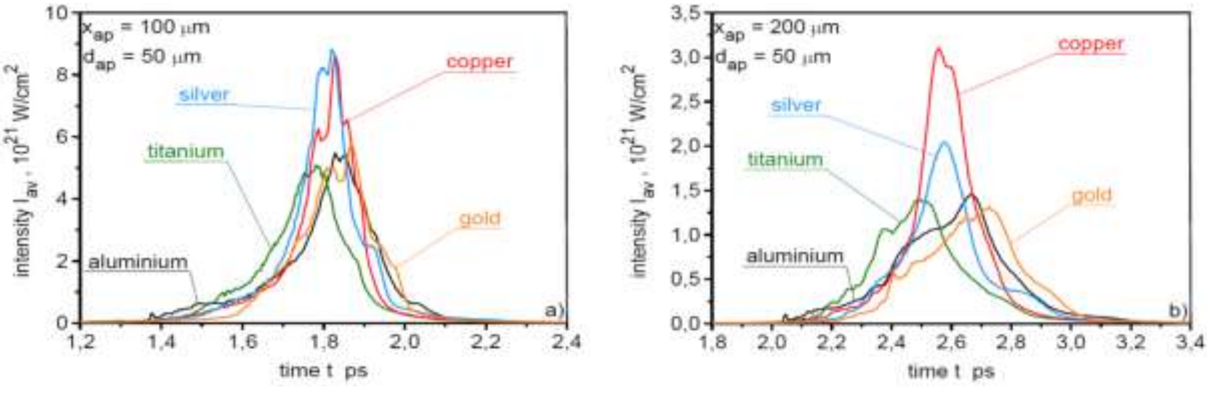

Fig. 19: Time distributions of laser-generated ion beams with different atomic masses at two different distances from the ion source [18].

It can be seen that while at small distances from the ion source (100 μm) the peak intensities of Cu beams and Ag are similar, at larger distances (≥ 200 μm) required to use the beam in FI or SI, the Cu ion beam achieves the highest intensities. A similar situation occurs in the case of other beam characteristics that determine fuel ignition, in particular the beam energy and fluence and the energy spectrum. In other words, it was found that the optimal beams for fuel ignition are Cu ion beams. Fig. 20 illustrates the result of searching for the optimal parameters of the laser accelerating the Cu ion beam, in this case the optimal laser energy. It shows the dependence of the ion beam parameters determining the possibility of ignition of the DT fuel as a function of the distance from the source. In the case of the FI variant, the required beam parameters: fluence ~ 1 GJ/cm2, energy ~ 10 kJ, intensity ~ 1020 W/cm2 at the required distance from the source x ~ 0.5 mm can only be achieved with the optimal laser energy of ~ 200 kJ (both at lower and lower higher laser energy, the beam parameters are much lower than those required for x ≥ 0.5 mm). Achieving ignition in the SI variant using two shock waves generated by an ion beam colliding in the fuel is potentially possible with much lower values of the ion beam parameters (at least several times lower for fluence and beam energy and several dozen times lower in the case of intensity) and the ion source can be at a shorter distance from the cylindrical fusion target.

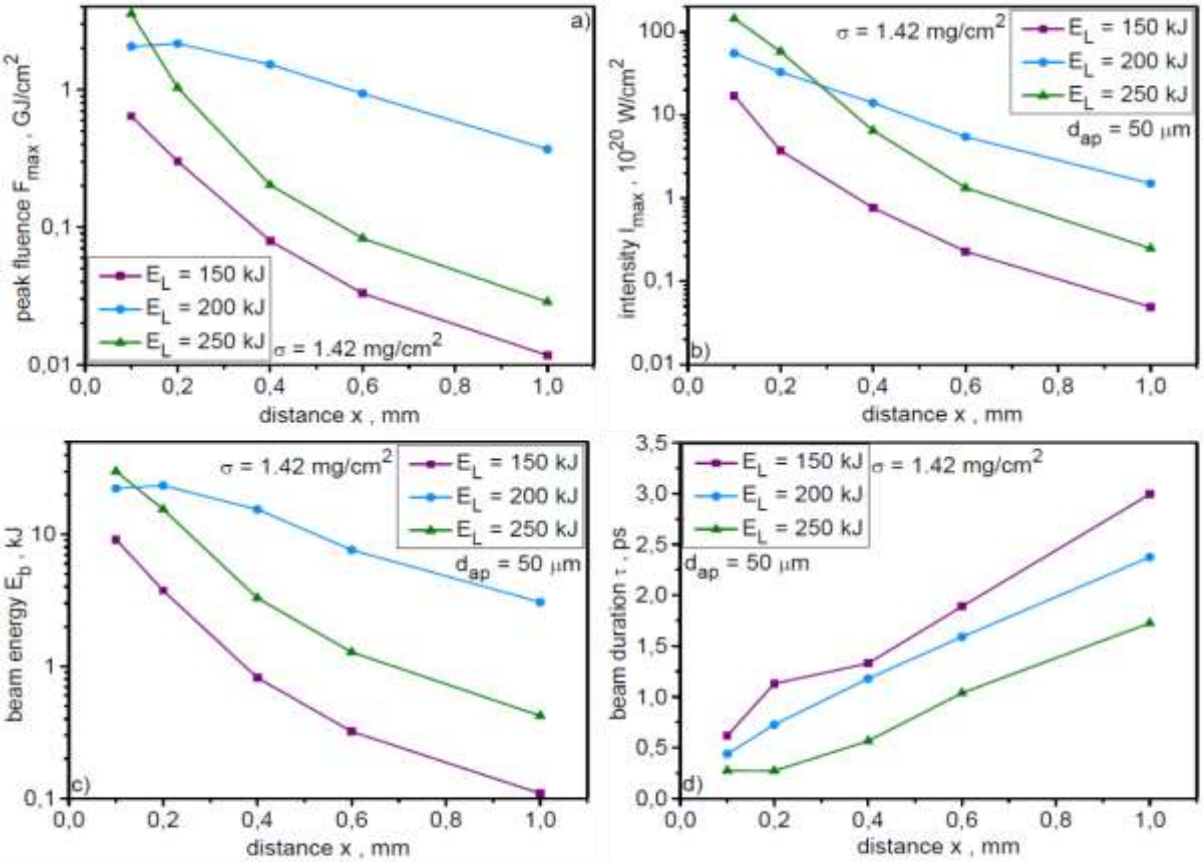

Fig. 20: Dependence of the Cu ion beam parameters on the distance from the ion source for different emergies of the ion accelerating laser [16].

The presented graphs therefore indicate that achieving the ion beam parameters required for SI is possible at laser energies much lower than 100 kJ. The results of the above-mentioned research were published in [18].

The presented results from individual diagnostics will be the subject of further analyses, interpretations and simulations in 2024, the aim of which will be to prepare scientific material for presentation at international scientific conferences and for publication..

Conclusions:

A preliminary analysis of HE emission data obtained in a wide range of intensities shows that only in the lower laser intensity range the energy of hot electrons deposited in the central part of the Cu disk in the presence of a magnetic field is higher than without it. Increasing the laser intensity does not lead to an obvious increase in the hot electron energy and associated flux, but limits the hot electron energy dose that is deposited in the central part of the Cu disk. This is consistent with the fact that the magnetic field helps in overall containment because it reduces the radial transport of hot electrons inside the plasma and thus reduces the conversion of laser radiation to HE energy. This proves that the magnetic field generated by the coil has a significant impact on the nonlinear characteristics of the hot electrons produced inside the plasma. Since the mechanism of hot electron generation is attributed to parametric instabilities such as forced Raman scattering (SRS) and two-plasmon decay (TPD), observations so far indicate that the magnetic field generated by the coil has a very significant impact on the occurrence of these instabilities.

Modification of the advanced three-dimensional (3D3V) particle-in-cell computer code - PIC EPOCH enables numerical modeling of HE propagation in magnetic fields generated in disc-coil (DC) targets under the conditions of the PALS experiment. Unlike the previously developed simplified code dedicated to the above issues, the EPOCH code takes into account the interaction between electrons in the HE stream, the interaction between HE and other charged particles such as thermal electrons, protons and multi-charged ions emitted from the target, as well as the electric and magnetic fields generated by HE and other charged particles.

Theoretical and numerical research developed at IFPiLM on alternative variants of laser fusion such as fast ignition (FI) and shock ignition suggest that in order to achieve the parameters of the ion beam required for fuel ignition, the selection of the type of (heavy) ion and its optimal mass is a particularly important issue. The numerical studies used the advanced multidimensional (2D3V) particle-in-cell PICDOM code developed at IFPiLM, whose unique feature, rarely found in other PIC codes, is the ability to accurately dynamically (on line) model the ionization process of atoms for virtually any element. In particular, this allows for modeling the process of creating and accelerating heavy ions with a high-power laser. The obtained simulation results therefore indicate that achieving the ion beam parameters required for SI is possible for Cu ions at laser energies much lower than 100 kJ. The results of the above-mentioned research were published in this paper.

Publications:

[1] T. Pisarczyk, et al. Plasma Physics and Controlled Fusion , **64,** 115012 (2022).
[2] L. J. Perkins, et al., Physics of Plasmas, **20**, 072708 (2013).
[3] W. M. Wang, et al., Phys. Rev. Lett., **114**, 015001 (2015).
[4] T. Johzaki, et al., Nuclear Fusion, **55,** 053022 (2015).
[5] M. Hohenberger, et al., Physics of Plasmas, **19**, 056306 (2012).
[6] J. P. Knauer, et al., Physics of Plasmas, **17**, 056318 (2010).
[7 B. Srinivasan el al., Physics of Plasmas, **20**, 056307 (2013).
[8] J.J. Santos *et al.*, New J. Phys **17**, 083051 (2015)
[9] M. Bailly-Grandvaux *et al.*, Nat. Comm. **9**, 102 (2018)
[10] T Pisarczyk et al., Plasma Physics and Controlled Fusion **62**, 115020 (2020).
[11] A. Zaraś-Szydłowka et al., AIP Adv. **10**, 115201 (2020).
[12] T. Pisarczyk et al., Journal of Instrumentation, **14**(11), C11024–C11024 (2019).
[13] T. Pisarczyk et al., Scientific Report **8**, 17895 (2018).
[14] M. Krupka et al., Rev. Sci. Instrum. **92**, 023514 (2021).
[15] Singh et al,. Plasma Physics and Controlled Fusion **64**, 105012 (2022).
[16] T. D. Arber et al., Plasma Phys. Control. Fusion **57**, 113001 (2015).
[17] J. Badziak, J. Domański, Nucl. Fusion **62**, 086040 (2022).
[18] J. Badziak, J. Domański, Physics of Plasmas **30**, 053107 (2023).

Within WP3 package, which is focused on exploring alternative innovative approaches to ICF and new sample concepts, experiments related to proton-boron fusion were performed. The proton-boron (pB) fusion reaction has long been considered the "Grail" of nuclear fusion that will enable future energy production. In fact, this reaction does not produce neutrons, unlike the reaction of deuterium with tritium. The lack of neutrons in the primary reaction means very little activation of materials in future reactors and therefore very little radioactive waste. Therefore, pB fusion is very pure and ecologically acceptable. Data on its behavior in extreme conditions play an important role in understanding the physics of boron. This applies in particular to obtaining data on the boron equation of state at very high pressures (up to 100 megabar). One aspect of proton-boron fusion studied in this program was to check the effect of a magnetic field acting on the orientation of the proton beam and α-particles, and thus influencing the generation of α-particles in a boron-containing target. Demonstrating the presence of the avalanche effect would be the key to the possible use of laser-driven plasma to generate energy in the pB fusion reaction and demonstrating the difference in the generation of α particles in various configurations in the presence and absence of a magnetic field. The broader effect of this research would be the actual initiation of a new area of nuclear fusion research in the field of energy production using proton-boron fusion. At the same time, the efficient generation of α-particles may be useful for developing a new generation of portable α-particle sources with high brightness and low capital cost, which may be of interest for medical applications. For this and other types of applications, it is fundamental to have sources that are well characterized in terms of spectral energy and angular distribution. Since laser-driven sources are relatively new compared to conventional accelerators, their energy and angle calibration is necessary. From this point of view, the simultaneous characterization of protons, electrons and hard X-ray radiation is important, which will be carried out using deuterated and boronated targets for the generation of deuterons and elementary particles resulting from proton-boron synthesis, and deuterons and α particles will be characterized as an example of minority ions with low Z produced in this interaction.

As part of this task, a complex experiment using discs in the form of coils was performed on the GEKKO/LFEX laser installation.

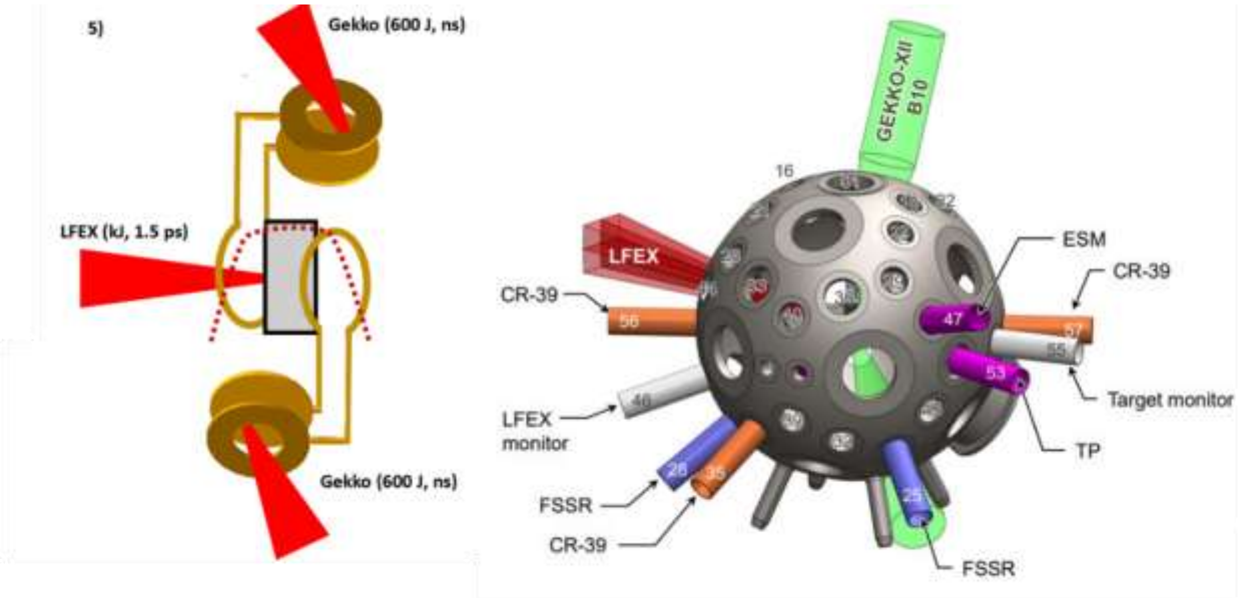

Fig. 21: a) A drawing showing the configuration of the target and coils with the indication of the LFEX and GEKKO laser beams. b) scheme of the vacuum chamber in which the experiment was carried out, along with the position of individual diagnostics and LFEX and GEKKO laser beams.

Four high-energy picosecond LFEX laser beams (1kJ, 1.5 ps) focused on boron-containing targets (e.g. HB, BN) were used to carry out the pB fusion reaction. Some targets were covered with a thin layer of plastic (CH). The magnetic field was generated as a result of the interaction of GEKKO laser beams (600 J, 1 ns) with complex capacitor-coil targets (Fig. 21a). Prototype coils and targets were made in several independent institutions. As part of the experimental campaign, 15 shots were performed, some of them were intended to determine the generated magnetic field, the others were performed in the presence of a magnetic field (using the GEKKO and LFEX laser) and several shots without generating a magnetic field (only in the presence of the LFEX laser) in order to compare the flux alpha particles produced under these two different conditions. Protons and alpha particles were measured using: a Thomson spectrometer,

time-of-flight (TOF) diamond detectors and CR39 detectors. Additionally, measurements were made using an electron spectrometer and an X-ray spectrometer (Fig. 21b).
Comparison of the alpha particle flux in conditions without and in the presence of a magnetic field for the BN target covered with a plastic layer (CH) indicates a significant increase in the number of alpha particles observed with the CR-39 detector. In the Fig. 22 shows a photo of the target in the configuration with coils (Fig. 22a) and the CR-39 measurement results in the presence (Fig. 22b) and without the presence of a magnetic field (Fig. 22c). This tendency is maintained when using different filter thicknesses (11, 22, 33 μm).

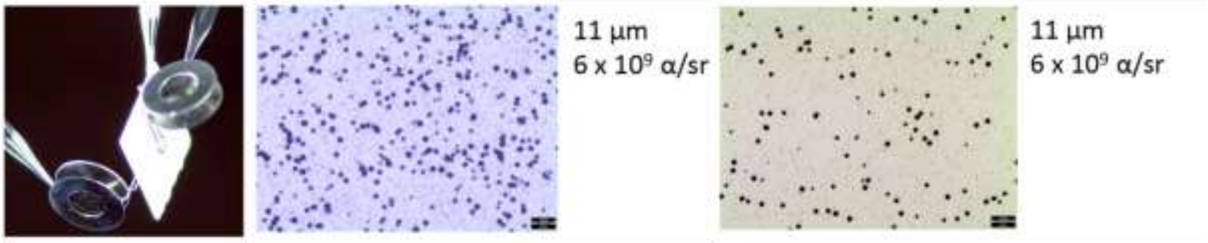

a) b) c)

Fig. 22: a) Photo of a flat BN target covered with a CH layer in a configuration with two coils, b) measurement results obtained using the CR-39 detector in the presence of a magnetic field, c) measurement results obtained using the CR-39 detector without the presence of a magnetic field.

Due to the very low statistics of shots, tests should be continued to confirm the results. As part of the same project, proton-boron fusion tests were carried out on the VEGA-3 laser installation (in Spain) characterized by completely different parameters (E = 30 J, t = 30 fs). The innovation of this experiment was to conduct an experiment on a laser installation with a high firing frequency at low laser energy. The main goal of the experiment was to estimate the amount of alpha particles produced. The research was carried out using various types of targets (BN, B, BNH6) in two configurations: "pitcher-catcher" and "in traget". The aim of the research was to fully characterize the sources of protons and alpha particles by using CG-39 detectors and activation techniques (including the use of a Ge detector to measure the gamma radiation emission spectrum and the method of decay of emission lines over time). Protons and alpha particles were measured using a Thomson spectrometer, time-of-flight (TOF) diamond detectors and CR-39 detectors.

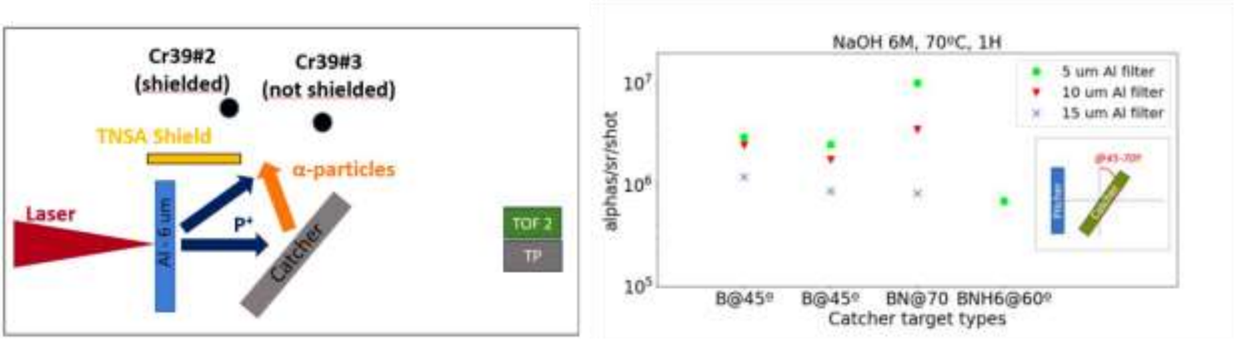

Fig. 23: a) "pitcher-catcher" configuration with the diagnostics position marked. b) results of preliminary estimates of the measured number of alpha particles.

Fig. 23a shows the configuration of diagnostics when conducting an experiment in the "pitcher-catcher" configuration. Preliminary data analysis carried out on the basis of measurements using BN-type targets indicates the production of alpha particles at the level of 10^6 particles/sr/shot (Fig. 23b). Dokonano również wstępnej analizy danych związanych z pomiarami przeprowadzonymi w konfiguracji „in direct". Fig. 24 shows a schene of the "in direct" configuration, showing the estimation of the number of alpha particles depending on the measurement angle. When changing the detection angle from 26 to 38 degrees, the number of particles increases within the error limit.
As expected, the alpha particle stream generated in the "in direct" configuration is characterized by the production of a larger alpha particle stream than the alpha particle stream generated in the "pitcher catcher" configuration.

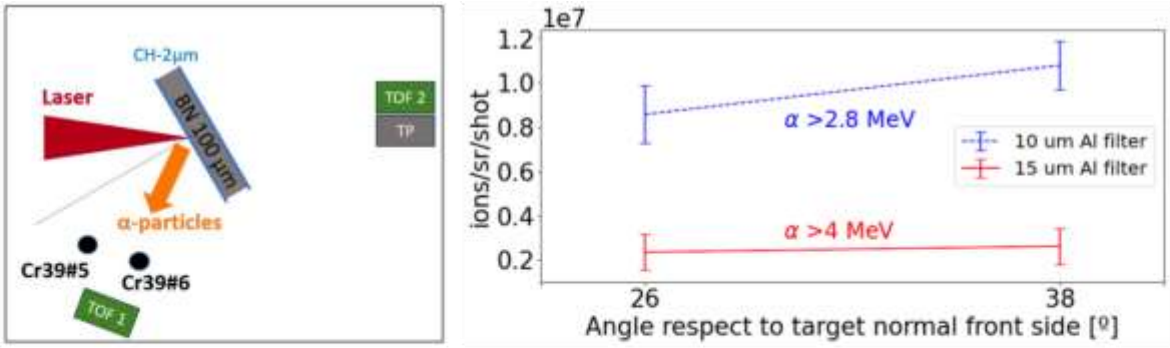

a) b)

Fig. 24: a) "in direct" configuration with the diagnostics position marked. b) results of preliminary estimates of the measured number of alpha particles.

Conclusions:

The presented preliminary assessment of experiments carried out on the LFEX/GEKKO laser installations indicates an increase in the number of measured alpha particles in the case of the proton-boron reaction in the presence of a magnetic field.

Based on the preliminary analysis of experimental data obtained during the campaign carried out on the VEGA3 installation, it was found that a larger stream of particles was produced in the "in direct" configuration than in the case of the "picher-catcher" configuration.

Collaboration

- Institute of Plasma Physics, Czech Academy of Sciences, 182 00, Prague, Czech Republic
- ELI Beamlines, Institute of Physics, Czech Academy of Sciences, 252 41, Dolni Brezany, Czech Republic
- Department of Radiation and Chemical Physics, Institute of Physics, Czech Academy of Sciences, 182 21, Praha, Czech Republic
- Faculty of Electrical Engineering CTU, 166 27, Prague, Czech Republic
- Univ. Bordeaux, CNRS, CEA, CELIA, UMR 5107, F-33405, Talence, France
- CLPU - Universidad de Salamanca, Salamanca, Spain

Related 2023 articles and conference presentations:

Articles:

1. J. Badziak, J. Domański, "*In search of ways to improve the properties of a laser-accelerated heavy ion beam relevant for fusion fast ignition*" , Physics of Plasmas **30**, 053107, 2023.

Conference presentation:

1. M. Rosinski, T. Pisarczyk, Z. Rusiniak, P. Tchórz, O. Renner, R. Dudzak, T. Chodukowski1, J. Domanski, J. Badziak, J. Dostal, M. Krupka, S. Singh, D. Klir, P. Gajdos, A. Zaras-Szydłowska, M. Szymanski, J. Krasa, T. Burian, J. Cikhardt, S. Jelinek, G. Kocourkova, D. Batani, K. Batani, J. Santos, C. Vlachos, V. Ospina-Bohórquez, S. Borodziuk, M. Krus, and L. Juha**.** „Influence of the magnetic field on properties of the electron and ion emission from plasma produced at laser irradiation of a disc-coil target by 1 and 3-harmonic of PALS iodine laser". *12th International Conference on Inertial Fusion Sciences and Applications 2023 September 25-29, 2023 | Denver, CO, USA*- poster presentation-**PsM1E-130**-https://bravuratechnologies.wixsite.com/ifsa2023.

2. J. Domański , J. Badziak , "Highly efficient acceleration of a mono-charge uranium ion by a multi-PW femtosecond laser", *PLASMA2023 International Conference on Research and Applications of Plasmas September 18-22 2023 ,Warsaw*-poster **ID**: **P3.3-** https://plasma2023.ipplm.pl/

3. J. Domański , J. Badziak, Z. Rusiniak, O. Renner, R. Dudziak, T. Chodukowski, J. Dostal, M. Krupka, S. Singh, M. Ehret, P. Gajdas, A. Zaras-Szydlowska, M. Szymański, J. Krasa, T. Burian, S. Jelinek, G. Kocourkova, D. Batani, K. Batani, J. Santos, C. Vlachos, V. Ospina-Bohórquez, L. Volpe, L. Juha,

M. Krus, S. Agarval and T. Pisarczyk , "Numerical investigation of the influence of the magnetic field on the hot electron flux generated at laser irradiation of a disc-coil target", *49th European Conference on Plasma Physics July 3-7 2023, Bordeaux* - poster - **ID**: **Fr_BPIF24**-https://epsplasma2023.eu/ .

4. Daniel Molloy, Thomas Carrière, Howel Larreur, Dimitri Batani, Marine Huault, Phillippe Nicolaï, Didier Raffestin, Diluka Singappuli, Alessio Morace, Yasunoba Arikawa, Yuki Abe, Evgeny Filippov, Sergey Pikuz, Aaron McNamee, Daniele Margarone, Katarzyna Batani, "Enhanced In-Target Alpha Particle Generation using the kJ LFEX Laser System", *The 3rd International Workshop on Proton Boron Fusion, 2-5 październik 2023, Praga* – (oral presentation), https://indico.eli-laser.eu/event/26/page/63-programme
5. Marine Huault,Thomas Carrière, Howel Larreur, Philippe Nicolaï, Didier Raffestin, Diluka Singappuli, Katarzyna Batani, Mattia Cipriani, Francesco Filippi, Massimiliano Scisciò, Claudio Verona, Lorenzo Giuffrida, Vasiliki Kantarelou, Stanislav Stancek, NARDJESSE Boudjema, Roberto Lera, Jose Antonio Pérez-Hernández, Luca Volpe, Aldo Bonasera, Marcia R. D. Rodrigues, Daniela Ramirez Chavez, Fabrizio Consoli, Batani Dimitri, "Advancements in Pulsed Laser Deposition of boron-based targets for p-11B studies", *The 3rd International Workshop on Proton Boron Fusion, 2-5 październik, 2023, Praga* – (oral presentation)- https://indico.eli-laser.eu/event/26/page/63-programme
6. K. Batani, L. Sayo, T. Carrière, H. Larreur, Ph. Nicolaï, D. Raffestin, D. Singappuli, M. Cipriani, F. Filippi, M. Scisciò, F. Consoli, C. Verona, L. Giuffrida, V. Kantarelou, S. Stancek, N. Boudjema, R. Lera, J.A. Pérez-Hernández, L. Volpe, A. Bonasera, M.R.D. Rodrigues, D. Ramirez Chavez, M. Huault and D. Batani, "Generation of radioisotopes using high-repetition, high-intensity lasers", *The 3rd International Workshop on Proton Boron Fusion, 2-5 październik, 2023, Praga* – (oral presentation-https://indico.eli-laser.eu/event/26/page/63-programme
7. Thomas Carrière, S Agarwa, M Alonzo, P L Andreoli, D Batani, K Batani, A Bonasera, M Cipriani, G A P Cirrone, F Consoli, G Cristofari, R De Angelis, G Di Giorgio, M Ehret, F Filippi, L Giuffrida, D Giulietti, G L Guardo, M Huault, M Krupka, M La Cognata, H Lareur, D Lattuada, R Lera, D Margarone, A McNamee, D Molloy, Ph Nicolaï, S Palmerini, J A Perez-Hernandez, G Petringa, D Raffestin, G G Rapisarda, M R D Rodrigues, M Scisciò, D Singappuli, S Singh, C Verona, L Volpe "Simulations of production of alpha particles sources through proton-boron nuclear reactions initiated by relativistic lasers", *The 3rd International Workshop on Proton Boron Fusion, 2-5 październik, 2023, Praga* – (oral presentation)- https://indico.eli-laser.eu/event/26/page/63-programme.

NCBJ: National Centre for Nuclear Research

WPPrIO: Preparation of ITER Operation

Title: NCBJ participation to NBTF operation (MITICA, SPIDER)

Authors: Roman Zagórski, Karol Kozioł

Introduction

The experimental fusion reactor ITER will be heated by injection of a fast neutral beam generated by acceleration and neutralization of negative ions. The negative ion source used for this purpose (SPIDER), constructed at Consorzio RFX (Italy), consists of 8 driver volumes where radio-frequency (RF) power is inductively coupled to the plasma electrons and an expansion chamber containing a magnetic filter (MF) [1],[2] (see Fig.1). Theoretical modelling is an important tool which can be successfully used in the optimization of the ion sources. This report presents recent developments of the 2D fluid model for the SPIDER negative ion source related to the neutrals dynamics. The extended model has been implemented into the FORTRAN code FSFS2D (Fluid Solver For SPIDER in 2D).. The simulation results are compared with the experimental data from SPIDER. The model, which is mostly based on the works of S.Lishev [3] and G. Hagelaar [4], has been already presented in [5, 6] and only main points and the new elements of the physical model are shortly discussed here.

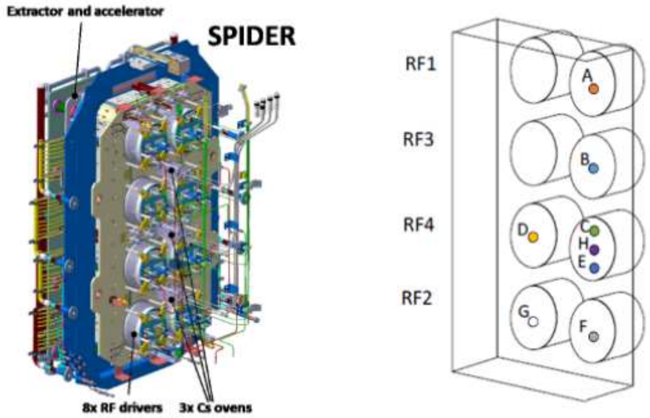

Figure 1: Design of SPIDER source (left) and schematic layout of Langmuir probes positions in SPIDER (right)

1. Physical Model

The plasma source in SPIDER is composed of four pairs of drivers of circular cross-section designed to operate at 200 kW to give a total power of 800 kW. The filling gas (H2 or D2) is injected at a pressure ~0.3 Pa and heated using induction coils wound around drivers. Presently, our 2D model refers to the cylindrical section of one driver open to the expansion chamber, with the integration domain in the (xy)-plane (at z=0), perpendicular to the MF (Fig.2). The plasma grid (PG) is assumed as a solid surface which is biased at a given potential (U_{PG}) with respect to the other grounded boundaries of the modelling domain. We explicitly solve particle balance equations for electrons, each positive ion species (H+, H2+, H3+), negative ions H-, and atomic and molecular hydrogen. These equations include contributions from both chemical reactions and transport [3]. The electron power balance equation is solved to calculate electron temperature, whereas gas and ion temperatures are assumed to be constant. The electrostatic potential Φ is calculated from the (modified) Poisson's equation [4] to determine the self-consistent electric field E= - $\nabla\Phi$ (see [5,6] for details). At the present

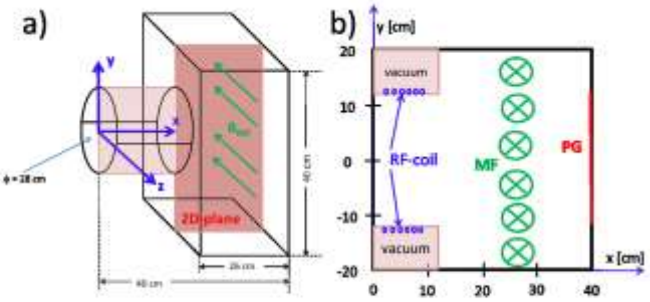

Figure 2. (a) Schematic representation of the source with its dimensions and the modeling domain (oriented perpendicularly to the MF); (b) The 2D-modeling domain used in the calculations; the RF-coil, the magnetic field direction and the PG are indicated; x goes along the cylinder axis.

stage of the development of the model, analytical approximations of the magnetic fields produced by the filter field coils is used.

In particular, we are solving continuity equations for each species α,

$$\frac{\partial n_\alpha}{\partial t} + \mathrm{div}\boldsymbol{\Gamma}_\alpha = S_\alpha \qquad (1)$$

where $\alpha = e$ for electrons, α = '−' for H^-, $\alpha = i = 1, 2, 3$ for H^+, H^+_2 and H^+_3 ions, $\alpha = a$ for atoms H and $\alpha = m$ for molecules H_2, $\boldsymbol{\Gamma}_\alpha$, n_α are the particle fluxes and densities of the different types of particles. The source terms S_α take into account the collisional processes that primarily contribute to the charged particles and neutral species production and destruction [7]. The transport of plasma species is based on the drift-diffusion approximation. The flux ($\boldsymbol{\Gamma}_\alpha$) of each charged species is described by the diffusivity tensor, $\mathbf{D}_\alpha$, and the mobility tensor, $\boldsymbol{\mu}_\alpha$. It takes into account effects due to electric and diamagnetic drifts. At the present stage of the development of the model, analytical approximations of the magnetic fields produced by the filter field coils is used.

Modelling of neutrals.

In our past simulations [5, 6], a state equation was solved for hydrogen molecules for simplicity. That led however to solutions, which for the cases without the magnetic filter field, are characterized by the maximum of the electron density approximately in the middle of the integration domain (property of diffusion equation with uniform sources and transport coefficients) which is in contrast to the experimental results from SPIDER showing rather peaked density in the driver region (see Sec.3). Therefore to improve predictive capabilities of our model and in order to capture correctly the neutral depletion and its impact on the plasma dynamics it appeared necessary to include also the continuity equation (1) for molecules in our model and to consider the corresponding surface chemistry. Cross-sections for collisions between neutrals inside the ion source volume as well as backscattering, dissociation or recombination probabilities against the ion source walls are required for the modelling of the neutral particle dynamics.

#	Reaction	Probability-$\gamma_{\alpha,\beta}$
1	$H^+ \rightarrow H_2$	0.4
2	$H^+ \rightarrow H$	0.6
3	$H_2^+ \rightarrow H_2$	0.2
4	$H_2^+ \rightarrow H$	0.8
5	$H_3^+ \rightarrow H_2$	1/3
6	$H_3^+ \rightarrow H$	2/3
7	$H \rightarrow H_2$	0.4
8	$H \rightarrow H$	0.6
9	$H_2 \rightarrow H_2$	1
10	$H^- \rightarrow H$	1

Table 1: Surface processes [9],[10].

Table 1 shows the surface processes and corresponding probability coefficients used in our simulations (assuming molybdenum coated walls). The boundary fluxes for the neutral atoms and molecules can be expressed as:

$$\mathbf{n}\cdot\boldsymbol{\Gamma}_\mathbf{a} = \begin{cases} \frac{1}{4}(1-\gamma_{a,a})v_{th,a}n_a - \Gamma_{a,back} \\ \qquad wall \\ \frac{1}{4}((1-g_t\gamma_{a,a})+Y)v_{th,a}n_a - g_t \times \Gamma_{a,back} \\ \qquad PG \end{cases} \qquad (2)$$

$$\mathbf{n}\cdot\boldsymbol{\Gamma}_\mathbf{m} = \begin{cases} \frac{1}{4}(1-\gamma_{m,m})v_{th,m}n_m - \Gamma_{m,back} - \Gamma_{inj} \\ \qquad wall \\ \frac{1}{4}(1-g_t\gamma_{m,m})v_{th,m}n_m - g_t \times \Gamma_{m,back} \\ \qquad PG \end{cases} \qquad (3)$$

where $\Gamma_{n,back} = \sum_{\beta\neq a}\frac{A_\beta}{A_n}\gamma_{n,\beta}n_\beta v_{\beta,w}$, n=(a,m) and $v_{\alpha,w}$ is the effective wall loss speed of the particles coming from the plasma, A_α is the particle mass and $v_{th,n}$ is the thermal velocity.

On the plasma grid (PG) boundary, the back flux is reduced by a constant factor $g_t = 1 - p_{prob}$, which models the effect that there is no back flux at the grid holes without having to resolve the individual holes in space (p_{prob} is the probability for neutrals to exit the domain through the PG apertures). In addition, Γ_{inj}

corresponds to the molecules influx at the source inlet at the back plate of the driver. It should be noted also, that in contrast to our past simulations, we are considering now that atoms and molecules can have different temperatures. Usually atoms are much hotter than molecules, $T_a \sim 1$ eV and $T_m \sim 0.1$ eV as indicated by other simulations [8] and experiments [9].

2. Experimental validation of the FSFS2D code results

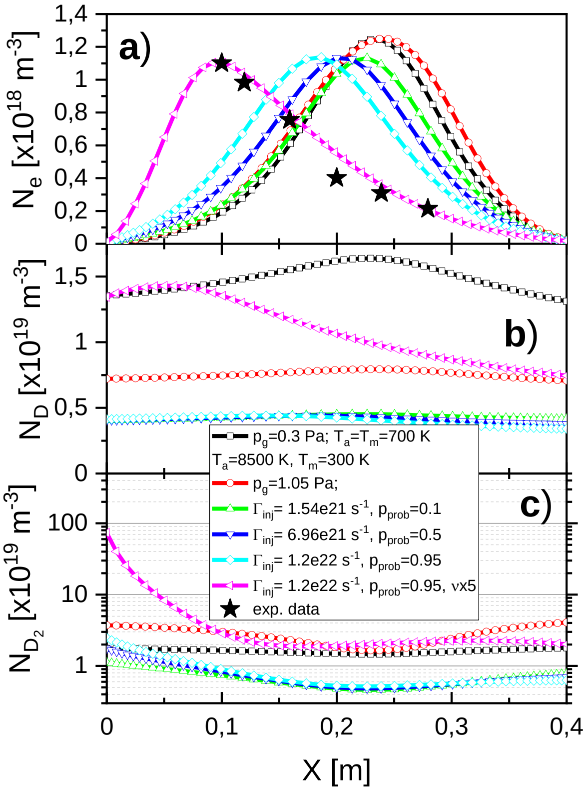

Figure 3: Profiles of electron density (a), atom density D (b) and molecules' density D_2 (c) along horizontal axis (y=0) for different model assumptions. Simulations are done for: P_{RF} =45 kW/m and the PG potential U_{PG} = 15 V.

The main aim of presented simulations is to validate the model by comparison of simulation results with experimental data. The existing data base of probe measurements at different positions in the SPIDER device (see Fig.1) [10], [11] provides a complete set of profiles of plasma parameters along the x direction (axial profiles) as well as parametric scans at fixed probe positions, in the driver and close to the plasma grid (PG). The simulations are done assuming (as in the experiment) only deuterium plasma.

We have started the comparison of the code results with the experimental measurements from the relatively simple situations when the magnetic filter field (B_z = 0) is not present. Therefore the RF coupling model has been switched off for simplicity, since as shown in Ref.[6], details of the heat deposition profile have no influence on the results if the MF field is zero.

Assessment of the neutrals model. As already mentioned, in our old simulations considering the state equation for D_2 molecules (Ref.[5]), resulting plasma density profiles (peaked in the centre of the source) are in contrast to the experimental findings showing maximum of plasma density in the driver region. In order to overcome this difficulty, continuity equation for molecules has been taken into account as described in Sec.2. In order to investigate the effect of the new model for neutrals on plasma parameters, simulations have been performed for deuterium plasma assuming different deuterium pumping probabilities and compared to the old model (see Fig.3). In these simulations, the RF heating is uniformly applied in the driver region ($P_{RF} = n_e \epsilon_{RF}$, where the energy gain per electron ϵ_{RF} is constant) P_{RF} =45 kW/m and the PG potential U_{PG} = 15 V. The gas pressure and /or injected D_2 flux (depending on the model used) have been adjusted in such a way to keep the maximum plasma density constant (~1.2×10^{18} m^{-3}) for a better comparison of the results.

First, it should be noted that the increase of the atom temperature leads to a strong reduction of the atom density and simultaneously gas pressure must be significantly increased from 0.3 to 1.05 Pa to keep the same plasma density (compare cases marked by squares and circles corresponding to solutions of the equation of state). The results with the continuity equation for D_2 molecules, are in principle very similar to the state equation case (red circles) unless the strength of the D_2 source is large enough to shift the density maximum into the driver region. That shift, even for relatively high pumping probability (injected flux) is quite moderate. Only, the increase of the neutrals collisionality by factor 5 or more together with a very intense influx of D_2 gas at the back side of the driver (gas inlet position) forces the movement of the density peak to the experimentally observed position. It should be pointed out, that we could obtain similar results with lower pumping but also lower coefficient for reaction 7 in Tab. 2 at the price of an increased atomic fraction. Change of the probability coefficient for reaction 7 from 0.4 to 0.2, requires the change of the pumping probability coefficient from 0.95 to 0.6 (having the same input particle flux) to keep the resulting plasma parameters almost not changed (see Fig.4). In all the simulations results presented below, the increase of the neutrals collisionality by factor 5 is kept. It should be stressed also, that ion-ion collisions can have strong effect on the simulation results for the typical plasma densities in SPIDER ($n_e > 10^{18}\ m^{-3}$) and ion temperatures of the order of 0.1 eV. In that temperature and density range, ion-ion collisions can dominate the plasma transport which makes the basic assumptions of our model of the weakly ionized plasma and drift-diffusion approximation questionable.

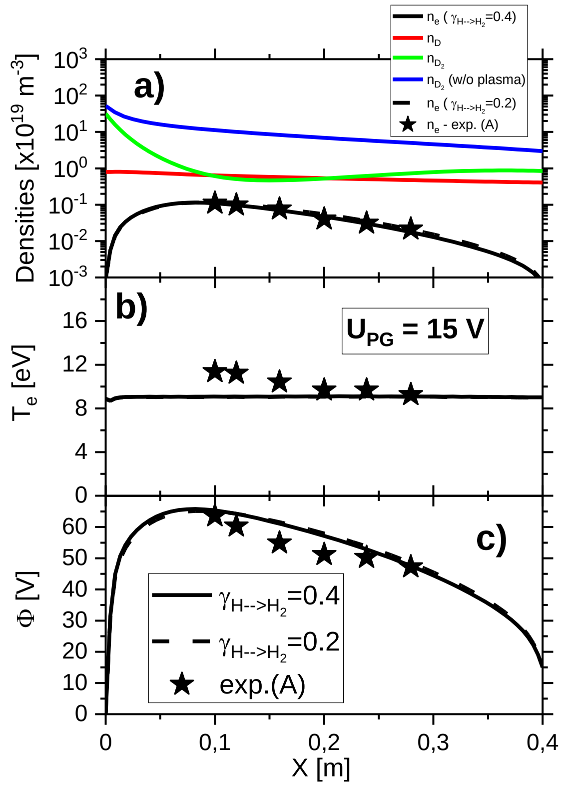

Figure 4: Axial profiles of densities of plasma species (a), plasma temperature (b) and plasma potential (c). Simulation results presented for two different values of the probability co- efficient for reaction 7 in Table.2, 0.4 and 0.2.

In order to reproduce the experimental data with our simulations, it was necessary to set the lower limit on the ion temperature in the formula for the Coulomb logarithm [12] to 1 eV, in the expressions for the ion-ion collisions, otherwise strong/unphysical increase of the plasma density was observed. It is done in all simulations presented in this report. This, however, is only a temporary solution and it might be necessary to extend the model in the future including momentum and energy equations for ions.

Axial profiles of plasma parameters. The correct profile of the plasma density only, does not necessarily mean that the model properly reflects the experimental data. However, there are also available profiles of the plasma temperature and plasma potential which should be simultaneously reproduced. In the Fig. 4, the experimental profiles of the main plasma parameters given by the Langmuir probe (position A, Fig.1) are shown together with the simulation results. The best case from Fig.3 is marked by the black solid lines. In the Fig.4, we also show the gas and molecules' density for the cases with and without plasma. It is clearly seen, that the filling gas density is strongly diluted with the plasma to produce deuterium atoms and electron density. It can be seen that all the experimental plasma profiles are quite reasonably reconstructed by our simulations.

Power scan. Another step in the code validation process is related to the comparison of the simulation results with the probe measurements in the case of the RF heating power scan. Corresponding measurements have been done with the probe A, at two axial positions: in the driver (x = 0.1 cm) and close to the plasma g (x = 38 cm). The comparison of the experimental results with the code results is shown in the Figs.5 and 6. It is apparent from the figures that the simulations can nicely reproduce the experimental data, in particular in the driver region. The plasma densities in the expansion region close to the PG are however lower than the measured values. This might be related to the fact, that the calculated results are here strongly affected by the boundary conditions imposed in the code, which do not really reflect the real situation in this region of the source. If the "code PG position" is assumed to be shifted slightly in the driver direction (x = 33 cm), then the fit to the experimental data is much better.

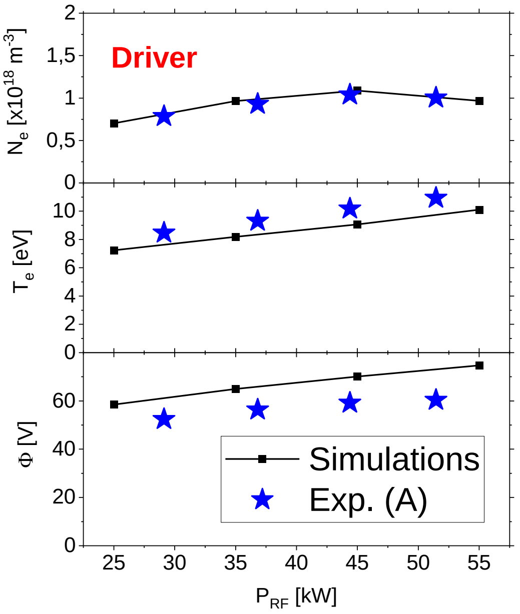

Figure 5: Experimental and calculated plasma parameters in the driver (x = 10 cm) versus RF heating power.

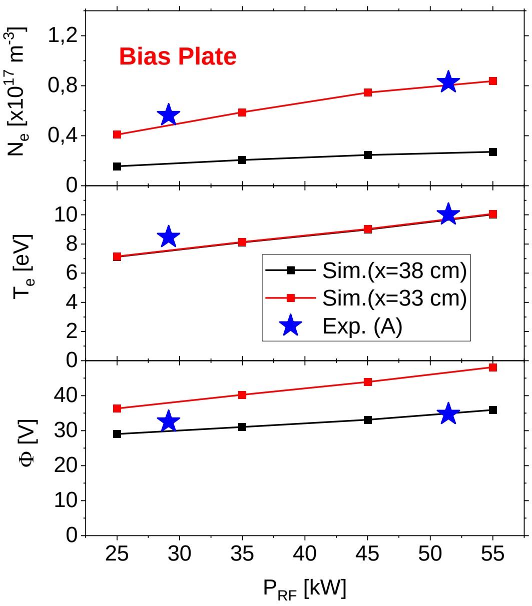

Figure 6: Experimental and calculated plasma parameters at the bias plate position (x = 33 and 38 cm) versus RF heating power.

3. Conclusions and Future Work

The two-dimensional self-consistent fluid model of an ITER-type ion source for neutral beam injection, FSFS2D, has been developed. Presently, the different particle species are described within the drift-diffusion approximation and are governed by separate continuity equations and electron energy equation for 2D Cartesian (or cylindrical) geometry. Recent developments of the neutral model (inclusion of the continuity equations for molecules) allow for simulations of the experimental profiles obtained in SPIDER with and without action of the magnetic filter. The best fit to the experimental data can be achieved only if the following conditions are imposed: strongly localized source of D_2 in the driver region and increased neutrals collisionality (by factor 5) together with some limitations to the collisions frequencies of ions and the reduction of the B field in the driver region. The need to increase the neutrals collisionality indicates that the diffusion model for neutrals might not be the most appropriate in this low pressure regime, whereas the strong effect of ion-ion collisions indicates that the basic assumptions of our model of the weakly ionized plasma and drift-diffusion approximation can be questionable. It might be necessary to extend our model in the future including momentum and energy equations for ions.

Collaboration

ENEA-RFX

References

[1] Agostinetti P et al 2016 Detailed design optimization of the MITICA negative ion accelerator in view of the ITER NBI Nucl. Fusion 56 016015

[2] Toigo V et al 2017, The PRIMA test facility: SPIDER and MITICA test-beds for ITER neutral beam injectors New J. Phys. (special issue)

[3] S Lishev, L Schiesko, D Wuenderlich, C Wimmer and U Fantz, Plasma Sources Sci. Technol. 27 (2018) 125008

[4] Hagelaar G J M, Fubiani G and Boeuf J-P 2011 Plasma Sources Sci. Technol. 20 015001

[5] R.Zagórski, E. Sartori and G. Serianni, ”2-D Fluid Model for Discharge Analysis of the RF-Driven Prototype Ion Source for ITER NBI (SPIDER),” in IEEE Transactions on Plasma Science, doi: 10.1109/TPS.2022.3175527

[6] R.Zagórski, D. Lopez-Bruna, E. Sartori and G. Serianni' „2D simulations of inductive RF heating in the drivers of the SPIDER device", Fusion Engineering and Design, Vol. 188, March 2023, 113427, https://doi.org/10.1016/j.fusengdes.2023.113427

[7] Jesse Soewito Santoso, "Production of Negative Hydrogen Ions in a High-Powered Helicon Plasma Source", PhD Thesis, Australian National University, 2018

[8] Boeuf J-P, Hagelaar G J M, Sarrailh P, Fubiani G and Kohen N, Plasma Sources Sci. Technol. 20 (2011) 0015002

[9] P. McNeely, D. Wunderlich and the NNBI Team, Plasma Sources Sci. Technol. 20 (2011) 045005 doi:10.1088/0963-0252/20/4/045005

[10] C. Poggi et al., IEEE Transactions on Plasma Science, Vol. 50, No. 11, November 2022

[11] E. Sartori et al., Fusion Engineering and Design 169 (2021) 112424

[12] A. S. Richardson, "NRL Plasma Formulary 2018", Naval Research Laboratory Washington, DC 20375-5320, NRL/PU/6790–18-640,

Related 2023 articles and conference presentations:

Published

1. R.Zagórski, et. Al., „2D simulations of inductive RF heating in the drivers of the SPIDER device", Fusion Engineering and Design, Vol. 188, March 2023, 113427
2. D. Marcuzzi, et al. "Lessons learned after three years of SPIDER operation and the first MITICA integrated tests", *Fusion Eng. Des., Vol. 191 No 113590 (2023)*, DOI: 10.1016/j.fusengdes.2023.113698
3. G.Serianni, et.al, "SPIDER, the Negative Ion Source Prototype for ITER: Overview of Operations and Cesium ", IEEE Trans. Plasma Sci Vol. 51 No 3 (2023) 927, DOI: 10.1109/TPS.2022.3226239

Submitted

1. R. Zagórski, , et.al, "Numerical simulations of the plasma parameters in the SPIDER device ", submitted to IEEE Trans. Plasma Sci .

Conference Presentations

1. **International Symposium on Discharge and Electrical Insulation in Vacuum(ISDEIV),** Naha, Okinawa, Japan, 25-30 June – 2023,
   R. Zagórski, et al*.," Numerical simulations of the plasma parameters in the SPIDER device",* poster presentation
2. **15th International Symposium on Fusion Nuclear Technology (ISFNT-15)**, Las Palmas, Spain, 10-15 October 2023:
   R. Zagórski, et al., *„Experimental validation of the fluid solver for SPIDER (FSFS2D)",* poster presentation

Research Unit: National Centre for Nuclear Research

WPENS: Early Neutron Source

Title: Early Neutron Source

Contribution of NCBJ to WPENS Test Systems area in 2023 covers the following subtasks:

- Analysis of the IEC-61508 standard in application to the IFMIF-DONES Test & Accelerator Systems scenarios;
- IPPLM contribution to safety requirements, 2023
- RAMI analysis for the Accelerator and related Ancillaries
- RAMI analysis for Test Systems and related Ancillaries
- Preparation of HFTM/STUMM electric connectors mock-up irradiation experiment at the MARIA reactor
- Irradiation of the HFTM heater mockups at MARIA Reactor in 2023
- Preliminary design of the neutron beam tube (NBT) and shutter (NBS) between the Test Cell and room R160
- System Responsible Officer for Facilities for Complementary Experiments

Analysis of the IEC-61508 standard in application to the IFMIF-DONES Test & Accelerator Systems scenarios

Author(s): S. Potempski

Introduction

This subtask was carried out within the area of Project Level Analyzes in the field of safety. The aim was to analyze the applicability of the IEC-61508 standard "Functional Safety of Electrical/ Electroin/ Programmable safety-related systems" for use in safety analyzes for the Test System and the Accelerator System. In this context, reference scenarios for both systems mentioned above were analyzed, paying particular attention to the signal detection systems used in them.

Results and conclusions:

- Full application of the IEC-61508 standard is performed in 16 steps, and the current information in the SAR (Safety Analysis Report) covers 15 of them, which shows this standard applicable.
- Determining the SIL (Safety Integration Level) parameters necessary to assess the protection layer can be performed basing on SAR.
- The preliminary assessment shows that two reference scenarios (RAS6: loss of helium in the HFTM subsystem and RAS16: leak in the D2/H2 gas supply system) should be examined in more detail as they may require the introduction of additional safeguards.

IPPLM contribution to safety requirements, 2023

Author(s): S. Potempski

Introduction

This subtask was also carried out within the area of Project Level Analyzes in the field of safety, being a continuation of 2022 task. The work was focused on identifying additional safety requirements for Test and Accelerator Systems, using the latest versions of these systems' designs, FMEA and RAMI analyses.

Results and conclusions:

The result of the work is:

- Identification of 13 safety requirements for further consideration, based on the Compilation and Update of Safety Requirements (C&U) document.
- Noticing some inconsistencies between the C&U document and the VISURE system - information about this was included in the report.
- Some part of the requirements, specified only in the design documents, will require further analysis.
- It is possible to use the IEC-61508 standard to specify safety requirements, which, however, requires additional analyses.
- Identifying parts of the requirements that may be considered no longer valid.

RAMI analysis for the Accelerator and related Ancillaries

Author(s): J. Kałowski

Introduction

RAMI studies on the Accelerator Systems (AS) and related ancillaries have been extended considering the last design updates, the progress in the control system, the maintenance policy and optimisation of the control system in preventing beam shutdown in case of single failure in the instrumentations.

Results and conclusions:

The result of the work is:

- Component-level Failure Mode and Effect Analyses (FMEAs) for AS oriented for the high-level functions and relevant failure modes, to identify all failures and malfunctions that can generate RAMI concerns, e.g. downtime and logistical, delays, redundancy requirements, etc.
- Update of the data list on failure models used in the specific RAMI analysis improving the data collection on failure rates, mean time to failure, repair time on components of AS.
- RAMI simulations and the first estimation of the availability targets to require to the different AS subsystems and components, e.g. Injector, RFQ, MEBT, SRF LINAC, HEBT, RFPS and ASA.

RAMI analysis for Test Systems and related Ancillaries

Author(s): T. Kwiatkowski

Introduction

RAMI studies on the Test Systems (TS) and related ancillaries have been extended considering the last design updates, the progress in the control system, the maintenance policy and optimisation of the control system in preventing beam shutdown in case of single failure in the instrumentations.

Results and conclusions:

The result of the work is:

- Component-level Failure Mode and Effect Analyses (FMEAs) for TS oriented for the high-level functions and relevant failure modes, to identify all failures and malfunctions that can generate RAMI concerns, e.g. downtime and logistical, delays, redundancy requirements, etc.
- Update of the data list on failure models used in the specific RAMI analysis improving the data collection on failure rates, mean time to failure, repair time on components of TS.
- RAMI simulations and the first estimation of the availability targets to require to the different TS subsystems and components.

Related 2023 articles and conference presentations:

1. A. Kaszko, S. Potempski "Contribution to the safety requirements of Test and Accelerator Systems", EUROfusion Report.
2. A. Kaszko, G. Mrugała, S. Potempski "Analysis of the IEC-61508 standard in application to the Safety of IFMIF-DONES", EUROfusion Report.
3. J. Kałowski, K. Kowal " RAMI analysis for the Accelerator and related Ancillaries", EUROfusion Report.
4. T. Kwiatkowski, K. Kowal "RAMI analysis for the Test and related Ancillaries", EUROfusion Report.

Preparation of HFTM/STUMM electric connectors mock-up irradiation experiment at the MARIA reactor

Author(s): G. Wojtania, Ł. Murawski, R. Prokopowicz, G. Raj, A. Zawadka

Introduction

The purpose of the task was to prepare the irradiation testing of the HFTM/STUMM electric connector mock ups in the MARIA reactor in cooperation with ENEA/PoliMi team developing detailed technical solutions of the in-core irradiation rig aimed at performing the tests.

Results and conclusions

The technical design of the irradiation rig aiming at testing the HFTM electric connectors in the MARIA reactor core has been developed by ENEA/PoliMi based on recommendations issued by NCBJ. The rig external connectors have been tested and selected. Preliminary plan of the PIE has been prepared. However, some of the PIE remote handling tools need to be developed. In 2024 the detailed technical model of the rig should be released. The rig components need to be manufactured. The detailed electric and instruments and control interface with the MARIA reactor control system need to be defined. The necessary internal NCBJ documentation regarding the rig installation and operation need to be developed. Assembling the rig at NCBJ need to be prepared.

Collaboration

Politechnico do Milano, ENEA/PoliMi

Irradiation of the HFTM heater mockups at MARIA Reactor in 2023

Author(s): G. Wojtania, G. Raj, A. Zawadka, M. Migdal, Ł. Murawski

Introduction

The MAKARONI rig is a custom-designed device developed at NCBJ to test the heating wires that are to be used at HFTM. The rig was installed in the MARIA reactor core in 2021. A day after installation and start-up, the rig cabinet identified malfunctioning of the rig, and halted its operation. The rig was unloaded from the reactor core. It was inspected after an appropriate time to allow the radioactivity of the rig to decrease. The cause of the failure was an unpressurized steel hose housing power cables has been found punctured. A repair method was developed, and the repair was successfully carried out.

Results and conclusions

The MAKARONI operation was resumed after the outage brake, in November 2023. Soon thereafter, precisely 11 hours following the restart, heater No. 1 was switched off as a result of the over-current protection. Whereas, 26 hours after restart, a similar incident occurred with heater No. 2. It is not possible to dismantle the rig from the core during the reactor operation. Thus, rig operation was continued for the next 5 days, until the end of the reactor operation cycle. Afterwards, the resistances between all the heater wires and between them and the housing were measured. The measurements showed that heaters No. 1, No. 2, No. 4 and No. 6 are electrically shorted to the housing. Thus, a decision was made to take the rig out of operation. Operation of the rig has been completed. The next steps should be aimed at explaining the cause of damage of the heaters.

Preliminary design of the neutron beam tube (NBT) and shutter (NBS) between the Test Cell and room R160

Author(s): G. Gałązka

Introduction

The objective of the task was a more detailed development of the design of neutron beam shutter for the Facilities for Complementary Experiments and specification and clarification of technical solutions proposed during the conceptual design phase. In the frame of the task the ongoing cooperation with neutronics engineers was maintained to provide current technical data along with modifications appearing in the design of the shutter.

Results and conclusions

Based on the already defined aims to fulfill in the year 2023, an optimized and refined concept of the NBS developed in the year 2022 was developed. A weight reduction of almost 49.5% was achieved principally at the expense of minimizing one massive cart and split it in two smaller carts with rails close to the axial plane height. A total depth of 3 530 mm was achieved, that although is slightly larger than the 2 725 mm (concept 2022) is still shorter that the overall length of 3 625 mm from the cart of the same year. After setting specific aims for the improvement of the concept 2022 like easier handling, more detailed features on the elements, decommissioning, etc. a richer in details concept hast emerged from this step.

System Responsible Officer for Facilities for Complementary Experiments

Introduction

This task was aimed to create a document summarizing activities of Facility for Complimentary Experiments responsible.

Results and conclusions

Following activities have been performed:

1. Review of all work, in particular of the design documents, concerning the system.
2. Discussing current issues with system coordinators and other system responsibles,
3. Development of DDD and other numerous documents describing the system status, interfaces, boundaries, requirements, etc..

The facility for complimentary research is in conceptual phase of development. There is a significant amount of documentation works still to be performed in 2024– especially in the interface definition.

Collaboration: Karlsruher Institut fur Technologie, Politechnico do Milano, ENEA/PoliMi

Related 2023 articles and conference presentations:

1. WPENS Technical meeting #16; 5.12.2023; Latest Progress on the Engineering Design of FCE system; G. Wojtania (NCBJ)
2. DDD Facilities for Complementary Experiments ; text document; EFDA_D_2QK5H5
3. Collection of interface documentation applicable to the FCE; EFDA_D_2RJ46Y

Research Unit: National Centre for Nuclear Research

WPMAT: Materials

Title: Mechanical characterization of RAFM steels and ODS Fe-Cr alloys

Introduction

Developing materials for fusion technologies is a critical component in advancing fusion development and facilitating its commercial application. Among the key challenges in this process is the need to preselect and rigorously test materials that can withstand the extreme conditions within a fusion reactor. This requirement has led to the exploration of advanced materials such as ODS (Oxide Dispersion Strengthened) and HEA (High Entropy Alloy) steels, which possess promising properties for fusion applications.

However, the successful implementation of these materials is contingent upon a multifaceted approach. In addition to material selection there is a need to optimize their production processes. Moreover it is imperative to refine fabrication techniques such as machining, joining, and heat or thermo-mechanical treatments of fusion reactor components.

This report focuses on two critical aspects of this effort: the assessment of the quality of electron beam welded joints in EUROFER97 blocks and the mechanical properties of Fe-14%Cr-based ODS steel. Both investigations aim to contribute to the overall goal of developing robust methodologies for material testing and optimizing the production of fusion reactor components.

Furthermore, it is important to note that adapting mechanical testing methods to the unique conditions of fusion applications, sometimes requires small-scale testing and the development of specialized protocols and methods. As a result, this report includes the testing of two different small sample sizes with different orientations to better understand the mechanical properties and behaviours of the materials under various conditions, also at high temperature.

Results

Examination of the electron beam welded joint in EUROFER97

Investigated object

The general aim of the whole investigation is to assess the quality of the joint, which is over 30 mm thick. A sample of the joint made by the Electron Beam Welding (EBW) method (see Figure 1) was delivered to the NCBJ Materials Research Laboratory for testing as part of the EUROfusion project. The material joined is steel 9%-Cr EUROFER97. The results presented in this report are a direct continuation of the examination conducted in the previous reporting period. While the examination process is addressed only briefly in this document, it is important to acknowledge that these findings build upon and are informed by the prior analysis.

Methodology

The comprehensive examination encompassed a broad scope of non-destructive tests, including surface-visual (VT), penetrant (PT), magnetic particle (MT), and volumetric - ultrasonic (UT), ultrasonic thickness scanning (UTT) methods. NDT examinations were followed by cross-section macro- and microstructure observations and mechanical tests (hardness, impact tests).

Figure 1. General view on the sample of the electron beam welded joint in EUROFER97

Results:

The objective of the investigation was to evaluate the quality of the electron beam joint in thick EUROFER97 samples exceeding 30 mm. The analysis indicated that the welding parameters used did not yield adequate penetration, resulting in improper fusion along the entire length of the sample. Furthermore, the examination revealed numerous defects such as cracks, microcracks, and voids within the fusion zone. Non-destructive tests corroborated these findings, and cross-sectional macro- and microstructure examinations validated the effectiveness of non-destructive testing (NDT) techniques for inspecting welded components. The study underscores the necessity for the development and optimization of welding parameters in fusion processes to broaden their application to thicker plates. The research demonstrated that NDT tests serve as an excellent screening tool when experimenting with various welding parameters, highlighting their potential in identifying issues and guiding the improvement of the joining process.

ODS steel characterization

Investigated object

The material was manufactured by UKAEA (UK) by means of High Isostatic Pressing (HIP) technique and delivered to the NCBJ Materials Research Laboratory for testing as part of the EUROfusion project (Figure 2a). The overarching goal is to assess both the mechanical properties and anisotropy inherent in the ODS steel canister, specifically produced through a defined processing route. Building upon the acquired results, the intention is to establish a robust methodology for testing other steel chemical compositions and HIP process parameters. In the final stages of examination, room and elevated temperature measurements will be incorporated to comprehensively characterize the material's behavior.

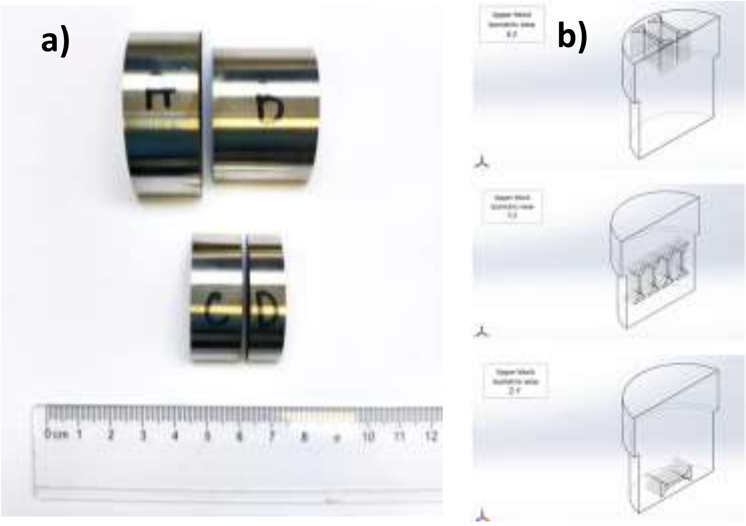

Figure 2. a) General view on the blocks of the ODS steel provided by UKAEA for mechanical testing; b) Schematic drawing showing the localization of the material blocks probed from the HIPed canister

Sample Orientation and Geometry:

Three main orientations of the samples were considered: X-Z, Y-Z, and Z-Y (see Figure 2b). These orientations were chosen to investigate the anisotropy of the material, as different orientations can affect the material's mechanical properties. Additionally, two distinct geometries were deliberately chosen for examination: a smaller geometry (Geometry 1) and a larger geometry (Geometry 2). The selection of two geometries aimed to systematically investigate and compare the obtained information, laying the foundation for a well-defined methodology that can be extrapolated for further examination of similar materials.

Testing Conditions:

The tensile tests were performed at room and elevated temperatures (200, 350, 500, and 700 °C). While data for 700°C is currently unavailable, tests are planned for the near future. The number of samples tested varied for each combination of geometry, orientation, and temperature reflecting ongoing testing.

Results:

The stress-strain curves obtained from the tensile tests were analysed to determine the ultimate tensile strength (UTS) and yield strength (YS) of the material. The representative stress-strain curves are shown on the Figure 3. Comparisons of the average UTS and YS values across different temperatures and geometries were also made using bar charts (see Figure 4).

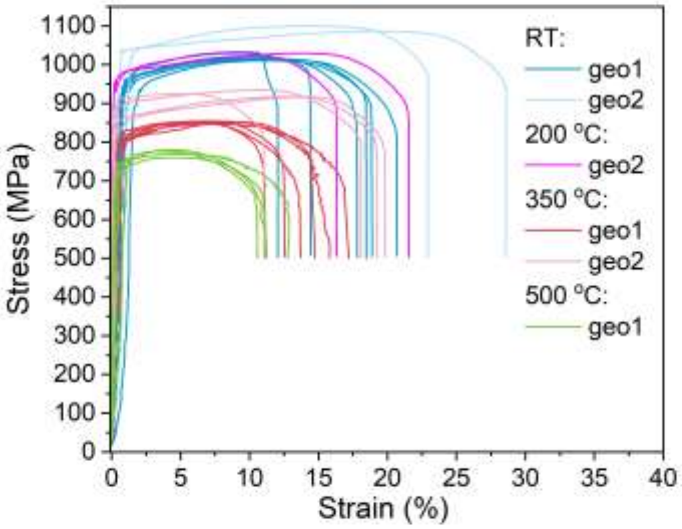

Figure 3. Representative stress-strain curves obtained

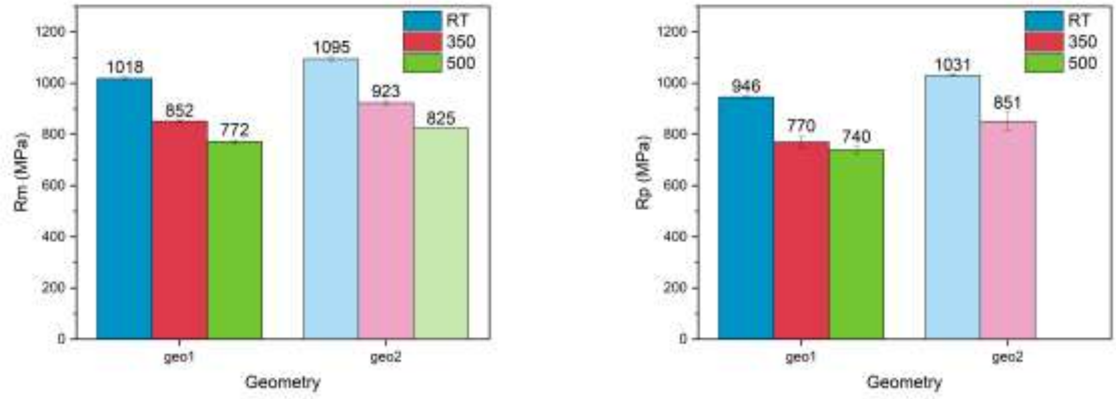

Figure 4. Comparison of average Ultimate Tensile Strength (left) and Yield Strength (right) values

Overall, the methodology allowed for a comprehensive investigation of the mechanical properties of the Fe-14%Cr ODS steel under varying conditions. The results provided valuable insights into the material's behavior and its response to different orientations, geometries, and temperatures. The data collected will serve as a basis for further research and the development of a robust methodology for testing other steel compositions and HIP process parameters.

Conclusions

The investigation into the quality of electron beam joints in thick EUROFER97 samples revealed inadequate penetration and numerous defects, highlighting the necessity for the development and optimization of welding parameters. Non-destructive testing proved effective in identifying issues and guiding process improvement. Additionally, the analysis of ODS steel mechanical properties highlighted the material's impressive mechanical performance and allowed for a development of the foundation of the refined approach for future testing.

Collaboration

The materials for examination were provided by UKAEA (United Kingdom Atomic Energy Authority) and KIT (Karlsruhe Institute of Technology).

Research Unit: National Centre for Nuclear Research

WPRM: Remote maintenance

Title: NCBJ contribution to the Remote Maintenance Work Package

Authors: Krystian Grodzicki (1st task, 3rd task), Jakub Szymanowski (2nd, 3rd tasks),
Grzegorz Gałązka (2nd task)

Introduction

NCBJ was involved in 3 tasks in WPRM in 2023. List of tasks:

- Task 1: In-Vessel Remote Maintenance Development WP4 -Rail Base Mover (RBM) – Concept Development (RM-T.01.01-T005-D005 - AWP23)
- Task 2: Port Remote Maintenance Development WP2 (RM-T.01.02-T001 - D003-AWP23)
- Task 3: Plant Architecture Assessments WP4 (RM-S.01.02-T003-D004 - AWP23)

Task 1: AWP23 - In-Vessel Remote Maintenance Development WP4 - Rail Base Mover (RBM) – Concept Development

This is the continuation of the work from previous year. The main aim of the first task was to develop the concept of the RBM (Rail Base Mover)(Figure 10). Inside the Tokamak there are BB (Breeder Blankets) which have to be replaced remotely every few years. On current stage of the project there is no tool which fulfill all requirements. The RBM is one of a few tools which are currently developing to replace BB from the VV (Vacuum Vessel).

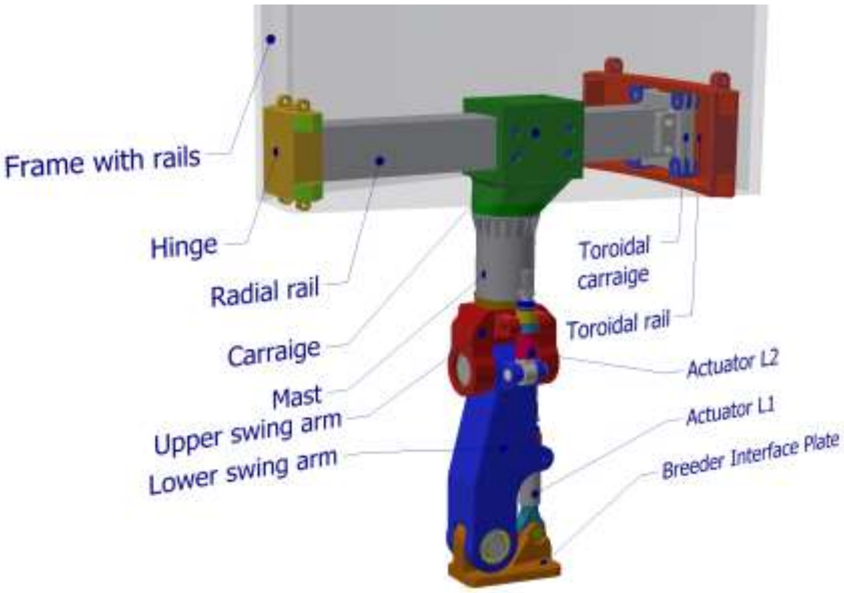

Figure 10 RBM with main parts

Main stages in 1st task:

- preparing computational models;
- performing kinematic calculations;
- performing calculations for joints, actuators, shafts, bearings;
- selecting subparts from the market based on performed calculations (bearings, motors)
- performing strength and displacement calculations.

Results

In 2023 the work was focus on the strength calculations of the structural parts. The RBM concept development is still in progress, but the main parts have been designed and even in the worst cases during seismic events the equipment can withstand the load arising out of blankets removal kinematics which is presented in the report (Grodzicki, Rail Base Mover (RBM) - Concept Development v2.0, 2023). On the Figure 11 showed the stresses on Blanket Interface Plates in the worst cased during replacing Right Outboard Blanket (ROB).
The work will continue in 2024.

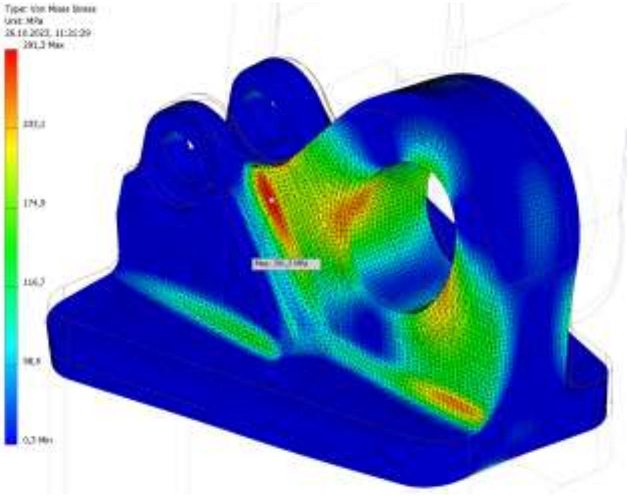

Figure 11 Von Mises Stress for the ROB in load condition 5

Conclusions

Main conclusions from the 1st task:

- Due to the high forces occurring in Joint-C, the construction of this joint takes up more space and to remove the BBs from the VV, adapters are needed.
- The height of the frame for the RBM depends on the position of the BBs before the crane lifts the frame with the RBM in the second lifting stage. If we assume that the CoG have to be directly under the first rotating joint, the height will change significantly.
- The kinematics was slightly corrected especially lilting angles due to the high forces occurring in the extremum positions.
- For all structural parts used material S355, to decrease the weight of the RBM the better material with higher Yield Point could be use.
- The RBM was designed to replace the BBs in the worst cases in the seismic environment. The initial strength calculations show that the majority of the structural components and COTS withstand these harsh requirements but at the expense of the large size and weight of the RBM elements.

Task 2: Port Remote Maintenance Development WP2

Introduction

The aim of the report [2] is to devise a maintenance strategy for the inner space of the three ports [Upper Port, Equatorial Port, Lower Port]. This approach is particularly important because document analysis indicates that there isn't always the possibility of accessing the ports' surfaces from the outside.

Results

To devise a strategy for conducting remote maintenance from within the ports, a list of port coating elements and their connections was compiled, followed by their description and proposed connections between them. The main type of proposed connections is welded connections, but in some cases, the use of bolted connections is necessary for easier assembly and disassembly of elements. Subsequently, methods for monitoring key connections in the ports were proposed and described. To obtain a complete picture of the maintenance strategy, a schematic of how RM tools reach the supervised location was described in the final step.

Conclusions

Key conclusions resulting from the report work include:

- External access to the ports is very limited. In the case of the lower port, external access is practically impossible.
- Port inspection should primarily be conducted from the inside.
- Adequate technology for inspecting connections in the conditions mentioned in this report is not available.
- There are no available systems for moving inspection and maintenance tools inside and outside the ports.
- The equatorial port mainly has sufficient internal space for inspection systems (visual or ultrasonic inspection). In this port, in EC sectors, an inspection passage is located. For other systems located in the meridional port, such a plate was not found.
- The upper and lower ports lack passages for inspection systems, which prevents maintenance or observational work without the need to open the entire channel.

Task 3: Plant Architecture Assessments WP4

Within this task, we were involved in 3 subtasks.

Further development of Inboard blankets overlapping lifting interfaces [3]

Introduction

The "Inboard blankets overlapping lifting interfaces" is a part of the Breeder Blankets responsible for connecting the cooling system and transferring thermal energy, as well as connecting the Breeder Blanket with the tool for extracting these elements from the device. The shape of the overlapping lifting interface element affects the Remote Maintenance strategy. The work in the task "Further development of Inboard blankets overlapping lifting interfaces" focuses on analyzing data regarding the distribution of interface elements on its surface and comparing proposals for the overlapping interface from the following reports:

- EUROfusion_IDM_ 2PL5JJ
- EUROfusion_IDM_ 2Q8Y5L
- EUROfusion_IDM_ 2QF94Z

Results

In the analysed work, a positive impact of the overlapping interface on the RM strategy was observed. The discussed system allows RM tools to access the lifting surface. Unfortunately, during the design phase at this stage, creators did not consider the need to integrate changes in the lifting interface with the other existing systems (Tube system, Guiding system).

For the purpose of a deeper analysis, assumptions were defined for all systems present in the Inboard interface area. With this information, it is possible to propose a new, more realistic overlapping lifting interface.

Conclusions

The existing systems on the lifting surface have an influence on the overlapping lifting interface. These systems are standardized and described in existing works. The overlapping interface has a positive impact on the RM strategy.

Influence of Tokamak Major Radius / Aspect Ratio on Remote Maintenance [4]

Introduction

In this task, collaboration is being carried out with research units UKAEA, VTT, EK, LUT to analyse the topic of the Largest Radius for Tokamak. These efforts involve analysing the parameters of BB while changing various Largest Radii for the same size of tokamak components (Vacuum Vessel, Breeder Blankets). The next stage of the analysis was to change the parameter of plasma-forming height and its impact on the device structure and RM strategy. The final assumed stage of work is to analyze the impact of changing the parameter of plasma-forming width and its influence on the device structure and RM strategy.

Results

In the work on the task, a strategy for task development focusing on changing the parameters of the Major radius, plasma-forming height, and plasma-forming width has been prepared. At the current stage, the analysis of the Major radius's impact on RM has been completed. Work on increasing and decreasing the parameters forming the plasma is still ongoing and is in the analysis phase.

Conclusions

Considering that the task is still being developed, we can only provide conclusions for the Major Radius subtask. The conducted work has shown that the maximum moment during the extraction of elements will vary depending on the size of the Major Radius parameter, ranging from 3.07 to 6.57 MNm, while the mass of the IBB element will change in the range of 39,300 to 71,960 kg. The ratio of mass to moment leads to the conclusion that a change in Major Radius radius results in a change in mass per 1 MNm. For a smaller tokamak radius, the influence of mass on the torque moment is greater than in the case of a larger tokamak radius.

Maintainable tokamak architectures - Bluemira

Introduction

EU-DEMO is a developing concept for a large port-based tokamak. It relies on replaceable blankets for tritium breeding, and there are technical risks for handling of the blankets remotely: high loads (~100 tonnes), restricted space and high radiation levels (~kGy/h). These risks can be broadly addressed as a balance between two approaches: 1) design of remote maintenance (RM) equipment around geometric contexts presented at the G1 pre-concept gate review, or 2) proposal of new geometries that are more sympathetic to the blanket handling challenge, including changes to the tokamak architecture.

Results

The next stage of work related to improving access was conducted in the area of changes to the Toroidal Field Coils (TFC). In the first step, the team was tasked with modelling the TFC coils and determining their impact on the device's operating range. To determine the design changes and responses to key questions, contact was established with the WPMAG group.

Conclusions

The proposed structural changes lead to an increase in the upper port area. However, works confirming the feasibility of implementing these changes are still being consulted with the WPMAG team.

Collaboration

1st task - Rail Base Mover (RBM) – Concept Development - Collaboration with Stuart Budden, Sinha Aditya, (UKEA)

2nd task - Port Remote Maintenance Development WP2 - Collaboration with William Brace (VTT)
3rd task - Plant Architecture Assessments WP4 - Collaboration with Stuart Budden, Michael Staniforth (UKEA), VTT, EK, LUT

References

[1] K. Grodzicki, Rail Base Mover (RBM) - Concept Development v2.0, EUROFusion (EFDA_D_2QFHXW), 2023.

[2] J. Szymanowski, „RM-T.01.02-T001 - D003-AWP23 - Port Remote Maintenance Development WP2,” 2023.

[3] J. Szymanowski, „Further development of IBB overlaping lifting interfaces,” EFDA_D_2RDSTR, 2023.

[4] M. Staniforth, „Influence of Tokamak Major Radius / Aspect Ratio on Remote Maintenance,” EUROFusion (EFDA_D_2R28DC), 2023.

Related 2023 articles and conference presentations:

Poster; SOFE 2023 OXFORD; Challenges of In-Vessel Maintenance within Large Port-Based Tokamak Devices; A. Sinha, S. Budden, M. Torrance, O. Crofts, W. Brace, H. Martikainen, K. Katajamaki, **K. Grodzicki**, **J. Szymanowski**

Research Unit: National Centre for Nuclear Research

WPTE: Tokamak exploitation

Title: Cherenkov detectors as auxiliary measurement tool for the determination of the runaway-electrons beams

Authors: Marek Rabiński PhD DSc Eng., Roch Kwiatkowski PhD, Jarosław Żebrowski PhD

Introduction

In a tokamak plasma, a sufficiently strong electric field can cause the continuous acceleration of the electrons, and gradually increases the characteristic time of their collision with other particles. When the energy of these electrons surpasses a certain threshold, they transform into runaway electrons (RE). Runaway electrons in tokamaks can reach energies in the range of tens of megaelectronvolts, especially during plasma disruptions, representing a major concern for the safety of large tokamaks and ITER especially. During such a disruption event in a tokamak plasma, a significant number of high-energy REs are generated. Uncontrolled rapid loss of runaway current is detrimental, severely damaging plasma-facing components due to the heat flow or generated radiation. The development of strategies for disruption and runaway electron mitigation is critical for safety of the future tokamak reactors. Several research efforts are then focused on studying and understanding RE electrons behavior and their production mechanisms, as well as the implementation of control methods to mitigate or suppress them. The Cherenkov detectors is one of diagnostic techniques which was proposed for runaway electron studies. The team from NCBJ develops this technique for many years. The project “Cherenkov detectors as auxiliary measurement tool for the determination of the runaway-electrons beams” which was conducted in 2023 is the continuation of the same project in 2022.

Results

The runaway electrons studies in 2023 within TCV tokamak was performed by means of the measuring head, which was equipped with diamond radiators of the stick shape (with one end of a semi-spherical form) and of a little bit greater volume than the previous one version. The semi-spherical ending of radiators of each channel were coated by molybdenum layers of different thickness, what distinguished a lower energy threshold for electrons, which could be recorded by these channels. The successive channels of this detector have these thresholds as follows: 58 keV, 132 keV and 197 keV. The discussed measuring head was designed and produced at NCBJ. The whole probe was applied during the second half of 2022 year and was unbroken after session, so it can wait for 2023 measurements in the rest position inside the TCV vessel. The studies by means of this detector in 2023 were performed within the framework of the Research Topic RT22-03: “Strategies for disruption and run-away electron mitigation”. The one of this topic Scientific Objectives (D4) was worded as “Determine the physics mechanisms generating run-away electrons in the current quench and in the plasma start-up phase” and the Cherenkov detector is helpful in studies devoted to this objective.

In 2023 the Cherenkov probe – continuing the studies performed in 2022 – was applied for measurements of Cherenkov signals of RE origin in the vicinity of TCV tokamak vessel wall in the upper corner of Low Field side. The member of the NCBJ research team prepared the detector for work and tested them just before the experimental session in November 2023 (which was dedicated to WP-TE RE measurements) and next take part in the same session. The obtained signals were analyzed with reference to other diagnostic techniques signals. Detectors system parameters (probe position and supply voltage) were permanently actualized. Peaks on Cherenkov detector channels traces were cause by the high-energy electron micro-beams. Due to peripheral region of the Cherenkov detector location, these micro-beams were diffuse and less clear in relation to the main RE beam recorded in the vicinity of tokamak’s equator. Mentioned peaks were record even when the main RE beam was no observed. The different thickness of molybdenum layer on three channels of Cherenkov detector are no important for signals amplitude due to the energy of micro-beams are of the MeV region. The differences between signals on the Cherenkov detector channels were connected with spatial displacement of the measurements region. The distance between centers of channels radiators is equal to 4.4mm. The signals on the Cherenkov detector channels were more visible after deuterium Massive Gas Injection (MGI).

The other main task of the RT22-03 November 2023 TCV session was “Runaway damage mitigation through benign termination”. A potential solution for RE mitigation is “Benign Termination” via low-Z injection and excitation of an MHD instability to expel the REs without regeneration, what was proposed by Carlos Paz-Soldan in 2019. The key to the success of this method is the conversion of magnetic energy to thermal energy and consequently radiated energy, thus spreading it over a large area. The results of earlier studies of “Benign Termination” performed in TCV were summarized in the paper [1].

Conclusions

- Signals amplitude recorded by means of the Cherenkov detector for individual channels are irrespective of thickness of channel molybdenum layer due to the energy of micro-beams are of the MeV range, but the differences between signals on the Cherenkov detector channels were connected with spatial displacement of the region of the measurements. The distance between centers of channels radiators is quite significant and is equal to 4.4mm.
- The signals on the Cherenkov detector channels were more visible during TCV tokamak discharges with deuterium Massive Gas Injection (MGI).
- It was confirmed that runaway electron beams emission in the vertical direction is very limited in the TCV facility, but during 2023 experimental campaign this emission was much more visible than during 2022 TCV measurements.

Collaboration

EPFL, Lausanne, Switzerland

References

[1] U. Sheikh et al. Plasma Phys. Control. Fusion 66 (2024) 035003

WUT: Warsaw University of Technology

WPPWIE: Plasma Wall Interactions and Exhaust

Title: Plasma Wall Interactions and Exhaust

Authors: Elżbieta Fortuna-Zaleśna, Maciej Spychalski, Witold Chromiński, Karol Szlazak, Łukasz Ciupiński

SP B. Experiments on erosion, deposition and material migration

Introduction

The main aspects of plasma-wall interactions in fusion reactors are related to assessing the materials' lifetime and long-term fuel retention in the plasma-facing components. This justifies the study of material migration processes, i.e. the phenomena of erosion, transport of eroded atoms/ions, and their re-deposition. All these processes significantly modify the surface of the materials. Access to the elements inside the chamber of the ITER experimental fusion reactor, currently under construction in Cadarache, will be very limited, which makes research aimed at determining the changes occurring on the surface of the plasma-facing materials due to plasma-surface interaction so important.

Results

Plasma exposed W7-X tile examination

A set of plasma-facing components was retrieved from the W7-X vessel after the OP1.2b campaign with an inertially cooled Test Divertor Unit (TDU) and analysed post-mortem to provide data on the plasma-surface interactions processes in the complex device geometry. In 2023, the examinations on the lower TDU horizontal target (HT) graphite tile HM19TM400hTE1, after the overloading experiment have been completed. The purpose of the work was to determine the tile damage and to examine the erosion-redeposition pattern in relation to the adjacent tile (HM19TM400hTE2 [1]) that did not suffer such damage.

The research carried out made it possible to characterize damaged areas, as well as remaining subfingers. The morphology, chemical composition, and internal structure of these zones were determined using scanning and transmission electron microscopy, focus ion beam, and optical profilometry. It was found that material removed from damaged areas had redeposited (partially) in their area, as well as in areas adjacent to them. This is evidenced by the presence of deposition, which has occurred in areas that would normally be erosion-dominated. For this reason, areas with morphology typical for eroded zones were not found on the studied tile.

The surface morphology in the damaged zone was described in detail (area located at the longer edge of the tile, at samples no. 4-6). TEM examinations of the material structure in the damaged zone and outside the damaged zone were completed (sample 5). The structure of deposits formed in the damaged zone differs from that formed during the normal operation of the device. The thickness of the re-deposit in this area exceeds 13 µm. Distinct differences in the surface morphology between Tiles 1 and 2 were observed. Among the most important differences is the lack of an erosion zone on Tile 1 (it was observed on Tile 2, samples no. 5-7, the inner HT strike line position). However, it was found that the target finger substructures located close to the outboard side did not show any evidence of redeposition or erosion (samples P17-P22, the same as in Tile 2). Differences in surface morphology concern the first of the transition zones. The deposition was found on all four samples (P0-P3), despite the differences in surface morphology. The distribution of surface roughness along the length of the tile obtained for TE1 and TE2 was similar, however, the roughness values obtained on element TE1 were significantly lower.

Characterization of tungsten plasma-facing components after the first phase of the WEST operation

Introduction

Turning Tore Supra into the WEST configuration has been achieved through the development of new plasma-facing components (PFCs) with tungsten surfaces in order to provide a full tungsten environment, as foreseen for future fusion devices. Five experimental campaigns (C1 to C5) were conducted between 2017 and the end of 2021 in WEST tokamak.

Results

Three samples from WEST C5 marker erosion tiles were examined, samples K and F from the 21o tile from the outer divertor and sample J cut out from the tile 33i from the inner divertor. On each of the samples, microscopic observations of the surface, EDX analysis of the marker layer and deposit (if any) and FIB cross-sections of both the marker layer and the tungsten coating were carried out.

A distinct deposit at the slope of the valleys, forming characteristic, directional bands, was found in sample F. It covers only the slopes located on one side of the irregularities formed during the tile machining (the tungsten coating reflects these irregularities to some extent). On slopes sloping in the opposite direction to the deposit-covered slopes, the thickness of the marker layer is reduced, indicating the erosion of these areas. As revealed on one of the cross-sections, the thickness of the marker layer locally was reduced to 0.2 µm. The thickness of the deposit layer is not uniform. In the examined locations, the deposit thickness was up to 8 µm. The morphology of the deposit is stratified, with sublayers varied in chemical composition. The marker layer thickness on sample K is in the range of 0.9-2.4 µm (maximum value at the cavity bottom). Locally, an extremely thin and discontinuous layer of re-deposited material can be seen on the surface.

A thick deposit layer (up to 45 µm) of directional character and complex structure covers the sample's surface from the inner divertor. The layered structure is visible. The morphology of the deposit resembles tiles or scales. Chipping (contributing to dust formation), cracks, and arc damage are visible on the surface. EDX measurements from the area clearly show the increased signal from B, O, C, and Cu and a small but distinct peak from N. Additionally, the spectra show a weak signal from iron, silver/chlorine, chromium, and molybdenum. Strong variation in chemical composition, thickness, and morphology was observed in most sublayers. Clear tendency to the transformation of the material into more equilibrium structures. What should be noted is the presence of areas of two- (or multi-) phase structure with boron-rich crystals, Fig. 1.

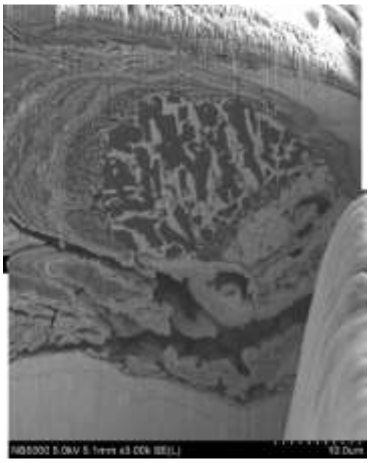

Fig. 1. *SEM images of the deposit and marker layer cross-sections, sample J, inner divertor, C5 campaign.*

Reference coatings

Introduction

The overall objective of this task was to characterize reference coatings which simulate the re-deposited layers observed in fusion devices and to investigate the role of different production parameters on their structure, composition, impurity content, and erosion and retention characteristics.

Results

Two samples, WFW988 and HP_W_207B (on pyramidal Si substrate) with tungsten reference coatings, were examined. The internal structure of reference coatings was examined by TEM. In the case of WFW 988 sample, between the coating and the substrate transition layer of ~ 170 nm is present. Coating thickness 1.2 µm. The coating is a mixture of amorphous and nanocrystalline matter. The crystallites are a few to 10 nm in size. The reference layer on sample 207 has a columnar morphology. Its shape reflects to some extend the morphology of the silicon substrate. The registered diffraction image proves the nanocrystalline structure of the layer.

Additionally, in 2023 we started examining samples with W coatings after high-energy dust bombardment. Their objective is to study how the W+O deposit delaminates/vanishes under the action of dust impact. Work in progress.

SPE.3 Post-mortem analysis of PFC and other objects in JET

Langmuir probes

Introduction

Examinations started in 2022 have been completed. Three Langmuir probes designated as LP-1, LP-3 and LP-5, removed from Module 16W, Tile 5, in 2015, after ILW-2 (probe 1 mounted at stack A, and probes 3 and 5 at stack B) were examined in order to assess their possible damage and changes in their mechanical properties. When examining the probes, we utilized the procedure successfully implemented when examining the probes removed after the ILW-2 campaign from Tile 3, presented in [2]. Mechanical properties were determined by nanoindentation (NI) using a Hysitron Ti-900 triboindenter. The nano-hardness measurements were carried out at the tip and the base.

Results

The most important result is the significant difference in the hardness value in the tip and the base of LP-5, 5.4 GPa versus 8.8 GPa, respectively. On the other two probes, the hardness values were similar to the probe in the initial state.

Cross-sections obtained using the FIB technique allowed the grain size to be determined in the tip and base of LP-5. The recrystallization of the material in the tip area explains the differences in hardness values between these areas. The grain size near the surface reached 40-55 um.

A module of bulk tungsten Tile 5 contains four stacks (A)–(D). The outer strike point in JET is located on stacks C and D and rather seldom on (B), while stack (A) was used for experiments on deliberate tungsten melting and studying melt layer motion. The differences in hardness on the base and tip of probes LP-1 and LP-3 were small, which was expected. Probe 5 was, however, mounted at the border with stack C, which may explain, to some extent, its tip overheating.

Bulk tungsten lamellae

Results

Two lamellae 157/B02 (ILW3) and 164/B12 (ILW1+3) from stack B of the bulk divertor were examined. Microscopic observations revealed that the surface morphology is strongly developed, with longitudinal cracks, regular with constant intervals, ca. 40 µm, and a network of finer cracks. There are visible traces of surface remelting. Redeposition is observed inside the cracks, locally in the cavities, and on edges (shadowed areas). EDX point measurements confirm higher levels of O and C, locally also N, Ni, and Fe in these areas.

To characterize the near-surface zone, a total of 14 FIB cross-sections were made. The cross-sections through the “hills” often correspond to re-solidified material. In the crack mouths a material with a different chemical composition than the substrate was accumulated (often of stratified character indicated re-deposition). The surface also showed changes that could be described as re-deposition. Such areas were not numerous, often located in surface depressions or on the slopes of structural projections.

The TEM observations of the internal structure revealed the bubbles (10-30 nm in diameter) which populate the region over 500 nm in depth. The size and distribution of the bubbles are consistent with what Tokitani observed at not-exposed lamella [3]. They are considered to be formed during the manufacturing process. Additionally, two areas with granular re-deposit were found. The extraneous material has been also found at the mouth of the crack. It was amorphous and had partly porous, and partly stratified structure.

SP C TEM analysis of damaged W-samples

Introduction

Tungsten single crystals with (100) orientation was subjected to ^{4}He ions implantation with 1 MeV energy at room temperature. Then, it was annealed in vacuum at 1700K for 30 minutes to create He bubbles within irradiated area. SRIM calculations allowed to predict that He distribution should be inhomogeneous with damage peak reaching 0.2 dpa at approx. 1.5 µm below the surface. Total irradiation depth is about 2 µm. This procedure was conducted in Max Plack Institute of Plasma Physics in Garching.

Results

Focused Ion Beam lift-out technique was used with the final Ar^{+} gentle polishing as a final treatment just before observations. ThermoFischerScientific Spectra 200 TEM was used as a main observation tool. The presence of bubbles was detected between 1000 and 2100 nm below the surface. For this reason, density was calculated on the intervals of 1000-1270, 1270-1500, 1500-1800, 1800-2100 nm. The upper part of the radiation-affected layer with some irradiation-induced dislocations but no bubbles is presented in the Figure 1(a). The next image (Figure 1(b)), shows bubbles distributed homogenously at the peak damage depth close to 1500 nm.

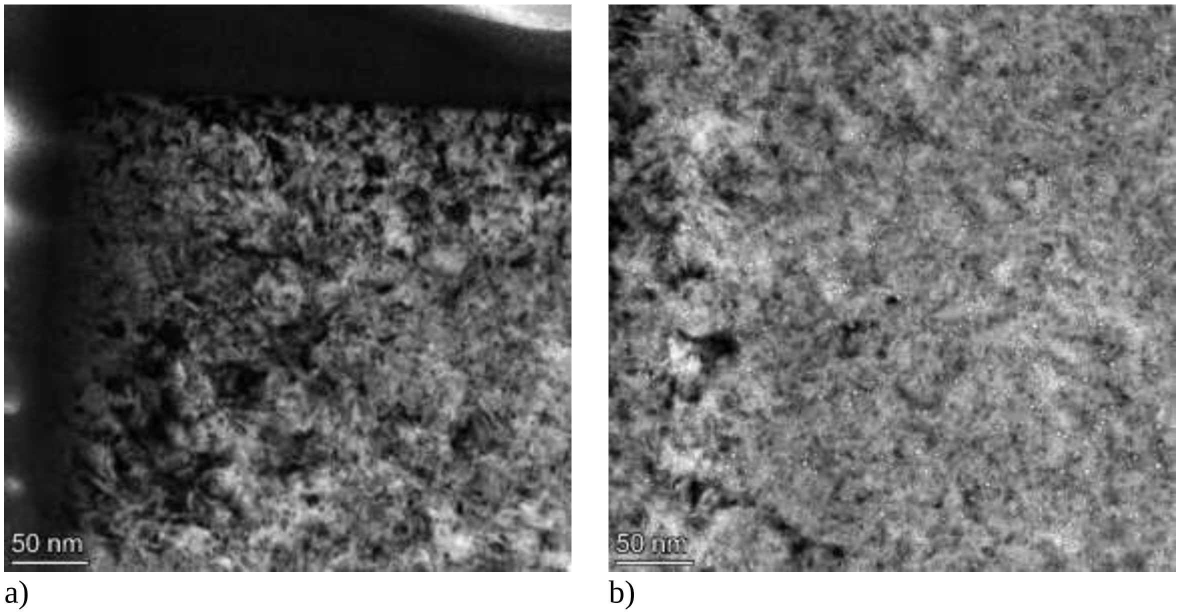

a) b)

Figure 1 Two different regions of the implanted surface (a)close to the surface with no bubbles (b) homogenous distribution of bubbles at peak damage depth

TEM micrographs were used to express the presence of the bubbles in a quantitative manner. More than 30 images were carefully analysed in this purpose. The example of the analysis is presented in the Figure 2(a). Graphical presentation of calculated values is depicted in Figure 2(b)

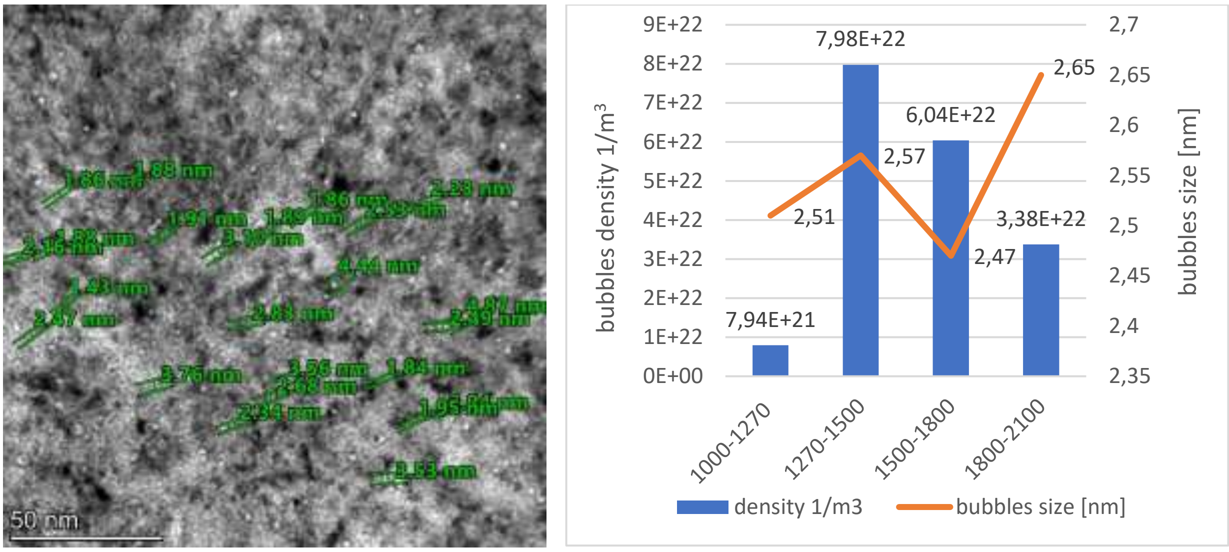

a) b)

Figure 2 Quantification of the TEM micrographs (a) an example of bubble size measurements (b) graphical representation of density and size of bubbles

The mean size of bubbles is close to 2.6 nm but it depends on the region of calculation. Nevertheless, variances are not significant. The density of bubbles, however, strongly depends on the depth. In the first region, where bubbles starts to appear, their number density is rather small, an order of magnitude smaller than in other parts. The deeper region approaching peak damage feature the highest density of bubbles. Then, the value gradually decreases down to the deepest parts affected by He implantation – 2100 nm.

Summary

The density of bubbles depends on the distance from the surface. The size does not follow the same tendencies, however reported variances in values are rather small and should not be treated as meaningful. TEM imaging combined with analysis of diffraction patterns can be successfully used for nanobubble studies in irradiated tungsten.

Conclusions

The surface morphology and internal structure of the material in the damaged zone of tile W7-X HM19TM400hTE1 after the overloading experiment were described in detail. It was found that material removed from damaged areas had redeposited (partially) in their area, as well as in areas adjacent to them. The structure of deposits formed in the damaged zone differs from that formed during the normal operation of the device.

One of the most important observations made during the examination of samples from the marker tiles from the WEST reactor was the presence of a very thick layer of deposit (45 µm) on the tile from the inner divertor after the C5 campaign.

The work on Langmuir probes has provided information on morphological changes of Langmuir probes from JET-ILW. It also constitutes the report on the mechanical properties of JET plasma-facing components determined by means of nanoindentation.

Because the morphology of the lamellae resembles the morphology of the material in its initial state, it is impossible to clearly determine which damage occurred at the material production stage (machining) and during operation.

TEM imaging combined with analysis of diffraction patterns can be successfully used for nanobubble studies in irradiated tungsten.

Collaboration

- KTH, Department of Fusion Plasma Physics – Alfvén laboratory, Stockholm, Sweden
- Forschungszentrum Jülich, Institut für Energie- und Klimaforschung-Plasmaphysik, Partner of the Trilateral Euregio Cluster (TEC), 52425 Jülich, Germany
- Max-Planck-Institut für Plasmaphysik, D-17491 Greifswald, Germany
- Max-Planck-Institute fur Plasmaphysik, Boltzmannstr.2, 85748 Garching, Germany
- CEA, IRFM, F-13108, Saint-Paul-Lez-Durance, France
- Institute for Plasma Science and Technology—CNR, Via R. Cozzi 53, 20125 Milan, Italy
- Department of Energy, Politecnico di Milano, Milan, Italy

References

[1] E. Fortuna-Zalesna et al. Fusion Engineering and Design 191 (2023) 113589

[2] M. Spychalski et al. Phys. Scr. 96 (2021) 124072

[3] M.Tokitani et al. Phys. Scr. T171 (2020) 014010

Related 2023 articles and conference presentations:

1. E. Fortuna-Zalesna, W. Zielinski, Ł. Ciupinski et al., *Erosion and redeposition pattern on the W7-X graphite test divertor unit tile*, Fusion Engineering and Design 191 (2023) 113589
2. M. Diez, M. Balden, S. Bresinzek, Y. Corre, N. Fedorczak, M. Firdaouss, E. Fortuna, J. Gaspar, J.P. Gunn, A. Hakola, T. Loarer, C. Martin, M. Mayer, P. Reilhac, M. Richou, E. Tsitrone, T. Vuoriheimo, *Overview of plasma-tungsten surfaces interactions on the divertor test sector in WEST during the C3 and C4 campaigns*, Nuclear Materials and Energy, Nuclear Materials and Energy 34 (2023) 101399,
3. D. Dellasega, G. Albeti, E. Fortuna-Zalesna, et al. “*Nanostructure formation and D retention in redeposited-like W exposed to linear plasma”*, Nuclear Materials and Energy 36 (2023) 101492
4. 15th International Symposium on Fusion Nuclear Technology (ISFNT-15), Las Palmas de Gran Canaria, Spain, *poster:* W. Chrominski et al., “Methods for characterization of voids and bubbles in S/TEM”

Research Unit: Warsaw University of Technology

WPENS: Early Neutron Source Definition and Design

Title: Early Neutron Source Definition and Design

In the WPMAT project, the Warsaw University of Technology implemented two tasks in 2023:

- Consolidated constructive concept for a non-maintainable TC floor (ENS-4.2.1.3-T012-04)
- Evaluation and Optimization of Structural and Shielding Concrete for IFMIF-DONES (ENS-2.2.6.6-T025-09)

Consolidated constructive concept for a non-maintainable TC floor

Author(s): Rafał Michalczyk, Kazimierz Józefiak, Karol Brzeziński

Introduction

In 2023 more parametric analyses was performed to study the influence of gap conductance coefficients on the maximum stead-state temperature in the bucket floor. Moreover, 2-accelerator IFMIF-DONES condition was considered, first by using nuclear heating data from the year 2022 simply multiplied by the factor of 2, and later (second half of 2023) by using most recent nuclear heating data provided by the neutronics team for the 2-accelerator condition. Furthermore, the FEM model was updated and a 50 mm thick bucket liner bottom plate was introduced (compare to 10 mm thick modelled previously) in order to check if such a thick plate can provide additional shielding of the bucket floor. Additionally, as a results of discussion and consultation with test systems coordinators of WPENS, it had been decided that assumptions concerning the thermal contact between bucket, bucket liner and TC liner might have been assumed too conservatively before (see [1, 2]). Thus, in the final heat-transfer calculations presented in this report, thermal contact assumptions were relaxed.

As the task continuation and extension, thermal-stress analysis of different scenarios that might impact structural integrity of TC liner, bucket liner and the concrete bucket floor is planned. One of the emergency scenarios considered is liquid lithium spillage on the bottom plate of the TC liner. In 2022, as described in [1], only simplified transient heat transfer liquid lithium spillage analysis was carried out which showed that the influence of this event on maximum temperature in the concrete bucket is negligible. However, lithium spillage most possibly will generate high temperature gradients in the bottom part of TC liner that might lead to destructible thermal stress. In order to perform thermal-stress analysis in the future, first more accurate temperature distribution during the spillage has to be assessed by means of numerical analysis. As part of activities carried out in 2023, the possibility of using distinct element method (DEM) for modelling the spillage was analyzed.

In 2023 also further attention was put into designing an experiment for determining thermal conductivity coefficient between concrete and steel. All heat transfer analysis presented so far (including these presented herein) were based on gap conductance values found in literature. As laboratory confirmation is necessary, one activity in 2023 was to carry out some FEM numerical simulations that will help to design the experiment better, thus avoiding conducting laboratory tests that might provide unusable or inconclusive results.

Results

Three parametric studies were conducted. The goal of the first parametric study was to analyse the influence of gap conductance coefficients on the maximum temperature in the concrete bucket floor. In this analysis local areas of contact between elements were assumed. 2-accelerator condition was simulated by multiplying 1-accelerator volumetric heat flux data by 2. Maximum values of temperature of every case of analysis are summarized in Table 1 (cases 1-0 to 1-8). The goal of the second parametric study was to analyse how values of gap conductance for bucket - bucket liner interface influence the maximum temperature in the bucket assuming that whole area of contact between bucket and bucket liner is taken into account. Maximum values of temperature of every case of analysis are summarized in Table 1 (cases 2-0 to 2-5). The third parametric study was similar to the second one. The goal of this parametric study was to analyse how values of gap conductance for bucket - bucket liner interface influence the maximum temperature in the bucket. The contact between TC liner and bucket liner was kept local (only around fixation points) but the area for every fixation point was increased to 3A where A is area of the steel plate used in the fixation solution [3]. Maximum values of temperature of every case of analysis are summarized in Table 1 (cases 3-0 to 3-4).

Table 3. Maximum temperatures in the bucket floor for different gap conductance coefficients for 1st, 2nd and 3rd parametric study.

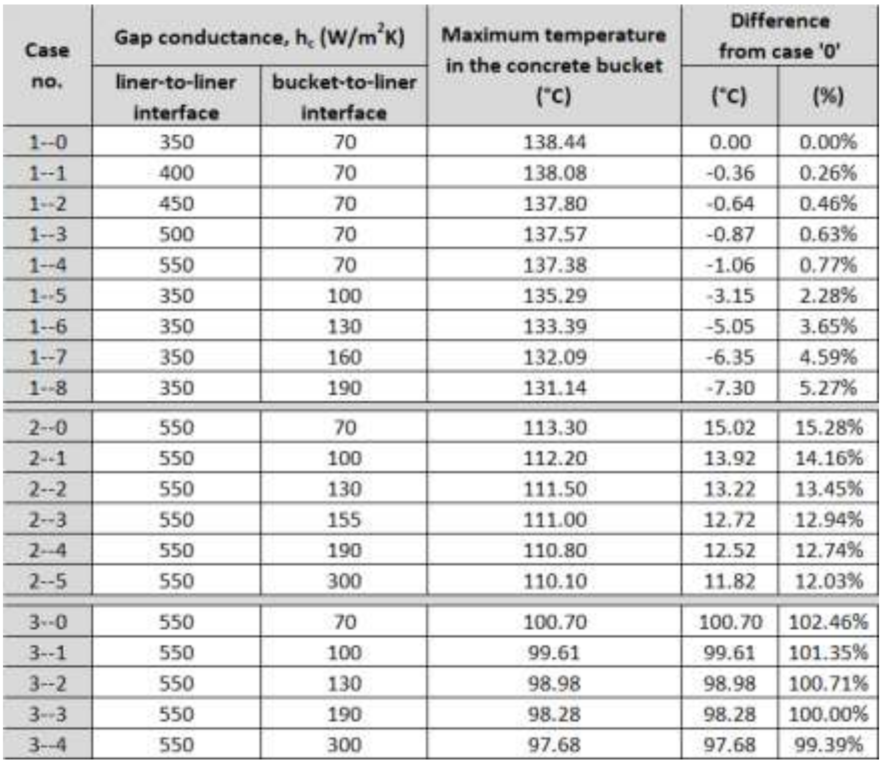

Case no.	Gap conductance, h_c (W/m^{2}K)		Maximum temperature in the concrete bucket (°C)	Difference from case '0'	
	liner-to-liner interface	bucket-to-liner interface		(°C)	(%)
1--0	350	70	138.44	0.00	0.00%
1--1	400	70	138.08	-0.36	0.26%
1--2	450	70	137.80	-0.64	0.46%
1--3	500	70	137.57	-0.87	0.63%
1--4	550	70	137.38	-1.06	0.77%
1--5	350	100	135.29	-3.15	2.28%
1--6	350	130	133.39	-5.05	3.65%
1--7	350	160	132.09	-6.35	4.59%
1--8	350	190	131.14	-7.30	5.27%
2--0	550	70	113.30	15.02	15.28%
2--1	550	100	112.20	13.92	14.16%
2--2	550	130	111.50	13.22	13.45%
2--3	550	155	111.00	12.72	12.94%
2--4	550	190	110.80	12.52	12.74%
2--5	550	300	110.10	11.82	12.03%
3--0	550	70	100.70	100.70	102.46%
3--1	550	100	99.61	99.61	101.35%
3--2	550	130	98.98	98.98	100.71%
3--3	550	190	98.28	98.28	100.00%
3--4	550	300	97.68	97.68	99.39%

In the second half of the year 2023, as the most recent nuclear heating data for 2-accelerator IFMIF-DONES condition became available (see [4]), heat transfer calculations were carried out for 2-accelerator case. A thicker bucket liner bottom plate (50 mm instead of originally designed 10 mm) was considered as an additional shielding for the concrete bucket floor. The nuclear heating data were provided for 50 mm thick bucket liner as well. Additionally, as a results of discussion and consultation with test systems coordinators of WPENS (Work Package Early Neutron Source), it had been decided that assumptions concerning the thermal contact between bucket, bucket liner and TC liner might have been assumed too conservatively before. Thus, in the calculation presented in this subsection, thermal contact assumptions were relaxed. The analysed cases are summarised in Table 2. Contour plots of temperature in the bucket for selected analysis cases are shown in Figure 1.

Table 4. Three cases analysed for the model with 50 mm thick bucket liner bottom plate.

No.	Thickness of bucket liner bottom plate	Bucket liner bottom plate FE type	Irradiation condition
1	50 mm	3D	1 accelerator
2	50 mm	3D	2 accelerators
3	10 mm	shell	1 accelerator

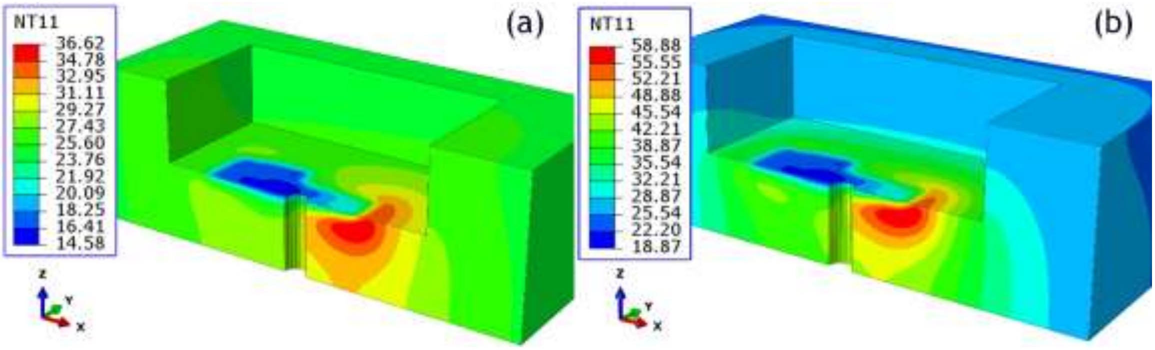

Figure 12. Contour plot of temperature in the bucket for 50 mm thick bucket liner bottom plate. Part of the model hidden for clarity. (a) 1-accelerator (case 1) and (b) 2-accelerator nuclear heating (case 2).

One of the activities carried out by WUT team was preliminary study using discrete element method for predicting temperature gradients in TC liner in the case of lithium spillage event. The results from subsequent stages of the simulation are presented in Figure 2 and Figure 3.

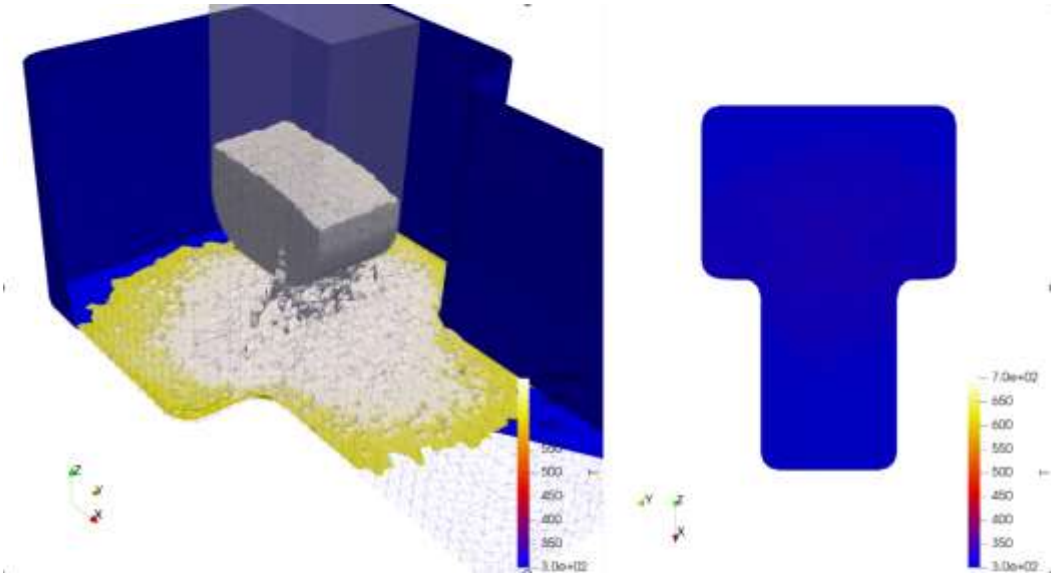

Figure 13. Temperature distribution about 5 seconds after liquid lithium release.

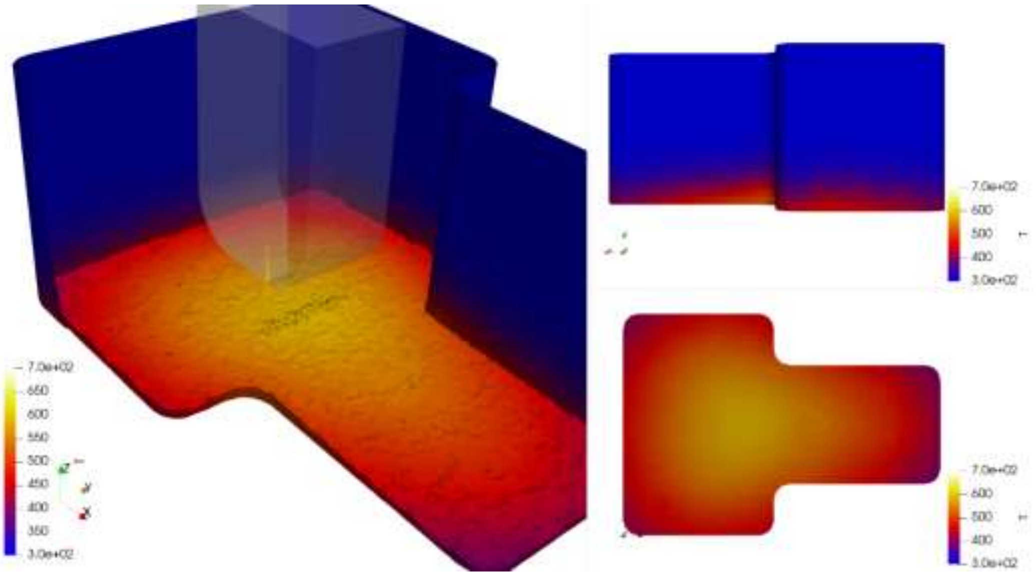

Figure 14. Temperature distribution 1 hour after liquid lithium release.

The numerical analysis prediction of steady-state temperature in the bucket floor depends on the gap conductance coefficient assumed for steel-to-concrete interfaces of thermal contact. An experiment is needed to confirmed thermal conductivity of such connection and verify gap conductance. In order to design the experiment well, first some numerical predictions were made. The following 4 possible types of the experiment were proposed:

- Type 1: concrete cube and steel rod. Size: 30 x 30 x 15 cm.
- Type 2: steel box filled with concrete. Size: 30 x 30 x 15 cm.
- Type 3: steel box filled with concrete. Size: 60 x 60 x 30 cm.
- Type 4: layered box composed of concrete and steel plates. Size: 60 x 60 x 30 cm.

Experimental setup type 4 gave most promising results. The temperature vs time curves are different for different gap conductance coefficients, and it can be easily noticed that the temperature rise is faster for higher values of gap conductance. Figure 4 shows temperature change in point E located in the lower-middle part of the layered concrete-steel box during the analysis. At the interface between steel plates and concrete, different gap conductance values ranging from 100 to 1000 W/m2K as well as perfect conductivity condition were assumed.

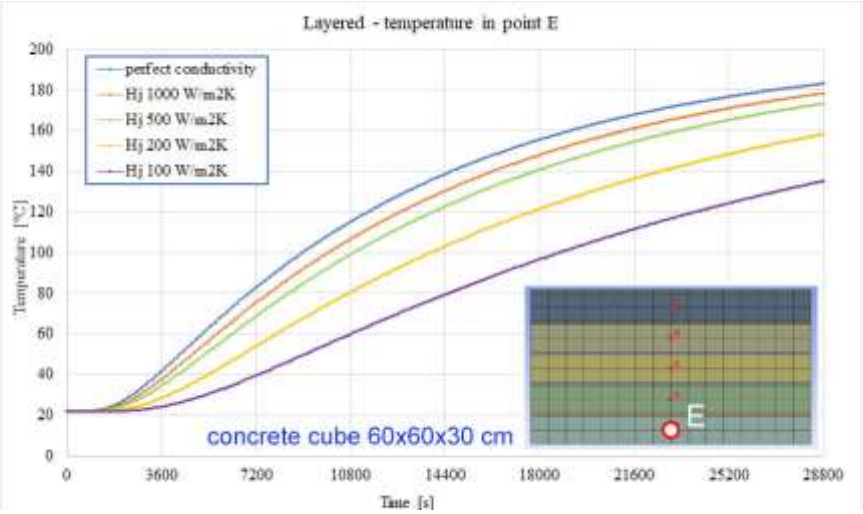

Figure 15. Temperature change as a function of time in point E for different gap conductance at concrete-steel interface for experiment type 4.

Conclusions

The following conclusions can be drawn based on parametric study results:

- Increasing steel-to-steel gap conductance has very little effect on maximum temperature in concrete.
- Large contact area between the Bucket Liner Floor and the Bucket Concrete has positive impact, even if conductance is small.
- Additionally increasing contact area between liners improves cooling even more.

The following conclusions can be formulated based on the heat transfer calculations for 2-accelerator conditions for 50 mm thick bucket liner bottom plate:

- Assuming small values of heat conductance but on the whole surface of contact between elements significantly lowers the maximum temperature in the bucket floor.
- Appropriate engineering solution must be chosen to provide heat transfer through the whole surface of contact.
- Increasing bucket liner bottom plate thickness does not provide better shielding for the bucket floor.
- Maximum temperature in the bucket floor for the 2-accelerator condition is in the safe zone, as long as the heat contact conditions assumed in the FEM model are true.

The following conclusions can be formulated based on the preliminary liquid lithium spillage simulation:

- The results of preliminary simulations show that it is feasible to model lithium spillage and it results in uneven temperature distribution in the TC liner.
- Lithium properties cannot be adopted directly from tables (literature) in DEM analysis (although the parameters can be calibrated based on the values from literature with a separate DEM simulation).
- The geometry of the model was simplified. Hence, it requires analysis whether the geometry of the model should be represented more realistically.
- More detailed assumptions still need to be determined (lithium volume, cooling system efficiency, initial temperature of the lithium and structural elements).
- There is no data available from experiments measuring lithium consistency.
- It is to be determined what spillage scenarios should be modelled.

The following conclusions can be formulated based on numerical analysis study for the design of experiment determining thermal conductivity between concrete and steel:

- In experiment type 1, featuring a concrete cube with an embedded rod, the temperature demonstrates minimal variation across different conductivities. This may present a challenge to accurately measure in practical settings.
- Experiment types 2 and 3 show improvement, yet the temperature variation remains marginal. Notably, the scale (considering both the size of the cube and time) impacts the results.
- Experiment type 4, with its layered concrete-steel design, appears to be the most effective, as it leverages a substantial contact area between concrete and steel, allowing for a more discernible assessment of conductivity variations.
- Careful design is crucial for the experiment, as detecting the slight variations in thermal conductivity between the settings poses a significant measurement challenge.

References

[1] Rafał Michalczyk, Kazimierz Józefiak, „2022 WUT Contribution to the Engineering Design of the Biological Shielding of the Test Cell”, Technical note EFDA_D_2PG4JB v1.1, Eurofusion IDM, 2022.

[2] Rafał Michalczyk, Kazimierz Józefiak, Łukasz Ciupiński, „2021 WUT Contribution to the Engineering Design of the Biological Shielding of the Test Cell”, Technical note EFDA_D_2PDKW5 v1.1, Eurofusion IDM, 2021.

[3] D. Kovács, B. Dombai, S.R. Simon, V. Viktor, T. Dézsi, “C3D contribution to the design of the Test Cell and HFTM”, Presentation EFDA_D_2Q6GHS, Eurofusion IDM, 2022

[4] Arkady Serikov, Yuefeng Qiu, “ENS-2.2.1.2-T024-01 Neutronics model updates of the test system in 2023”, Presentation, Neutronics session of the #16 WPENS Technical Meeting, 2022

Evaluation and Optimization of Structural and Shielding Concrete for IFMIF-DONES

Author(s): Tomasz Piotrowski

Introduction

The objective of the work has been evaluation and optimization of structural and shielding concrete for IFMIF-DONES. This is a continuation and extension of activities from the 2022. The evaluation and optimization studies were conducted in the following areas:

- accurate measurement of the atomic composition of ordinary and heavy concrete samples,
- accurate estimation of the hydrogen content, which has a significant impact on neutron shielding characteristics, through available experimental infrastructure,
- simulations to optimize the gamma and neutron shielding efficiency by adjusting the concrete compositions,
- simulations and measurements of the structural and technological properties, and thermal properties for heat removal.

Results

Accurate measurement of the atomic composition of ordinary and heavy concrete samples

To conduct research on the atomic composition of ordinary and heavyweight concrete samples, XRD analysis was performed. Five samples with dimensions of 40x40x160 mm were submitted for analysis. The following sample designations were adopted: **B1A** and **B1B** – CEMENT-PASTE 29/06/23, **B2** – MC 12/07/23 CONCRETE, **B3** – OC 12/07/23 CONCRETE, **B4** – OC 10/07/23 MORTAR, **B5** – MC 04/07/23 MORTAR. Due to the visible difference in the appearance of the light-coloured outer layer and the dark core of sample B1, it was decided to analyse the outer layer and the core separately. During the XRD studies, samples were examined immediately after grinding and after annealing in a muffle furnace at temperatures of 400, 600, and 800°C. The heating program for annealing was as follows: Heating time to the desired temperature: 2 hours, annealing time: 8 hours, followed by cooling to room temperature.

The main phases for samples B1A and B1B, according to the reference diffraction patterns, are identified as $Ca(OH)_2$ and $CaCO_3$. For the initial samples B2 and B5 the main phases are magnetite, hematite, and quartz. Annealing at temperatures between 600-800°C causes the oxidation of Fe_3O_4 to Fe_2O_3, resulting in the presence of mainly hematite and quartz in samples B2 600, B5 600, B2 800, and B5 800. For the initial samples B3 and B4 the main phase is dolomite. At an annealing temperature of 800°C, diatomite undergoes decomposition primarily into CaO and MgO.

Accurate estimation of the hydrogen content

The hydrogen content analysis was performed using the LECO ONH 836 elemental analyzer. The highest hydrogen content was observed in samples B1A and B1B, measuring 2.32% and 2.37%, respectively. Among the materials containing dolomite (B3 and B4), a higher hydrogen content was found in material B4, with a hydrogen content of 0.498%. Within the materials containing magnetite (B2 and B5), material B5 exhibited a higher hydrogen content, measuring 0.322%. The next step involved conducting thermogravimetric analysis coupled with mass spectrometry. The study was performed twice for each sample in a ceramic crucible. The percentage hydrogen content in the analyzed samples was estimated based on the desorbed water from the sample.

Simulations to optimize the gamma and neutron shielding efficiency

In order to calculate the radiation shielding efficiency, a method based on macroscopic cross-sections for a different interaction. The critical aspect in assessing shielding efficiency lies in determining the atomic composition. In the case of concrete, it was hypothesized that only 20% of the cement mass consists of chemically bound water during cement hydration. Subsequently, weight fractions for specific elements within the concrete and the partial densities derived from the oxide composion of the constituents were computed.

Table 5. Weight fraction of concretes

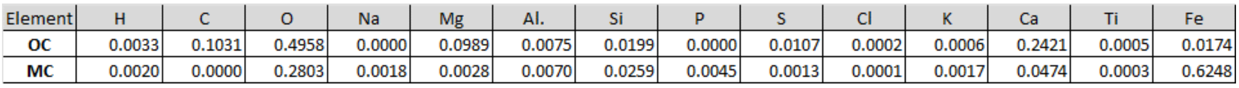

Element	H	C	O	Na	Mg	Al.	Si	P	S	Cl	K	Ca	Ti	Fe
OC	0.0033	0.1031	0.4958	0.0000	0.0989	0.0075	0.0199	0.0000	0.0107	0.0002	0.0006	0.2421	0.0005	0.0174
MC	0.0020	0.0000	0.2803	0.0018	0.0028	0.0070	0.0259	0.0045	0.0013	0.0001	0.0017	0.0474	0.0003	0.6248

The calculated radiation shielding efficiency indicates that OC is worse than MC from every point of view. MC has higher values of fast neutron effective cross-section by 22%, neutron scattering cross-section by 25%, thermal neutron absorption cross-section by 838% and total macroscopic neutron attenuation cross-section by 34%.

Simulations and measurements of the structural and technological properties, and thermal properties for heat removal

Density, compressive, flexural strength and indirect tensile strength for ordinary concrete (OC) and heavy concrete (HC) at 28, 40 and 90 days were conducted. Additionally, tensile strength and the corresponding modulus of elasticity for each type of concrete were investigated. The most remarkable fact is the higher tensile strength and lower E-modulus for the HC, compared to the OC. Subsequent studies focused on thermal properties determined using the hot disc method. In the case of cement paste B1, a thermal conductivity of 0.518 W/(mK) was achieved, while the other materials exhibit conductivity above 2.0 W/(mK). Cement paste B1 has the lowest specific heat. For the remaining composites, specific heat values are close, ranging from 1.95 to 1.99 × 10^6 J/(m^3K). The lowest thermal diffusivity value was recorded for cement paste B1, while concretes B2 and B3 obtained values of 1.083 and 1.062 × 10^{-6} m^2/s, respectively. Slightly higher thermal diffusivity was observed for mortars B4 and B5.

Conclusions

The investigation and design focused on two types of concrete: Ordinary Concrete (OC) and Magnetite Concrete (MC), intended for use in the IFMIF-DONES Test Cell structure. The structural OC, with a target density of 2.5 g/cm³, exhibits superior mechanical properties and radiation shielding, while MC excels in both density (3.9 g/cm³) and compressive strength (80 MPa, equivalent to OC). Neutron shielding efficiency is depending strongly on atomic composition and the biggest influence is due to aggregate type used. Neutron shielding efficiency comparison between the two concretes revealed that MC outperforms OC by approximately one-fourth when considering a wide energy range or only fast neutrons, and by more than 8 times when considering only thermal neutron absorption.

Collaboration

Universidad de Granada, Spain; *Karlsruhe Institute of Technology*, Germany; *Nuclear Physics Institute of the Czech Academy of Sciences*, Řež, Czech Republic; *United Kingdom Atomic Energy Authority, Culham Centre for Fusion Energy, Oxon*, United Kingdom.

References

[1] T. Piotrowski M.J. Martínez-Echevarría Romero, P. Prochoń et al. Optimization and evaluation of structural and shielding concrete for IFMIF-DONES, Nuclear Materials and Energy, 38, 101597 (2024) https://doi.org/10.1016/j.nme.2024.101597

Research Unit: Warsaw University of Technology

WPMAT: Materials

Title: Materials

Authors: Jan Wróbel, Małgorzata Lewandowska, Marta Ciemiorek, R. Molak, M. Wieczorek-Czarnocka, Agnieszka Krawczyńska, Michał Gloc, Łukasz Ciupiński

In the WPMAT project, the Warsaw University of Technology implemented four tasks in 2023:

- DFT modelling and the development of ML potentials for FeCrHe
- Development of 9-14 %Cr ODS for the fabrication of first wall components
- Contribution to the pilot-run. Investigation of the effect of the surface treatment on the tensile properties at RT
- Irradiation testing of mirrors: microscopy studies of surface

The summary report includes information about the most important results obtained within the framework of these tasks.

DFT modelling and the development of ML potentials for FeCrHe

Introduction

Fe-Cr forms the base alloy system for EUROFER steel used in fusion reactors. Neutron irradiation induces radiation defects and produces elements like He and H in Fe-Cr-based alloys. The presence of these radiation defects and impurities results in localised distortions within the crystal lattice, thus giving rise to long-range interactions between these defects. This information concerning the eigenstrains of radiation defects is crucial for the simulations using the finite element method for designing fusion reactor components.

One of the methods that enables to compute the eigenstrains of defects in an effective way is molecular dynamics (MD). However, the accuracy of predictions obtained using MD depends very much on the accuracy of the interatomic potentials. To the best of our knowledge, only one interatomic empirical potential exists for the Fe-Cr-He system [1], but it was not specifically designed to investigate the eigenstrains induced by He atoms and defects in Fe-Cr alloys. Consequently, there is a need to develop a suitable potential for the Fe-Cr-He system, which can be extended to larger systems as Fe-Cr-He-H or Fe-Cr-C-He.

Results

The interatomic potential for the Fe-Cr-He system has been developed by using a combination of density functional theory (DFT) calculations and machine learning (ML) methods [2][3]. Nearly one thousand DFT calculations have been conducted for representative structures of Fe-Cr alloys with He for various alloy compositions and different classes of calculations: structure optimisations, calculations with applied strains, with presence of point defects, as well as ab initio molecular dynamics simulations, both for bcc and liquid phases. Different ML approaches, namely linear ML, quadratic noise ML and kernel models, and various types of atomic descriptors, have been tested in order to achieve a good balance between accuracy, speed and predictive power. The optimal machine learning potential (MLP) has been achieved with a linear ML approach featuring hybrid descriptors comprising 451 parameters. This setup incorporated fast pairwise descriptors for radial atomic environment representation and bispectrum SO(4) descriptors based on hyperspherical function. The root-mean-square errors between the energies, forces and stresses computed using DFT and the best MLP equal 2.5 meV/atom, 125 meV/Å and 8 meV/Å3, respectively. The errors between the formation energies of vacancies and He atoms in Fe-5%Cr and Fe-10%Cr alloys computed using MLP and DFT are below 2%. The agreement between MLP and DFT was less satisfactory for predicting relaxation volumes of point defects, and the improvement of this agreement will be one of the main objectives for the upcoming year. Molecular dynamics simulations using MLP were applied to compute the formation energies and relaxation volumes of vacancies and He atoms in Fe-5%Cr and Fe-10%Cr alloys for a larger number of structures. The results obtained using MLP show the decrease of relaxation volumes of He atoms and vacancies and the decrease of formation energies of vacancies with an increase of Cr content in the alloy.

Conclusions

Overall, the results obtained using MLP for the Fe-Cr-He system are promising and reasonable. The current version of MLP can serve as the basis for further improvements

Collaboration

A. Goryaeva (CEA), D. Nguyen-Manh (UKAEA), M.-C. Marinica (CEA)

References

[1] A. Caro, J. Hetherly, A. Stukowski, M. Caro, E. Martinez, S. Srivilliputhur, et al., Properties of Helium bubbles in Fe and FeCr alloys, J. Nucl. Mater. 418 (2011) 261–268.

[2] A.M. Goryaeva, J.B. Maillet, M.C. Marinica, Towards better efficiency of interatomic linear machine learning potentials, Comput. Mater. Sci. 166 (2019) 200–209.

Development of 9-14 %Cr ODS for the fabrication of first wall components

Executive summary

In this work fracture surfaces of impact toughness specimens of 5 various 9-14Cr ODS alloys were characterized. From each alloy, 4 specimens subjected to an impact toughness test at a temperature range from -75.3°C to 150.1°C were selected for fracture surface examinations using SEM and stereoscopic microscopy. Surface topography in macro- and microscale was investigated and typical features of ductile, brittle or mixed fracture modes were described for each sample. Additionally, an EDS analysis of the particles found on the fracture surface was conducted. It was concluded that most of the fracture surfaces were mixed type, characterized by features typical for ductile and brittle modes. In some specimens, particles were observed, that acted as void nucleation sites, which were identified as oxides. Fully ductile fracture surfaces were observed for specimens tested at temperatures exceeding 100°C, except for the sample containing 14% of Cr, which at 125°C featured mixed fracture mode, as regions of cleavage and microvoids coalescence were observed. The results are summarized in Table 1.

Tab. 2. List of samples designations, testing temperatures, fracture mode and occurrence of features typical for fracture modes

			Cleavage	Craks	Microvoids coalescence	Particles as void-nucleation sites
N37-M6-9	-50.5	mixed	+		+	+
N37-M6-4	-25.5	mixed	+	+	+	+
N37-M6-7	-0.6	mixed	+	+	+	+
N37-M6-10	100.1	ductile			+	+
H29-03	-75.3	brittle	+	+		
H29-02	-24.8	brittle	+	+		
H29-09	24.1	mixed	+		+	
H29-06	150	no sample	no sample	no sample	no sample	no sample
H30-01	-25	mixed	+		+	

H30-04	27.7	mixed	+		+	+
H30-07	74.5	mixed	+	+	+	
H30-06	150.1	ductile			+	+
H31-11	-25.1	mixed	+	+	+	
H31-08	-0.2	mixed	+		+	
H31-12	24.5	mixed	+		+	
H31-06	100	ductile			+	+
H32-09	-25.5	mixed	+	+	+	
H32-08	25.2	mixed	+		+	
H32-07	49.8	mixed	+		+	
H32-01	149.8	ductile			+	
H33-07	-25.4	mixed	+	+	+	
H33-06	24.3	mixed	+		+	
H33-09	49.8	mixed	+		+	
H33-11	124.6	mixed	+		+	

Collaboration:

CEA Saclay, France

Related 2023 articles and conference presentations:

1. 21st International Conference on Fusion Reactor Materials, Grenada, Hiszpania – poster presentation “Characterisation of new 9-14 %Cr ODS RAF(M) steels for advanced fusion reactors”, authors: V. de Castro, T. Leguey, M. Lewandowska, M. Ciemiorek, J. Henry, Y. de Carlan

Contribution to the pilot-run. Investigation of the effect of the surface treatment on the tensile properties at RT

Introduction

Within the framework of the first part of this task, activities were planned to analyze the effect of specimen machining, i.e. the roughness resulting from WEDM processing parameters, on mechanical testing, particularly the mechanical parameters determined in static tensile testing. The second part of the ongoing task consisted of conducting static tensile tests for three specimen geometries defined by the consortium leader. The specimens were made of Eurofer97 steel, which the leader supplied. The tests were conducted as part of so-called inter-laboratory tests.

Results

In 2023, an experimental analysis of the effect of surface preparation on the mechanical properties of P92 steel was carried out. For this purpose, a static tensile test was carried out on miniature specimens whose surface was prepared differently. The differentiating factor here was the final surface roughness resulting from the WEDM machining parameters used. The static tensile test of the miniature specimens was then carried out with simultaneous characterization of their surfaces defined by the machining parameters. For the first part of the task, P92 steel, previously heat-treated to homogenize the microstructure and reduce internal stresses, was used. Then, 4 different test surfaces resulting from different parameters of WEDM machining of specimens were defined. The different surfaces were analyzed qualitatively (SEM observations, 2D and 3D surface maps) and quantitatively (optical profilometer – see Table 1). The analysis indicated that the machining process, regardless of the WEDM parameters used (E2, E7, E10 and E11), produces a homogeneous surface with a development consistent with the model data (data provided by the WEDM manufacturer) and the processing itself is a stable and repeatable process.

TAB.1. Roughness parameters as a function of WEDM machining

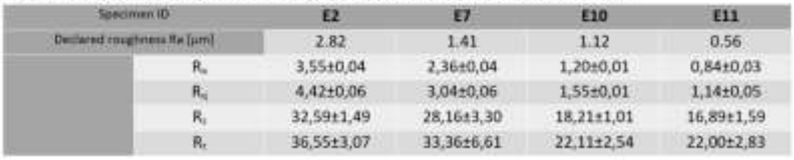

Specimen ID		E2	E7	E10	E11
Declared roughness Ra [µm]		2.82	1.41	1.12	0.56
	R_a	3,55±0,04	2,36±0,04	1,20±0,01	0,84±0,03
	R_q	4,42±0,06	3,04±0,06	1,55±0,01	1,14±0,05
	R_z	32,59±1,49	28,16±3,30	18,21±1,01	16,89±1,59
	R_t	36,55±3,07	33,36±6,61	22,11±2,54	22,00±2,83

Based on the results, it can be concluded that in the case of both yield points (R_{EL} and R_{EH}) and ultimate tensile strength (R_m) there is a slight increase in parameters with a decrease in roughness. Only for the sample marked E7, there is a slight decrease in mechanical properties, bringing it closer to the initial sample marked E2. On the other hand, it can be concluded that a decrease in the roughness of the miniature samples results in an increase in their elongation to rupture (A)

– see Table 2.

TAB.2. Mechanical properties determined with the use of miniature specimens as a function of WEDM machining

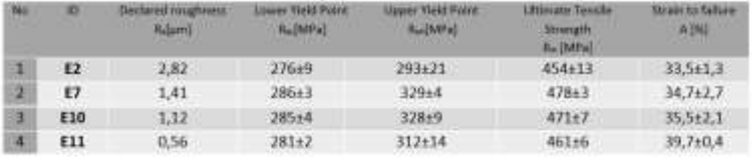

No	ID	Declared roughness R_a[µm]	Lower Yield Point R_{eL}[MPa]	Upper Yield Point R_{eH}[MPa]	Ultimate Tensile Strength R_m [MPa]	Strain to failure A [%]
1	**E2**	2,82	276±9	293±21	454±13	33,5±1,3
2	**E7**	1,41	286±3	329±4	478±3	34,7±2,7
3	**E10**	1,12	285±4	328±9	471±7	35,5±2,1
4	**E11**	0,56	281±2	312±14	461±6	39,7±0,4

During the execution of this part of the task (inter-laboratory studies), the surface roughness of three specimen geometries was analyzed first. For one of the geometries, a lower roughness was obtained due to different machining methods for flat and cylindrical specimens (milling vs. WEDM). A static tensile test was then carried out.

Based on the results, it was found that the most pronounced effect of specimen geometry was found for the ultimate tensile strength R_m. This parameter reached a significantly higher value for SS-J3 specimens than EUflat and SCK-CEN specimens – see Table 3.

TAB.3. Pilot Run results

No	ID	Yield strength $R_{0,2}$[MPa]	Ultimate Tensile Test R_m [MPa]	Elongation to failure A[%]
1	EuFlat	567±10	674±9	23,0±1,56
2	SCK-CEN cylindrical	526±17	661±8	27,4±2,1
3	SS-J3 flat	550 ±19	739±1	23,3±0,8

Conclusions

- WEDM machining parameter slightly affects the mechanical properties determined with the use of miniature specimens (R_{EL}; R_{EH}; R_{EH}; and A);
- the specimen geometry of the miniature specimens affects the determined mechanical properties.

Collaboration

The whole consortium engaged in the Task participated in the inter-laboratory tests.

Irradiation testing of mirrors: microscopy studies of surface

Introduction

Scanning and transmission electron microscopy investigations were carried out in different mirrors as irradiated by the VR group. The nature of ion-induced damage was determined, and the defects have been characterized and quantified with the reference to Mo poly-crystals.

Results

First experiment: The verification of the threshold dose when helium bubbles start to appear in TEM images when using STEM Spectra 200 Thermo Fisher Scientific. **Second experiment:** The verification of bubble creation in polycrystalline (PC) and single crystal (SC) Mo mirror samples irradiated with He implantation condition (**Fig.1**).

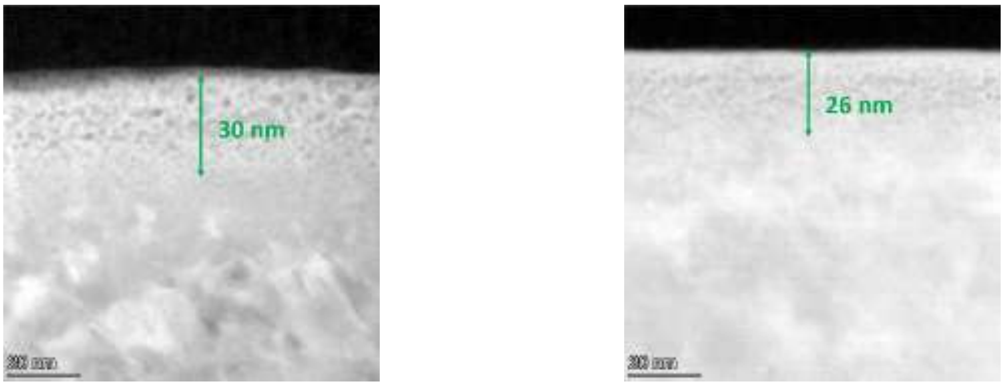

Fig. 1 Cross sections of Mo mirrors a) II SC,b) PC; – HAADF-STEM mode

Conclusions

1. No He bubbles were created in the sample irradiated with 30keV Mo $1.5x10^{15}$ and 2keV He $1x10^{16}$ cm^{-2}. Therefore, it can be stated that the dose of $1x10^{16}$ cm^{-2} He is too low to induce bubble formation that can be imaged under TEM. In the sample irradiated with 2keV He $8x10^{16}$ cm^{-2}, bubbles up to 22 nm beneath the sample surface were observed of roughly 1.5 nm in diameter. They are still present in the sample after 5 years of irradiation.

2. Slightly bigger bubbles were noticed in the SC sample than in the PC sample after irradiation with either 2keV He $5x10^{16}$ cm^{-2} or 2keV He $1.2x10^{17}$ cm^{-2}.

Collaboration

Department of Fusion Plasma Physics, KTH Royal Institute of Technology, 100 44 Stockholm, Sweden

Related 2023 articles and conference presentations:

1. Dittrich L, Petersson P, Laabadi H, Pitthan E, Rubel M, Widdowson A, Krawczyńska A, Szlązak K, Ciupiński Ł. Impact of ion irradiation and film deposition on optical and fuel retention properties of Mo polycrystalline and single crystal mirrors. Nuclear Materials and Energy. 2023;37:1–10. doi:10.1016/j.nme.2023.101548

Research Unit: Warsaw University of Technology

WPTE: Tokamak exploitation

Title: Tokamak exploitation

Author: Andrzej Wojeński

Introduction

The work concerned developing and using a soft X-ray detection system (SXR) based on GEM (Gas Electron Multiplier) detector technology for tomographic monitoring of tungsten transport. GEM detectors are used for radiation imaging, combined with FPGAs allows to analyze signals from individual photons, making this project a novel and innovative endeavor. Attention is being paid to tungsten because this material has become a prime candidate for the plasma-interacting wall material in the ITER reactor and future fusion reactors. Measuring soft X-rays in the range of 0.1 – 20 keV from magnetically held plasmas is a standard way to provide important information on dopant transport and magnetic configuration. We refer to the development of a system based on GEM detectors to conduct tomographic research focused on the emission of tungsten radiation from plasma for future ITER-like machines - e.g., the WEST project.

The main goal of the task in 2023 (WP-TE) was to validate, maintain/support and analyze results of the SXR GEM measurement system during the experimental campaign in CEA WEST tokamak (France). The necessary work was carried out locally both at the Warsaw University of Technology (Poland) and during the experimental campaign stay at the - WEST CEA Cadarache research center in France.

Results

A brief summary of the undertaken actions and results of the carried out work during the 2023 year:

- Analyzing the operation of the GEM-FPGA measurement system during the experimental campaign on the WEST tokamak and integration with the infrastructure. As a result the system was integrated in cooperation with the CEA IRFM WEST team. The system operated in both manual and automatic mode, performing subsequent measurement series during the experimental campaign.
- Validation of the data quality and the results obtained was carried out. In particular, the obtained energy spectra of soft radiation were analyzed. Based on the results, a new version of the data acquisition algorithm was implemented, it is now used for continuous high-performance data acquisition.
- Maintenance of the measurement system in the tokamak environment. One of the results is the development of additional software for rapid data conversion for postprocessing by specialized physical algorithms. The work also includes the process of integrating IT tools with the tokamak infrastructure.
- The work performed was also a result of scientific cooperation between the team from Warsaw University of Technology (WUT, Poland), CEA Cadarache IRFM WEST (France) and Institute of Plasma Physics and Laser Microfusion (IPPLM, Poland).

An exemplary specific actions were needed to be carried out in order to achieve the results:

- Maintenance work on the GEM-SXR-FPGA measurement system on the WEST tokamak – continuation of the preparation of the system to work during experimental campaign
- Analysis of the measurement system operation and data validation
- Implementation of the automatic system operation scheme with CEA WESTBOX software
- Analysis of the operation of the GEM-SXR-FPGA measurement system during the experimental campaign including:
  - Analysis of the operation of the GEM-SXR-FPGA measurement system in the reference FPGA global acquisition mode
  - Analysis and validation of the operation of the GEM-SXR-FPGA measurement system in the optimized FPGA serial acquisition mode

- Calibration of the GEM-SXR-FPGA measurement system

An examples of results from carried out actions are presented in this section. The following example plot (Fig.1, Fig. 3) present the acquired data during the spring 2023 experimental campaign at WEST tokamak. The registered spectra of energy, topology and time traces is the result of the carrier out above actions making system properly designed, configured, optimized and integrated, to register data from the GEM detector during plasma experiments. This is the most important result.

Very long pulses were recorded using the newly introduced firmware for FPGAs – including acquisition of the peak plasma duration times in 2023 at the WEST tokamak. The important achievement of the implementation was the registration of long plasma pulses (~60 seconds and more) in raw data mode. The ability to acquire analog traces of signals is a unique feature of the designed system. As presented in figure 1, pulse number 58328 was recorded by FPGAs in serial acquisition mode during an experimental campaign on the WEST tokamak introduced as one of the results from the 2023 task.

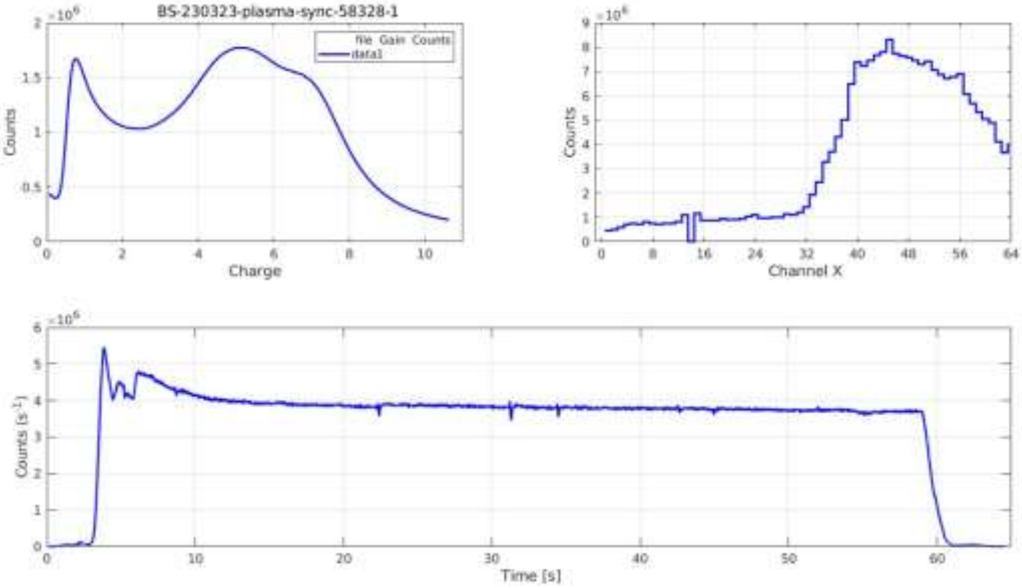

Fig. 1 Pulse 28328 registered during the 2023 spring experimental campaign at WEST tokamak. The system can register very long pulses in raw data mode, a unique world-scale feature of the designed diagnostic system.

Another example result from the performed tasks is high voltage scanning of the detector. The series of long data registrations were run to properly select the optimal conditions for the GEM detector in terms of gain and energy scale for further data (plasma) registration. An example scan of the voltages using the newly introduced firmware for FPGA is presented in Figure 2.

Conclusions

The GEM-SXR-FPGA diagnostic system was properly prepared during the task and took part in the international spring measurement campaign on the WEST tokamak. It was also pre-integrated with the WEST tokamak infrastructure, which enabled the automatic triggering of measurements throughout the day and their recording in the appropriate format on the server storing experimental data. Based on technical analyses, necessary corrections were made to the FPGA and embedded software.

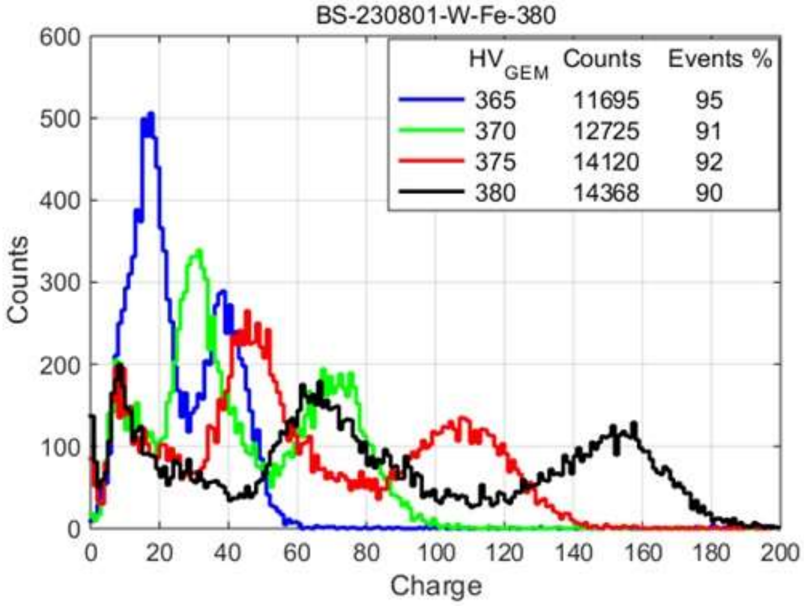

Fig. 2 Calibration of the GEM detector using high voltage modifications. As a reference radiation source, the Fe^{55} *isotope was used.*

The current version of the system has unique properties - the ability to perform very long measurements (over a minute) and record signal waveforms of each event. An example of a comparison of the system with other diagnostics is shown in Fig. 3. The data obtained is used and further analyzed by the cooperating institutions, IPPLM and IRFM CEA Cadarache, in order to compare the results with other measurement systems and validate them against the physical phenomena.

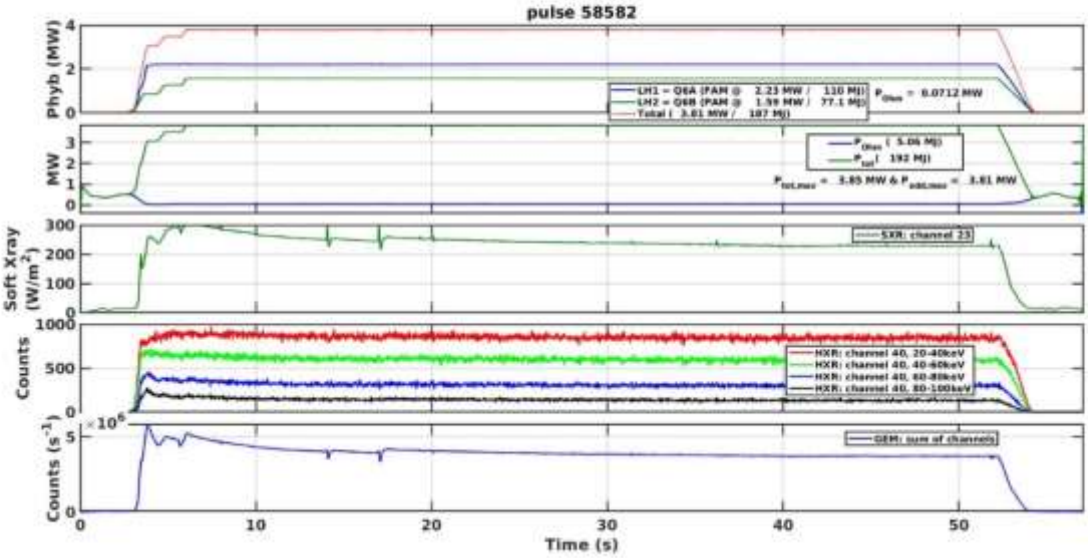

Fig. 3 Comparison of results between GEM FPGA SXR system and other diagnostics working on WEST tokamak during the plasma reaction number 58582 at WEST CEA Cadarache tokamak

The work carried out concerned supporting development and validation of a soft radiation measurement system based on GEM detectors to study tungsten transport during a thermonuclear reaction in ITER-oriented tokamaks - project WEST (CEA Cadarache). The measurement of tungsten is because this material has become the leading candidate for the material of the first wall interacting with the plasma in the ITER reactor and future fusion reactors. Soft X-ray (SXR) measurement from plasma in the 0.1-20 keV range by the GEM detector provides information on particle transport and magnetic configuration. The diagnostic system is a highly technologically advanced structure. In particular, it is worth emphasizing the unique mode of determining the exact energy of single photons based on signal data (raw data) from the GEM detector and then constructing appropriate spectra (energy and topology) with configurable time resolution by an embedded computer. The introduced solutions make the diagnostic system highly competitive (in scope of features and costs) compared to other designs, e.g., specialized ASIC systems. Working with signal data allows to perform advanced computational analysis and ensure high-quality results, that is especially important when performing measurements in a tokamak environment. In 2023, work was carried out on the analysis, validation, and maintenance of the measurement system, particularly in ensuring the highest possible data quality. During the international experimental campaign, long plasma reaction times were obtained (approx. 60-100 seconds) and recorded by the developed system. Thus, the system shows potential for use in complex projects, like the ITER project. The implemented new serial acquisition mode ensures optimal registration of measurement data and the possibility of measuring from many channels simultaneously.

Collaboration

- Commissariat à l'énergie atomique et aux énergies alternatives (CEA) Cadarache IRFM, France
- Institute of Plasma Physics and Laser Microfusion, Poland

References

[1] Paper: Kolasiński P, Poźniak KT, Wojeński A, Linczuk P, Kasprowicz G, Chernyshova M, Mazon D, Czarski T, Colnel J, Malinowski K, et al. High-Performance FPGA Streaming Data Concentrator for GEM Electronic Measurement System for WEST Tokamak. Electronics. 2023; 12(17):3649. https://doi.org/10.3390/electronics12173649

[2] Poster presentation: „Measuring X-ray and neutron spectra with gas detectors, from models to measurements.": Mazon D., Jardin A., Wojenski A., Peysson Y., Scholz M., et al.. Conference: EPS 2023 - 49th European Conference on Plasma Physics, Jul 2023, Bordeaux, France; https://eps2023.github.io/

[3] Presentation: "Overview of GEM Diagnostic activities during WEST C7 Campaign: measurements and validation", speaker: Didier Mazon in the framework of collaboration WUT - Andrzej Wojeński, Grzegorz Kasprowicz, Krzysztof Poźniak, Paweł Linczuk, Piotr Kolasiński; IPPLM - Maryna Chernyshova, Karol Malinowski, Tomasz Czarski, Ewa Kowalska-Strzęciwilk, Sławomir Jabłoński, Michał Jagielski; IRFM CEA - Julian Colnel, Denis Guibert; IFJ PAN – Axel Jardin; meeting of group Task Force Leaders in CEA Cadarache IRFM – tokamak WEST

UO: Opole University

WPW7X: W7-X Exploitation

Title: Development and exploitation of the diagnostic system “C/O monitor for W7X”

Authors: I. Książek and UO team

Introduction

The "C/O monitor for W7-X" is a spectrometer designed to monitor the intensity of the Lyman-α line emitted by hydrogen-like ions of light impurities (namely B, C, N, and O) in W7-X plasmas. Each spectral line is measured by an independent detection channel which includes a dispersive element, an optical system, and a detector. The spectrometer is divided into two subsystems, each containing two channels enclosed in a common vacuum chamber. Each sub-spectrometer has its own vacuum system and gate valve that opens to the plasma vessel. Because of the specific construction of the system, the final adjustments were possible only using the radiation of the plasma produced in W7-X. Final tuning and adjustments require a widespread source of XUV radiation. Because such laboratory sources do not exist the above-mentioned activities had to be realised in the initial phase of operation. The appropriate procedures were performed during the OP 2.1 campaign. After the adjustments the temporal variations of the carbon and oxygen lines were regularly registered.

Results

The first recorded signals allowed for the study and analysis of registered spectra. One of the initial steps was to determine the optimal settings of the detector, such as the mode of operation (burst mode was selected), the number of rows for binning (16 rows), and other relevant parameters. Additionally, it was essential to establish a connection with the external triggering system (ITTE module) and define its parameters. The camera setting provided a time resolution of up to 1 ms, but the timeframes needed to be separated by 5 ms. The position of the dispersive elements was initially set in the laboratory based on the calculated angle. The rotational piezodrive was fixed in such a way that the working position ought to be near the zero position of the drive. The detector registers only part of the line profile, and appropriate adjustment allows to observe the top of the line and part of its wings. The fine adjustment allowed to define the most appropriate angle associated with the central wavelength (Fig.1).

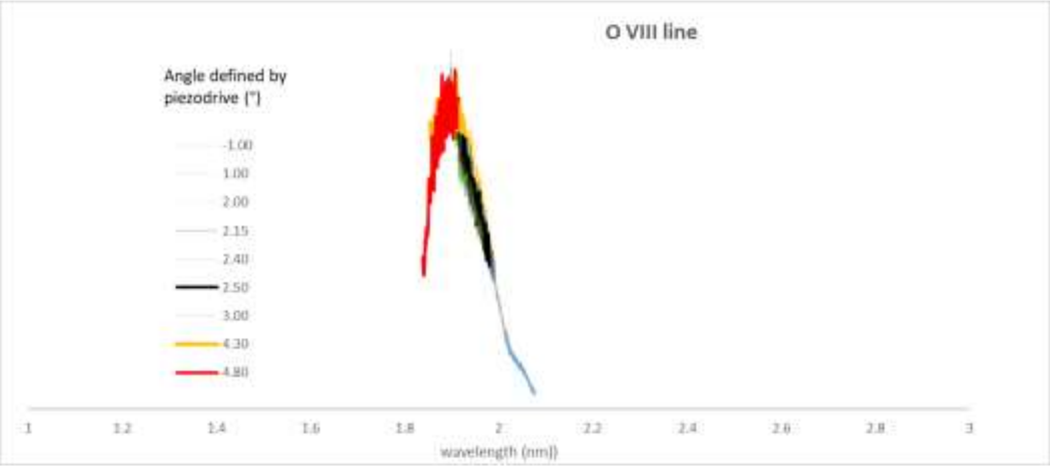

Fig. 1 Example of the spectra registered by different settings of the rotational piezodrive (the intensities were adjusted to reconstruct the spectral line profile).

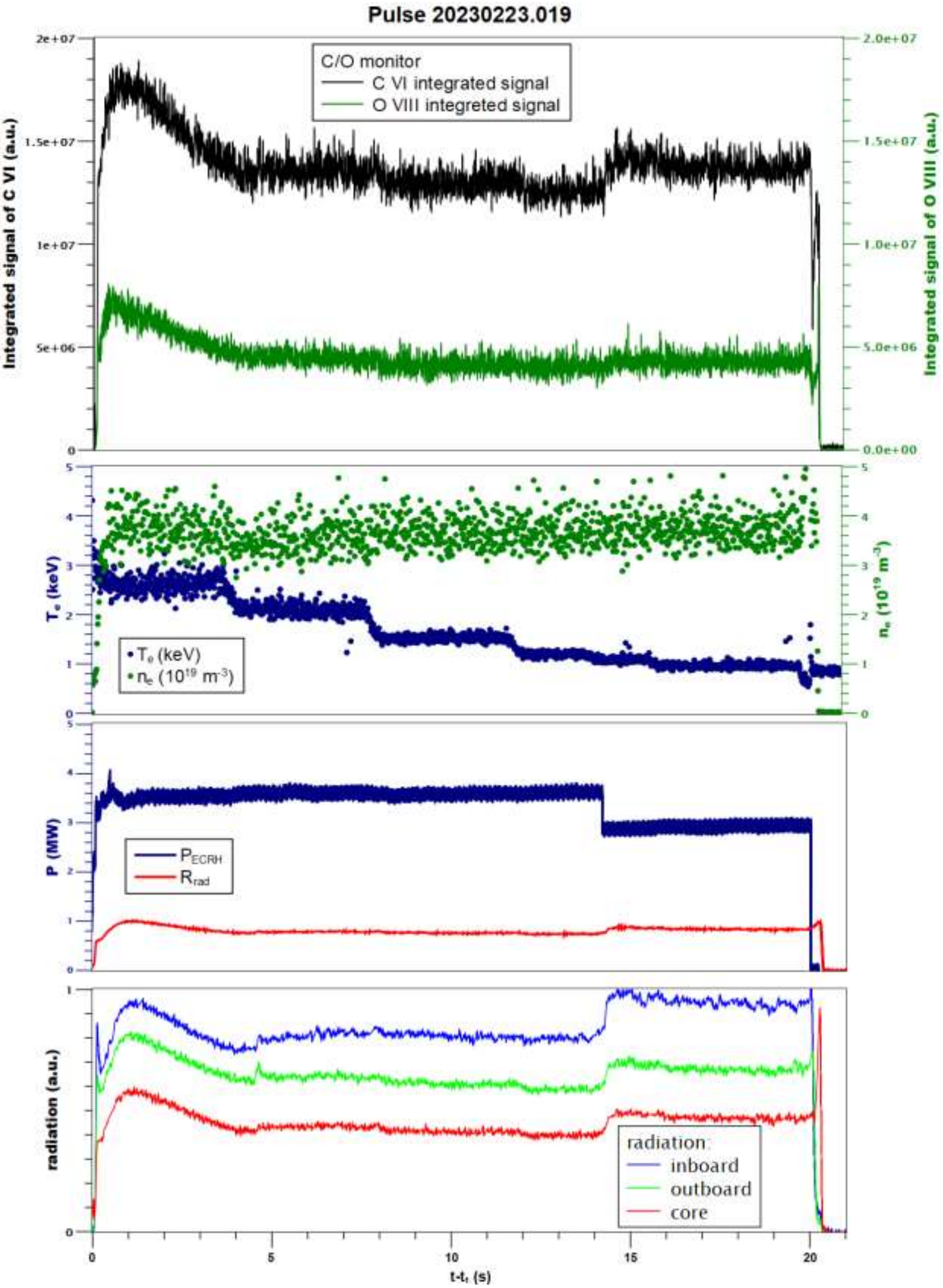

Fig. 2 Example of the time traces of carbon and oxygen spectral lines together with the averaged parameters of the discharge.

After the adjustments, the spectrometer data were locally stored. A computer code has been developed to read and analyze the binary data stored in the files generated by the detector. In order to determine the line intensity, it has been decided to subtract the background, defined by a given set of points, and integrate the curve using the Simpson method. It is important to note that this procedure does not produce the full intensity of the spectral line, but rather a value that is proportional to it (provided that the apparatus function determines the shape of the line); this value can be considered representative of the line intensity. However, during the calibration process, it is necessary to take into account that the experimental value represents only a fraction of the actual intensity of the spectral line (but this fraction is a constant value).

The temporal changes of integrated value described above are regarded as time-trace of the intensity of a given spectral line.

The code has been further developed to allow the definition of absolute and relative timescales for plasma. The data is now being prepared to be stored in the W7-X database. The structure of the data to be published in this database has also been defined. The time-traces registered in experiments of the campaign OP2.1 are in agreement with the modelling predictions which suggest that the signal produced by the system is weakly sensitive to changes of the temperature and almost linearly proportional to the plasma density.

The spectral line C VI 3.4 nm is registered also by the HEXOS spectrometer. The results produced by the C/O monitor system reveal similar shape of the time-trace curve but with much better signal to noise ratio.

Conclusions

The "C/O monitor for W7-X" system has been successfully commissioned based on the results obtained during the initial phase of operation in the experimental campaign OP2.1 of Wendelstein 7-X. After the initial fine-tuning and adjustments, the spectrometer has consistently registered signals associated with the spectral lines of hydrogen-like carbon and oxygen.

Even in the initial qualitative analysis, it is clear that the constructed diagnostic system has potential usefulness. The system can provide valuable information about changes in the level of light impurities, which are typically introduced to the plasma by the interaction of the plasma and its radiation with the first wall of the plasma vessel. When compared to signals from the high-resolution spectrometer HEXOS, the "C/O monitor for W7-X" system appears to provide data with a better signal-to-noise ratio and increased sensitivity to changes in the outer layers of the plasma. However, this is achieved at a lower time, spatial, and spectral resolution. The data provided by this diagnostic system can make a significant contribution to the analysis of experiments conducted in the Wendelstein 7-X stellarator.

Collaboration

Institute of Plasma Physics and Laser Microfusion, Warsaw, Poland

Max-Planck-Institut für Plasmaphysik, Greifswald, Germany

Related 2023 articles and conference presentations:

1. T. Fornal, M. Kubkowska, I. Ksiazek, B. Buttenschön, Investigation of oxygen signal level measured by the C/O monitor system from the W7-X plasmas, Plasma 2023 - International Conference on Research and Applications of Plasmas, 18-22 września 2023 (Warszawa, Polska) – poster

2. I. Książek, T. Fornal, B. Buttenschoen, M. Kubkowska, R. Burhenn, K. Książek and W7-X team, First results obtained by the ‘C/O Monitor’ system from the Wendelstein 7-X plasmas, Plasma 2023 - International Conference on Research and Applications of Plasmas, 18-22 września 2023 (Warszawa, Polska) – poster

Research Unit: University of Opole

Work Package: Tokamak Exploitation

Title: Spectroscopy of impurities in tokamak plasmas

Authors: Ewa Pawelec and OU team

Introduction

2023 was the fortieth and last year of the JET tokamak operation, so the main objective was the measurement of all the data which may have been needed to analyze and interpret all the findings during JET campaigns, with special stress on the D-T operation and relevant reference programs in deuterium. DTE3 campaign at the end of the year also was an attempt to fill any experimental gaps left from 2021 deuterium-tritium campaign, which also resulted in new fusion energy record [1]. Analysis of those data will be performed yet for several years. In the case of the part pertaining to tritium retention and tungsten surface results (RT-06 experiment), which is a part of the JET decommissioning program, the data will still be collected.

Results

Information of the impurity content and type was provided in real time during experimental sessions for experiments (within RT-01):

- the baseline and neon -seeded high power pulses in different isotopes (D/T/DT)
- the low v* hybrid and peeling-limited scenarios (D/T/DT)
- the L-H transition pulses (D/T/DT)

Analysis of the impurity content of the L-H database pulses in different isotopes was continued and refined, including new pulses and impurity transport scenarios which led to the improvement and enlargement to the existing database.

Tritium molecular spectra from detachment experiments were analyzed for rotational temperatures and intensities, and correlated with ion flux to the divertor. DT molecule spectra in similar experiment were measured and main Q branch peaks identified.

The molecular parameters of beryllium hydrides (BeH, BeD and BeT) were calculated from high-resolution spectral measurements and the results were correlated with first estimation of edge plasma parameters, using the beryllium line ratios.

The spectroscopic estimation of cleaning and gas exchange efficacy during the working gas change between different isotopes of hydrogen, or hydrogen to helium and back, was performed and analyzed for different vessel locations.

Conclusions

During this year most JET experiments were ongoing without any shutdown, so in-real-time participation was crucial. Much less time was devoted to in-depth after-experiment analysis, though much of deuterium-tritium data was preliminary analyzed and presented by the end of the year Fusion Energy Conference. Analysis of collected JET data under the ongoing WPTE collaboration are planned for 2024, 2025 and beyond, and the correlation between them and the data collected in other tokamaks will continue to be crucial for ongoing experiments and modelling.

Collaboration

Culham Centre for Fusion Energy, Culham, Great Britain

References

[1] https://euro-fusion.org/eurofusion-news/dte3record/

Related 2023 articles and conference presentations:

1. M. Groth et al (E. Pawelec): Characterisation of divertor detachment onset in JET-ILW hydrogen, deuterium, tritium and deuterium–tritium low-confinement mode plasmas, Nuclear Materials and Energy 34 101345 (2023) https://doi.org/10.1016/j.nme.2022.101345
2. G. Birkenmeier et al (E. Pawelec): The role of isotope mass and transport for H-mode access in tritium containing plasmas at JET with ITER-like wall, Plasma Phys. Control. Fusion 65 054001 (2023) https://doi.org/10.1088/1361-6587/acc423
3. Y. Kovtun et al (E. Pawelec): Comparison of ion cyclotron wall conditioning discharges in hydrogen and helium in JET, Nuclear Materials and Energy 37 101521 (2023) https://doi.org/10.1016/j.nme.2023.101521
4. E.R. Solano et al (E. Pawelec): L-H transition studies in tritium and deuterium–tritium campaigns at JET with Be wall and W divertor, Nucl. Fusion 63 112011 (2023) https://iopscience.iop.org/article/10.1088/1741-4326/acee12
5. D. Matveev et al (E. Pawelec): Tritium removal from JET-ILW after T and D–T experimental campaigns, Nucl. Fusion 63 112014 (2023) https://iopscience.iop.org/article/10.1088/1741-4326/acf0d4
6. E. Pawelec et al, Influence of impurity radiation loss on the L-H transition power threshold, 49th European Physical Society Conference on Plasma Physics, 3-7 July 2023 (Bordeaux, France)
7. F. Causa et al (E. Pawelec), Prompt effects of partially ionised W dust in the JET shallow SOL, 49th European Physical Society Conference on Plasma Physics, 3-7 July 2023 (Bordeaux, France)
8. E. Pawelec et al, Chemically assisted physical sputtering of beryllium – temperature and density dependence in different hydrogen isotopes, Plasma 2023 - International Conference on Research and Applications of Plasmas, 18-22 września 2023 (Warszawa, Poland)
9. E. Pawelec et al, Challenges in the analysis of the spectra of tritium-containing molecules, 2nd IAEA Technical Meeting on the Collisional-Radiative Properties of Tungsten and Hydrogen in Edge Plasma of Fusion Devices, 28 listopada-1 grudnia 2023 (Vienna, Austria) – invited talk
10. S. Brezinsek et al (E. Pawelec) The Competition Between W Nanostructure Formation And W Annealing, W Erosion And Low-Z Co-Deposition In The Divertor Of Metallic Fusion Devices, 29th IAEA Fusion Energy Conference, London, United Kingdom, 16th October 2023
11. C. Giroud et al (E. Pawelec) Similarities in integrating a neon-seeded radiative divertor in ELMy H-mode in JET-ILW Deuterium-Tritium and in Deuterium, 29th IAEA Fusion Energy Conference, London, United Kingdom, 16th October 2023
12. A. Chomiczewska et al (E. Pawelec) ICRH-Related Impurity Source And Control Across Experiments In H, D, T Plasmas At JET-ILW, 29th IAEA Fusion Energy Conference, London, United Kingdom, 16th October 2023
13. I. Borodkina et al (E. Pawelec) Modelling of plasma facing component erosion, impurity migration, dust transport and melting processes at JET-ILW, 29th IAEA Fusion Energy Conference, London, United Kingdom, 16th October 2023
14. G. Gervasini et al (E. Pawelec), Hydrogen isotopic ratio by Residual Gas Analysis during the JET DT campaigns, 29th IAEA Fusion Energy Conference, London, United Kingdom, 16th October 2023
15. E.R. Solano et al (E. Pawelec), L-H transition studies in recent Tritium and Deuterium-Tritium campaigns at JET, 29th IAEA Fusion Energy Conference, London, United Kingdom, 16th October 2023
16. D. Douai et al (E. Pawelec), Overview of Plasma-Wall Interactions studies in JET-ILW H, D, T and DT campaigns, 29th IAEA Fusion Energy Conference, London, United Kingdom, 16th October 2023
17. M. Groth et al (E. Pawelec), Impact of H, D, T and D-T hydrogenic isotopes on detachment in JET ITER-like Wall low-confinement mode plasmas, 29th IAEA Fusion Energy Conference, London, United Kingdom, 16th October 2023
18. T. Wauters et al (E. Pawelec), Changeover between helium and hydrogen fuelled plasmas in JET and WEST, 19th International Conference on Plasma-Facing Materials and Components for Fusion Applications (PFMC-19), Bonn, Germany, 22nd May 2023.
19. S. Brezinsek et al (E. Pawelec), Spectroscopic Studies of W Sputtering Processes in JET Helium Plasmas , 19th International Conference on Plasma-Facing Materials and Components for Fusion Applications (PFMC-19), Bonn, Germany, 22nd May 2023.

IFJ PAN: Institute for Nuclear Physics Polish Academy of Sciences

WPENR: Enabling Research

Title: Enabling Research: Development of GEM detector as a compact neutron spectrometer for fusion plasmas (NS-GEM) (ENR-TEC.01.IPPLM-T001)

Authors: M. Scholz, W. Dąbrowski, K. Drozdowicz, A. Jardin, A. Kulińska, A. Kurowski, B. Łach, D. Mazon, U. Wiącek, U. Woźnicka

Introduction

The goal of this project is to develop the concept of an innovative compact neutron spectrometer based on a gas electron multiplier detector (NS-GEM) that could be proposed for the ITER HRNS system. This project includes the construction of a laboratory demonstrator of NS-GEM and tests its experimental possibilities on 14 and 2.5 MeV neutron sources. The project consists of on the following three topics:

1. Theory and modelling: NS-GEM synthetic diagnostic: Assumptions and design requirements for ITER neutron spectrometers.
2. NS-GEM Demonstrator: Initial stage of MCNP NS-GEM system modelling and technical design.
3. Neutron generator IGN-14: MCNP modelling of the radiation field in the IGN-14 hall and the technical design of the measuring set-up.

The progress of works completed in 2023 is presented below.

Results

Based on the simulation results, the concept of the NS-GEM spectrometer was developed, and a detailed detector design was prepared, starting with a standard 3-stage GEM detector. A detector model for GEANT4 simulation was built and extensive Monte Carlo simulations with appropriately large statistics were performed. The simulation results allowed us to evaluate the energy resolution of our demonstration detector, considering the following issues:

- recoil proton generation efficiency,
- recoil proton scattering in the converter and detector,
- proton energy losses in the converter and detector.

By taking these effects into account, we can generate dE/dx calibration curves as a function of the initial energy of the recoil protons.

The simulation results clearly show that the converter thickness is a critical parameter affecting the neutron energy resolution. The thickness of the converter should be kept below 0.5 mm and preferably around 0.1 mm, although a thinner converter means lower recoil proton production efficiency. The expected neutron energy resolution is approximately 21% FWHM for the ArCO2 gas mixture at 1 atm and 15% FWHM at 2 atm. The dominant contribution to the uncertainty of the neutron energy estimate comes from the fluctuations in the proton energy losses dE/dx in the detector volume.

In parallel with modeling the detector response, work on the detector design was carried out. As proposed in the initial phase of the project, our demonstration detector is based on the standard 3-stage GEM detector, but with the thickness of the drift region increased to up to 10 mm compared to the standard thickness of 3 mm. This modification required the design and construction of a new detector frame and appropriate modification of the voltage divider to ensure the same electric field level in the drift area as in the standard design. In addition, the new frame includes an adapter containing a neutron converter and a mechanical interface for connecting a neutron collimator. The entire assembly must be gas-tight to prevent leakage of the gas mixture.

The NS-GEM detector together with the electronic readout system and the detector polarization system were transported to the Institute of Nuclear Physics and assembled in the IGN-14 generator. The detector and collimator were aligned and positioned in front of the tritium target. Fig. 1 shows two photos of the detection system installed in the IGN-14 laboratory.

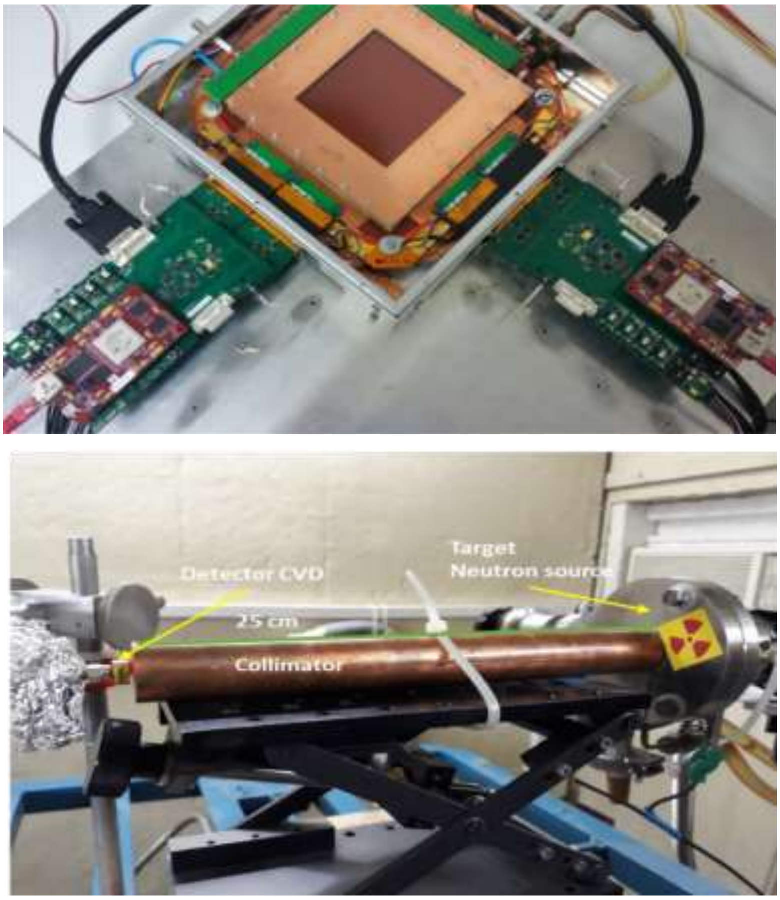

Fig. 1. Detector system installed in the IGN-14 laboratory.

The reconstruction of proton paths and filtering of background events is shown in the figure 2 below. As you can see, the reconstruction and filtering algorithms work very well. From the data collected during 15 minutes of measurement and initial reconstruction of over half a million events, only about 150 qualify as interesting candidates for the proton generated in the converter and scattered in the angle range from 0 to 35 degrees. The obtained trace value ratio is reasonably consistent with that expected from the GEANT4 simulations. It is worth emphasizing that the obtained results confirm the ability of the developed NS-GEM detector to detect recoil protons and reconstruct their traces in the active volume of the detector.

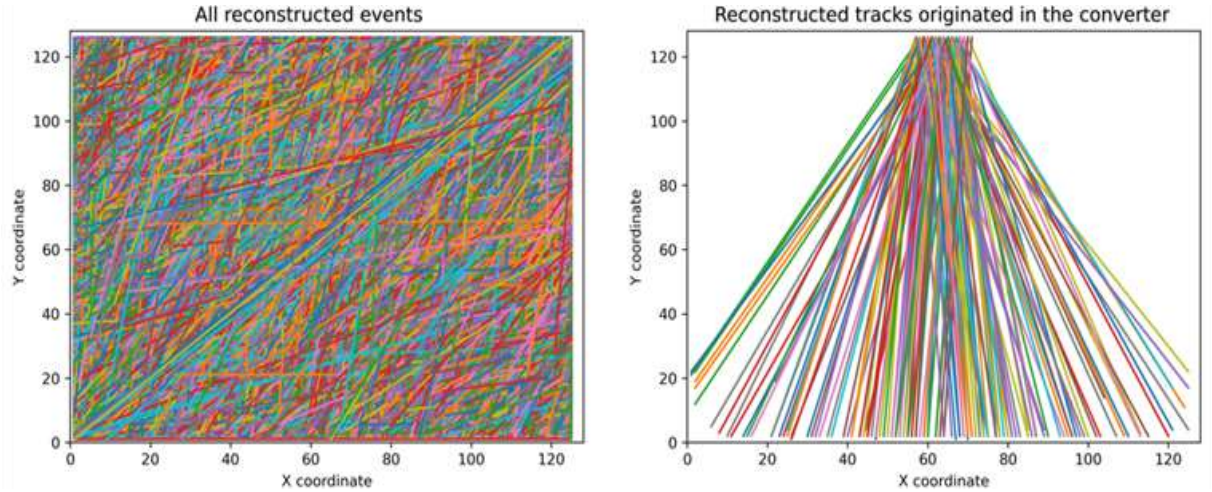

Fig. 2. Reconstruction of proton traces: all reconstructed events (left), reconstructed proton traces from the converter (right).

Conclusions

The NS-GEM spectrometer concept was developed based on simulation results, and the detailed detector design was elaborated using the standard 3-stage GEM detector. A detector model for GEANT4 simulations was constructed, and extensive Monte Carlo simulations with sufficient statistics were performed. The simulation results were used to evaluate the energy resolution of our demonstrator detector, considering the following: efficiency of generation of recoil protons, scattering of recoil protons in the converter and detector, and energy losses of protons in both components. All these processes must be considered when generating calibration curves of dE/dx versus the initial energy of recoil protons.

The simulation results clearly indicate that the thickness of the converter is a critical parameter that affects the neutron energy resolution. The converter thickness should be kept below 0.5 mm and preferably around 0.1 mm. However, a thinner converter results in lower efficiency of production of recoil protons. The expected neutron energy resolution is approximately 21% FWHM for the $ArCO_2$ gas mixture at a pressure of 1 atm and 15% FWHM at 2 atm. The primary source of uncertainty in estimating neutron energy is fluctuations in proton energy losses (dE/dx) within the detector volume.

It should be noted that our demonstrator detector is only capable of registering a small fraction of each proton track, with a maximum length of 11 cm. Although it is possible to construct a detector with a much longer sensitive region of up to 1 m and use a gas mixture at higher pressure to achieve an energy resolution of about 5% FWHM, such a long detector is beyond the scope of the current project.

The NS-GEM demonstrator was designed, built, and used for initial measurements in the IGN-14 neutron generator. The procedures for reconstructing recoil proton tracks have been proven to be highly efficient and robust, even in the presence of a large background of signals generated by scattered neutrons and recoil protons in the detector structural materials rather than in the polyethylene converter. Optimizing the working parameters of the detector is necessary to accurately measure energy losses (dE/dx).

Collaboration

CEA; AGH

References

[1] M. Scholz, U. Wiącek, K. Drozdowicz, A. Jardin, U. Woźnicka, A Kurowski, A. Kulińska, W. Dąbrowski, B. Łach, and D. Mazon: “Concept of a compact high-resolution neutron spectrometer based on GEM detector for fusion plasmas”, in print: Journal of Instrumentation, JINST.

[2] A. Jardin et al., “X-ray and neutron diagnostics of fusion plasmas”, Plasma 2023 - International Conference on Research and Applications of Plasmas, Warsaw, September 18-22, 2023.

[3] M. Scholz et al., “Proton-recoil spectrometer for fast neutron spectrum based on GEM gas detector”, Proceedings of 49th Conference on Plasma Physics - Bordeaux - July 3-7, 2023.

WPENS: Early Neutron Source definition and design

Title: Early Neutron Source definition and design

Authors: W. Królas, U. Wiącek, D. Dworak, A. Kulińska, A. Kurowski, J. Kotuła, R. Ortwein, G. Tracz, M. Turzański

Subtask ENS-4.4.1.3-T018-07: 2023: Update of the Engineering Design of the STUMM

Subtask ENS-4.4.1.0-T018-05: STUMM System Responsible duties in 2023

In 2023, the performed work was a continuation of the development of the STUMM module. The following changes in the model were performed:

- The distance of the current connectors from the pressure plate has been increased.
- The cooling pipe system has been changed according to the latest solution for HFTM.
- The model of the elements of the STUMM positioning system in the TC has been updated (at the upper part and the lower part of STUMM).
- The stiffening of the whole set of rigs during the replacement was proposed, by the concept of connecting four RIGs by the dedicated holder.
- The width of the RIG plates was reduced from 100 mm to 96 mm. It increased the distance between the RIGs to 18.2 mm and changed the arrangement of all elements in individual segments. This procedure was used to ensure better tightness of the system and better access for RH during the replacement of RIGs (Fig. 1a).
- Centered the detector positions about the center of the segments.
- The distance between the Container cover and the RIGs has been increased from 1 mm to 3 mm.
- Changed the concept of one large seal to 8 thin (3 mm) seals for each Rig separately.
- A new concept for replacing damaged RIGs outside of STUMM was proposed.

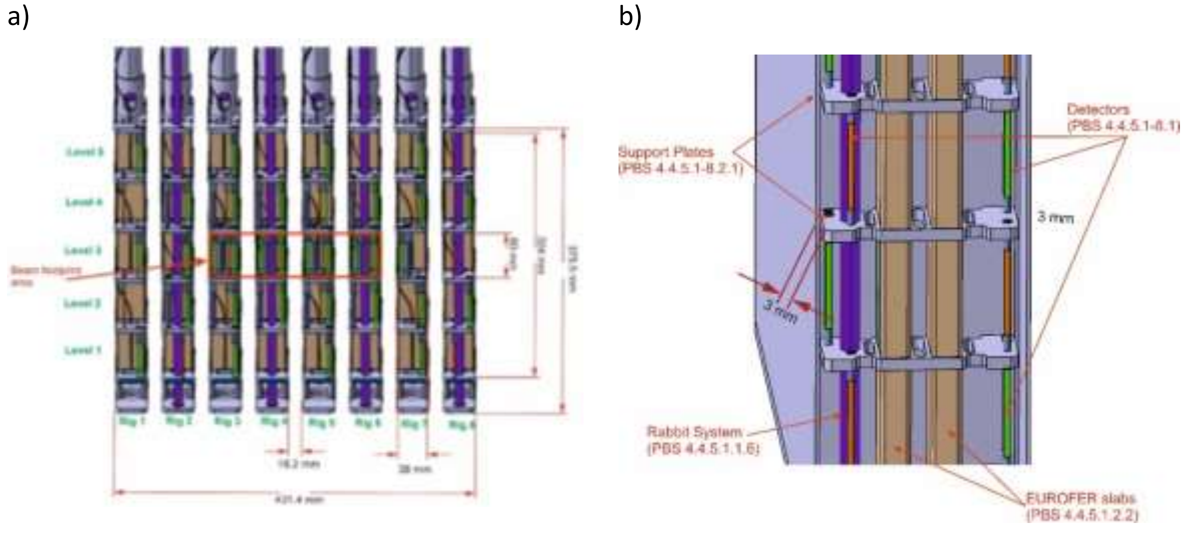

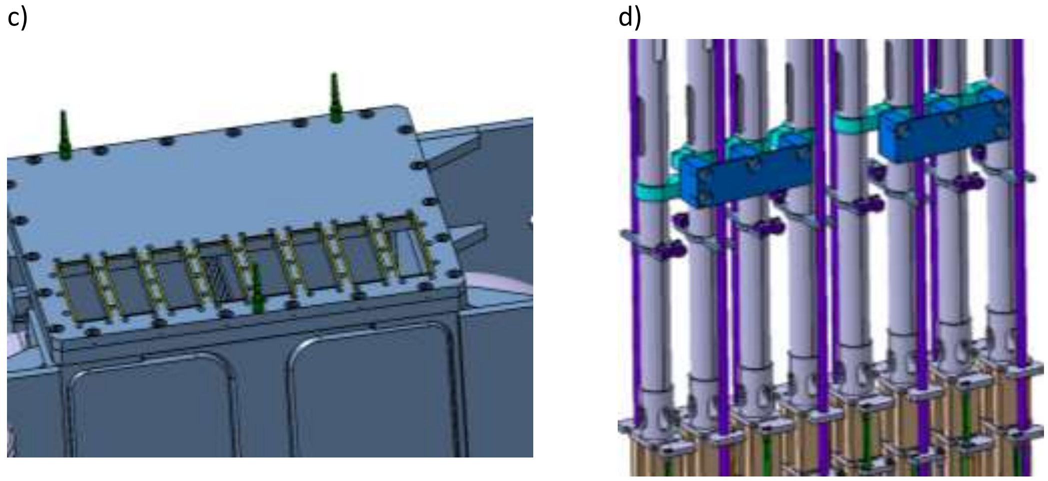

Fig. 1. Changes in the STUMM module proposed in 2023: a) dimensions in the Container area, b) Distances between Container cover and RIGs, c) Set of 8 gaskets for RIG set, d) RIG stiffening system

Another iteration of thermo-hydraulic and strength calculations was performed for the STUMM model (ver. 2.9), showing the impact of changes in the model on parameters such as the total heat production in the system, pressure drop in the system, temperatures of individual system elements and mechanical deformations. The calculations showed, among other things, that compared to the previous iteration, the drop in cooling gas flow pressure increased by approximately 2 times, while heat production decreased by approximately 11%, which also contributed to changes in temperature distribution.

Subtask ENS-4.4.3.0-T018-06: Experimental validation of the re-use of PEEK gasket

In 2023, the first experimental tests were carried out examining the impact of mechanical deformations on the possibility of reusing the gasket in the STUMM model (ver.2.9 with one gasket for a set of RIGs). These tests were performed by measuring the tightness of the system by repeatedly unscrewing and tightening the front flange, sealed with the tested gasket. These tests were carried out based on a simple system consisting of the following elements:

- High vacuum chamber in which the pressure during typical experiments is maintained to ~ $3x10^{-6}$ mbar
- Front flange DN 210 ISO-K (uses compression fittings)
- DN 210 ISO-F rear flange (uses screw connectors)
- Pumping system – a set of rotary and turbomolecular pumps
- IONIVAC manometer (combination of cold cathode and Pirani) for pressure measurement - can measure pressures ~10-10 mbar
- GRAPHIX manometer controller for pressure control
- PEEK seals with dimensions corresponding to the STUMM model in the full version and with holes for mounting screws

Fig. 2. System for testing changes in the tightness of the system and thus the possibility of reusing the PEEK (and CU) gasket after replacing a single RIG, b) Solid PEEK gasket, c) PEEK gasket with hollow holes for mounting screws.

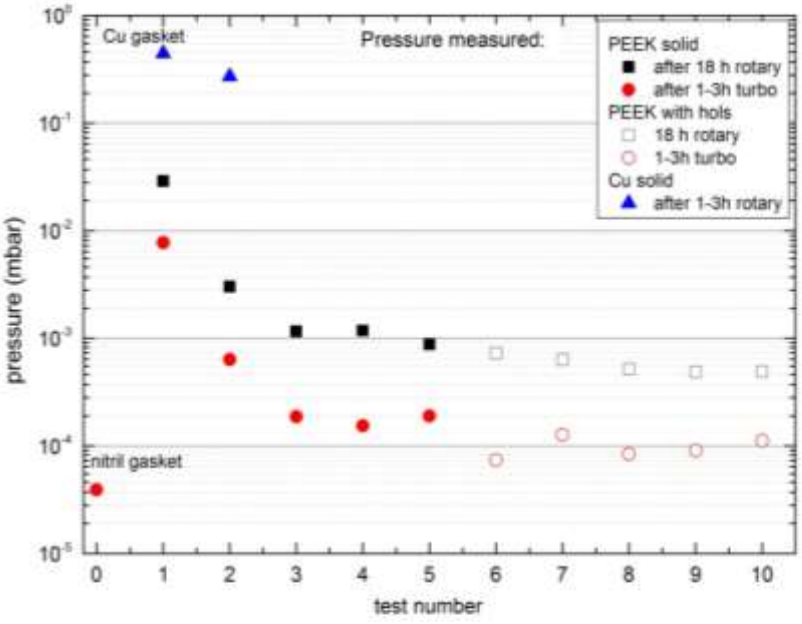

Fig. 3. Pressure change in subsequent measurement cycles for considered gaskets in the STUMM module

The value of the leakage coefficient that is acceptable for STUMM is 2 x 10-4 Pa m^3/ s. The tests carried out confirmed that the Cu gasket is a single-use gasket and the leakage coefficient (~4 x 10-2 Pa m^3/s) is twice higher in comparison to that allowed in STUMM. The tests also showed that subsequent assembly and disassembly cycles improve the tightness of the system with the PEEK gasket and the obtained leakage coefficient values are below the acceptable value:

- for solid gasket – 5 x 10^{-6} Pa m^3/ s
- for gasket with holes for mounting screws – 2 x 10^{-6} Pa m^3/ s
- To reliably confirm this thesis, further temperature and radiation tests are necessary.

Subtask ENS-2.2.4.2-T025-08: Shielding optimizations for the complementary experimental room during operation

The research carried out in 2023 is a continuation of work started in 2022. Performed work showed that biological doses in rooms adjacent to CEH (Complementary Experimental Hall) exceed the acceptable limits.

To reduce doses in the mentioned areas, several modifications were made: the thickness of the CEH walls was increased from 100 cm to 150 cm, an additional polyethylene cover (20 cm thick) was used in selected locations, and the HVAC installation was moved to the side wall behind the barrier in the CEH. Because the biological dose was still above the acceptable limits, the next shielding modification was replacing the polyethylene layer on the CEH ceiling with borated polyethylene (50 cm).

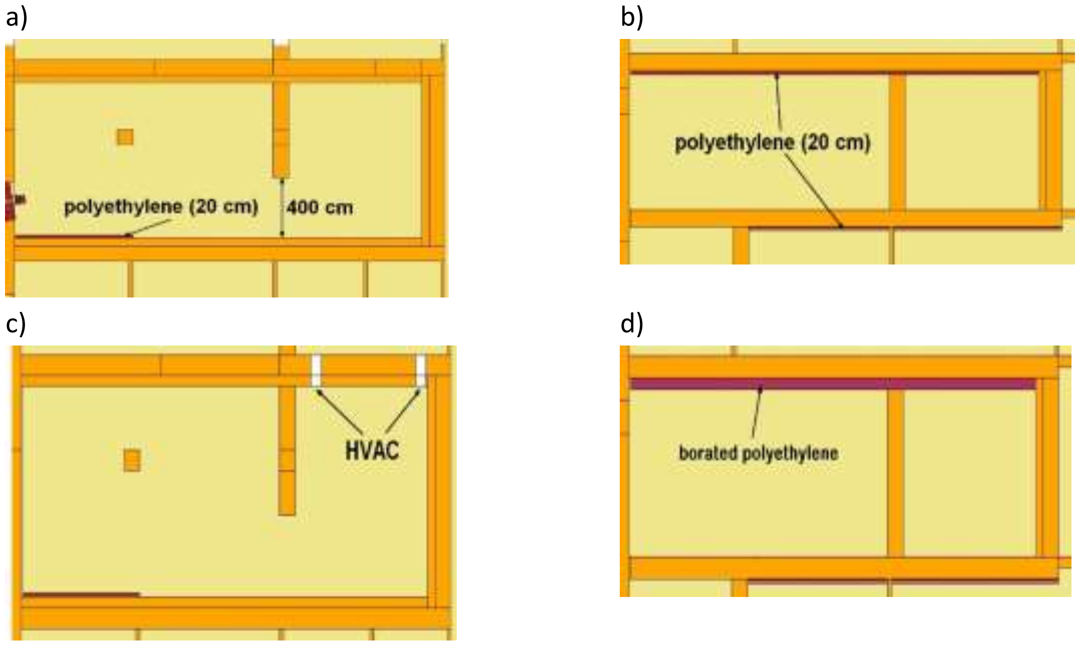

Fig. 4. CEH after modifications: a), c) horizontal section, b), d) vertical section

Monte Carlo simulations were performed to obtain 3D high-resolution spatial maps (20 × 20 × 20 cm^3 voxels) for both biological dose rate and silicon absorption dose in CEH with wall thicknesses up to 150 cm. In the corridor and outside the facility solely the biological dose rates were computed. Moreover, the effect of the HVAC hole was examined.

Thanks to these modifications, the biological dose in room 145-1 is satisfactory, i.e. below the required 10 µSv/h. Unfortunately, in the AC, room 145-1, and the corridor, the radiation level is still too high and exceeds the accepted limits. Radiation leakage through HVAC in the new location is lesser but still needs to be reduced. Polyethylene blocks are considered to fix the problem.

For the silicon absorbed dose in CEH, the calculations were performed for configurations without geometry changes. The calculated values of the total Si dose rate are mostly from 10^{-6} MGy/fpy to 10^{-2} MGy/fpy, except higher values (up to 1 MGy·fpy^{-1}) at the outlet of the duct between TC and CEH and the beam line.

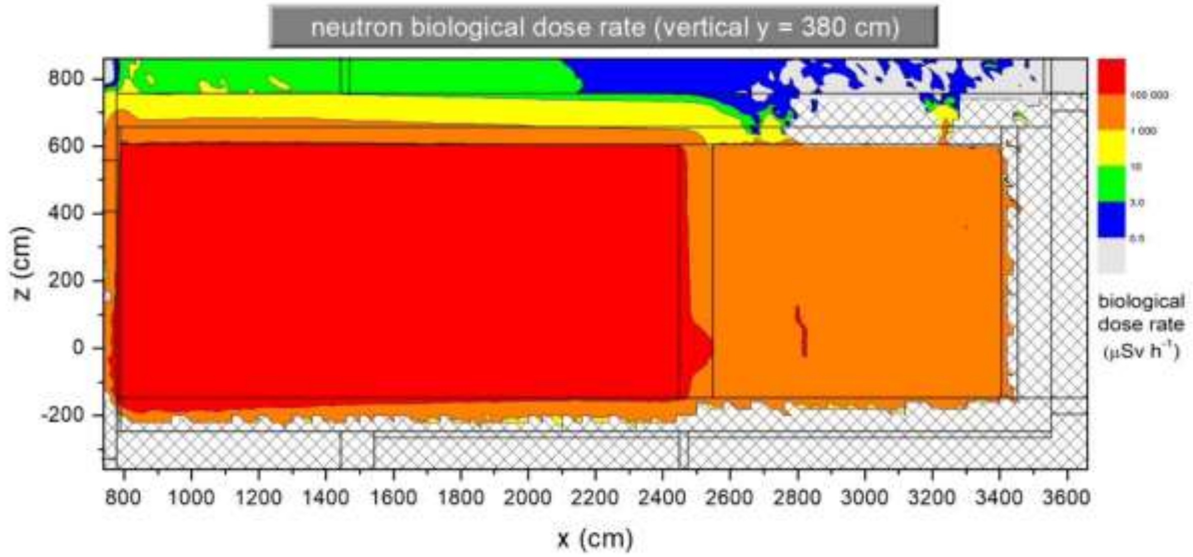

Fig. 5. Vertical neutron biological dose rate map for an additional layer of borated polyethylene on the ceiling (50 cm). The white dashed area is the unsampled area

Subtask ENS-2.2.5.1-T025-07: Neutronics Modeling and Nuclear Analyzes for the STUMM Design Optimization

The main aim of this task was to support the process of optimization of the engineering design of the STUMM module. Based on the MCNP model created in 2022, Monte Carlo numerical simulations were performed to obtain 3D maps of the spatial distributions for nuclear heating, radiation damage (DPA), and gas production, as well as distributions of biological dose rate and absorbed dose in silicon and PEEK at the upper part of STUMM. In the case of nuclear heating, there is a decrease in its total value by approximately 11% compared to the previous STUMM model (ver.2.5). The maximum values of total nuclear heating are observed in the front part of the Container's cover and are up to ~15 W/cm^3. Analyzing the dose absorbed from neutrons and gamma radiation in the upper area of STUMM, it amounts to ~95 MGy/fpy for PEEK and ~30MGy/fpy for Si, respectively.

Doses after the end of STUMM operation, so-called beam-off analyses, were also calculated for the following cooling times: 0 h, 1 h, 1 day, and 1 week. The calculations show that after a week of cooling, the doses in the AC at a distance of 1 m from STUMM are above 108 µSv/h.

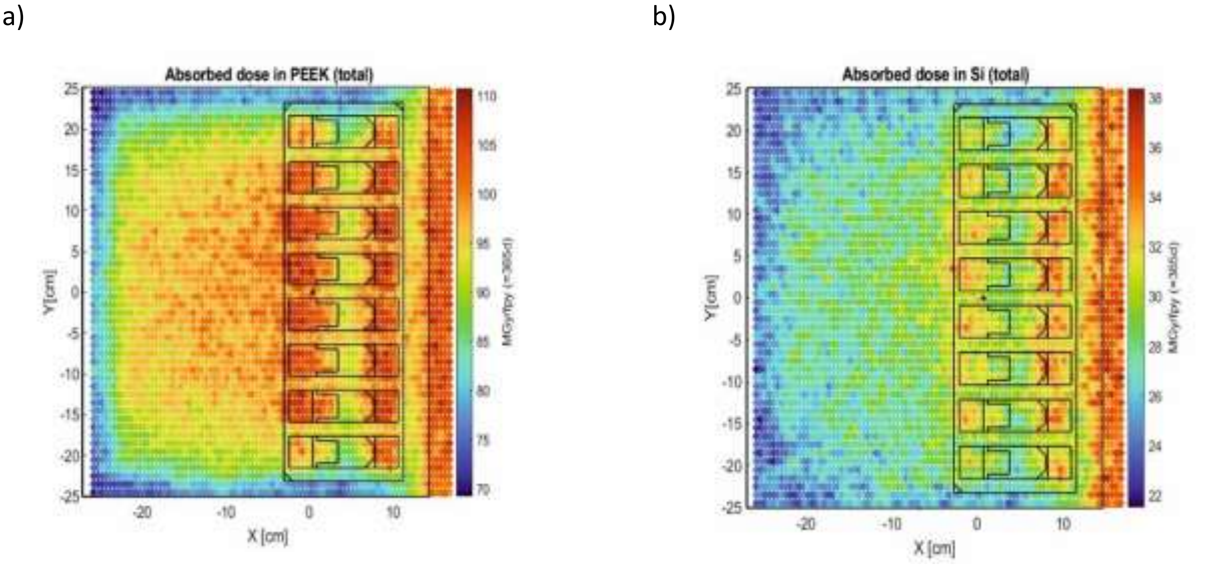
a)

b)

Fig.6. Total absorbed doses at the upper part of STUMM: a) in PEEK, b) in Si.

References

[1] 3D CAD model of STUMM EFDA_D_2N5PTM v.3

[2] U. Wiącek ; 2023 Update of the STUMM Engineering Design – in preparation

[3] U. Wiącek, A. Kurowski, J. Kotuła; System Design Description Document for the IFMIF-DONES Start-Up Monitoring Module (STUMM); Report IDM Ref. No. EFDA_D_2N6MBJ ver.2023 – in preparation

[4] U. Wiącek; "Summary of STUMM System responsible activities in 2022" – in preparation

[5] U. Wiącek, W. Janik, A. Kulińska, J. Kotuła, M. Turzański; Experimental activities for the definition of the gasket solution of the STUMM; Report IDM Ref. No. EFDA_D_2R3PC4 v.1.0

[6] G. Tracz; Shielding optimizations for the complementary experimental room during beam-on operation; Report IDM Ref. No. EFDA_D_2QGGMX v.1.0

[7] D. Dworak, U. Wiącek; Neutronics modeling and analysis for STUMM design – in preparation.

Related 2023 articles and Conference Presentations:

1. R. Ortwein, U. Wiącek; Conjugated heat transfer analysis of the Start-Up Monitoring Module (STUMM) for IFMIF-DONES including heat generation mapping, Fusion Eng. Des., 188 (2023) 113451, doi: 10.1016/j.fusengdes.2023.113451,
2. C. Torregrosa-Martin, (W. Królas, U. Wiącek) et al.; Overview of IFMIF-DONES diagnostics: Requirements and techniques, Fusion Eng. Des., 191 (2023) 113556,
   doi: 10.1016/j.fusengdes.2023.113556,
3. U. Wiącek, "Feasibility study and validation of PEEK gasket for DONES STUMM module", AMICI-I.FAST Workshop on Facilities for Beam Test of Accelerator Components, Kraków, 12.10.2023

Research Unit: Institute of Nuclear Physics Polish Academy of Sciences (IFJ PAN)

WPMAG: Magnet System

Title: DEMO Magnets design

Authors: R. Ortwein, Monika Lewandowska, Aleksandra Dembkowska, Michał Bonk

Introduction

An updated design of the DEMO TF coil (high current design [1]) has recently been proposed by the Swiss Federal Institute of Technology Lausanne – Swiss Plasma Center (EPFL-SPC) team (PSI Villigen, Switzerland). The goal of the work of the IFJ PAN team in 2023 was the electromagnetic and mechanical analysis of the TF coil design by EPFL-SPC – based on the analysis performed in 2022 [2]. The benchmark analysis with the CEA models was finalized, showing good agreement in the EM forces, deformations and stresses, validating the models developed in 2022. In 2023 the work was focused on the update of the CEA geometry and the electromagnetic and mechanical analysis of the high current graded EPFL-SPC design. The IFJ PAN team also contributed to the thermal – hydraulic analysis of the EPFL-SPC design of the DEMO TF coil.

High Temperature Superconductors (HTS) are promising materials to be applied in future fusion magnets HTS conductors are already considered as a possible option for some components of the superconducting magnet system of the EU DEMO tokamak, which are being designed by the EUROfusion consortium, Geometric and thermo-physical characteristics of HTS and LTS conductors differ significantly, therefore it can be expected that numerical simulations of the behavior of HTS conductors may require specific approaches, different from those which are successfully used for LTS conductors, particularly in cases when fast transient processes (such as e.g. quench or the breakdown) are considered. In order to provide data for better understanding of the quench evolution in HTS conductors as well as for testing different numerical approaches and proper tuning of the numerical codes, a series of dedicated HTS 15-kA sub-size samples with different geometries were produced and tested by the EPFL-SPC team in 2021 at the SULTAN facility in the Quench Experiment. Further experiments on AC losses generation in HTS conductors with different geometries are also currently being performed by the EPFL-SPC team at the SULTAN test facility. Our tasks on HTS conductors included completion of the work on the analysis and interpretation of the results of the selected run of the Quench Experiment using different numerical approaches, and development of the ANSYS Mechanical APDL model of a short piece of the HTS conductor, based on the CORC® concept, designed for the innermost layer of the DEMO CS coil by the Advanced Conductor Technologies (ACT) and the University of Twente (UT) team.

Results

1. <u>Electromagnetic analysis of the EPFL-SPC design of the DEMO TF coil</u>

The global electromagnetic model was developed and solved to compute the EM forces on the EPFL-SPC design (Figure 16). The three characteristic points of the plasma cycle were considered, namely: PREMAG (end of the Premagnetization phase), SOF (Start of flat-top) and EOF (End of flat-top). The unit forces along the centerline of the TF coil coils were computed and compared (**Błąd! Nie można odnaleźć źródła odwołania.**) showing very similar values for the for the radial and vertical force for all 3 characteristic points. The only differences were observed in the lateral force (Fy), for which clear differences were observed.

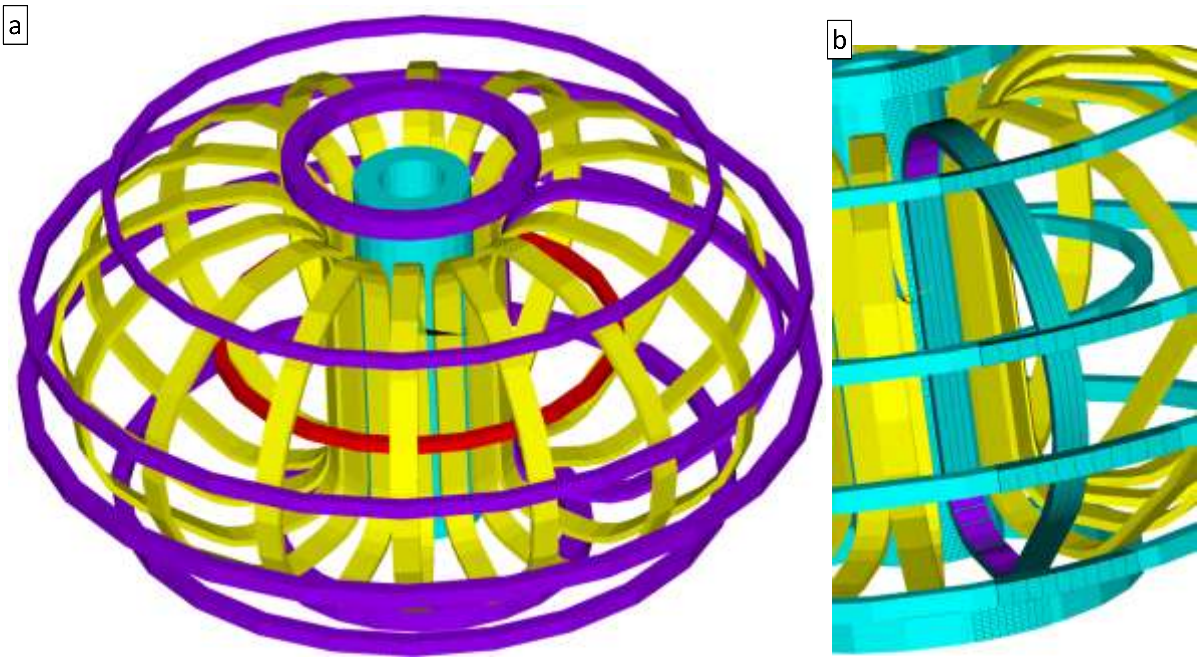

Figure 16. Global EM model of the DEMO tokamak with the high current EPFL-SPC design: a) Current source SOURC36 primitives; b) Solid mesh overlapped on the current sources.

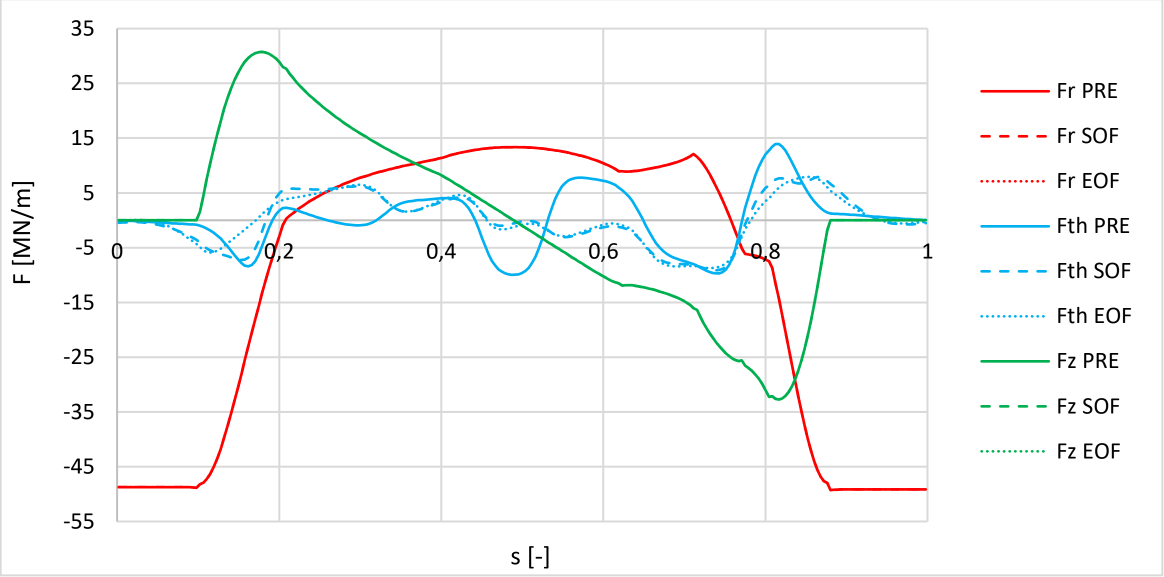

Figure 17. Forces per unit length of the TF coil (Fr – radial force, FZ – vertical force, Fth- lateral force (Fy))

2. Homogenization analysis

The average orthotropic properties of the 8 layers of the TF winding were computed with dedicated homogenization models (**Błąd! Nie można odnaleźć źródła odwołania.**). The results at 4.2 K are listed in Table 6. The homogenization model was extended to compute the secant coefficient of thermal expansions and implemented in the Ansys APDL parametric environment to speed-up the simulation time. The sensitivity of the homogenization model to the mesh density was analyzed in details, ensuring that the presented results represent the converged solution.

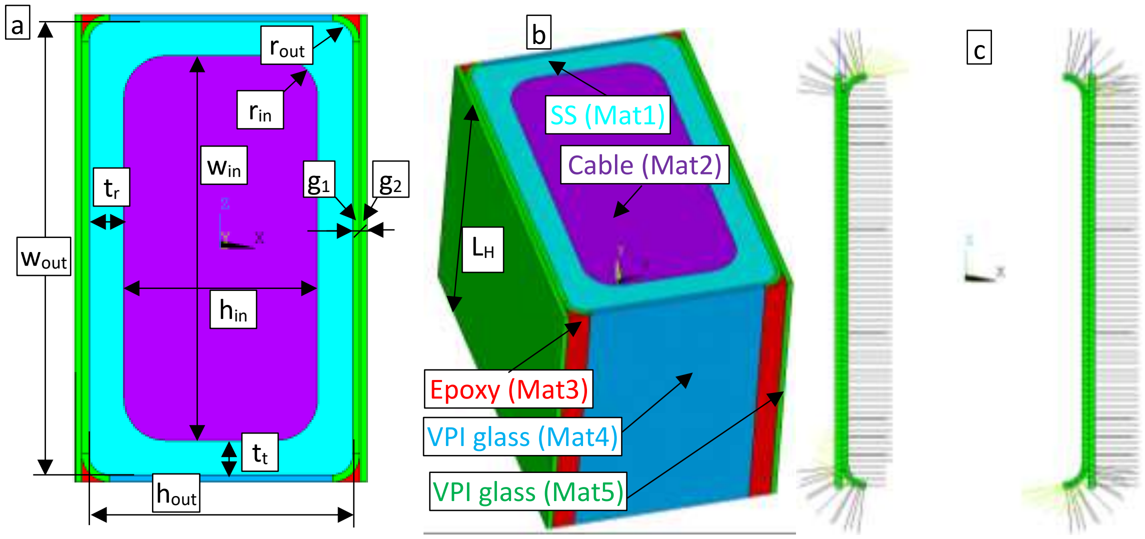

Figure 18. Dimensions of the WP#4 homogenization model: CEA – black, IFJ PAN- green

Table 6. Results of the homogenization analysis for the EPFL-SPC high current design at 4.2 K

Parameter	**L1**	**L2**	**L3**	**L4**	**L5**	**L6**	**L7**	**L8**
E_x [GPa]	19.420	20.696	22.591	24.637	26.590	28.239	30.353	32.582
E_y [GPa]	72.032	74.979	79.638	83.510	87.772	93.261	96.673	99.644
E_z [GPa]	42.320	44.465	47.263	49.329	51.917	56.035	57.898	59.309
G_{xy} [GPa]	10.952	11.506	12.475	13.462	14.432	15.353	16.336	17.330
G_{yz} [GPa]	19.154	20.000	21.238	22.153	23.282	25.025	25.832	26.456
G_{xz} [GPa]	1.545	1.693	2.051	2.400	2.843	3.515	4.007	4.487
ν_{xy} [-]	0.078	0.080	0.082	0.085	0.088	0.088	0.091	0.095
ν_{yz} [-]	0.284	0.285	0.285	0.285	0.285	0.286	0.286	0.286
ν_{xz} [-]	0.140	0.137	0.139	0.142	0.145	0.146	0.149	0.152
α_x [1/K] 10^{-6}	11.589	11.526	11.497	11.455	11.430	11.437	11.402	11.364
α_y [1/K] 10^{-6}	10.302	10.310	10.316	10.322	10.327	10.331	10.335	10.338
α_z [1/K] 10^{-6}	10.569	10.570	10.581	10.590	10.598	10.605	10.611	10.616

3. Global 3D mechanical model

3D model was build, meshed and solved in the Ansys Mechanical APDL software. Based on the computed Lorentz forces the homogenized thermo-mechanical properties, the cool-down and powering scenarios were simulated. The resulting deformation maps are show in **Błąd! Nie można odnaleźć źródła odwołania.** including the PREMAG, SOF and EOF, with the EOF scenario giving the largest deformations. The stress field was analyzed for the TF casing showing that the stresses are within the acceptable limits.

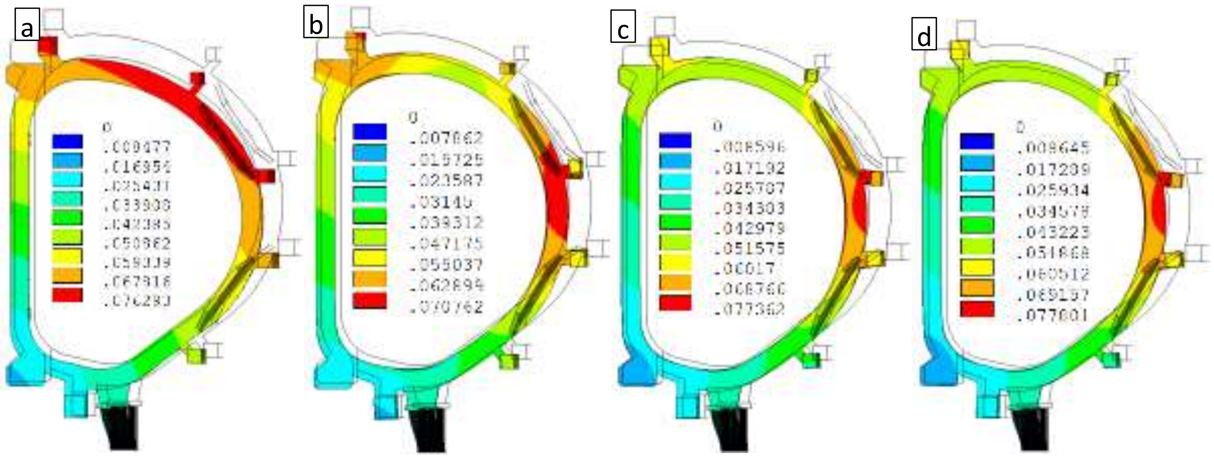

Figure 19. Deformation maps [m] (magnification 20x) for the 3D model (mesh1):
a) After cool-down; b) After PREMAG; c) After SOF; d) After EOF

4. Thermal – hydraulic analysis of the EPFL-SPC design of the DEMO TF coil

a. Analysis of the results of the pressure drop test of the RW3 TF conductor with the blocked cooling channel

A short sample of the prototype React & Wind Nb_3Sn conductor for the DEMO TF coil (Fig. 4 left) has been produced by the EPFL-SPC team and the pressure drop test of this conductor with the blocked cooling channel has been performed at the SULTAN test facility

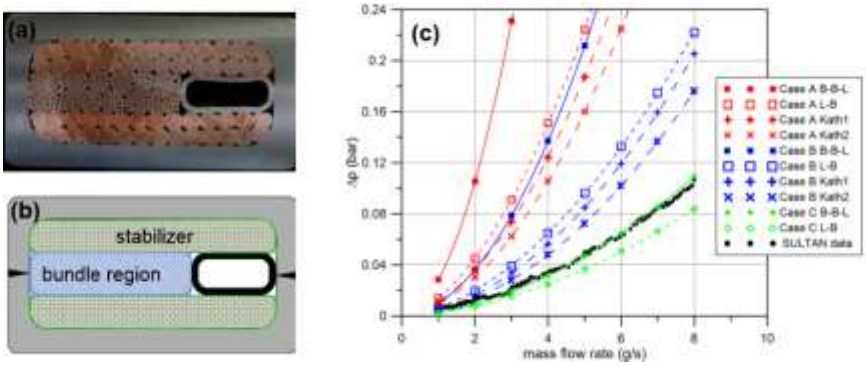

Figure 20. Cross section of the TF conductor prototype (a), its idealized geometry assumed in the hydraulic models (b), and comparison of the pressure drop computed using different approaches with the experimental data.

We computed the pressure drop in this sample using different bundle friction factor correlations taken from literature [4-6] and taking into account (or not) flow in the empty “holes” adjacent to the corners of the cooling channel. We selected the model of flow which reproduced most accurately the experimental data to be used in further thermal-hydraulic analysis.

b. Estimation of the minimum temperature margin in the TF conductors.

For each of 10 conductors designed for different layers of the TF coil we calculated, using the simplified steady state models,

- the maximum value of the helium mass flow rate (assuming no heat load),
- the mass flow rate as well as p, T, T_{cs} and ΔT_{marg} profiles along the conductor at the characteristic points of the plasma cycle (end of Premag or SOF and EOF).

5. Continuation and completion of the analysis and interpretation of the results of the selected run of the Quench Experiment (in collaboration with the WPUT team).

As a continuation of efforts started in 2022, we completed THEA simulations of the selected run of the Quench Experiment using two conductor models with different level of complication and different pairs of values of the uncertain model parameters (contact heat transfer coefficient between different solid cable components and copper RRR). The results of the performed analysis were presented at CHATS on Applied Superconductivity and in the respective article submitted to *Cryogenics.*

6. Preparation of the 3D thermal model of the short piece of the HTS CORC conductor designed by ACT and the UT team for the innermost layer of the DEMO CS coil.

A novel 3D parametric thermal model was developed in the Ansys Mechanical APDL software, including 3D mesh of the solid parts and 1D mesh of the fluid inside (Figure 6). The model includes non-linear material properties dependent on temperature and magnetic field (taken into account as time dependence), the Dittus-Boelter correlation for the heat transfer coefficient between fluid and solid and the presence of thermal resistances between materials. The model was used to simulate the temperature distribution of the CORC cable due to the heating by AC losses and validated by comparison with the respective results obtained with the 1D THEA code. The model will be used for analysis and interpretation of experimental data resulting from the AC losses test of the CORC conductor foreseen in 2024.

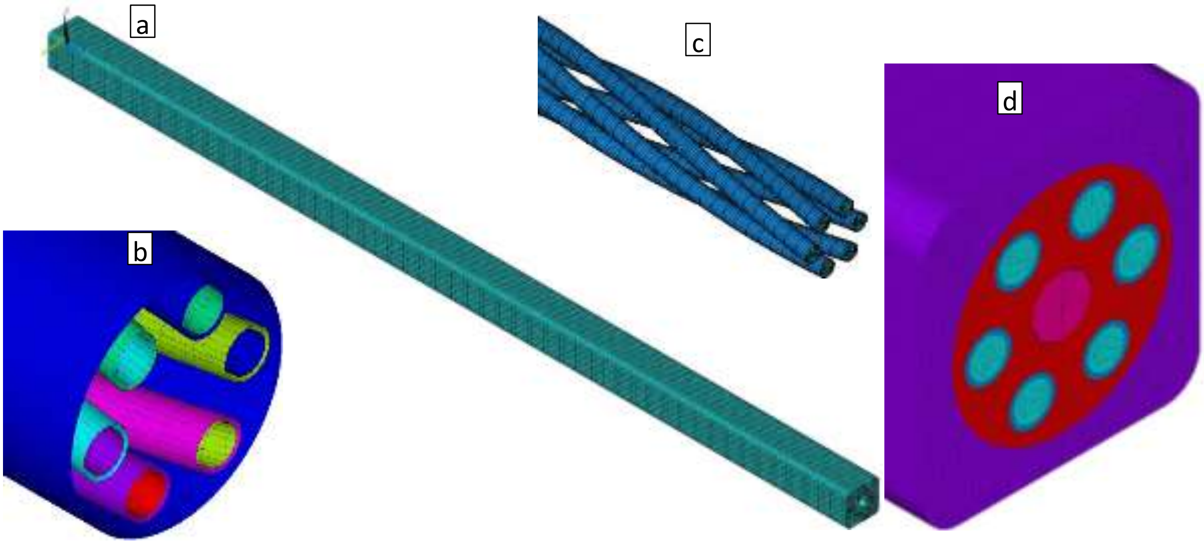

Figure 21. a) Mesh of the thermal model of CORC cable; b) Contact elements; b) Mesh of the twisted cables; d) Ending zone colored by materials used

Conclusions

- Based on the electromagnetic and mechanical analyses of the EPFL-SPC design of the DEMO TF coil it was concluded that the design satisfies the strength criteria defined in the norms. A margin of ~25% was identified, showing a room for a possible improvement of the design.
- It results from the thermal-hydraulic analysis of the EPFL-SPC design of the DEMO TF coil, that in all layers the minimum temperature margin should be well above the 1.5 K acceptance criterion.
- Preliminary simulations with the 3D thermal model of the CORC cable showed low thermal gradients within the cable cross-section. This indicates that the use of 1D models, such as e.g. those developed with the THEA code, might be justified for the considered conductor geometry.

Collaboration

WPUT (Szczecin)
EPFL-SPC (PSI Villigen, Switzerland)
University of Twente (Enschede, Netherlands)
CEA Saclay (France)

References

[1] F. Demattè. TF WP design for the high current, nom. Field. MAG-S.01.01-T001-D001, EFDA_D_2P8XLN (2022)
[2] R. Ortwein. Update of the mechanical analysis of the TF WP#4 EFDA_D_2Q7VLF v1.2 (2023)
[3] R. Ortwein, Mechanical analysis of the DEMO winding packs (2023) MAG-S.01.04-T013-D001
[4] M. Bagnasco, L. Bottura, M. Lewandowska, Cryogenics, vol. 50, pp. 711-719, 2010.
[5] M. Lewandowska, M. Bagnasco, Cryogenics, vol. 51, pp. 541-545, 2011.
[6] H. Katheder, Cryogenics, vol. 34, Supplement 1, pp. 595-598, 1994.

Related 2023 articles and conference presentations:

1. R. Ortwein, F. Nunio: "Mechanical analysis of the DEMO TF with 2D and 3D models: homogenized and fully detailed – comparison of accuracy", oral presentation at the CHATS on Applied Superconductivity (CHATS-AS 2023), 3-5 May 2023, Torino, Italy, submitted for publication in Cryogenics.
2. M. Lewandowska, A. Dembkowska, D. Bocian, R. Ortwein, O. Dicuonzo, K. Sedlak: "Modeling and Analysis of Quench in the 15-kA HTS Conductor" – oral presentation at the CHATS on Applied Superconductivity (CHATS-AS 2023), 3-5 May 2023, Torino, Italy, submitted for publication in Cryogenics.
3. M. Lewandowska, A. Dembkowska, A. Nijhuis, G. Anniballi, L. Giannini, D. Van Der Laan, J. Weiss: "Analysis of AC losses and thermal – hydraulic simulations" – oral presentation at the Seminar on HTS Magnets within EU-DEMO Cooperation, 21-23 November 2023, Hefei, China.

Research Unit: Institute of Nuclear Physics Polish Academy of Sciences (IFJ PAN)

WPPrIO: Preparation of ITER Operation

Title: Preparation of ITER Operation

In the WPPrIO project, the Institute of Nuclear Physics Polish Academy of Sciences implemented two tasks in 2023:

- Report on analysis of DTE2 neutron flux measurements with TLDs and preparation of streaming experiment for DTE3 (PrIO-5.3.NEXP-T002-D002)
- Evaluation and Optimization of Structural and Shielding Concrete for IFMIF-DONES (ENS-2.2.6.6-T025-09)

Report on analysis of DTE2 neutron flux measurements with TLDs and preparation of streaming experiment for DTE3

Author: Mariusz Kłosowski

Introduction

The first part of the report concerns the activities undertaken to prepare detectors for the DTE3 campaign at JET. For the third D-T campaign, 23 measurement sets were prepared at JET, containing thermoluminescent detectors of the MCP-N and MCP-7 types, as well as sets for background measurement. A total of 780 TL detectors were produced and prepared. Four of the sets had additional boxes with detectors located on the plug pin. Additional detectors were designed to measure external radiation fields in locations A3, B3, B5 and C1. On 15 August 2023, the sets were placed in the polyethylene moderators inside and outside the JET torus hall at the same positions of DTE2. On 13 November 2023, calibration for detectors in the gamma ray field (Cs-137) was performed at IFJ.

The second part of the study focuses on the analysis of detector reading data from previous DD, TT and DTE2 campaigns. Comparisons of the current results of fluence measurements using experimental and computational methods show discrepancies. Since the neutron spectra at the measurement locations in the environment around JET differ from the calibration conditions, the use of a constant conversion factor from dose to fluence causes large uncertainties in the results. In order to minimize the error in determining the neutron fluence, literature data were used to find the most probable function of the detector's relative response to neutrons for the 10-inch moderator. The sensitivity coefficients determined during the calibration of the detectors in the D-D and D-T fields were preliminarily adjusted using this function. On this basis, the dose measurement results were converted by the derived conversion coefficients and the most probable neutron fluence results at each measurement point were obtained.

The objectives of the work were:

- Completion of the analyses of DTE2 neutron flux measurements with TLDs
- Continuation STRE benchmark experiments during DTE3
- Pre-analysis studies for DTE3
- Preparation of TLDs assemblies and shipment to JET

Results

1. **Preparation of TLDs and pre-irradiation for calibration.**

The MCP-N (^{nat}LiF:Mg,Cu,P) and MCP-7 (^{7}LiF:Mg,Cu,P) detectors were manufactured at the Institute of Nuclear Physics of the Polish Academy of Sciences in Kraków. To prepare the MCP TL detectors for measurement, a standard annealing cycle before irradiation (two-phase heat treatment) was used: 260°C for 10 minutes and then 240°C for 10 minutes. Detectors placed on aluminum plates (Fig. 1 Left) were heated in a Carbolite LHT4/30 oven with convection.. A process of assessing the individual response factors (IRF) of the detectors was carried out. During this process, all detectors were irradiated with the same dose of 1 mGy (Cs-137) and readout using an manual TL reader Harshaw TLD 3500. Taking each detector's signal into account in relation to the average TL signal value for all detectors of the same type, individual response factors (IRF) were determined for the detectors. After determining the IRF coefficients, statistical analysis was performed. Detectors with a deviation greater than or less than 10% from the mean were rejected. All detectors then underwent a second annealing procedure before irradiation to prepare them for the measurement campaign.

Fig. 1 (Left) Image of detectors prepared for the annealing process, (Right) Components of boxes with detectors. The boxes filled with detectors were screwed to the plugs.

After selecting the detectors due to the deviations of the IRF coefficients, they were divided into three groups: those suitable for measurements, those for calibration and those for background measurements. Detectors intended for measurements were placed in boxes. Each set consisted of a rectangular and circular box. Each box was filled with 5 MCP-N and MCP-7 detectors (Fig. 1 Right). The detectors were arranged alternately, first MCP-N, then MCP-7 and so on.

2. Method of minimizing errors in determining neutron fluence using a variable calibration factor

Neutron fluence is calculate the by dividing the neutron dose by the calibration factor:

$$\Phi_n = \frac{D_n}{\alpha}$$

The neutron dose is measured using thermoluminescent detectors placed in a polyethylene moderator. Two types of detectors are used, one containing lithium-6 and the other containing lithium-7. The neutron dose is calculated by subtracting the dose measured with the lithium 7 detector (not neutron dose) from the dose measured with the lithium 6 detector (neutron and not neutron dose):

$$D_n = D_{TLD6} - D_{TLD7}$$

the calibration factor allows to convert the neutron dose into fluence. the calibration factor is determined in standard neutron radiation fields.

The uncertainty in the neutron fluence determination will depend on:

- *the precision of the dose measurement*
- *the uncertainty of the calibration factor.*

Below is a list of identified errors affecting dose measurement and the determination of the calibration factor (errors influence on calibration factor were marked blue):

I. Errors related to dosimetric properties od LiF: Mg,Cu,P:
Nonlinearity from few Gy, Fadding, Neutron energy dependence
II. Production batch errors:
Standard deviations of batch, Individual reference factors
III. Calibrations:
Gamma reference calibration error, Neutron calibration error
IV. Background measurements error
V. Errors related to TLD's readouts:
Fadding, Influence of filter in the reader, Reader sensitivity instability, Influence of thermal annealing after exposition, Time between readouts of batches
VI. Data processing:
Integration range, Calibration reference errors
VII. Errors related to geometry measurements:
Horizontal and Vertical boxes errors, Shadowing of the neutron beam by detectors, Thickness of polyethylene moderator, Distance from tokamak and positioning level of the samples
VIII. External radiation source error:
Error total fluence of neutrons, Lack of knowledge of the energy spectrum of neutrons at measurement points.

The greatest error in determining neutron fluence is caused by the uncertainty of the calibration coefficient value due to the variability of the neutron energy spectra distribution.

The uncertainty on calibration coefficient is analysed below.

The value of the calibration factor (dose to fluence conversion factor) depends on:

- detector sensitivity [1],
- moderator thickness,
- neutron energy spectra distribution,
- neutron fluence level[2].

[1] The sensitivity of the detectors depends on the production batch, but their dose response is calculated using gamma calibration, so the sensitivity can be assumed to be constant and similar during measurements and calibrations.

[2] This dependence occurred only for high fluences (corresponding to doses above 10 Gy) during calibration DT irradiations at high doses in ENEA at the Frascati Neutron Generator performed in 2021.

3. Graphical determination of αN-α7 conversion factors for characteristic measurement locations.

The moderator set with TL detectors used in the experiment can be compared to the use of measuring devices known as rem-meters or Bonner spheres. For such devices, response curves to neutron fluences of various energies are determined. These curves vary depending on the wall thickness of the device (moderator). Such curves were obtained from the literature for moderators and 10-inch spheres. This size corresponds to the moderator used in the experiments.

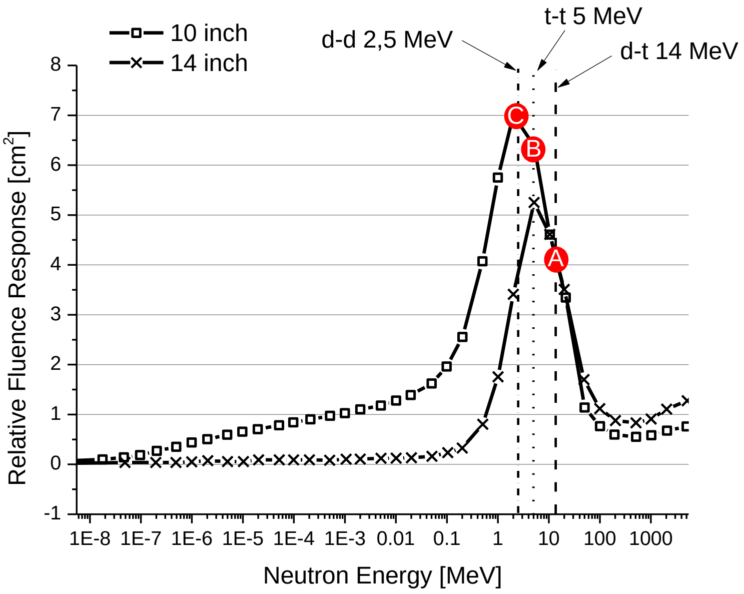

Fig. 2. Fluence response, as a function of neutron energy for two separate thicknesses of polyethylene 10 inch and 14 inch. A – relative response of 10 and 14 inch moderators for an energy of 14 MeV (d-t), B - maximum response for energy 5 MeV (TT) and moderator 10 inch, C- response for energy 2,5 MeV (DD) example of response to lower neutron energies. Reproduced from [1].

Points A, B, C were determined on the response curve, corresponding to the D-D, D-T and T-T reactions (Fig. 2). In order to determine individual calibration factors for measurement sites, a comparison of doses received in the TT and DT campaigns was carried out. During the DT campaign, the share of 14 MeV neutrons in the total neutron emission was 99.44%. Therefore, for this campaign, the dose recorded by the TL detectors can only be attributed to neutrons coming from this reaction. In the TT campaign, the share of 14 MeV neutrons was 40.2%, and the rest came from the TT reaction. Neutrons passing through the reactor and building walls lose their energy due to scattering. At the measurement site, at the entrance to the moderator containing detectors, the neutron energy depends on the initial energy and the degree of scattering. By comparing measurements from the same places for two campaigns differing in the share of neutrons of different energy, it is possible to calculate the percentage of each in the dose (Fig. 3).

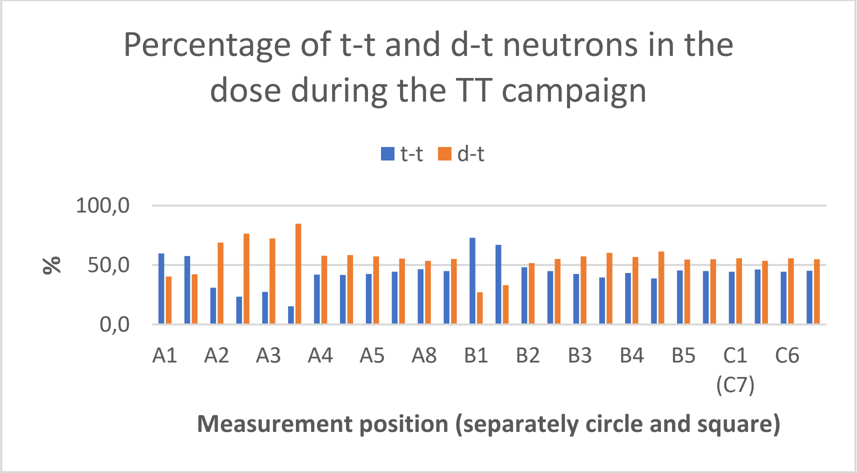

Fig. 3. The share of neutrons from the DT and TT reactions during the TT campaign calculated based on the comparison of the DTE2 and TT campaigns.

Using curves, individual alpha coefficients were determined for each measurement site. Then, based on them and the read doses, the neutron fluence was determined in each of the campaigns so far.

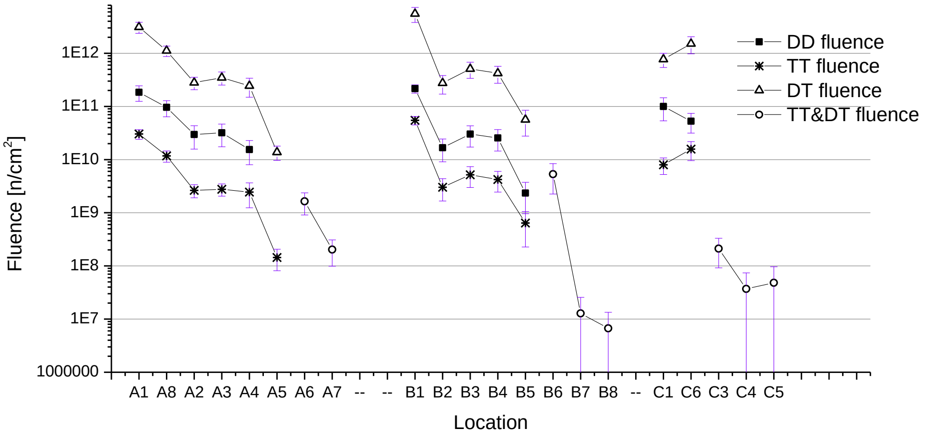

Fig. 4. Preliminary Neutron fluences in the DD, TT and DTE3 campaigns determined using variable αN-α7 calibration factors.

Conclusions

The task achieved two main goals. The first one concerned the preparation of a batch of detectors and placing them at measurement stations. 23 sets with thermoluminescence detectors were prepared for the D-T campaign. Irradiation took place at the end of 2023. The second part analyzed the existing data from previous D-D, D-T, T-T campaigns. In order to reduce the uncertainty in the determination of neutron fluence, individual dose-to-fluence conversion factors were determined graphically. Since the data on the detectors' response to neutrons of a given energy were taken from the literature, the fluence results are preliminary. MC response curve calculations for the actual moderator are needed to confirm and obtain accurate data.

Collaboration

This task was realized in collaboration with ENEA Frascatti.

References

[1] Panfeng WANG, Simulation of the response function s of Extended Range Neutron Multisphere Spectrometer using FLUKA program, https://doi.org/10.48550/arXiv.1409.5550

Related 2023 articles and conference presentations:

1. Contribution to oral presentation: R. Villari “Key technological aspects of recent DT operations at JET” Conference: 15th International Symposium on Fusion Nuclear Technology (ISFNT-15), Las Palmas de Gran Canaria, Spain, 10-15 September 2023.
2. Contribution to oral presentation: I. Lengar “Characterisation of the neutron field for streaming analyses in TT operations at JET”, 15th International Symposium on Fusion Nuclear Technology (ISFNT-15), Las Palmas de Gran Canaria, Spain, 10-15 September 2023 – submitted to Fusion Engineering and Design.

Report on the IPPLM – IFJ measurements of the samples following DTE2 and techniques for low activation measurements

Authors: Renata Kierepko, Jerzy W. Mietelski, Arshiya Ahmed, Krzysztof Gorzkiewicz, Anna Wójcik-Gargula

Introduction

The PrIO ACT sub-project aims to irradiate the ITER material components in the JET long-term irradiation station (LTIS) under conditions as close as possible to those expected during the ITER operation. The samples of ITER materials and dosimetry foils were irradiated over 715 days within the 2020-2022 DTE2 (C41), TT (C40B) and DD (C-42) experimental campaigns. The main motivation of this study was to improve confidence in post-irradiation nuclide predictions and residual radiation fields as well as to explore deviations in elemental and impurity composition of materials between different suppliers using nuclear techniques.

Irradiated samples were retrieved from LTIS on 25/09/2022 and distributed among involved European laboratories. A package with 13 samples intended for the measurement at the IFJ PAN (Poland) was delivered in November 2022. The measurements started at the end of 2022 have been continued in 2023. The received set of samples included a.o. SS316L(N), EUROFER, CuCrZr, A-286 alloy as well as tungsten - used in various structural elements of the tokamak vacuum chamber, divertor, toroidal and poloidal field magnetic coils - from various suppliers (Industeel, R Kind GmBh, SIMIC – CNIM, Atmostat, Villares Metals International B.V); and dosimetry foils made of high-purity cobalt and yttrium.

Results

The measurements were performed using a low-background digital gamma-ray spectrometer with passive and active shields equipped with a 30% efficiency HPGe detector with carbon window and ultra–low–level U cryostat (< 1ppb for Th and U in construction materials) produced by Baltic Scientific Instrument (Latvia) [1]. The top view of the detection system and the set of results (activity concentration) for identified isotopes in ITER samples are presented in Figure 1.

These analyses indicated almost the same isotopic composition for all samples with Fe as a major component. In general, in the analysed spectra the gamma-lines from Co-56, Co-57, Co-58, Co-60, Fe-59, Cr-51, Zn-65, Mn-54 and Nb-95 were observed. The presence of Zn-65 or Nb-95 was however not expected based on analysis of materials certificates with their chemical composition (lack of Zn or Cu and Zr or Nb). It was therefore also not predicted in the calculations performed with the use of the FISPACT-II code.

Comparative analyses of the results were performed through the determination of C/E values. Most of the results obtained by FISPACT calculation agreed with those obtained by measurements (C/E ratio close to value 1). The most significant discrepancies were found for two samples: CuCrZr and EUROFER-97. This observation is hypothesised to stem from the inaccuracies in the chemical composition of the samples as well as the overestimation of thermal neutron flux within the MCNP model.

The presence of Zn-65 in the analysed samples has been explained with the use of the SEM-WDS (Scanning Electron Microscopy – Wavelength Dispersive Spectroscopy) technique. The measurements of unirradiated ITER material samples performed at UKAEA (United Kingdom Atomic Energy Authority) indicated the deposition of Cu and Zn on the surface of the samples, which can be related to the brass disposition on the surface of the samples introduced during the cutting of samples with the use of EDM (electrical discharge machining) [2].

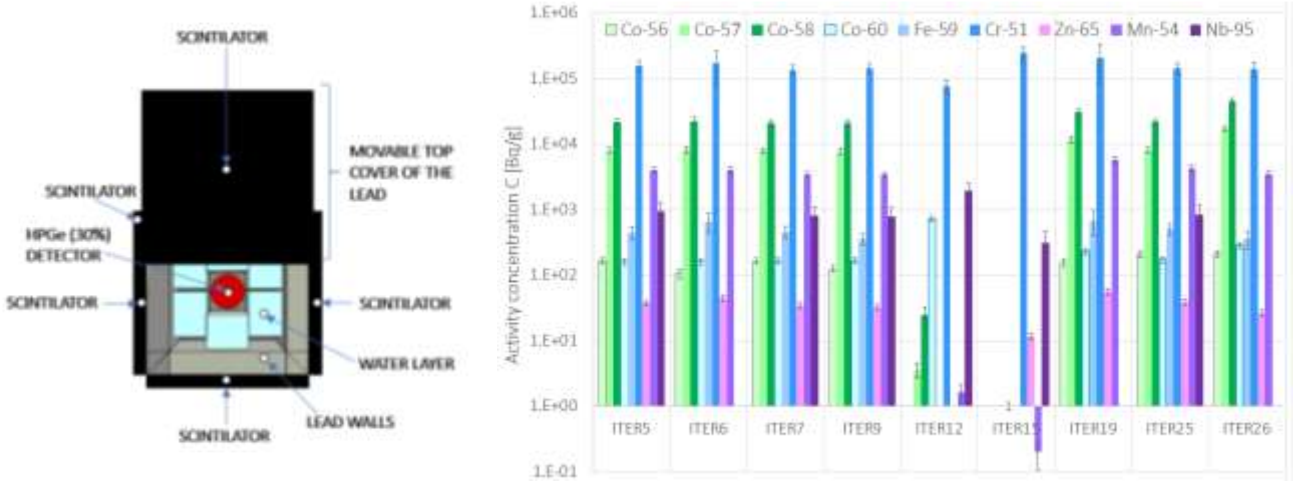

Figure 1. (Left) Top view of the detection system and (Right) Set of results for Co-56, Co-57, Co-58, Co-60, Fe-59, Cr-51, Zn-65, Mn-54, Nb-95 in irradiated ITER samples (data corrected for the reference date (21/12/2022)).

One of the more interesting results obtained in the gamma-ray spectrometry measurements of activated ITER material samples performed in IFJ PAN was the observation of 657.76 keV, 706.676 keV, 763.942 keV, 884.676 keV, 937.485 keV, 1384.293 keV, 1505.028 keV gamma-lines from Ag-110m (T1/2= 245 d) in the irradiated sample of CuCrZr alloy (Figure 2).

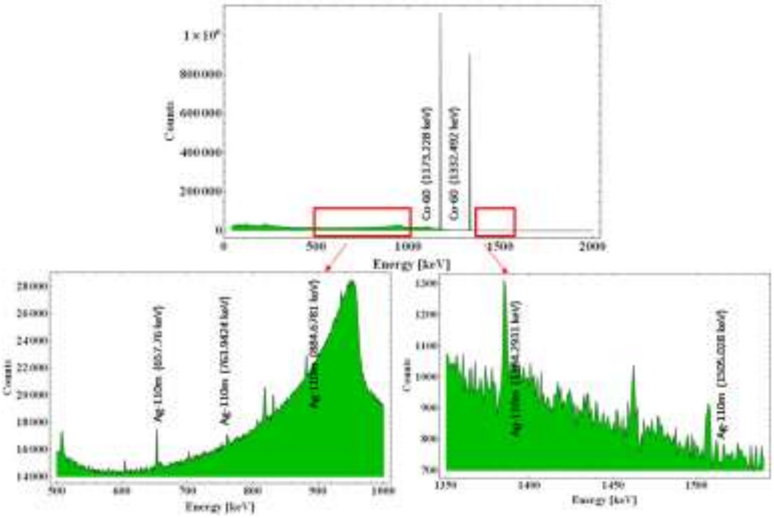

Figure 2. (TOP) Gamma-ray spectrum of ITER#12 sample (position 7-1 in LTIS) with clearly seen Co-60 gamma-lines and (BOTTOM) enlarged fragments of this spectrum in the energy rages from 500 – 1000 keV and from 1350 – 1550 keV with marked gamma-lines from Ag-110m.

IFJ PAN was the first who report such observation. Since only the group from UKAEA confirmed such observation in their re-analysed measurements of CuCrZr samples, IFJ PAN proposed to perform and test the radiochemical procedure shown in Figure 3 to separate Ag fraction and to confirm the presence of Ag-110m in the studied CuCrZr samples. Application of the proposed radiochemical procedure allowed for improving the ratio of the activity of Ag 110m to the activity of Co-60 about 1600 times (activity ratio before to activity ratio after radiochemistry. The identification of Ag-110m in CuCrZr sample suggested also the possibility of other long-lived silver isotopes being present in this irradiated material such as e.g. Ag-108m (T1/2= 438y). The thermal-neutron capture cross-section for the production of Ag-108m is (0.477±0.033)b [3]. Due to the long half-life of Ag-108m, this has not been confirmed in the measurements carried out so far.

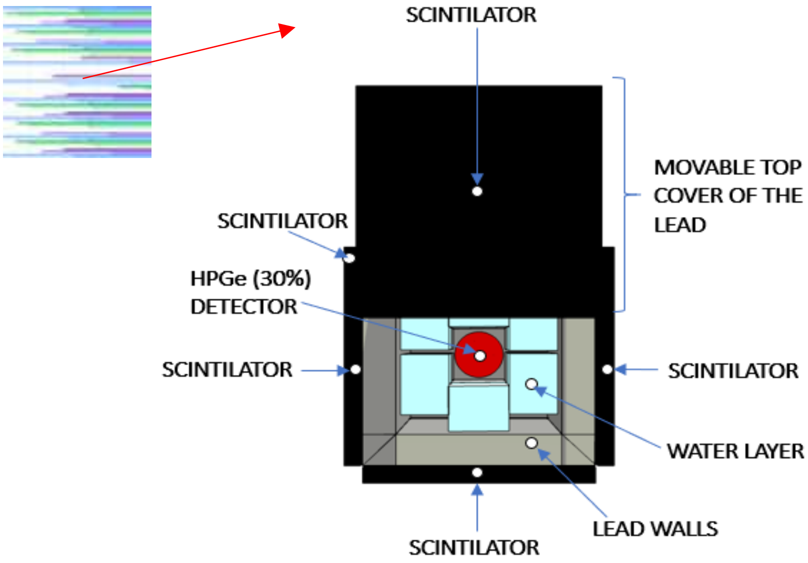

Figure 3. Procedure of Ag fraction separation from CuCrZr ITER sample used at IFJ PAN.

Conclusions

The gamma-spectrometry analyses showed almost the same isotopic composition for all ITER samples with Fe as a major component. Identification of unexpected isotopes like Ag-110m indicates the need to use some analytical methods (such as e.g. XRF or ICP-MS) to verify the certificates of the studied materials. Confirmation of the presence of Ag-110m also confirms the presence of another long-lived silver isotope: Ag-108m. The presence of silver isotopes in irradiated copper-based alloys means an additional contribution to long-lived radioactive waste from the ITER tokamak, which should be taken into account in the planned radioactive waste management strategy. Further investigations into the chemical composition of the materials and overestimation of thermal neutron flux within the MCNP model may be warranted to enhance the precision of future predictive modelling in similar irradiation scenarios.

Collaboration

UKAEA, ENEA, NCSRD, IPPLM

References

[1] K. Gorzkiewicz et al., Low background digital gamma-ray spectrometer with BEGe detector and active shield: commissioning, optimisation and software development, Journal of Radioanalytical and Nuclear Chemistry (2019) 322:1311–1321, https://doi.org/10.1007/s10967-019-06853-7

[2] C. Grove, C. Nobs, L. Packer, T. Turner, “Report on the removal of ACT holder from JET and UKAEA measurements of ITER material foils”, IDM Ref.: EFDA_D_2Q9LLD

[3] M. Gavrilas, V. P. Guinn, „Environmental importance of the $^{07}\mathrm{Ag}(n,\gamma)^{108}\mathrm{Ag}^{m}$ reaction in nuclear power reactors and new $\sigma_{\gamma}^{0}$and I_{γ} measurements”, Journal of Radioanalytical and Nuclear Chemistry, Articles, Vol. 113, No. 2 (1987) 327-332

Related 2023 articles and conference presentations:

1. L. Packer et al., ITER materials irradiation within the D–T neutron environment at JET: Post-irradiation analysis outcomes and recommendations”, conference presentation at 29th IAEA Fusion Energy Conference (FEC 2023), 16–21 October 2023, London, UK
2. L. W. Packer et al., „ITER materials irradiation within the D-T neutron environment at JET: post-irradiation analysis outcomes and recommendations", submitted to Nuclear Fusion (02.01.2024)

Research Unit: Institute of Nuclear Physics Polish Academy of Sciences (IFJ PAN)

WPTE: Tokamak exploitation

Title: Tokamak exploitation

Author: A. Jardin

Introduction

In this work package, we perform preparation of experiments and data analysis of plasma discharges on WPTE tokamaks (TCV, WEST, AUG, MAST-U). In 2023, the contribution was devoted to TCV and WEST devices, through X-ray plasma tomography for impurity transport studies and identification of internal transport barriers from kinetic profiles, in the research topics RT22-04 “Physics-based machine generic systems for an integrated control of plasma discharge” [1] on WEST and RT22-08 “Physics and operational basis for high beta long pulse scenarios” [2] on TCV.

Summary

The work for RT22-04 was restricted in 2023 to data analysis and interpretation of the WEST DTOMOX and GEM diagnostics, in order to study impurity radiation and transport by SXR tomography during plasma ramp-up and H-mode entry, in link with the scientific objectives D2 and D5:

D2*. Develop machine independent strategies for the H-mode entry and exit and off-normal events supported by modelling*

D5. Optimize plasma start-up and current ramp-up schemes supported by modelling in ITER like scenarios

On TCV, the work was focused the analysis of selected shots of the RT08 December 2022 session, see Table 1. Overviews of RT08 results were presented in [4-6]. Two aspects were investigated: data analysis and interpretation of the TCV RADCAM diagnostic to study X-ray plasma emissivity distribution and MHD activity by tomographic inversion, and the identification of Internal Transport Barriers (ITB) during high-beta long pulse, in link with the scientific objectives D2 and D4:

D2. Quantify the compatibility of high b long pulse with mitigated ELMs and/or with exhaust in metallic wall devices.

D4. Develop projection schemes of long pulse at high beta as potential reactor scenario.

Summary of the analysis and observations, presented at a WP-TE progress meeting [7]:

- the dynamics of SXR power and emissivity profile was calculated,
- SXR spectra are calmer for shots with higher performance,
- based on ref. [3], an attempt to produce ρ_{T*} maps and observe some ITB dynamics (criteria on $\rho_{T,ITB*}$ and ε_T may be refined),
- ITBs seem to start during ECRH at mid-radius between q=1 and q=3/2, then progressively shift towards the plasma edge,
- positive correlation of ITB strength (ρ_{T*}) with normalized beta for electrons.

Table 1. TCV discharges performed at the RT08 December 2022 session

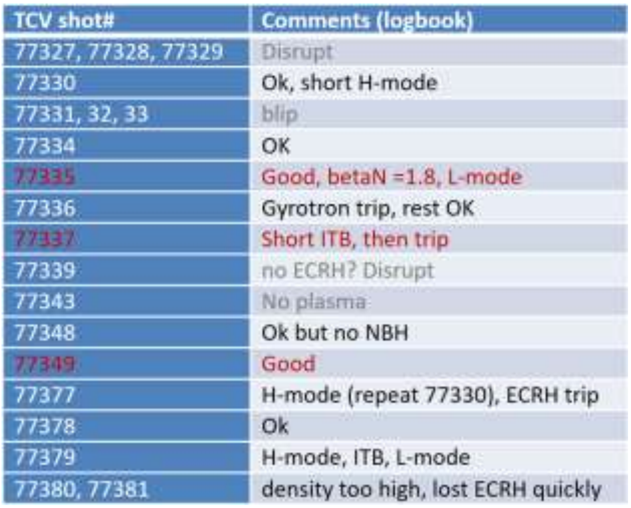

TCV shot#	Comments (logbook)
77327, 77328, 77329	Disrupt
77330	Ok, short H-mode
77331, 32, 33	blip
77334	OK
77335	Good, betaN =1.8, L-mode
77336	Gyrotron trip, rest OK
77337	Short ITB, then trip
77339	no ECRH? Disrupt
77343	No plasma
77348	Ok but no NBH
77349	Good
77377	H-mode (repeat 77330), ECRH trip
77378	Ok
77379	H-mode, ITB, L-mode
77380, 77381	density too high, lost ECRH quickly

Figure 1 depicts the time evolution of the profiles of ρ_{T*} and of the SXR emissivity during the discharge #77349, showing the appearance of ITB at mid-radius. A time slice of the ρ_{T*} and T_e profiles at t = 1.3 s is also presented.

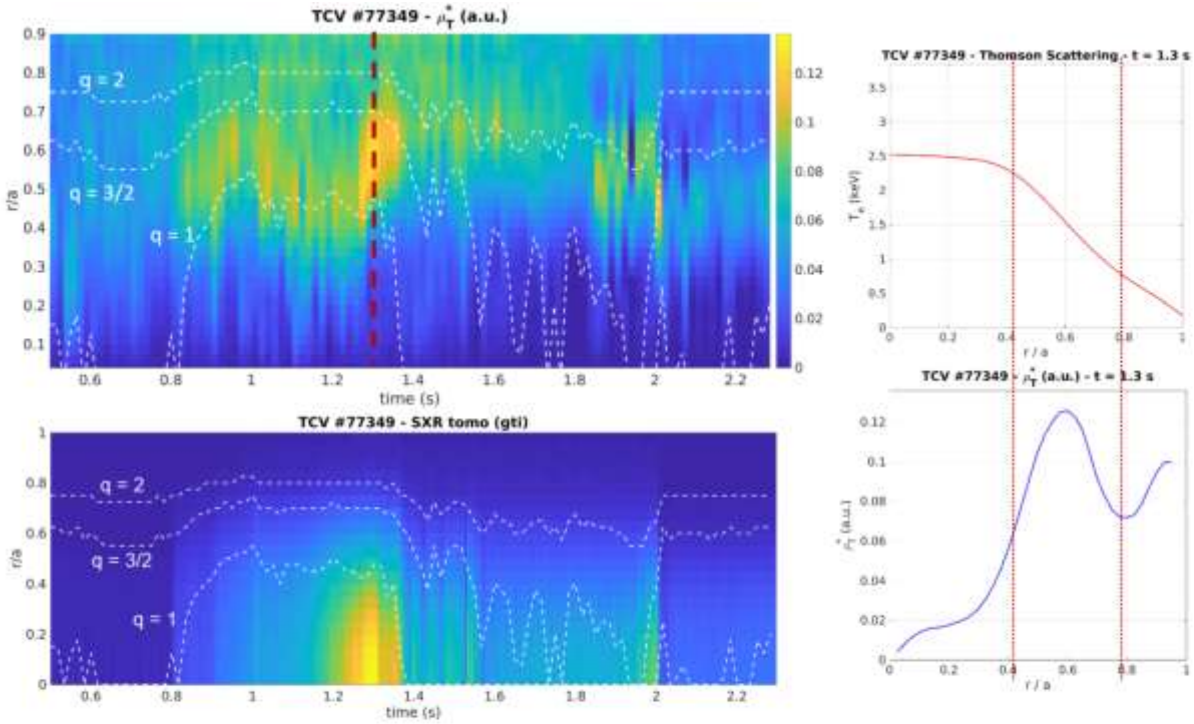

Figure 1. Left: time evolution of SXR emissivity and ρ_{T*} profiles in TCV #77349.
Right: ρ_{T*} and T_e profiles at t = 1.3 s.

Perspectives

The analysis could benefit from some transport studies (e.g. turbulence) that would confirm local reduction of transport and ITB formation. Cross-validation of measured profiles with other diagnostics (ECE, T_i measurements) would strengthen the results, as well as a comparison of different inversion methods (e,g. with anisotropic regularization). There is also the suggestion to use synthetic diagnostic tools to compare the dynamics and identify impurity influx.

New dedicated experiments are foreseen in 2024 on TCV and WEST in the research topics RT04 and RT08, that will require some data analysis.

Collaboration

The experiments are performed on the WP-TE tokamak facilities, therefore in collaboration with the IRFM-CEA, IPP Garching and SPC Lausanne institutes, in the framework of the EUROFusion programme.

References

[1] https://wiki.euro-fusion.org/wiki/WPTE_wikipages:_Experimental_campaign_2023:_RT22_04

[2] https://wiki.euro-fusion.org/wiki/WPTE_wikipages:_Experimental_campaign_2023:_RT22_08

[3] G. Tresset et al., Nucl. Fusion 42 (2002) 520.

[4] C. Piron, (A. Jardin) et al., in Proc. of 49th EPS Conf. on Plasma Physics (2023).

[5] I. Voitsekhovitch, (A. Jardin) et al., in Proc. of 49th EPS Conf. on Plasma Physics (2023).

[6] S. Coda, (A. Jardin) et al., in Proc. of the 29th IAEA Fusion Energy Conference (2023).

[7] A. Jardin et al/, *Preliminary analysis of ITB identification and SXR measurements*, TCV WPTE-RT22-08 progress meeting, 2023 Feb 10th.

UoS: University of Szczecin

WPW7X: W7X Exploitation

Title: Analysis of the heat flux distribution on W7-X divertor tile

Author: M. Ślęczka, M. Jakubowski, B. Zamorski

Introduction

Understanding the interaction between plasma parameters and the strike line behaviour is crucial for maintaining safe power exhaust in fusion reactors, like the Wendelstein 7-X (W7-X), which employs an island divertor for heat flux management. Modelling the plasma boundary's complex three-dimensional nature is challenging. Using analysis tools like Proper Orthogonal Decomposition (POD) to study these interactions provides valuable insights, essential for optimising plasma control. W7-X's ten water-cooled divertor units, observed by IR cameras, are central to this effort. The substantial data collected reveal the intricacies of plasma behaviour, underscoring the need for a more thorough theoretical understanding. Research into the role of control coils, especially their influence on magnetic island dynamics, is fundamental for divertor operation and reactor safety.

Results

Our research employs Proper Orthogonal Decomposition (POD) to dissect the intricate dynamics of divertor heat flux distributions. In stellarators like Wendelstein 7-X (W7-X), the complexity of the three-dimensional field makes it difficult to predict heat and particle loads accurately, often exceeding the capabilities of standard models.

High-dimensional data, such as those obtained from IR camera systems, can be effectively analysed using the Proper Orthogonal Decomposition (POD) method. This method reduces the data into a low-dimensional approximation, simplifying the complex behaviour of plasma systems and uncovering deterministic patterns in what appear to be random phenomena.

Specifically, this work concentrated on the program where control coils were used in AC mode, as demonstrated in the 20180816.016 discharge. Figure 1 shows an overview plot of this discharge, where ECRH reached up to 3 MW and I_{tor} 8 kA, lasting about 16 seconds. The discharge was performed in an asymmetric scenario, with phase-shifted control coil currents between the upper and lower modules. We created a data matrix to average the wetted area on W7-X divertors, analyzing upper and lower divertor data separately to address complex configurations and minimise error field inaccuracies. This matrix helps to understand diverse behaviours across divertor regions and to reduce data inconsistencies, providing a spatial-temporal comparison of upper and lower divertors and facilitating a comprehensive analysis of plasma-divertor interactions (Fig. 1 left).

POD modes were calculated and are presented in Fig 2 (middle). The contribution ratio of each modes were also calculated. Each mode's contribution, in descending order of magnitude, is essential optimizing mode selection in data set reconstruction. Additionally, beyond a certain point, further modes have negligible effects, as their values fall below the level of experimental measurement. Third mode reconstructs original dataset with a substantial accuracy of 8.3%. Furthermore, taking into account all three modes gives almost 95% accuracy. It is visible also that only first two time coefficients change in time (Fig.2 lower plot) and rise with wetted area for TM2h (lower divertor).

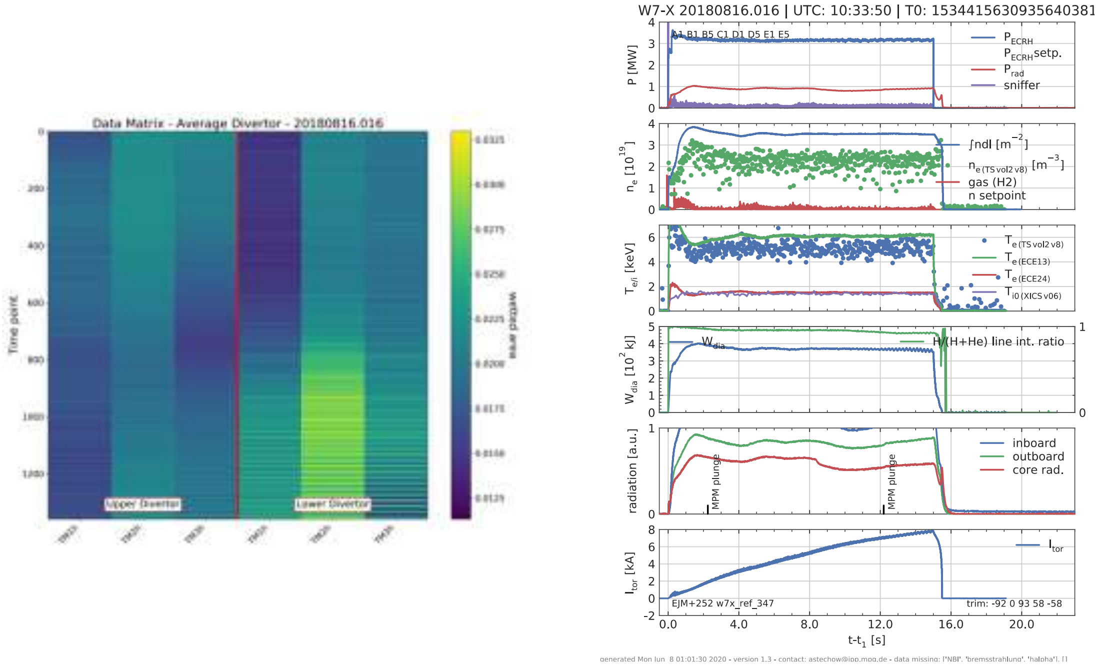

Fig. 1 Data matrix of wetted area calculated from the average divertor for campaign OP 1.2b (left). Discharges were performed with control coils with AC scenario. Overview plots for main plasma parameters (right).

The influence of the additional magnetic field generated by control coils is manifested by the oscillation of the toroidal current (Fig 1, left). We have noticed that the oscillation is stronger when the control coils are in-phase compared to the off-phase scenario. It is clearly seen in Fig. 4 where the overview plots of the 20221201.054 discharge is presented. The averaged temperature as well for upper as for lower divertor module oscillates also.

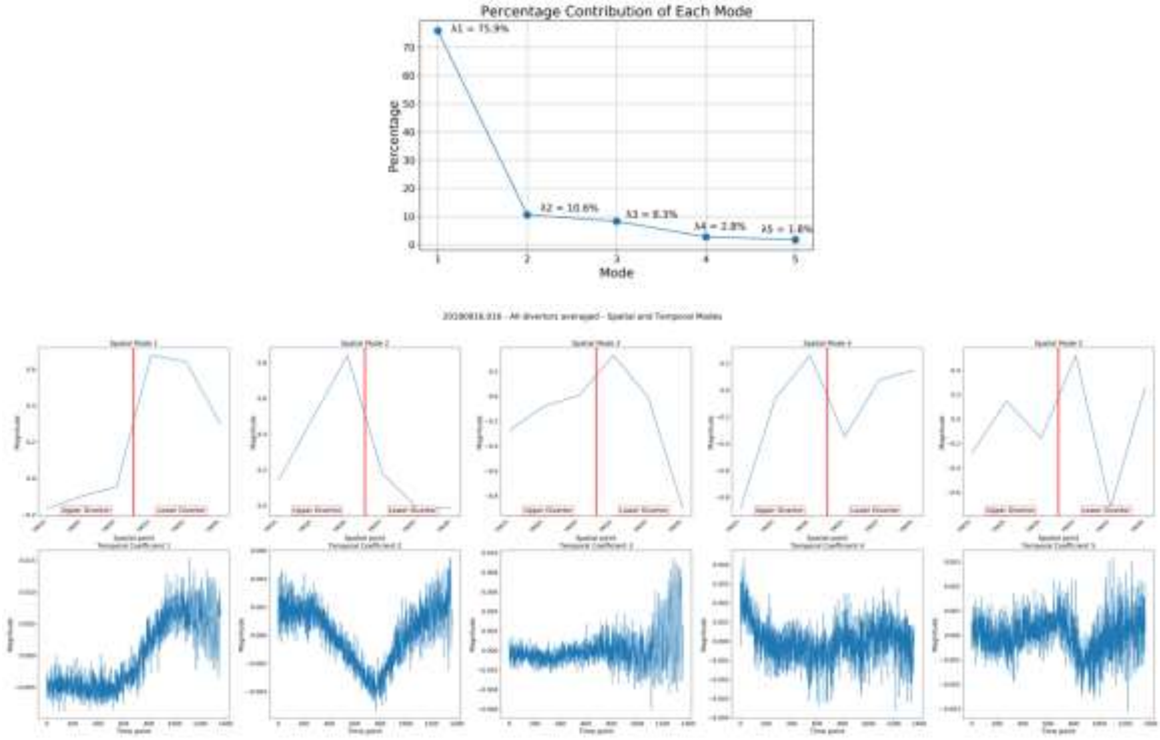

Fig. 2 Discharge number #20180816.016. Contribution ratio of each POD mode. Essentially, the first two modes determine variation of the wetted area (top). Spatial vectors and time coefficient of the POD are plotted for the first five modes. It is clearly visible that the first two time coefficients oscillate in time (bottom).

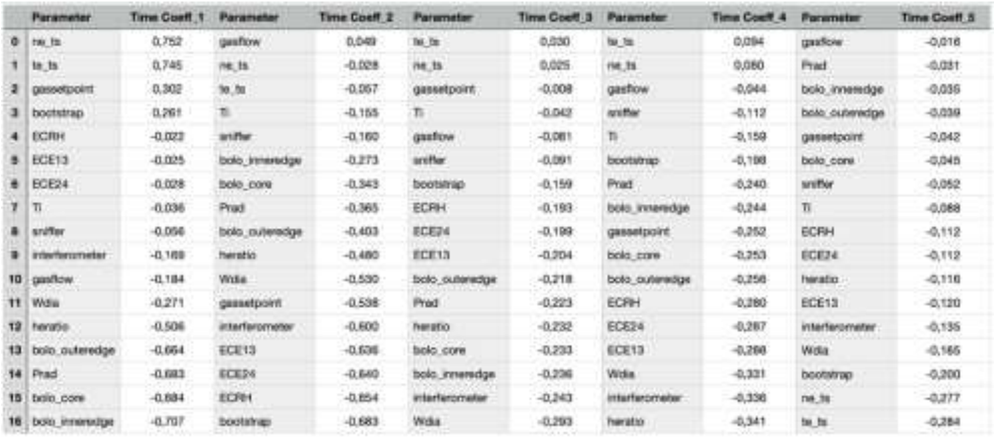

	Parameter	Time Coeff_1	Parameter	Time Coeff_2	Parameter	Time Coeff_3	Parameter	Time Coeff_4	Parameter	Time Coeff_5
0	ne_ts	0,752	gasflow	0,049	te_ts	0,030	te_ts	0,094	gasflow	-0,016
1	te_ts	0,745	ne_ts	-0,028	ne_ts	0,025	ne_ts	0,080	Prad	-0,031
2	gassetpoint	0,302	te_ts	-0,057	gassetpoint	-0,008	gasflow	-0,044	bolo_inneredge	-0,035
3	bootstrap	0,261	Ti	-0,155	Ti	-0,042	sniffer	-0,112	bolo_outeredge	-0,039
4	ECRH	-0,022	sniffer	-0,160	gasflow	-0,081	Ti	-0,159	gassetpoint	-0,042
5	ECE13	-0,025	bolo_inneredge	-0,273	sniffer	-0,091	bootstrap	-0,198	bolo_core	-0,045
6	ECE24	-0,028	bolo_core	-0,343	bootstrap	-0,159	Prad	-0,240	sniffer	-0,052
7	Ti	-0,036	Prad	-0,365	ECRH	-0,193	bolo_inneredge	-0,244	Ti	-0,068
8	sniffer	-0,056	bolo_outeredge	-0,403	ECE24	-0,199	gassetpoint	-0,252	ECRH	-0,112
9	interferometer	-0,169	heratio	-0,480	ECE13	-0,204	bolo_core	-0,253	ECE24	-0,112
10	gasflow	-0,184	Wdia	-0,530	bolo_outeredge	-0,218	bolo_outeredge	-0,256	heratio	-0,116
11	Wdia	-0,271	gassetpoint	-0,538	Prad	-0,223	ECRH	-0,280	ECE13	-0,120
12	heratio	-0,506	interferometer	-0,600	heratio	-0,232	ECE24	-0,287	interferometer	-0,135
13	bolo_outeredge	-0,664	ECE13	-0,636	bolo_core	-0,233	ECE13	-0,288	Wdia	-0,165
14	Prad	-0,683	ECE24	-0,640	bolo_inneredge	-0,236	Wdia	-0,331	bootstrap	-0,200
15	bolo_core	-0,684	ECRH	-0,654	interferometer	-0,243	interferometer	-0,336	ne_ts	-0,277
16	bolo_inneredge	-0,707	bootstrap	-0,683	Wdia	-0,293	heratio	-0,341	te_ts	-0,284

Fig 3. Correlation coefficients between the POD time coefficient and plasma parameters for discharge #20180816.016

The analysis of the relationship between plasma parameters and temporal coefficients for discharge number 20180816.016 is presented in Figure 3. It reveals that the toroidal current has a weak correlation (0.26) with the first mode but shows a strong anticorrelation (-0.683) with the second one. In contrast, a significant correlation (0.75) is observed between the first temporal coefficient and the electron density, which remained consistent throughout the discharge. This is in stark contrast to the relationship between the first temporal coefficient and P_{rad}, where a strong anticorrelation (-0.68) is distinctly evident.

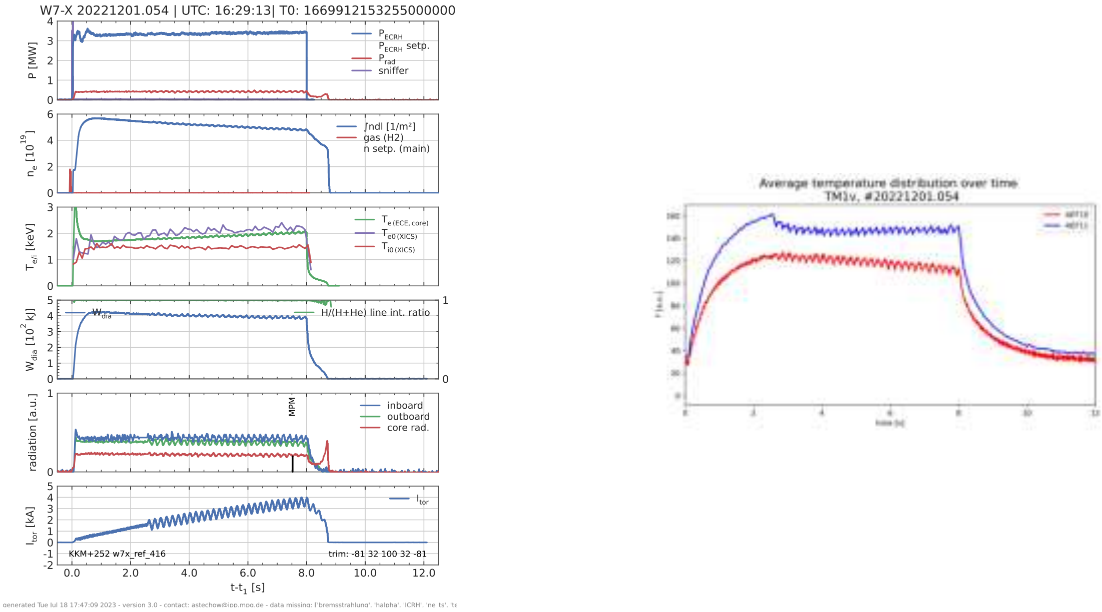

Fig. 4 Preliminary results from the campaign OP2.1. Left: main plasma parameters. Right: time evolution of the temperature on the divertor's surface localized in the target module TM1v (vertical module) is presented. It is clearly noticeable that the temperature is oscillating with the toroidal current what is connected with the magnetic island evolution caused by additional magnetic field generated by the control coils in the AC mode.

In the currently presented work on the analysis of plasma behaviour in W7X, Proper Orthogonal Decomposition (POD) was utilized to investigate the complex dynamics of divertor heat flux distributions. While POD provided valuable insights, particularly in establishing correlations between plasma parameters, it fell short in capturing the full dynamical behaviour of plasma.

The POD method, although efficient in data reduction and revealing dominant patterns, essentially offers a static snapshot, lacking the ability to accurately capture the temporal evolution and dynamic processes of plasma flow. This limitation becomes particularly evident in the context of magnetic confinement devices, where plasma behaviour is inherently dynamic and complex. The method's reliance on static modes means it cannot effectively model the time-dependent aspects of plasma behaviour, which are crucial for a deeper understanding of plasma dynamics in devices like tokamaks and stellarators.

To overcome the limitations of Proper Orthogonal Decomposition (POD), we propose employing Dynamic Mode Decomposition (DMD). DMD is adept at analysing dynamic systems, capturing their spatial and temporal dynamics by breaking down plasma flows into modes linked with specific frequencies and growth rates. Adopting DMD would improve the modelling of plasma's time-sensitive behaviours, enriching our grasp of its transient dynamics and reactions to changes. This shift to DMD could significantly refine our analyses and enhance the control of plasma dynamics in fusion research.

Conclusions

We applied the POD method to discharges where control coils were in AC mode. This mode changes the magnetic field topology over time, causing the strike line to sweep across the divertor surface. Additionally, a clear oscillation of I_{tor} was observed. The impact of the control coils was noticeable during the discharge and in the subsequent data analysis, particularly in the changes observed in the POD time coefficients, primarily the first order. We have shown that the first two modes accurately describe over 85% of the variation in the wetted area. Our analysis of the correlation between plasma parameters and POD time coefficients underlines that a limited number of modes can significantly elucidate plasma dynamics, as evidenced in Figures 2 and 3. Additionally, the correlation coefficient effectively identifies which plasma parameters have a substantial impact on the dynamics of the wetted area.

In addition to our findings using the POD method, it's important to recognise the limitations of this approach, particularly in capturing the full dynamic behaviour of plasma in magnetic confinement devices. To address these limitations, the use of Dynamic Mode Decomposition (DMD) is recommended. DMD excels in analysing complex systems by not only capturing spatial features but also temporal dynamics, crucial for understanding the rapidly evolving plasma behaviours in devices like W7-X. By decomposing plasma flow into modes associated with specific frequencies and growth rates, DMD offers a more comprehensive picture of plasma behaviour over time. Transitioning to DMD in future research could lead to more accurate models of plasma dynamics, facilitating better control and understanding of the processes at play in fusion reactors.

Collaboration

M. Jakubowski, Y. Gao, A. Puig Sitjes – IPP
S. Masuzaki, H. Tanaka - NIFS

References

[1] A. Puig Sitjes et. al, *Observation of thermal events on the plasma facing components, JINST* **14** C11002 (2019)

[2] H. Tanaka et. al, *Characterised divertor footprint profile modification with the edge pressure gradient in the Large Helical Device, Plasma Phys. Control. Fusion* **60** 125001 (2018)

[3] H. Tanaka et. al, *Analysis of indefinite divertor footprint with proper orthogonal decomposition in hydrogen/deuterium plasmas in LHD, Nucl. Mater. Energy* **19** 378-383 (2019)

Related 2023 articles and conference presentations:

1. B. Zamorski, M. Ślęczka, M. Jakubowski, A. Puig Sitjes, Y Gao and W7-X Team, *Dependence of strike line characteristics on plasma parameters as seen through proper orthogonal decomposition*, 49th Conference on Plasma Physics, Boradeaux, France, 3-7 VII 2023 (poster)
2. M. Ślęczka, M. Jakubowski, A. Puig Sitjes, Y. Gao, B. Zamorski and W7-X Team, *Usability of the control coils in terms of modification of the strike line pattern,* PLASMA 2023, International Conference of Research and Application of Plasma, Warsaw, Poland, 18-22 IX 2023 (poster)

TUL: Łódź University of Technology

WPDC: Diagnostic and Control

Title: Design activities for Prad (Radiated Power and Soft X-ray Core Intensity) diagnostics

Author: Dariusz Makowski

Introduction

The overall goal of this work package is to prepare the Prad diagnostic necessary for the operation and control of DEMO tokamak. DEMO will rely on a range of diagnostic systems to control the plasma during operation. These include radiated power (Prad) and core soft X-ray intensity diagnostic systems, which measure photons from the plasma. Radiated power measurement contributes to H-mode control by measuring the plasma core's radiated power as input to calculate the power above the separator. This task is realised by IPPLM and TUL. TUL is involved in specification development, analysis of radiation detectors suitable for Prad diagnostics, design of a real-time I&C system for Prad, and development of a prototype data acquisition system for testing GEM and LVIC detectors. The prototype of GEM detector including the data acquisition and processing system is planned to be developed in 2023 and 2024.

Results

In 2023, scientists from the TUL-DMCS were responsible for update of the specifications for Soft X-ray (SXR) detectors, taking into account the magnetic field, gamma radiation doses and neutron fluences generated during the operation of the DEMO tokamak. The missing information and corrections reported by reviewers were implemented. The report was updated taking into consideration the latest results for GEM and LVIC detectors.

Within the year the initial design was finalised and all the considered hardware components were purchased. The 8-channel front-end module was designed and manufactured. Finally the test stand for testing the GEM prototype was developed at Lodz University of Technology, Department of Microelectronics and Computer Science (TUL-DMCS). First signals were collected from function generator, oscilloscope etc. Once preparations are completed this year, thorough testing of the IPPLM to-be-produced GEM detector prototype is scheduled for 2024.

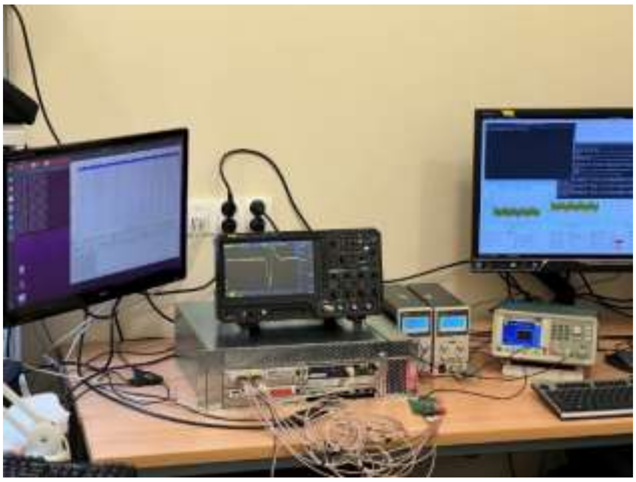

Figure 1. Test-stand build at TUL-DMCS laboratory.

All hardware components except the Adnaco FMC168 module were ordered according to the plan. The Adnaco company refused to sell a single FMC168 module, the Minimum Order Quantity (MOQ) is 4.

However, during the development and tests FMC168 module from TUL-DMCS laboratory was used. The module will be used also in 2024.

Additional tests were conducted at IPPLM laboratory with the model GEM detector. This made it possible to evaluate the raw signals obtained from a model detector irradiated with a laboratory ^{55}Fe radiation source. The block diagram of the data acquisition is shown in Fig. 2.

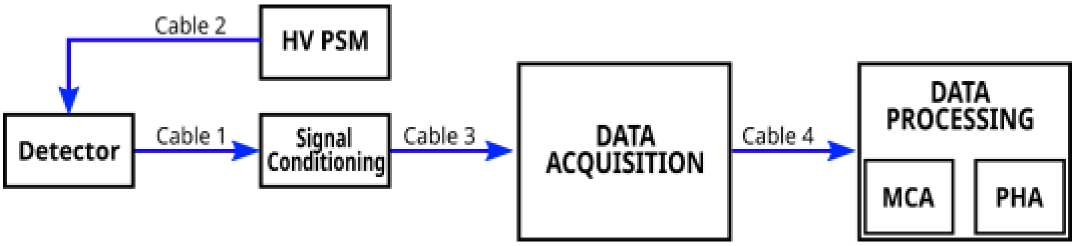

Figure 22 A block diagram of GEM detector data acquisition and processing system.

As a result this work 3 documents were provided:

1. Final report on specification for radiation detectors and verification of their suitability for Prad system, EFDA_D_2PF76N v1.1
2. Design Description Document of Radiated Power and Soft X-ray Core Intensity System, EFDA_D_2MYU3T v1.4
3. Report on the grant deliverable DC.T.01-002, EFDA_D_2PGAQU v1.1

Conclusions

The final report on specification for radiation detectors and verification of their suitability for Prad system was updated according to the current state-of-the-art including the requested corrections. Both GEM and LVIC detector seems to be suitable for Prad diagnostics.

The concept for Prad I&C readout for GEM detector was developed. The prototype for GEM detectors testing will be developed and build in 2023-2024. In 2023 the hardware components for GEM data acquisition and processing were purchased and the test setup was developed at TUL-DMCS. More tests are planned in 2024 when the first prototype of GEM detector will be manufactured.

Collaboration

Work on the Prad diagnostic system for the DEMO project was carried out in a close cooperation with the Institute of Plasma Physics and Laser Microfusion in Warsaw and institution involved in WPDC package.

References

[1] Final report on specification for radiation detectors and verification of their suitability for Prad system, EFDA_D_2PF76N v1.1
[2] Design Description Document of Radiated Power and Soft X-ray Core Intensity System, EFDA_D_2MYU3T v1.4
[3] Report on the grant deliverable DC.T.01-002, EFDA_D_2PGAQU v1.1

PCSS: Poznan Supercomputing and Networking Center

WPAC: Advanced Computing

Title: Hub (ACH-04) and Data Management Plan

Authors: Marcin Płóciennik, Michał Owsiak

Introduction

Advance Computing Hubs are supporting the EUROfusion researchers in different domains. ACHs provide essential expertise and support in computer science, scientific computing, data management, code integration, and software engineering for the entire E-TASC (EUROfusion – Theory and Advanced Simulation Coordination) initiative and the EUROfusion Theory and Simulation programme. The consortium of partners led by PSNC has been selected in 2021 as the host for one of the hubs in the area of the Integrated Modelling and Control. The PSNC ACH is joined effort of the PSNC, IPPLM, Chalmers/VR, CEA and IST.

The main objectives of the PSNC /IPPLM ACH(ACH-04) are:

- IMAS ecosystem development
- provide support for developers in terms of code adaptation to IMAS,
- provide help during integration process (integration of codes within IMAS based workflows),
- take care of the management of the source code repository for the community developed research software,
- provide production support of the integrated modeling tools, user support and training.

Main focus on the ACH-PSNC/IPPLM activities in 2023 was put on: IMAS ecosystem development, providing support for developers in terms of code adaptation to IMAS, user support and training, code repositories. These activities were addressed in cooperation with various TSVVs. In 2022 in particular the focus was on collaboration with TSVV-11(DYON, HFPS), TSVV-08(JOREK), TSVV-03, TSVV-05 (EIRENE), TSVV-09(DREAM), TSVV-10 (HYMAGYC), TSVV-12(ASCOT). PSNC ACH(ACH-04) participated in developments related to containerization, installation/upgrade of libraries and software packages, configuration of the environment, CI/CD setup and tutorials development. Continued maintenance and development for the WP CD developed workflows is provided by the ACH, mainly European Transport Simulator (ETS) and MHD equilibrium reconstruction and stability workflows.

The tasks also included support in the implementation of the data management plan for EUROfusion - Data Management Plan.

Results

The 2023 activities has been grouped in 6 kind of tasks, their main results are presented below. Many of those tasks are the joined efforts of the partners. It is also clearly marked which of the tasks are being managed by ACH partners other than PSNC, but they are presented here to show the comprehensive overview of the activities and results.

Developments, deployments, support and maintenance of IMAS Ecosystem Infrastructure (to be applicable to ALL CODES)

ACH-04/IPPLM-PCSS has participated in numerous activities related to adapting existing codes into IMAS infrastructure. One of the core activities of ACH-04 is the maintenance of IMAS infrastructure at Gateway. This activity involved a few tasks: installation of IMAS platform, investigation of SPACK based installation procedure, investigation of EasyBuild based procedure. SPACK based releases were provided on: Gateway, Marconi and Leonardo. Apart from that, Gateway was updated with number of IMAS releases: IMAS 3.37.1/4.11.1, IMAS 3.38.1/4.11.1, IMAS 3.38.1/4.11.3, IMAS 3.38.1/4.11.4, IMAS 3.39.0/4.11.6, IMAS 3.39.0/5.0.0. In addition to IMAS, a number of components were upgraded to the most recent releases: iWrap, IDSTools, Boost, MUSCLE3, IMASPy. ACH-04 maintains Docker based releases of IMAS - they were updated to AL 5. Furthermore, UDA is now included and tested for AL 5. It became an integral part of imas/ual Docker images. Docker images (imas/ual) are now an integral part of projects: JINTRAC, DMP. Custom image building scripts were replaced with bleeding-edge Docker Bake. Additionally, Docker images have been provided and are maintained for these tools for both Access Layer 4 and 5: IDSTools, Muscle3, FC2K, iWrap , Kepler

Thanks to integration with Gitlab Pages it is also possible to build, release and publish source code documentation directly inside CI/CD plans. Support for the users was provided via JIRA system installed at: https://jira.eufus.psnc.pl/browse/ACH04SUPP

In 2023 ACH-03 started and pursued activities towards automated release of IMAS infrastructure based on SPACK and EasyBuild. Environments were prepared using SPACK on GW, MARCONI and LEONARDO: IMAS 3.37.0/4.11.0 - gcc/oneapi, IMAS 3.38.1/4.11.0 with ggd/1.10.3, amns/1.4.0 and xmllib/3.3.1 - dependencies: gcc/oneapi. A step-by-step guide (https://gitlab.eufus.psnc.pl/-/snippets/26) on how to prepare such an environment was prepared. MUSCLE3 tutorial (https://gitlab.eufus.psnc.pl/g2knizn/muscle3-tutorial) in the form of code samples was prepared. There are examples of unified and robust coupled simulations demonstrating integration of the codes with IMAS, iWrap and Docker. It is possible to run samples in various environments: Gateway, SDCC and local machine (for Docker example). As a part of proof of concept, we have created Docker image containing Helena codes.

Adaptation of codes to IMAS

One of the tasks performed by the whole ACH-04 team is support in the process of adapting physical codes to the IMAS platform. In 2023, the implementation of this task included the following applications: ASCOT5, BEAMS3D, VMEC, DYON, EIRENE, ERO2.0, SPICE2, MEMOS-U, SDTrimSP, RAVETIME,FELTOR, GBS, GRILLIX, SOLEDGE3X, GENE, ORB5, GRILLIX, GYSELA, GVEC , HYMAGIC, JOREK, LIGKA, ORB5. Due to the varying degree of advancement of work in this area, ACH-04 activities included:

- analysis of requirements for individual computational models,
- implementation of interfaces between computational models and the IMAS platform,
- implementation of interfaces directly between computational models,
- adaptation of data structures (so-called Data Dictionary) to new model requirements,
- implementation of extensions of the IMAS platform resulting from new requirements of physical applications,
- adaptation of the IMAS platform to solutions based on containerization,
- improvement and adaptation of the ETS platform to the latest solutions offered by the IMAS platform,
- organizing working meetings (both online and on-site),
- preparation of online training regarding the process of adapting physical codes to the integration process with the IMAS platform.

Support related to HFPS workflow development

The implementation of Continuous Integration and Continuous Deployment (CI/CD) for the HPFS project has been meticulously established, centering around the HFPS mirror hosted on the GitLab repository at gitlab.eufus.psnc.pl. This robust CI/CD infrastructure ensures the seamless integration of changes, rigorous testing, and efficient deployment of the IMAS based HFPS. To enhance the versatility and capabilities of the CI/CD environment, a privileged GitLab runner is employed. This runner is configured with elevated permissions, enabling it to execute tasks that require additional privileges, such as interacting with the underlying system or utilising certain features within Docker containers. The use of a privileged GitLab runner is particularly beneficial when working with Singularity inside Docker.

Docker based images of `IMAS` were extended with `Muscle 3` components. This activity was later extended with multi container based approach. This resulted in producing a multi container, IMAS based solution managed and executed using `Muscle 3` manager. On top of that, Singularity solution was also delivered.

Performance tests for JINTRAC were prepared. The entire JINTRAC was tested, and a performance comparison was conducted depending on the used backend (HDF5, MDSPLUS) and the data retrieval method (get, partial_get). The results and testing methodology were described at following location: https://confluence.eufus.psnc.pl/display/PSNCACH04/Python+profiling#Pythonprofiling-Testingdescription.

Support for DATABASES related activities.

CSV based export was heavily improved and adapted to most recent requirements of Pedestal DB. Development was discussed and analysed as part of ACH-04 activities and then implemented.

Provision of Devops environment

As part of DevOps related activities, ACH-04-PSCN team have performed a number of activities and have taken numerous actions related to day-to-day maintenance of CI/CD platform. Platform was extended with the Gitlab Pages system (it was integrated with other components). At the moment, the whole software infrastructure consists of: Confluence - system for handling documentation pages (so called WIKI pages), JIRA - system for hosting projects and issues that are raised by users and developers. Gitlab - source control system. Gitlab Pages - tool for publishing automatically generated documentation. In a typical project setup, parts of documentation can be easily generated on top of the source code (e.g. documentation of the API). Gitlab pages fullfill this requirement and provide additional means of documenting the development process - as an addition to the Confluence. All the components are successfully linked with the KeyCloak installation provided by PSNC. This way, it is possible to provide Single Sign On for all these services. It makes the whole experience way more user friendly. All the components, including Gitlab Pages, are hosted using Docker based installation. This way it is possible to perform upgrades very rapidly and in case of issues with a particular release of the platform to revert to the stage before the upgrade. Dedicated tutorials on how to get access and configure a JIRA account were prepared. This includes a description of how to: access the service, request account creation for TSVV/ACH users, prepare documentation in Confluence (starting with a project creation), create and manage projects in JIRA, integrate one's project between Gitlab and JIRA. All the components of the software platform were maintained on a regular basis. As a part of CI/CD plan users can run codes either locally (inside Docker containers) or remotely (on Gateway cluster). Remote execution simulates execution of the code as if run on the Gateway itself. This way, it provides a near to ideal environment for testing purposes.

Data Management Plan implementation

As part of the Data Management Plan project (development of the platform developed in the Fair4Fusion project), the ACH-04 team carried out tasks related to:

- optimization and development of the Fair4Fusion platform,
- installation and implementation of the platform demo installation
- updating the authorization and authentication system included in the solution implemented as part of the project
- development of new functionalities of the Fair4Fusion platform
- removing errors reported by project members and external users
- continuous integration, testing and providing support to users

A number of updates were made as part of the refactoring process. The Simulation Catalog application has been integrated with the latest version of Access Layer (version 5.0). UDA (Universal Data Access) technology is used to transfer data from remote servers. The server part was implemented using Spring Boot 3 and Java (JDK 19) technologies. These updates improved overall performance, introduced new features and improved security of the overall solution. Refactoring the application for cataloging experimental results did not focus solely on the software layer. Performance tests were carried out on various database engines: Elastic Search, HBASE, InfluxDB, PostgreSQL, MongoDB, NoSQL, MariaDB. After a detailed analysis, it turned out that databases based on solutions based on storing data in the form of documents (so-called documenta-based databases) are not the optimal solution for storing data based on time series. It was decided to implement an alternative solution based on the PostgreSQL database. This task included migrating the database schema, adapting application codes to the new database engine and developing components based on containerization.

Conclusions

The activities for 2023 has been grouped into 6 multi-year tasks, many results of those activities has been delivered, with a follow-up in 2024. The IMAS infrastructure ecosystem have been also maintained and upgraded as requested by users. Support to developers and users has continued, mainly driven by tracker systems and a high level of commitment to follow different TSVV's requests. Data Management Plan activities has been carried out introducing changes to the Simulation Catalogue and the F4F Dashboard.,

Collaboration:

CEA, Chalmers, IST

The project activities are co-financed by Polish Ministry of Science and Higher Education from financial resources of the programme entitled "PMW"

ZUT: West Pomeranian University of Technology

WPBOP: Balance of Plant

Title: WCLL BoP Direct with Small Energy Storage Concept Design: PCS design point architecture (“maximum of maximum”) and Gate Cycle Analysis (2023)

Authors: Monika Lewandowska, Leszek Malinowski

Introduction

The Primary Heat Transfer System (PHTS) transfers heat from the reactor sources, namely: Breeding Blanket (BB), Divertor (DIV) and Limiters, to the secondary circuit called Power Conversion System (PCS) in which thermal power is converted into electricity. One of problems faced by the DEMO plant designers is the cyclic tokamak operation: 2-hours long plasma pulses will alternate with dwell phases lasting 10 min. To cope with the drastic power drop of the reactor heat sources during dwell (down to 1 % of the nominal values), an Energy StorageSystem (ESS) filled with Molten Salt (MS) is included in DEMO plantconfigurations. As a result of the DEMO pre-conceptual studies two reference concepts of the BB and the respective PHTS have been selected: the Helium Cooled Pebble Bed (HCPB) with the large ESS and indirect coupling between PHTS and PCS (via the Intermediate Heat Transfer System) and the Water Cooled Lithium-Lead (WCLL) directly coupled to the PCS and with small ESS [1-3].

In 2022 the new DEMO Energy Map was issued, according to which there are significant uncertainties regarding the partition of the fusion power among different reactor sources. Because of these uncertainties 12 possible operational scenarios are considered for each of the HCPB and WCLL variants [4]. Since the Limiters of Plasma Facing Units (PFU) and the Shield Block Limiters require similar cooling conditions as the DIV PFU and DIV cassette (CAS), respectively, they are cooled by the embedded cooling circuits. The thermal power extracted from the Vacuum Vessel (VV) will not be used in PCS, because of its low value and low temperature grade, as compared to the respective values foreseen by the previous DEMO Energy Map.

In 2022 we created the GateCycle (GC) model of the “maximum of maximum” PCS cycle, in which all circuit components were sized to absorb the maximum possible power of all the reactor heat sources (the“max of max” cycle) [5]. We also verified [6] that the proposed PCS can operate according to the A2-1 scenario, in which characteristics of the heat sources was close to those of “max of max” cycle (i.e. thermal power extracted from the BB (Breeding Zone and First Wall) was close to the maximum values that the energy map can envisage).

Recently, however, it was checked that the PCS cycle developed in 2022 was unable to reach the most problematic operational scenario (A1-2), in which the DIV power is the highest, whereas the BB power is the lowest. To cure the observed modification of the PCS configuration was proposed by industry [7]. In the present study we developed the GateCycle model of this updated PCS circuit assuming the “max of max” scenario. Then we verified if the proposed PCS circuit could operate according to the A1-2 scenario.

Results

For the PCS operating according to the “max of max” scenario in the pulse phase we developed the detailed, convergent GC model in “Design” mode, as shown schematically in Fig. 1. This first stage of our analysis provided preliminary sizing of all the circuit components. In the second stage we obtained three convergent “Off-design” cases of this model, corresponding to the: (i) “max of max” - dwell phase, (ii) A1-2 – pulse phase, and (iii) A1-2 dwell phase.

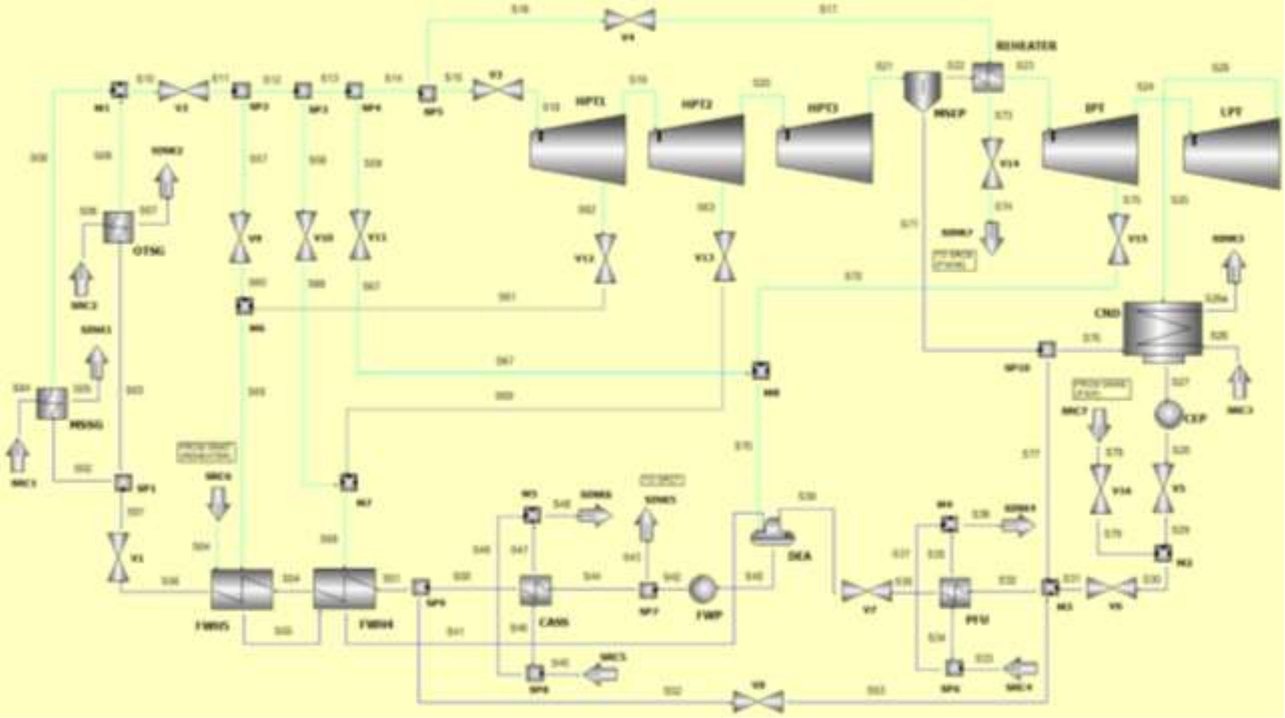

Fig. 1. Scheme of the GateCycle model of the considered PCS circuit.

In Table 1 we compiled: thermal power provided to the different heat exchangers in the circuit, shaft power of the high, intermediate and low pressure (HP, IP and LP) turbines, power of the pumps (Condensate Extraction Pump (CEP) and Feedwater Pump (FWP)) in the PCS circuit, as well as the total rate of heat supplied to the cycle from different sources, the net electrical power produced by the cycle, and the cycle efficiency**.**

Table 1. The results of power (in MW) and efficiency (in %) evaluation

	max of max		**A1-2**	
	PULSE	**DWELL**	**PULSE**	**DWELL**
Q_{OTSG}	1883.99	18.83	1813.02	18.13
Q_{CASS}	230.03	2.30	230.05	2.30
Q_{PFU}	238.00	2.38	238.03	2.38
Q_{MSSG}	12.27	266.01	12.27	266.76
W_{HPT1}	77.45	7.05	73.89	6.86
W_{HPT2}	80.99	8.33	77.52	8.98
W_{HPT3}	82.57	8.25	80.14	7.59
W_{IPT}	134.65	16.74	128.68	16.74
W_{LPT}	412.62	36.11	399.81	36.70

Conclusions

We developed the detailed convergent GateCycle model of the updated PCS circuit for the EU-DEMO plant option WCLL BB with small ESS for the „max of max" scenario in which the plant components were sized to incorporate the maximum power of all the reactor heat sources. The model provided preliminary design and sizing of the main PCS circuit components which will help in their cost estimation (available in the detailed GateCycle reports). We performed simulations of steady-state operation of the Rankine PCS cycle during the plasma pulse and during the dwell phase.

The proposed PCS „max of max" cycle operates with the electrical power (W_{cycle}) of about 720 MW and 61 MW during the pulse and dwell phases, respectively, and the power cycle efficiency $\eta_{cycle\ av}$ (averaged over the whole operation period of the cycle) of about 30.36 %, which was verified independently by the industry with the EBSILON code. These values revise the preliminary estimations for the "max of max" variant considered in 2022. GateCycle simulations, in the „Off design" mode, of the cases A1-2 pulse and A1-2 dwell confirmed that the proposed PCS circuit should be able to reach the most problematic A1-2 operational scenario. In the A1-2 scenario the electrical power of the cycle was about 692 MW (during pulse) and about 61 MW (during dwell), whereas the averaged power cycle efficiency was only slightly lower than in the respective "max of max" scenario (30.07%).

The PCS cycle has been complemented with a bypass line on feed water after DIV CASS HX, that should allow to control the plant in all the 12 operative scenarios envisaged by the new Energy Map, in particular for those power distributions (such as A1-2), in which the thermal load provided to PFU and CASS HXs is the highest. This solution guarantees stable OTSG thermodynamic conditions in all the scenarios. Finally, the bypass mass flow delivered to PFU HX inlet to increase FW temperature and reduce thermal stress in that HX.

Collaboration

Ansaldo Nucleare (Italy)

References

[1] L. Barucca, et al., Pre-conceptual design of EU DEMO balance of plant systems: objectives and challenges, Fusion Eng. Des. 169 (2021) Art. No. 112504.

[2] L. Barucca, et al., Maturation of critical technologies for the DEMO balance of plant systems, Fusion Eng. Des. 179 (2022) Art. No.113096.

[3] A. Del Nevo, Final Report For the Task BOP-2.2-T013-D001, 2019. https://idm.euro-fusion.org/default.aspx?uid=2MN55V.

[4] I. Moscato, Intermediate Progress Report, 2021. https://idm.euro-fusion.org/?uid=2P6G7T.

[5] L. Malinowski, M. Lewandowska, L. Barucca, E. Giuffra, A. D'Alessandro, A. Burlando, A.J. Rovira De Antonio, Design of the secondary circuit for the WCLL BB option of the EU DEMO power plant based on the new Energy Map, Fusion Eng. Des. 191 (2023) Art. No.113502.

[6] M. Lewandowska, L. Malinowski, WCLL BoP direct with small energy storage concept design: PCS gate cycle analysis of operational point A2-1 (PCS concept (PCS concept "maximum of maximum") (2022). Final report for the task BOP-S.02.02-T012-D002.

[7] M. Di Prinzio, A. Burlando, Review of the WCLL BoP direct with small energy storage pcs architecture in BOP-S.02.02-T001-D001 architecture update of the power conversion system (PCS), industry. Final Report For the Task BOP-S.04.02-D001, 2023. https://idm.euro-fusion.org/?uid=2R58ZE.

Related 2023 articles and conference presentations:

1. Poster: L. Malinowski, M. Lewandowska, L. Barucca, A. Burlando: "Analysis and optimization of the secondary circuit for the option WCLL BB direct coupling with small ESS of the EU DEMO power". Presented at the 15th International Symposium on Fusion Nuclear Technology (ISFNT-15), Las Palmas (Spain), 10-15.09.2023.

2. L. Malinowski, M. Lewandowska, L. Barucca, A. Burlando: "Analysis and optimization of the secondary circuit for the option WCLL BB direct coupling with small ESS of the EU DEMO power". Fusion Engineering and Design 199 (2024) 114130.

Research Unit: West Pomeranian University of Technology

WPMAG: Magnet System

Title: Thermal – hydraulic analysis of the DEMO winding packs and hydraulic tests

Authors: Monika Lewandowska, Aleksandra Dembkowska, Paweł Herbin

Introduction

Recently the designs of the PF winding packs have been proposed by the CEA IRFM, Cadarache and EPFL-SPC, PSI Villigen teams, and they are presently undergoing comprehensive analyses. According to the CEA design [1], each PF coil will be double pancake wound using a rectangular NbTi Cable-in-Conduit conductor (CICC) with a central cooling channel delimited from the bundle region with a steel spiral. The outer diameters of the central spirals in the PF3, PF4 and PF6 conductors designed by the CEA IRFM team are in the range 13.6 - 15.8 mm. Spirals with such large diameters have never been tested for pressure drop, so it is uncertain if the available friction factor correlations, developed based on measurements or CFD simulations performed for spirals with smaller diameters D_{in}/D_{out} = 8/10 mm or 9.9/11.9 mm, are sufficiently accurate for them. Pressure drop tests of samples with geometry identical to the PF3, PF4 or PF6 spiral would be desired. It would also be interesting to check if the 3D printing technology could be used to prepare WPMAG relevant samples for hydraulic tests.

High Temperature Superconductors (HTS) are promising materials to be applied in future fusion magnets HTS conductors are already considered as a possible option for some components of the superconducting magnet system of the EU DEMO tokamak, which are being designed by the EUROfusion consortium, Geometric and thermo-physical characteristics of HTS and Low Temperature Superconductors (LTS) conductors differ significantly, therefore it can be expected that numerical simulations of the behaviour of HTS conductors may require specific approaches, different from those which are successfully used for LTS conductors, particularly in cases when fast transient processes (such as e.g. quench or the breakdown) are considered. In order to provide data for better understanding of the quench evolution in HTS conductors as well as for testing different numerical approaches and proper tuning of the numerical codes, a series of dedicated HTS 15-kA sub-size samples with different geometries were produced and tested by the EPFL-SPC team in 2021 at the SULTAN facility in the Quench Experiment. Further experiments on AC losses generation in HTS conductors with different geometries are also currently being performed by the EPFL-SPC team at the SULTAN test facility. Recently the novel design of the conductor for the innermost layer of the DEMO CS coil, based on the HTS CORC® strands, was proposed by the Advanced Conductor Technologies (ACT) and University of Twente (UT) teams.

Our tasks on HTS conductors included completion of the work on the analysis and interpretation of the results of the selected run of the Quench Experiment using different numerical approaches (in tight collaboration with the IFJ PAN team), and continuation of the work on the thermal-hydraulic analysis of the CORC conductor at normal operating conditions, started in 2022.

Results

1. Hydraulic tests

Samples for hydraulic tests, with the geometry similar to cooling channels of LTS CICCs, are usually produced by inserting a spiral into the tight steel or rubber pipe [2], which is very problematic. A new

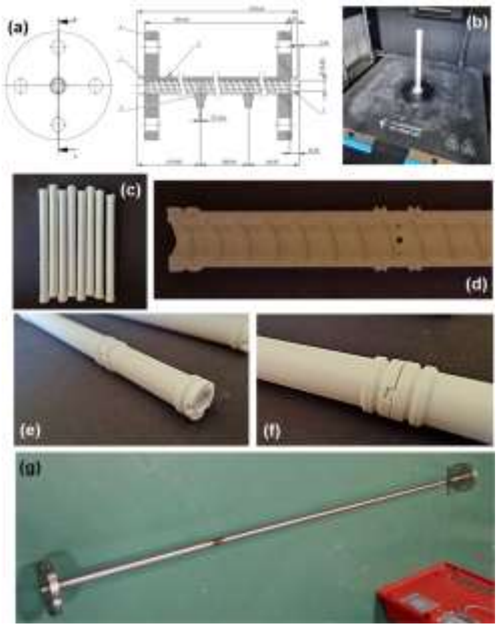

Fig. 1. Preparation of the Showa sample a) schematic drawing, b) printing of a single sample component, c) printed components of the Showa sample, d)-f) details of the sample component, g) Showa sample ready for the hydraulic test.

method of preparation samples suitable for hydraulic tests, utilizing the 3D printing technology, have been developed. The subsequent stages of the sample preparation are presented in Fig. 1. Several sample components were connected in series, as shown in Fig. 1f, and inserted into a steel tube equipped with the pressure taps. At the location of pressure taps 6 holes were drilled at the equal distances along the sample perimeter (see Fig. 1d and 1e). To ensure tight fitting of the sample components to the tube and prevent flow of the working fluid between the outer surface of the sample components and the inner surface of the tube, we placed seals at both end of each sample component, and at both sides of the drilled sections.

As the first step, we produced a sample with a geometry identical to the Showa spiral used in some of ITER CICCs. This spiral had already been tested in the Othello installation (CEA Cadarache, France) using nitrogen at room temperature [2]. This stage was aimed at checking whether spiral samples produced by 3D printing have the same hydraulic resistance as the respective samples obtained in the traditional way. A second sample prepared by us had the geometry identical to the central channel of the DEMO PF3 CICC designed by the CEA team.

Each sample was subjected to a hydraulic test at the THETIS installation [3,4], which involved measuring the pressure drop as a function of the mass flow rate, using demineralized water at three temperatures as a working fluid. The obtained results in dimensionless form (friction factor vs. Reynolds number) are presented in Figs. 2.

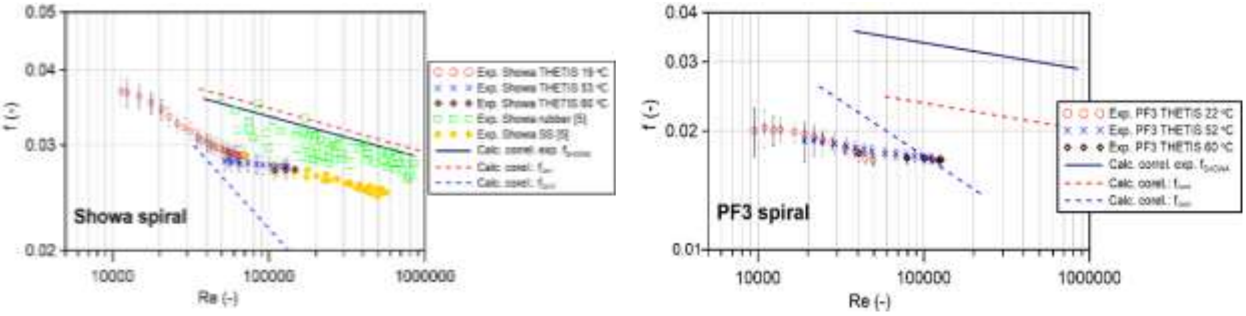

Fig. 2. Results of the hydraulic test of the Showa sample (left) and the PF3 spiral sample (right).

For comparison, we added in Fig. 2 predictions of three friction factor correlations for flow in the spiral channels available in the literature [6-8]. It is seen in Fig. 3 that the test results of the Showa sample obtained at THETIS are fully consistent with those measured earlier on the Showa spiral inserted in the steel tube [2],[5]. It can also be noticed in Fig. 3, that predictions of the friction factor correlations available in literature are not very accurate for spirals with large diameters.

2. Thermal-hydraulic analysis of the HTS CORC conductor for the DEMO CS coil

Preliminary thermal – hydraulic analysis of the HTS conductor based on the CORC concept, designed by the Advanced Conductor Technologies and the University of Twente team for the innermost layer of the central CS1 module of the DEMO central solenoid, was performed. Normal operation of the conductor according to the simplified current scenario (without breakdown), shown in Fig. 3, and a tentative model of heat loads due to the hysteresis and coupling losses was simulated using the THEA code. Two variants of the CS1 geometry were considered: the single CS1 module and the CS1 module split into 2 submodules CS1L and CS1U. In the latter variant the hydraulic length of the conductor is twice smaller. Time evolution of the minimum temperature margin (ΔT_{marg}) during the two subsequent current cycles was analyzed (see Fig. 4).

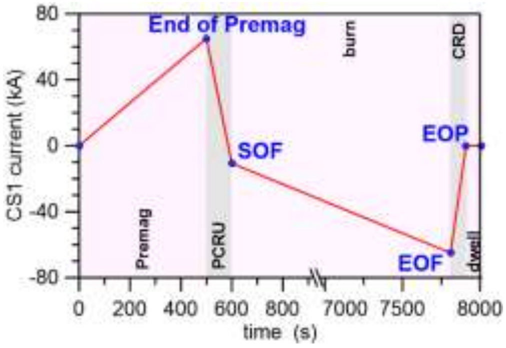

Fig. 3. The current scenario assumed in the analysis

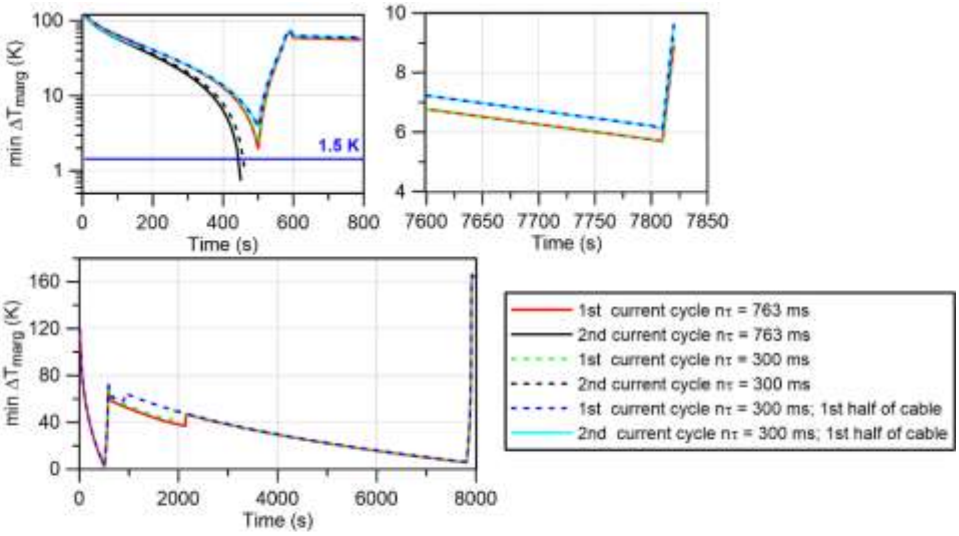

Fig. 4. Time evolution of the minimum temperature margin.

The global minimum of ΔT_{marg} was observed at the end of the Premag phase. For the assumed model of the heat loads the minimum ΔT_{marg} drops below 1.5 K in the second cycle for both considered $n\tau$ values for a single CS1 module, but for the central module split into CS1U and CS1L the minimum ΔT_{marg} was sufficiently large.

3. Continuation and completion of the analysis and interpretation of the results of the selected run of the Quench Experiment (in collaboration with the IFJ PAN team).

As a continuation of efforts started in 2022, we completed THEA simulations of the selected run of the Quench Experiment using two conductor models with different level of complexity and different pairs of values of the uncertain model parameters (contact heat transfer coefficient between different solid cable components and copper RRR).

Summary and conclusions

We developed a new procedure of preparation samples with the same geometry as cooling channels in CICCs, suitable for hydraulic tests at THETIS. We checked that the hydraulic characteristics of the spiral Showa sample prepared was fully consistent with that prepared in a traditional way (steel tube with a tight spiral insert). Thus, it was confirmed 3D printing can be considered as a cheap and convenient method to prepare WPMAG relevant samples for hydraulic tests. Hydraulic tests of the samples with geometry identical to the cooling channels of the DEMO PF4 and PF6 conductors is planned in 2024.

The preliminary thermal-hydraulic analysis of the CORC HTS conductor revealed that the minimum temperature margin at operating conditions can be too low, which calls for attention of the conductor designers. Further, more detailed studies should be performed in 2024. Heat loads due to the eddy current losses in the copper structure and the breakdown phase could be included in the model. Other scaling law and alternative models of heat generation due to hysteresis losses should also be considered. Increasing the diameter of the cooling channel, reducing the tape width or increasing the superconductor cross section (e.g. by reducing the gap fraction) could be considered by the conductor designers.

Collaboration

IFJ PAN, Kraków (Poland)
CEA Cadarache (France)
University of Twente (the Netherlands)

References

[1] L. Zani, CEA TF, CS and PF winding packs designs, Final report for the task MAG-2.1-T026 (2020), https://idm.euro-fusion.org/?uid=2N9WUY.

[2] S. Nicollet, et al.: Review of Singular Cooling Inlet and Linear Pressure Drop for ITER Coils Cable in Conduit Conductor, AIP Conference Proceedings 823 (2006) 1757.

[3] M. Lewandowska, W. Rachtan, A. Dembkowska, L. Malinowski, L. Zani, Fusion Eng. Des. 124 (2017) 1191-1194.

[4] M. Lewandowska, A. Dembkowska, L. Malinowski, IEEE Trans Appl. Supercond. 28 (2018) 480090.

[5] R. Zanino, et al., Fusion Eng. Des. 81 (2006) 2605–2610.

Related 2023 articles and conference presentations:

1. A. Dembkowska, M. Lewandowska, R. Ortwein, A. Nijhuis, G. Anniballi, L. Giannini, D. C. van der Laan, J. Weiss: Thermal-hydraulic analysis of the CORC® conductor for the DEMO CS coil. Poster PS2-79 presented at 15th International Symposium on Fusion Nuclear Technology (ISFNT-15), Las Palmas (Spain), 10-15.09.2023

AGH: AGH University of Science and Technology

WPENR: Enabling Research

Title: Enabling Research: Development of GEM detector as a compact neutron spectrometer for fusion plasmas (NS-GEM)

Authors: W. Dąbrowski, B. Łach, A. Korba, P. Wiącek

Introduction

The goal of this project is to develop the concept of an innovative compact neutron spectrometer based on a gas electron multiplier detector (NS-GEM) that could be proposed for the ITER HRNS system. This project includes the construction of a laboratory demonstrator of NS-GEM and tests its experimental possibilities on 14 and 2.5 MeV neutron sources. The project consists of the following three topics:

1. Theory and modelling: NS-GEM synthetic diagnostic: Assumptions and design requirements for ITER neutron spectrometers.
2. NS-GEM Demonstrator: Initial stage of MCNP NS-GEM system modelling and technical design.
3. Neutron generator IGN-14: MCNP modelling of the radiation field in the IGN-14 hall and the technical design of the measuring set-up.

The work is realized in close collaboration between AGH University of Krakow and the Institute of Nuclear Physics Polish Academy of Sciences. The AGH team focus on topics 2 and 3. In 2023 two tasks have been accomplished:

1. Assessment of measurement capabilities of the NS-GEM detector: modelling and test result.
2. Design and commissioning of the silicon detector for recoil proton measurements.

Results

<u>Assessment of measurement capabilities of the NS-GEM detector: modelling and test result.</u>

The most important parameter of the designed spectrometer is its energy resolution. To evaluate the capabilities of the chosen measurement technique, we continued detailed investigations of the associated physical effects. Simulations were performed for different variants of the detection system, considering different thicknesses of the converter and different pressures of the gas mixture.

The results of simulations presented in the previous reports have been obtained using the SRIM (Stopping and Range of Ions in Matter) software. Despite many advantages this software is not fully suitable for complex detailed simulations. Therefore, we decided to employ the GEANT4 simulator – a powerful toolkit widely used in the high energy, nuclear and accelerator physics. In comparison to SRIM, it allows for: detailed study of the entire detection system and ongoing processes (neutron conversion to proton at the converter, proton passage through the active detector volume, information about δ-electrons and other secondary particles), tracking of proton trajectories and energy depositions with user defined granulation.

A sketch of the detector model created in the GEANT4 software and used for the performed simulations is shown in Fig. 1. The developed model consists of 10 mm diameter circular converter with variable thickness, neutron source placed in the center of the converter and two separate cuboid-shaped active ($100\times100\times10$ mm^3) and dead ($17\times100\times10$ mm^3) detector volumes.

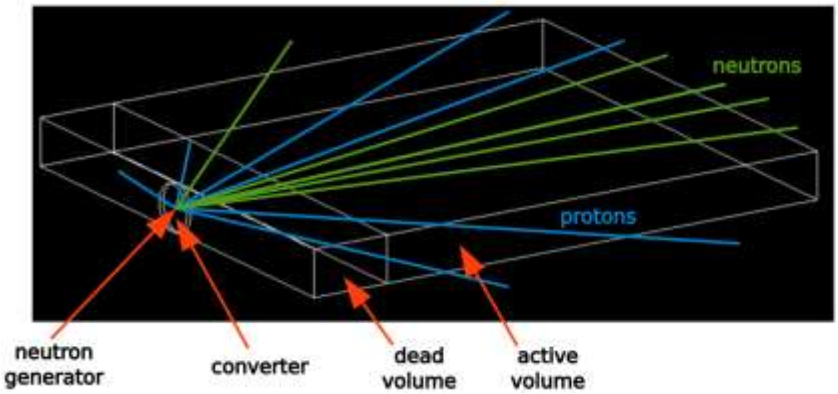

Fig. 1. Sketch of the detector geometry model created for the GEANT4 simulations [1].

Based on the simulation results, the concept of the NS-GEM spectrometer has been worked out and the detailed detector design has been elaborated starting from the standard 3-stage GEM detector. The detector model for GEANT4 simulations has been built and extensive Monte Carlo simulations with sufficiently large statistics have been performed. The simulation results allowed us to evaluate the energy resolution of our demonstrator detector and generate the calibration curves of *dE/dx* as a function of the initial energy of recoil protons, taking into account the following effects,

- efficiency of recoil proton generation,
- scattering of recoil protons in the converter and in the detector,
- proton energy losses in the converter and in the detector.

The simulation results show clearly that thickness of the converter is a critical parameter, which affects the neutron energy resolution. The thickness of the converter should be kept below 0.5 mm and preferably be around 0.1 mm, although the thinner converter the lower efficiency of production of recoil protons. The expected neutron energy resolution is of about 21 % FWHM for the $ArCO_2$ gas mixture at pressure of 1 atm and 15% FWHM at 2 atm. The dominant contribution to uncertainty of neutron energy estimation comes from fluctuations of the proton energy losses dE/dx in the detector volume.

In parallel with modeling the detector response, work on the detector construction was carried out. As proposed in the initial phase of this project, our demonstrator detector is based on a standard 3-stage GEM detector, however, with the thickness of drift region enlarged up to 10 mm compared to the standard thickness of 3 mm. This modification required designing and manufacturing of a new detector frame and proper modification of the voltage divider to ensure the same level of the electric field in the drift region as in the standard design. Furthermore, the new frame includes a mechanical interface for mounting of the neutron converter and the neutron collimator. Fig. 2 shows two photos of the detection system set up in the IGN-14 laboratory.

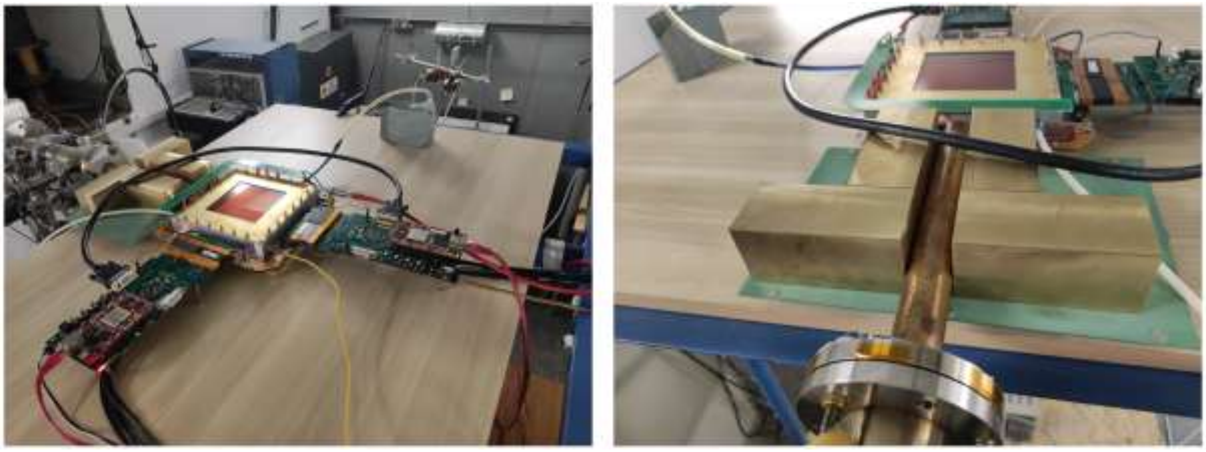

Fig. 2. Detector system set up in the IGN-14 laboratory [1].

The results of reconstruction of the proton tracks and filtering of the background events is shown in Fig. 3. As one can see, the reconstruction and filtering algorithms are working very well. From data collected within 15 minutes of measurement, and initial reconstruction of more than half of million events, only about 150 are qualified to be interesting candidates for proton originated in the converter and scattered within the angle range 0 to 35 deg. The obtained rate of tracks value is quite consistent with the one expected from GEANT4 simulations. It is worth noting that the obtained results confirm the ability of the developed NS-GEM detector to detect recoil protons and reconstruct their tracks in presence of very high background of scattered protons from different sources.

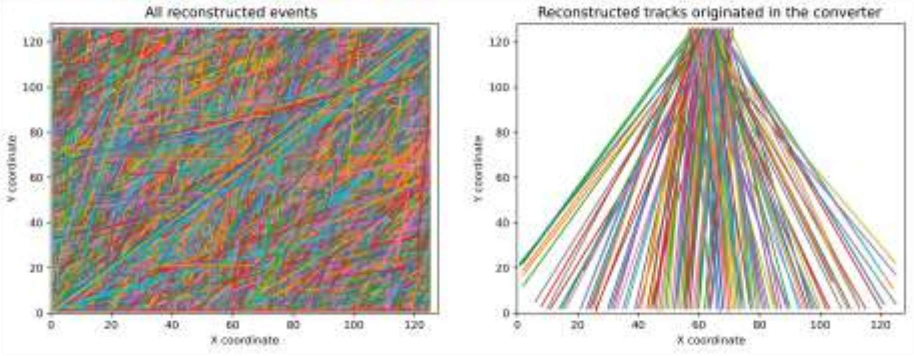

Fig. 3. All reconstructed events (left), Reconstructed proton tracks originating in the converter (right) [1].

Design and commissioning of the silicon detector for recoil proton measurements.

A silicon detector is a suitable device to construct a compact proton-recoil neutron spectrometer. The idea is to use a polyethylene thin layer as a neutron-proton converter. The energies of recoil protons can be then measured precisely in silicon detector with high energy resolution. There are, however, a few problems to be addressed in such a concept. For 14 MeV neutrons provided by neutron generator the range of recoil protons energy is from 0 to 14 MeV depending on the recoil angle. Thus, for low energies minimizing of dead layer in front of the silicon detector is critical. For the upper energy range the thickness of the detector is critical, e.g. for 14 MeV protons thickness of 1.4 mm will be needed to stop completely the protons in the silicon detector.

There are no commercially available detectors that meet these requirements. Therefore, we have designed and constructed a prototype detector using a easily available Si PIN photodiode as the proton sensor. In the prototype device we have implemented a 300 μm thick photodiode, which is easily available, but the device is designed in such a way that the SI sensor be replaced by a thicker one if available. Visualization of the detector and preamplifier assembly is shown in Fig. 4. The device has been built, parameterized and used successfully for measurements of recoil protons in the in the IGN-14 laboratory. The measurements allowed us to estimate the flux of the recoil proton and calibrate the simulation results accordingly.

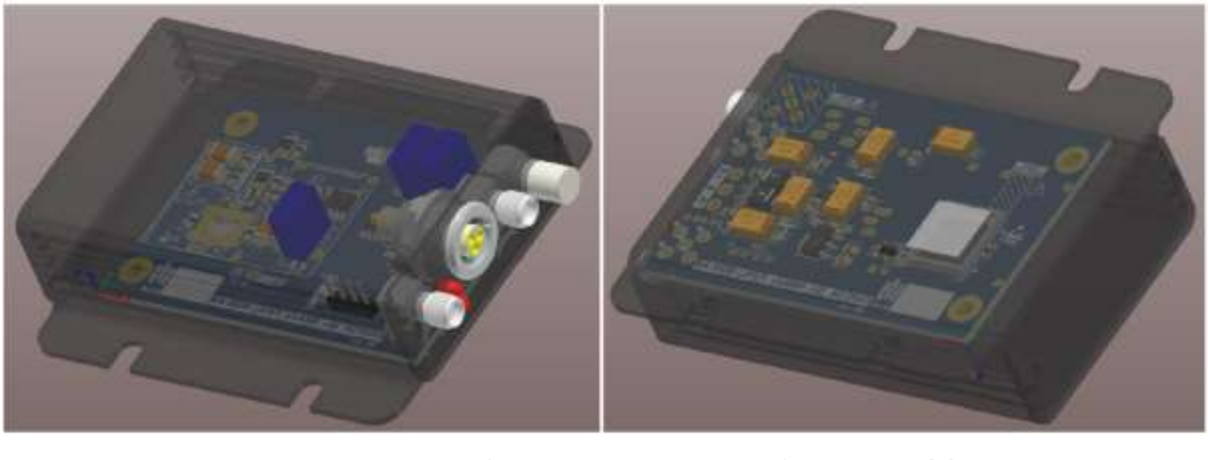

Fig. 4. Visualization of the detector and preamplifier assembly [2].

Conclusions

Based on the simulation results the concept of the NS-GEM spectrometer has been worked out and the detailed detector design has been elaborated starting from the standard 3-stage GEM detector. The detector model for GEAN4 simulation has been built and extensive Monte Carlo simulations with sufficiently large statistics have been performed. The simulation results allowed us to generate the calibration curves of dE/dx vs initial energy of recoil protons, taking into account the following effects:

- efficiency of recoil proton generation,
- scattering of recoil protons in the converter and in the detector,
- proton energy losses in the converter and in the detector.

The simulation results show clearly that thickness of the converter is a critical parameter, which affects the neutron energy resolution. The thickness of the converter should be kept below 0.5 mm and preferably be around 0.1 mm, although the thinner converter the lower efficiency of production of recoil protons. The expected neutron energy resolution is of about 21 % FWHM for the $ArCO_2$ gas mixture at pressure of 1 atm and 15% FWHM at 2 atm. The dominant contribution to uncertainty of neutron energy estimation comes from fluctuations of the proton energy losses dE/dx in the detector volume.

It is worth noting that in our demonstrator detector we can register only small fractions of proton tracks up to maximum length of 11 cm. Constructing a detector with much longer drift region up to 1 m and using gas mixture at higher pressure, achieving energy resolution of about 5% FWHM is quite feasible. However, construction of such a long detector is beyond the scope of the current project.

The demonstrator detector has been designed, built and used for first measurements in the IGN-14 neutron generator. Elaborated procedures for recoil proton tracks reconstruction have been proved to be very efficient and robust ever for very large background of signals generated in the detector due to scatter neutrons and recoil protons generated in the detector structure materials and not in the polyethylene converter. Measurements of energy losses dE/dx requires further optimisation of the detector working parameters.

A compact detector-preamplifier module using silicon PIN photodiode as the proton sensor has been developed. The module enables measurements of recoil protons using various types of neutron-proton converters and it is suitable to be used in the neutron generator facility. The test results confirm that the parameters of the developed detector meet the specification requirements.

Collaboration

IFJ PAN, CEA IRFM

References

[1] W. Dąbrowski, B. Łach, A. Korba, P. Wiącek; Assessment of measurement capabilities of the NS-GEM detector: modelling and test results. Technical Report, 2023.

[2] W. Dąbrowski, B. Łach, A. Korba, P. Wiącek; Design and commissioning of the silicon detector for recoil proton measurements, Technical Report, 2023.

Related 2023 articles and conference presentations:

1. M. Scholz et al., *Concept of a compact high-resolution neutron spectrometer based on GEM detector for fusion plasmas*, 2023 JINST 18 C05001.
2. M. Scholz et al., Proton-recoil spectrometer for fast neutron spectrum based on GEM gas detector, 49th Conference on Plasma Physics - Bordeaux - July 3rd to 7th 2023.
3. A. Jardin et al., X-ray and neutron diagnostics of fusion plasmas, Plasma 2023 - International Conference on Research and Applications of Plasmas, *Warsaw, September 18th to 22nd 2023.*

S2I: S2Innovation

Work Package: WPENS

Title: Update of DONES EPICS infrastructure design to reflect current versions of tools

Authors: Dawid Dwojewski, Grzegorz Lak, Piotr Goryl

Introduction

S2Innovation was involved in two DONES tasks:

- ENS-8.1.4.0-T013-01 - Multiple EPICS IOCs communication performance in the MPS architecture
- ENS-8.2.7.0-T013-02 EPICS to OPC-UA pilot implementation

The purpose of the first task was analyse the impact of multiple EPICS IOCs on communication delays occurring between PLC controllers and multiple EPICS IOCs in the MPS architecture. To complete the task, it was necessary to create a test stand that enabled the EPICS server to communicate with multiple PLCs. Considering the types of communication in the MPS architecture, the local testbed was equipped with two main types of communication: in-direct and direct, which were tested for latency. During the implementation of the task, to obtain the most extensive database of results, IOCs were implemented, the purpose of which was to simulate physical devices located on the LICS side of the MPS.

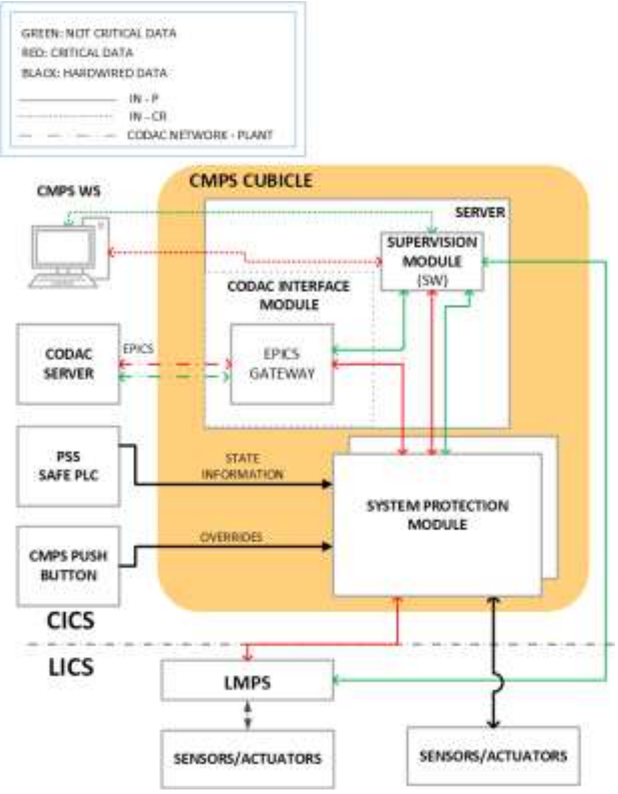

Figure 23 MPS Data Flow

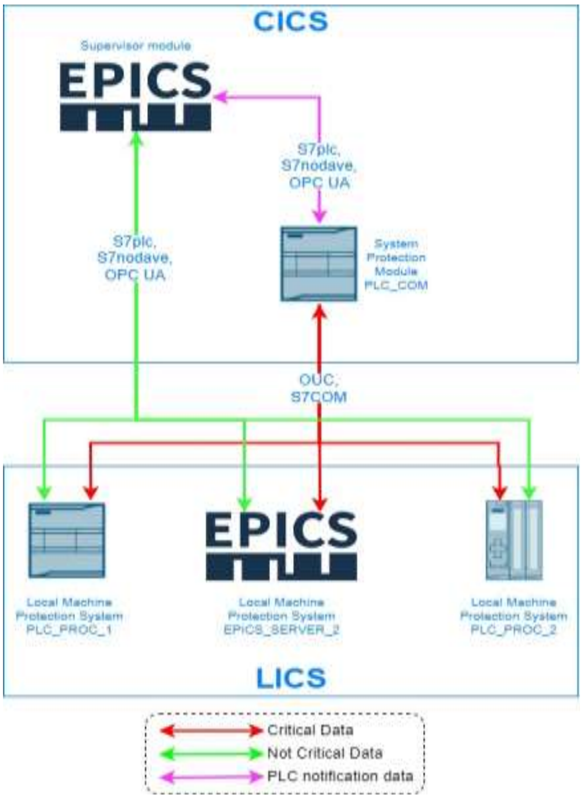

Figure 2 Test stand simplified architecture

The second task aimed was to analyse in detail the communication based on OPC UA technology, taking into account the basic delays of the control device (PLC and IPC) and the impact of changing communication procedures on the communication time. In order to implement the discussed task, a local test stand was created enabling the simulation of possible dependencies occurring in LIPAc. The implementation of the task allows you to analyse the impact of individual components of the test stand on the delays occurring in OPC UA communication.

Results

Detailed results are provided in reports [1] and [2]. Analyzing the data obtained during the tests, it is possible to notice certain dependencies occurring during the use of individual devices. For each device, the average delay value using the OPC UA controller is the highest and ranges from 460ms (for PLC_COM) to 50ms (for EPICS_2). In the case of other technologies, the data obtained indicate lower average values of communication time with individual devices. In the case of the PLC_COM device, it can be observed that the CV coefficient for the three technologies obtains similar values, which for S7plc and S7nodave are around 0,2, respectively. Communication with the OPC UA controller presents lower values of the CV parameter, which amount to 0,15. By analyzing the average values of delays obtained during communication with PLC_COM, it is possible to observe a significant impact of the selected technology on the communication time, which is caused by a change in the communication protocols used. When comparing the PLC_PROC_1 and PLC_PROC_2 devices, a reduction in the average delay value can be observed in favor of PLC_PROC_2, which, for example, translates into a 65% reduction in delays for communication with the S7nodave controller. This dependence is caused by the use of the Siemens S7-1500 device, and not as is the case with PLC_PROC_1 (S7-1200). When two EPICS servers communicate, you can observe the lowest average latency values compared to other physical devices. In the case of the EPICS secondary server, CV coefficient values are the highest for OPC UA technologies. Range for tested technologies is from 0,64 to 0,93. The earlier test also confirmed that the secondary server could serve as a replacement device for PLC devices; with the additional data generated, the impact of multiple IOCs on the MPS architecture can be analyzed.

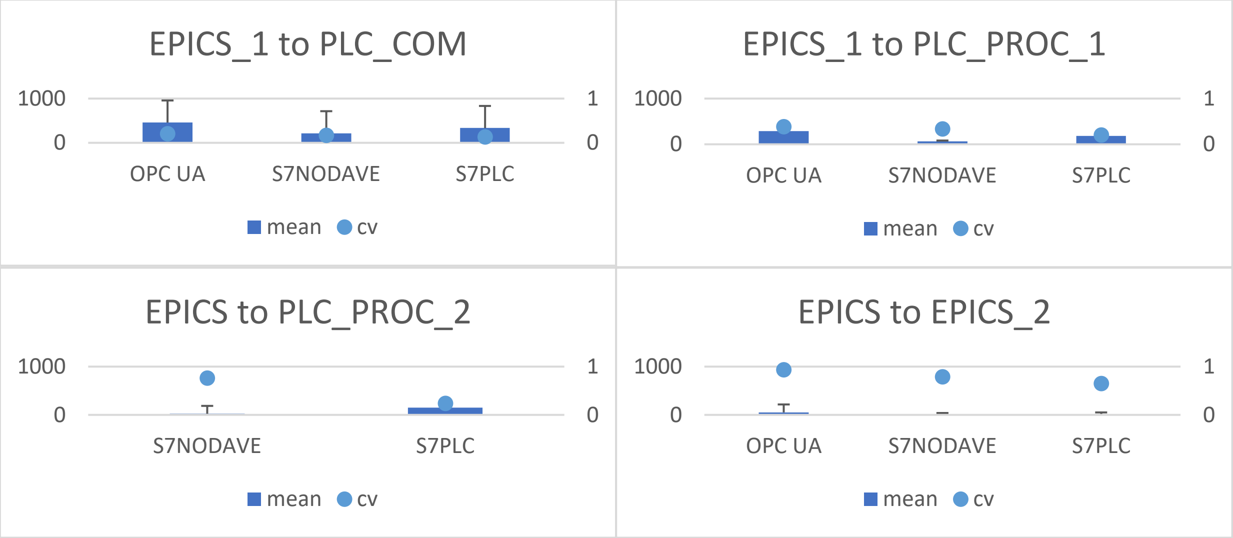

Figure 3 Summary of direct communication test results

The following is a summary of the statistical parameters obtained during in-direct and direct communication tests for twelve end devices located on the LICS side of the MPS architecture simulation. The OPC UA controller allows us to observe that in the case of in-direct communication, the average latency value for PLC devices is significantly higher.

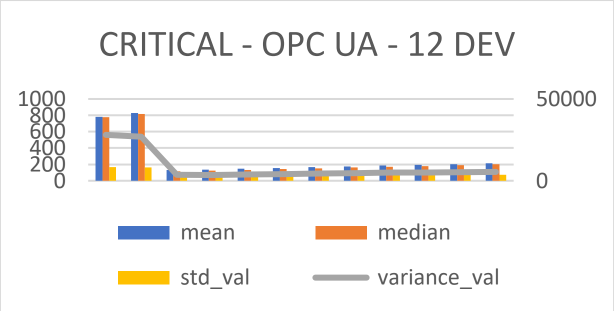

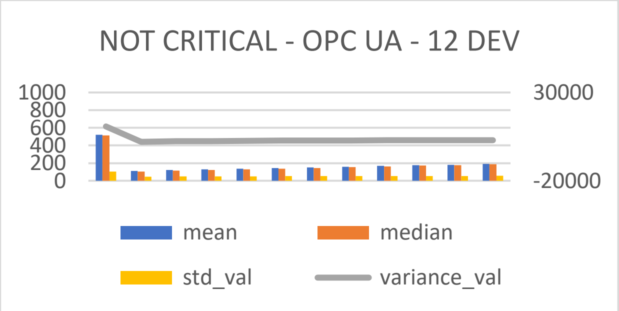

Figure 4

In-direct communication for 12 devices - Single Bit – OPC UA

Figure 5

Direct communication for 12 devices - Single Bit – OPC UA

By analyzing the statistical parameters obtained during in-direct and direct communication for the S7nodave controller, it is possible to observe the limitations of the capabilities of the Siemens S7-1200 PLC controller used as the System Protection Module. In the case of PLC_PROC_1 and PLC_PROC_2 devices, a significant increase in the average delay value is visible. PLC_PROC_1 achieved five times lower delay values for direct communication, and PLC_PROC_2 achieved nine times lower delay values.

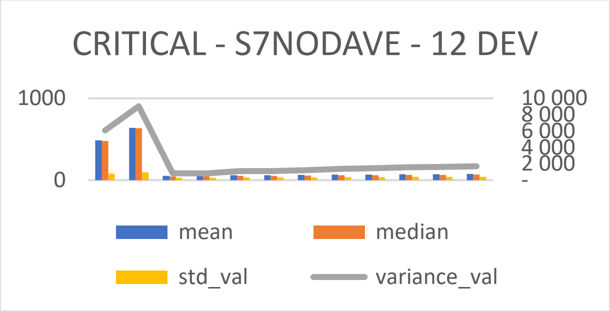

Figure 6

In-direct communication for 12 devices - Single Bit – s7nodave

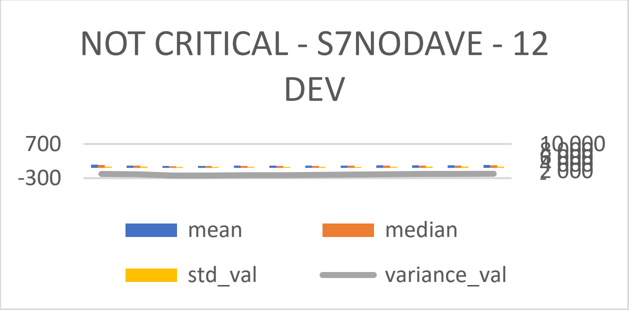

Figure 7

Direct communication for 12 devices - Single Bit – s7nodave

In-direct and direct communication tests based on S7plc technology allow you to observe the impact of an additional PLC device used as a SPM on average delay values during communication with devices located on the LICS side. In the case of PLC_PROC_1 and PLC_PROC_2 devices in in-direct communication, an increase of 10% in the average delay value is visible for the S7-1500 device.

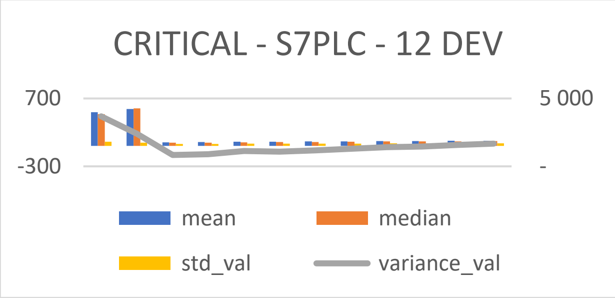

Figure 8

In-direct communication for 12 devices - Single Bit – s7plc

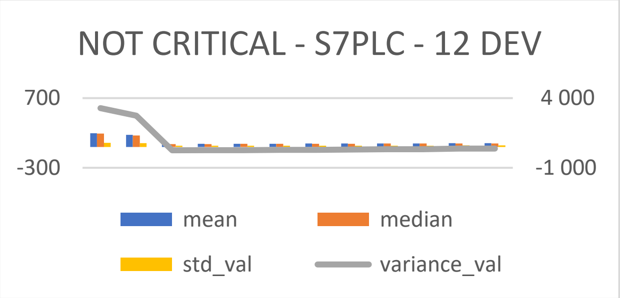

Figure 9

Direct communication for 12 devices - Single Bit – s7plc

The chart below (EPICS-PLC Direct communication test results) summarizes the average CV and standard deviation parameters for the tests discussed in this chapter. As summarized in the paragraph above, the differences between data types are negligible and do not exceed 3 ms. In addition, it can be seen that the value of the CV parameter is the same for all data types, which is due to the fact that as the average values increase, the value of the standard deviation increases proportionally.

Summarizing the data obtained during the test (EPICS – PLC – EPICS Indirect communication), one can notice a slight impact of the data type used on the average delay values during communication of two EPICS servers using a PLC device as an intermediary device. The lowest average values were obtained for the exchange of the value of a single bit and this value was rounded to 515ms. The highest average delay value was obtained for the EPICS analog value, which was rounded to 540ms. The difference between these values does not exceed 5% of the minimum value obtained during testing. The value of the coefficient of variation is low and ranges from 0,13 to 0,18.

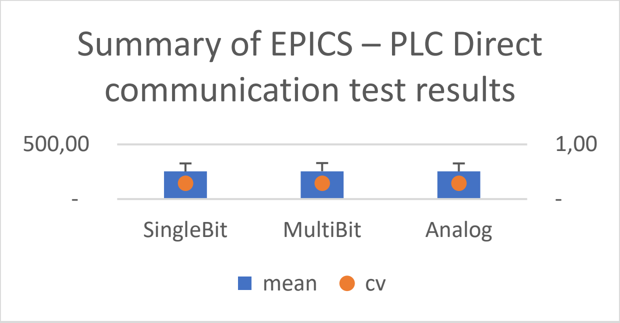

Figure 10

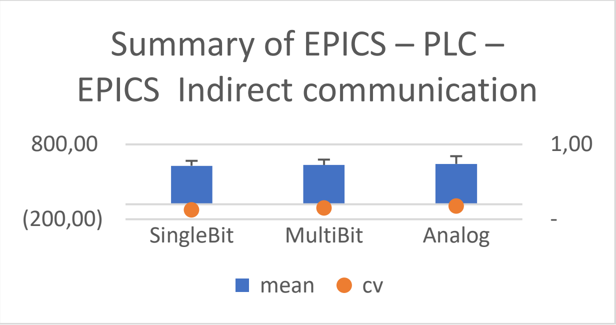

Figure 11

Conclusions

OPC UA, S7plc, and S7nodave are technologies used in automation to communicate with industrial devices. OPC UA is an open communication standard that is not tied to a specific manufacturer and supports various transport protocols, including TCP, HTTP, and MQTT. S7plc refers to Siemens logic controllers and uses specific Siemens S7 communication protocols. S7nodave is a third-party software that also allows communication with Siemens PLC devices using the S7 protocol and can use transport protocols such as TCP/IP and ISO-on-TCP. It's worth noting that OPC UA is more vendor-agnostic and cross-platform, while S7plc and S7nodave are more specific to Siemens products. Based on the data obtained during the tests, it is possible to observe the impact of the communication technology used on the average delay values occurring in the MPS architecture.

In the case of communication based on the OPC UA driver, it can be observed that in the tests performed, the communication driver used in the tests was not susceptible to additional delays related to the different type of the data packet in the network. This phenomenon occurred in each of the tests performed. Additionally, in the case of tests of indirect communication of two EPICS servers, it can be seen that the average delay value more than doubled compared to direct communication of the EPICS server with PLC_COM, which shows the importance of the complexity of the PLC software on the device's operation time. In tests carried out using the IPC device, very low average delay values were obtained, which was due to the greater computing power of the device and the greater capabilities of the S7-1500 PLC device built inside. Two-way communication tests show high repeatability of the communication cycle delay values, which confirms the obtained data.

Collaboration

The work has been performed in collaboration with the following institutes:

- Instituto de Plasmas e Fusao Nuclear, Portugal, http://www.ipfn.ist.utl.pt
- Department of Fusion and Nuclear Safety (FSN), Frascati Research Center, Italy, http://www.enea.it
- ANSALDO Nucleare, Italy, http://www.ansaldoenergia.com

References

[1] G. Lak et al., Multiple EPICS IOCs communication performance in the MPS architecture, ENS-8.1.4.0-T013-01
[2] D. Dwojewski et al., EPICS to OPC-UA pilot implementation, ENS-8.2.7.0-T013-02
[3] European Spallation Source EPICS environment source code; https://gitlab.esss.lu.se/e3/e3
[4] S7plc EPICS module source code; https://github.com/paulscherrerinstitute/s7plc
[5] s7nodave EPICS module documentation; https://oss.aquenos.com/epics/s7nodave
[6] opcua EPICS module source code; https://github.com/paulscherrerinstitute/s7plc
[7] Docker website; https://www.docker.com/
[8] Phillip Klaus's repository with Docker containers for EPICS https://hub.docker.com/r/pklaus/phoebus
[9] X11 docker source code; https://www.github.com/mviereck/x11docker/
[10] SLAC Archiver Appliance documentation https://slacmshankar.github.io/epicsarchiver_docs/

Related 2023 articles and conference presentations:

1. W. Bińczyk et al., Implementation of the MPS architecture to enable interface solutions based on new emerging technologies and tools, ENS-8.1.4.0-T008-01
2. M. Nabywaniec et al., Containerization deployment of EPICS based on the ESS E3 EPICS, ENS-8.2.7.0-T003-02-N1
3. M. Nabywaniec et al., Upgrade of EPICS7 tools for data management and alarms handling, ENS-8.1.4.0-T003-01-N1
4. W. Bińczyk et al., Implementation of the MPS architecture to enable interface solutions based on new emerging technologies and tools, ENS-8.1.4.0-T008-01

UMK: Nicolaus Copernicus University in Toruń

WPSES: Work Package Socio-Economic

Title: Public attitudes and stakeholder engagement

Author: Piotr Stankiewicz

Introduction

1. Public attitudes towards fusion

The objective of the task was to prepare a questionnaire survey at European level to assess public attitudes towards fusion. This task is a continuation of the EUROfusion European Survey (EES) launched in 2018, involving an in-depth survey of more than 20,000 respondents from 21 countries (participating in EUROfusion).

The survey was re-run in 2023 to track changes in attitudes and to include current climate and energy issues. This edition, like the previous one, was designed to:

- conduct an assessment of public attitudes and acceptance: to collect data on the views of the general public and the level of acceptance of fusion energy;
- to identify factors influencing perceptions of fusion: to examine individual, attitude-related, socio-demographic and situational factors that shape public opinion and acceptance of fusion energy and fusion research;
- to assess the impact of expert information and framing: to investigate how people's attitudes change after receiving and evaluating expert information on the implications of fusion energy;
- make comparisons between countries: produce a report detailing the differences in public awareness, attitudes and acceptance of fusion energy in different European countries.

The knowledge gained from this task is essential for guiding future research into the socio-economic dimensions of fusion development and informing strategies for engaging the public in the development of this technology.

Key aspects of this task included:

1. survey design: the survey questionnaire was developed by the Socio-Economic Survey (SES) research team. This design process involved careful consideration of the factors critical to accurately measuring public attitudes to fusion energy.
2. Consultant engagement: a specialist consultant was engaged specifically to implement the second edition of the EUROfusion European Survey on public attitudes towards fusion. The consultant's responsibilities covered all aspects of the survey implementation, ensuring a smooth process from start to finish.

2. Stakeholder Engagement

The objective of the task was to organise side-event workshops at fusion conferences to gather the views and opinions of energy experts. The assignment was based on the results of the stakeholder mapping carried out in the previous project year.

Results

Data collection for the Eurofusion European Survey (EES) was carried out in November and December 2023. The process involved the following key stages:

- sample recruitment: in November 2023, individuals aged 18 years and older were selected from extensive national panels in each participating country. This recruitment strategy ensured a broad and diverse sample, representative of the entire population.

- total sample size: The comprehensive survey sample comprised 19,144 European citizens, providing a robust basis for analysis.
- quota implementation: The use of specific quotas ensured a balanced representation of several demographic variables, such as:
  - Geographical region within each country.
  - Gender distribution.
  - Age groups.
  - Education.

Concerning the stakeholder engagement activities, two editions of a workshop entitled. "Nuclear Fusion: Talking about what's beyond the science" as side events at conferences focused on the scientific and technological aspects of fusion development:

- 30th Symposium on Fusion Engineering SOFE, Oxford, 12 July 2023.
- 29th IAEA Fusion Energy Conference (FEC), London 18 October 2023.

The target group was scientists, engineers, managers and policy makers attending the above conferences. A total of 78 people attended. The aim of the workshop was to:

- to gather views on SES research in relation to fusion and the current socio-economic, climate and energy context, starting with specific questions relevant from a societal perspective;
- to start a dialogue within the fusion research community itself.

The issues addressed in the workshop were divided into three thematic groups:

- the pathway to fusion and the time needed to get there;
- the relationship between fusion and sustainable development and climate change;
- public attitudes and public acceptance of fusion development.

Both workshops were recorded (with the consent of the participants) and the dialogue results obtained were analysed to guide further work in the SES package and discussed at the Consortium's annual meeting in Padua in November 2023. They will also form the basis of a scientific article to be prepared after the realisation of the next planned workshops during the SOFE 2024 conference.

Conclusions

Both tasks conducted within WP SES have been conducted according to plan and will be continued in the next years.

Collaboration

All activities were conducted as parts of research tasks coordinated by consortium members.

Related 2023 articles and conference presentations:

1. Paper “SOCIO ECONOMIC PERSPECTIVES ON FUSION POWER FOR A SUSTAINABLE FUTURE ENERGY SYSTEM" by: Bustreo, Chiara; Biberacher, Markus; Bongiovi, Gaetano; Börcsök, Endre; Čadenović, Rade; Čok, Vanja; Colucci, Gianvito; De Marchi, Eliana; Dongiovanni, Danilo Nicola; Ferencz , Zoltan; Geysmans, Robbe; Giacometti, Alessio; Gracceva, Francesco; Jones, Christopher; Kembleton, Richard; Kenens, Joke; Lamut, Urša; Lechon, Yolanda; Lerede, Daniele; Lopes Cardozo, Niek; Meskens, Gaston; Müller, A; Nizar, B. A.; Olahne Groma, Veronika; Oltra, Cristian; Orlando, Maria Teresa; Povh, Janez; Prades, Ana; Savoldi, Laura; Stankiewicz, Piotr; Trotta, Antonio; Turcanu, Catrinel; Vitiello, Silvia; Ward, Samuel submitted for publication in *Nuclear Fusion*
2. Poster “EUROFusion Work programme on Socio Economic Studies” at 29th IAEA Fusion Energy Conference (FEC), London 16-21 October 2023.